

UNCLASSIFIED

AD

①  
CB

# Surface Studies of Photoemissive Materials

AD734849

Final Report

November 1, 1968 to October 31, 1970

Edited by  
W. T. Peria

JUNE 1971

DDC  
RECEIVED  
JAN 9 1972  
B  
Or

U.S. Army Research and Development Laboratories  
Fort Belvoir, Virginia

Physical Electronics Laboratory ✓  
Department of Electrical Engineering  
University of Minnesota ✓  
Minneapolis, Minnesota 55455 ✓  
Contract No. DAAK02-69-C-0155 ✓

Reproduced by  
NATIONAL TECHNICAL  
INFORMATION SERVICE  
Springfield, Va 22151

UNCLASSIFIED

176

UNCLASSIFIED

Security Classification

DOCUMENT CONTROL DATA - R & D

Security classification of title, body of abstract and indexing annotation must be entered when the overall report is classified

ORIGINATING ACTIVITY (Corporate author)

University of Minnesota  
Minneapolis, Minnesota 55455

2a. REPORT SECURITY CLASSIFICATION

UNCLASSIFIED

2b. GROUP

REPORT TITLE

SURFACE STUDIES OF PHOTOEMISSIVE MATERIALS

DESCRIPTIVE NOTES (Type of report and, inclusive dates)

Final report Nov. 68 - Oct 70

AUTHOR(S) (First name, middle initial, last name)

Peria, W.T.

REPORT DATE

Jun 71

7a. TOTAL NO OF PAGES

173

7b. NO OF REFS

98

8. CONTRACT OR GRANT NO.

DAAKO2-69-C-0155

9. PROJECT NO.

9a. ORIGINATOR'S REPORT NUMBER(S)

9b. OTHER REPORT NO(S) (Any other numbers that may be assigned this report)

13. DISTRIBUTION STATEMENT

11. SUPPLEMENTARY NOTES

12. SPONSORING MILITARY ACTIVITY

U.S. Army Research and Development  
Laboratories  
Fort Belvoir, Virginia

3. ABSTRACT

Results of a photoelectric study of clean and cesiated Si(100) are presented and discussed. Both valence band and surface state emission was observed from the clean and cesiated silicon. The band bending at the silicon surface was determined as a function of cesium coverage.

An apparatus was constructed to measure energy and angular distributions of secondary electrons. Results are presented demonstrating inelastic diffraction and characteristic losses.

A preliminary study of surface inhomogenities due to heating GaAs is presented. The effect of such patches severely limits the long wavelength emission from GaAs-Cs photoemitters prepared on such substrates.

A deconvolution technique for increasing the resolution of Auger electron spectra obtained with conventional analyzers is described. The resultant spectra agree well with those obtained using high resolution instruments (ESCA).

DD FORM 1473

(PAGE 1)

5/11 0101-807-6811

UNCLASSIFIED

Security Classification

1-31464

UNCLASSIFIED

Security Classification

14 KEY WORDS	LINK A		LINK B		LINK C	
	ROLE	WT	ROLE	WT	ROLE	WT
Silicon Photoemission Surface States Surface Potential Electron Scattering Germanium Gallium Arsenide Auger Spectroscopy						

DD FORM 1473 (BACK)  
1 NOV 65

S/N 0101-507-6821

UNCLASSIFIED

Security Classification

A-3140-1

**SURFACE STUDIES OF PHOTEMISSION MATERIALS**

**Final Report**

**November 1, 1968 to October 31, 1970**

**Edited by**

**W. T. Peria**

**June 1971**

**U. S. Army Research and Development Laboratories**

**Fort Belvoir, Virginia**

**Physical Electronics Laboratory  
Department of Electrical Engineering  
University of Minnesota  
Minneapolis, Minnesota 55455  
Contract No. DAAK02-69-C-0155**



## FOREWORD

The research described in this report is aimed at the improvement of existing photocathodes. The reporting period is November 1, 1968 to October 31, 1970. The technical work was carried out by R. L. Erickson, P. A. Lindfors and W. M. Mularie. The research was supervised by W. T. Peria, Professor of Electrical Engineering.

Published papers and oral presentations on work supported in whole or in part by this contract.

- W. M. Mularie and W. T. Peria, "Deconvolution Techniques in Auger Electron Spectroscopy," Surface Science 26, 125 (1971).
- W. M. Mularie and T. W. Rusch, "Inelastic Effects in Auger Electron Spectroscopy," Surface Science 19, 469 (1970).
- M. R. Jeanes, W. M. Mularie and W. T. Peria, "Photoelectric Studies of Clean and Cesium-terminated Ge(100) and Si(100)," to be published.
- D. G. Fisher, "Photoelectric Study of  $\text{Na}_3\text{Sb}$  Films," to be published.
- M. R. Jeanes and W. M. Mularie, "Photoelectric Studies of Clean and Cesium-terminated Ge(100) and Si(100)," presented at the Conference on Physical Electronics of the American Physical Society, Washington, D. C., March 1971.
- W. M. Mularie and W. T. Peria, "Deconvolution Techniques in Auger Electron Spectroscopy," presented at the 17th National Symposium of the American Vacuum Society, Washington, D. C., October 1970.
- D. G. Fisher, "Photoemission Studies of the Growth of  $\text{Na}_3\text{Sb}$  Thin Films," presented at the Conference on Photoelectric and Secondary Electron Emission, Minneapolis, August 1967.
- W. M. Mularie and T. W. Rusch, "Inelastic Effects in Auger Electron Spectroscopy," presented at the Conference on Photoelectric and Secondary Electron Emission, Minneapolis, August, 1969.
- W. T. Peria, Colloquium talk at the University of Guelph, Ontario, March 5, 1971. Colloquium talk at the University of Wisconsin, Milwaukee, April 6, 1971.

## SUMMARY

Results of a photoelectric study of clean and cesiated Si(100) are presented and discussed. Both valence band and surface state emission were observed from the clean and cesiated silicon. The band bending at the silicon surface was determined as a function of cesium coverage.

An apparatus was constructed to measure energy and angular distributions of secondary electrons. Results are presented demonstrating inelastic diffraction and characteristic losses.

A preliminary study of surface inhomogeneities due to heating GaAs is presented. The effect of such patches severely limits the long wavelength emission from GaAs-Cs photoemitters prepared on such substrates.

A deconvolution technique for increasing the resolution of Auger electron spectra obtained with conventional analyzers is described. The resultant spectra agree well with those obtained using high resolution instruments (ESCA).

## TABLE OF CONTENTS

	<u>Page</u>
1. Photoemission Processes of Clean and Cesiumated Silicon	1
(100) - W.M. Mularie	
1.1 Introduction	1
1.1.1 General Considerations	1
1.1.2 Basic Concepts of Photoemission Measurements	2
1.1.3 Volume Photoelectric Emission Processes in Semiconductors	3
1.1.4 Threshold Emission Processes in Semiconductors	6
1.2 Experimental Techniques and Apparatus	6
1.2.1 Vacuum System and Accessories	6
1.2.2 LEED-Auger Electron Spectroscopy (AES)	8
1.2.3 Crystal Cleaning Facilities	9
1.2.4 Cesium Ion Deposition - Work Function Measurements	9
1.2.4.1 Oxygen Contamination of Cesium Depositions	11
1.2.4.2 Work Function Measurement Techniques	13
1.2.5 Photoelectric Measurement	13
1.2.5.1 Photoelectric Yield	15
1.2.5.2 Photoelectron Energy Distribution	16
1.2.6 Sample Preparation	21
1.3 Experimental Results	21

## TABLE OF CONTENTS (continued)

	<u>Page</u>
1.3.1 Characterization of the Clean Surface	21
1.3.2 Photoemission from Clean Si(100)	22
1.3.2.1 Photoelectric Yield:LEED	22
1.3.2.2 Photoelectron Energy Distribution	24
1.3.3 Characterization of Cesium-Covered Si(100)	26
1.3.3.1 Work Function Measurements	26
1.3.3.2 Photoelectric Yield from Cesium-Covered Si(100)	27
1.3.3.3 Photoelectron Energy Distributions from Cesium-Covered Si(100)	27
1.3.3.4 Determination of $ E_v - E_f $ vs. Cesium Coverage	31
1.3.4 Gas Adsorption on Clean and Cesium-Covered Si(100)	32
1.3.4.1 CO Adsorption	32
1.3.4.2 Oxygen Adsorption	33
1.3.4.3 Auger Spectroscopy of Si(100) ( $Cs+O_2$ )	35
1.4 Discussion	36
1.4.1 Attainment of Clean Si(100)	36
1.4.2 Characterization of Optical Transitions in Silicon	36
1.4.2.1 Interpretation of the High Yield	37
1.4.2.2 Threshold Emission Processes - Clean Silicon, Cesiumated Silicon	41
1.4.3 Band Bending at the Clean and Cesiumated Silicon Surface	45

## TABLE OF CONTENTS (continued)

	<u>Page</u>
1.4.4 Surface States on Clean and Cesium Si(100)	48
1.4.4.1 Intrinsic Surface States	49
1.4.4.2 Energy Distributions of Surface States	50
1.4.5 Model for Cesium Adsorption on Si(100)	52
1.4.6 Conclusion	53
2. Low Energy Electron Scattering Study of Germanium	54
(100) - R.L. Erickson	
2.1 Introduction	54
2.2 Experimental Apparatus	55
2.2.1 Vacuum System	55
2.2.2 Electron Gun and Scattering Chamber	56
2.2.3 Energy Analyzer	57
2.2.4 Apparatus Alignment	59
2.2.5 Target Assembly and Manipulator	60
2.2.6 Ion Bombardment Cleaning Apparatus	60
2.3 Experimental Procedure	61
2.3.1 Vacuum Processing	61
2.3.2 Secondary Electron Measurements	62
2.3.3 Auger Measurements	63
2.3.4 Electron Diffraction; Characteristic Loss and Inelastic Diffraction Measurements	64
2.3.5 Target Preparation and Cleaning	65

## TABLE OF CONTENTS (continued)

	<u>Page</u>
2.4 Experimental Results and Discussion	66
2.4.1 Secondary Electron Energy Distributions	66
2.4.2 Inelastic Scattering Measurements	67
2.5 Conclusions	
3. Study of Gallium Arsenide Thin Film Samples	70
P.A. Lindfors	
3.1 Experimental Results and Discussion	70
3.2 Conclusions	70
4. Study of Gallium Arsenide - Cesium	71
W.M. Mularie	
4.1 Introduction	71
4.2 Experimental Techniques	71
4.3 Results and Discussion	72
4.4 Conclusion	74
5. Deconvolution Techniques in Auger Electron Spectroscopy	76
W.M. Mularie	
5.1 Introduction	76
5.2 Formulation of the Deconvolution Technique	77
5.2.1 Mathematical Procedure	77
5.2.2 Specification of the Broadening Function, $B(E)$	78

## TABLE OF CONTINUED (continued)

	<u>Page</u>
5.3 Physical Basis for the Deconvolution Technique	79
5.3.1 The Equivalence of Auger and Primary Electron Scattering	79
5.3.2 The Effects of Instrument Broadening	80
5.4 Experimental Techniques and Results	82
5.4.1 Experimental Technique	82
5.4.2 Experimental Results	82
5.4.2.1 Inner Level Transitions	82
5.4.2.2 Adsorbate Transitions	85
5.4.2.3 Chemical Effects in O:KLL Spectra	87
5.5 Conclusions	90
6. References	91
7. Figures	96

## LIST OF ILLUSTRATIONS

<u>Figure</u>	<u>Page</u>
1 Principle of photoelectric retarding potential technique.	96
2 Expected behavior of the energy distribution curves for emission dominated by a) indirect and b) direct transitions.	97
3 Top and front view of ultrahigh vacuum system.	98
4 Manipulator and sample holder assembly.	99
5 Vacuum system for photoemission studies.	100
6 Cesium ion gun and zeolite ion source used for overlayer studies.	101
7 Total pressure and partial mass spectrum. Ion gun operated in (A) normal mode (B) biased to suppress ion impact current.	102
8 Hemispherical photoelectric analyzer.	103
9 Block diagram of photon source.	104
10 Photoelectric analyzer.	105
11 Auger spectra of contaminated Si(100).	106
12 Auger spectra of Si(100) during cleaning procedure.	107
13 Auger spectra of clean Si(100).	108
14 Spectral yield from clean and contaminated Si(100).	109
15 Effect of reflectivity corrections upon spectral yield from clean Si(100).	110
16 Normalized photoelectric EDC from Si(100).	111
17 Work function of Si(100) vs. cesium coverage.	112
18 Spectral yield of Si(100)-cesium.	113



## LIST OF ILLUSTRATIONS (continued)

<u>Figure</u>		<u>Page</u>
19	EDC's at 0.155 monolayers cesium coverage.	114
20	Threshold EDC's at 0.155 monolayers cesium coverage.	115
21	EDC's for $h\nu \geq 4.5$ eV, $\theta = 0.25$ Cs (contaminated).	116
22	EDC's for (a) $h\nu \geq 4.1$ eV and (b) $h\nu \geq 4.0$ eV showing coincidence of high energy edge.	117
23	EDC's at high photon energies from fully cesiated silicon.	118
24	EDC's from fully cesiated silicon between $h\nu = 5.0$ eV and 3.0 eV.	119
25	EDC's from fully cesiated silicon at photon energies above 5.0 eV.	120
26	EDC's from fully cesiated silicon showing onset of structure.	121
27	Method of determining band bending $ E_v - E_f $ vs. cesium coverage.	122
28	Results of band bending analysis using EDC data.	123
29	Auger spectrum of Si(100)-Cs without $O_2$ (b) with $O_2$ added to maximize yield.	124
30	Energy band diagrams-silicon (a) $E$ vs. $x$ (b) $E$ vs. $k$ , (c) $E$ vs. density of states.	125
31	Determination of photothresholds $\phi_v$ and $\phi_{ss}$ from $y^{2/5}$ plot.	126
32	Spectral yield of Si(100)-Cs: $\sim y^{2/5}$ plot inset.	127
33	Surface state emission as a function of cesium coverage.	128
34	Schematic diagram showing the band bending profiles of clean and cesiated Si(100).	129
35	Schematic diagram of vacuum chamber.	130

## LIST OF ILLUSTRATIONS (continued)

<u>Figure</u>		<u>Page</u>
36	Schematic diagram of experimental apparatus.	131
37	Energy distributions taken from the two modes of analyzer operation.	132
38	Schematic diagram of ion bombardment cleaning apparatus.	133
39	Schematic diagram of apparatus for secondary electron measurements I.	134
40	Schematic diagram of apparatus for secondary electron measurements II.	135
41	Schematic diagram of apparatus for Auger measurements.	136
42	Auger spectrum of carbon contaminated germanium.	137
43	Auger spectrum of clean germanium.	138
44	Secondary electron energy distribution (SEED) in specular scattering direction for $E_p = 21$ eV.	139
45	Secondary electron energy distribution (SEED) in specular scattering direction for $E_p = 31$ eV.	140
46	Secondary electron energy distribution of scattering angles of $37^\circ$ , $41^\circ$ and $45^\circ$ for $E_p = 12$ eV.	141
47	Elastically scattered intensity plot for specular scattering with $45^\circ$ angle of incidence.	142
48	Secondary electron energy distributions for annealed and sputtered surfaces.	143
49	Typical characteristic loss spectrum.	144

## LIST OF ILLUSTRATIONS (continued)

<u>Figure</u>		<u>Page</u>
50	Characteristic loss spectra.	145
51	Intensity vs. angle for (01) diffraction beam and 10 eV loss peak (01 Azimuth).	146
52	(a) Work function vs. Cs coverage for heated GaAs(110) surface. (b) I-V characteristic showing structure due to surface patches.	147
53	(a) Width of I-V curve as a function of Cs coverage and heating cycles. (b) (I-V) characteristics showing the shift due to cesium migration.	148
54	(I-V) characteristics showing the effect of surface patches on Cs migration.	149
55	(I-V) characteristics showing the effect of oxygen adsorption on the composite cesiated surface.	150
56	Phenomenological model for Auger and primary electron energy broadening in a LEED-Auger spectrometer.	151
57	Energy broadening encountered by Auger and primary electrons through scattering in the solid and instrument broadening,	152
58	(a) Experimentally observed Auger energy distribution from indium. (b) Elastic peak at the In. transition energy.	153
59	In. Auger spectrum deconvoluted using. (a) only elastic peak (b) entire spectrum, of EP(e) spectrum.	154
60	Elastic peak and Cd-M <sub>4,5</sub> N <sub>5</sub> N <sub>5</sub> Auger energy distribution from Cds(0001).	155
61	Comparison of experimental and deconvoluted Cd-M <sub>4,5</sub> N <sub>5</sub> N <sub>5</sub> spectrum.	156

## LIST OF ILLUSTRATIONS (continued)

<u>Figure</u>	<u>Page</u>
62 Comparison of ESCA Cd-M <sub>4,5</sub> photoelectric data with deconvoluted Cd-M <sub>4,5</sub> N <sub>5</sub> spectrum.	157
63 Comparison of oxygen KLL spectrum from TiO <sub>2</sub> (ESCA) with oxidized Ti using deconvoluted AES data.	158
64 Deconvoluted oxygen KLL spectrum of oxidized Mo.	159
65 Comparison of oxygen KLL spectra from Al <sub>2</sub> O <sub>3</sub> and adsorbed oxygen on aluminum.	160

# 1. PHOTOEMISSION PROCESSES OF CLEAN AND CESIATED SILICON(100)\*

## 1.1 Introduction

### 1.1.1 General Considerations

Interest in high-efficiency infrared photoemitters has recently been centered upon the study of alkali-covered semiconductor systems. Efficient photoemission from metals is unobtainable due to the large optical reflectivity and the short photoelectron mean free path characteristic of metals. Semiconductors, although possessing larger absorption coefficients and longer photoelectron path lengths, have photoelectric thresholds for efficient photoemission (i.e. valence band emission) which lie in the ultra-violet spectral region. However it was shown by Scheer and van Laar<sup>1</sup> that the adsorption of alkali metals in monolayer amounts decreased the semiconductor work function sufficiently to extend the photothreshold to the near-infrared spectral region. Phenomenologically, the work function reduction is produced by the formation of a surface dipole layer and by a change in the electrostatic potential of the semiconductor surface with respect to that of the bulk (band bending). There exists a causal relationship between the latter process and the existence of allowed electronic states in the band gap at the surface. The deposition of an alkali which, at least at low coverages, adsorbs as an ion, changes the surface state occupancy-hence the Fermi level at the surface with respect to the band edges. It follows that the photoemissive properties of the alkali-semiconductor photocathode depend strongly upon the density and distribution of these surface states.

Many techniques have been employed to determine the electrostatic potential and surface state densities at the semiconductor surface, e.g. surface conductivity and field effect measurements. Although each possesses some unique capability, these methods are basically indirect and have inherent conceptual or experimental limitations. A more direct technique, which allows greater insight

---

\*The work described in this section was partially supported by Contract No. 33615-69-C-1063 with the U.S. Air Force Avionics Laboratory, Wright-Patterson Air Force Base. It will also be reported under that program.

and observation capabilities than the above, is that of photoemission measurements. Allen and Gobeli,<sup>2</sup> and Fischer,<sup>3</sup> have to a great extent developed the photoemission techniques used in the present experiment. It should be noted that, although the photoemission measurement techniques are direct in nature, ambiguities (mainly due to experimental limitations) have previously led to disagreement in interpreting the nature of alkali adsorption upon semiconductors using these techniques.<sup>4,5</sup>

The primary motivation for this work was the need to determine in a direct manner, i.e., without recourse to other than the simplest of physical models, the effect of alkali adsorption upon band bending at a semiconductor surface. The system investigated was cesium adsorbed on silicon (100).

### 1.1.2 Basic Concepts of Photoemission Measurements

Emission of electrons from a metal or semiconductor, resulting from illumination of the surface with monochromatic light, is characterized experimentally by measurement of the spectral yield,  $Y(h\nu)$ ; i.e. the number of emitted electrons per absorbed photon, measured as a function of photon energy  $h\nu$ , and, by the measurement of the external kinetic energy distribution of emitted photoelectrons (proportional to  $\frac{dY}{dE}(h\nu)$ ) at a fixed photon energy,  $h\nu$ . Briefly, the photoemission process characteristic of volume excitation may be phenomenologically described in terms of a three-step process, involving: (a) excitation of electrons (resulting from absorption of a photon) from occupied states in the solid to higher-lying empty states, (b) the transport process of these photoelectrons to the surface and, (c) the escape or transmission of these photoelectrons into vacuum. In view of the uncertainties introduced in accounting for these three mechanisms in the externally observed photoemission data, it is not surprising that several internally-consistent theories can account for the data. However, the main features of the photoelectric emission data, characteristic of volume emission in semiconductors, can be interpreted in terms of energy band structure and scattering processes proposed by Kane.<sup>6</sup> Confirmation of this analysis was first obtained experimentally by Gobeli and Allen.<sup>7,8</sup> Using the concepts

developed by Kane, a brief resume' describing the relationship between externally observed photoelectric data and information regarding the electron states in the crystal will now be presented.

### 1.1.3 Volume Photoelectric Emission Processes in Semiconductors

It has been observed for silicon and germanium, that typical escape depths of photoelectrons are  $< 50 \text{ \AA}$ . Thus the appropriate semiconductor parameters to consider are those associated with the surface region of the crystal, as shown in an idealized model in Fig. 1. The electron affinity,  $\chi$ , is defined as the work required to remove an electron from the lower edge of the conduction band to the vacuum level at the surface, i.e.,  $\chi = E_{\text{VAC}} - E_{\text{C}}$ . Correspondingly, the work function,  $\phi$ , is defined as the work required to remove an electron residing at the Fermi energy in the crystal to the vacuum level. The photoelectric threshold,  $\phi$ , is the energy difference between  $E_{\text{VAC}}$  and the highest emitting state contributing to the externally observed photoemission. For our present purpose, it can be assumed that this threshold coincides with emission from the top of the valence band. Figure 1, considered in its totality, presents a phenomenological model for photoelectric emission from semiconductors and for the measurements of the energy distribution of emitted photoelectrons by the retarding potential technique. Illuminating the semiconductor with monochromatic light of energy  $h\nu$  raises electrons from occupied valence band states to higher-lying conduction band states as shown by the vertical lines on the left side of Fig. 1. This produces an internal energy distribution  $N(E)_{\text{int}}$  whose highest lying state is located  $h\nu$  above the highest filled state; in this case the valence band edge. As previously stated, the internal distribution will be modified by the transport and transmission properties of the solid and solid-vacuum interface. In the retarding potential measurement mode, whose parameters are illustrated in Fig. 1, the energy,  $E$ , of a group of emitted photoelectrons is measured with respect to the Fermi level of the semiconductor, i.e.

$$E - E_{\text{f}} = V_{\text{app}} + \phi_{\text{c}}, \quad (1)$$

where  $\phi_{\text{c}}$  is the work function of the collector and  $V_{\text{app}}$  is the potential applied between the semiconductor and retarding field electrode. Thus, the external energy distribution of photoelectrons,  $N(E)_{\text{ext}}$ , is obtained by varying  $V_{\text{app}}$  over a

range  $\phi - \phi_c \leq eV_{pp} \leq E_f + h\nu - \phi_c$ . Several important relationships can be derived using Fig. 1. The highest energy at which electrons are emitted, in this model equal to  $h\nu$  and appearing at  $V_{app} = h\nu - \phi_c - E_f$ , is independent of emitter work function. Conversely, the lowest energy emitted photoelectron (zero external kinetic energy) is determined by the emitter work function,  $\phi$ . The energy width of the external energy distribution is thus equal to  $h\nu - \phi$ . A more realistic model for a semiconductor (Si) surface will be examined later. However, the preceding serves to demonstrate the important parameters to be considered.

The internal and external photoelectron energy distributions are related, as mentioned previously, by the energy-loss mechanisms encountered in diffusion of photoelectrons toward the surface and upon the nature of the energy barrier at the surface. The main energy loss mechanism in diffusion toward the surface is electron-electron collision which excites a hole-electron pair across the energy gap. The mean free path for this scattering process is quite short, approximately 20-30 Å, hence, the process must be considered in interpretation of the photoelectric yield and energy distribution curves (EDCs). This scattering process, which displaces a large number of high energy electrons to lower energies in the EDCs, becomes less important when the electron affinity,  $\chi$ , becomes less than approximately twice the band gap. In this case, electrons which have energies greater than the photothreshold have insufficient energy to create hole-electron pairs. Energy losses to lattice scattering are small over the typical photoelectron escape depths; approximately 0.03 eV per scattering event (at 300°K) with a mean-free path of approximately 100 Å.

The effect of the barrier at the surface will modify the internal distribution according to the energy dependence of the electron reflection coefficient. However, the phenomenon becomes important only for electrons emitted with nearly zero kinetic energy. The main interest in this experiment is the character of the high energy edge of the EDCs, where electron energies are usually well above  $E_{VAC}$ . Hence, barrier reflection will not usually affect the analysis.



Optical transitions which contribute to the observed yield can be characterized according to Kane in terms of direct and indirect processes. In the former, the process of absorption of a photon involves both simultaneous energy and momentum conservation. Since the momentum associated with the photon,  $h/\lambda$ , is negligible compared to the electron momentum  $\hbar k$ , the final state will be located on the  $E$  vs.  $k$  diagram by a vertical line ( $k_{\text{final}} = k_{\text{initial}}$ ) at an energy  $E_{\text{final}} - E_{\text{initial}} = h\nu$  above the initial state. Conversely, in an indirect process, energy is conserved but the  $k_{\text{final}} \neq k_{\text{initial}}$ . In this process a continuum of final states is possible through exchange of arbitrary amounts of momentum with the crystal lattice. In general, the threshold for valence band emission is characterized by indirect processes since direct processes typically have a higher energy threshold.<sup>9</sup>

The characterization of the photoelectron energy distributions in terms of direct or indirect processes can be made according to Fig. 2. In the center is displayed an  $E$  vs.  $k$  diagram for a hypothetical solid. The corresponding behavior of the EDCs for indirect and direct processes are shown in (a) and (b) respectively. To distinguish between these processes, the measured EDCs are plotted with the initial states of the photoelectrons as abscissa. This is done by shifting each EDC downward by  $h\nu$ , the photon energy at which the EDC is measured. If the transitions are indirect, electrons can be excited out of the top of the valence band at all energies - hence the initial states of highest energy will coincide, as shown in Fig. 2(a). If the transitions are direct, varying the photon energy will, in general, vary the initial state of the highest energy photoelectrons, as shown in Fig. 2(b). In this case, the relationship between the initial state and the photon energy will be determined by the  $E$  vs.  $k$  topology of the solid. Experimental evidence has been obtained,<sup>10</sup> consistent with Kane's theory, showing that the high quantum yield region of the spectral yield curves are characteristic of direct optical transitions in the bulk. The relatively low yields encountered near photothreshold has been shown to be indicative of indirect optical transitions. Kane<sup>6</sup> has predicted a power-law dependence of the spectral yield upon photon energy near threshold, viz.

$$Y(h\nu) = C_n (h\nu - \phi)^n. \quad (2)$$

The exponential factor,  $n$ , is dependent upon the excitation and scattering characteristic of the photoemission process. The factor,  $\phi$ , is the apparent threshold for the process and  $C_n$  is a constant. Kane predicted a linear dependence ( $n = 1$ ) of the yield upon photon energy for direct processes and, for indirect processes, exponents of  $n = 2, 3/2$  or  $5/2$  dependent upon the nature of the indirect process. For Si(111) it was found by Gobeli and Allen<sup>9</sup> that the spectral yield could be fitted by assuming linear and cubic dependences of the yield in the high quantum yield region and threshold region, respectively.

#### 1.1.4 Threshold Emission Processes in Semiconductors

Near the photoelectric threshold the photoelectric yield from most materials can be ascribed to indirect processes involving the valence band and/or to emission from localized electron states, lying near or above the valence band maximum, at the surface. The latter states, proposed by Tamm<sup>11</sup> and Shockley,<sup>12</sup> arise from the termination of the bulk periodic potential at the surface and appear at energies not allowed for bulk states i.e. in the band gap of the semiconductor.

In the absence of surface states, and external fields, there exists no electrostatic potential difference between the semiconductor bulk and the surface i.e., the bulk energy bands continue flat up to the surface. However, the introduction of acceptor states below or donor states above the Fermi level at the surface causes a potential difference or "band bending" to be established, in equilibrium, between the surface and the bulk. The effects of band bending upon photoemission measurements depends upon the distribution and concentration of impurity and surface states of the semiconductor. In this experiment, the choice of high resistivity, pure material minimized the uncertainties in interpretation of the photoemission data, since for this material the amount of band bending over a photoelectron escape length was small. This allowed unambiguous separation between bulk and surface photoemission processes as will be shown in Sec. 1.4.

### 1.2 Experimental Techniques and Apparatus

#### 1.2.1 Vacuum System and Accessories

The requirements of several measurement capabilities, and the necessity of surface contamination-free conditions for a minimum of several thousand seconds, dictated that

the experiment be carried out in a u.h.v., ion-pumped, system capable of  $< 10^{-10}$  Torr pressure. The system used was an Ultek TNB-X metal belljar system (similar to the system shown in Fig. 3) with zeolite sorption pumping from atmospheric to  $10^{-3}$  Torr pressure and 100 liter/sec titanium ion pumping (with auxiliary titanium getters) to ultimate pressures of  $< 10^{-10}$  Torr after bakeout to  $280^{\circ}\text{C}$ . The pumping well was capable of being isolated from the upper chamber, housing the experimental apparatus, by a poppet valve. However, the sealing surface on the poppet valve, a Viton "O" ring, was removed to prevent contamination from the Viton outgassing products, mainly  $\text{Cl}_2$  and  $\text{F}_2$ . Omission of the "O" ring, however, did not severely limit the usefulness of the poppet valve. Used as a variable impedance, it facilitated studies involving controlled gas admission and also prevented cross-contamination between experimental and pumping sections e.g. hydrocarbon contamination resulting from outgassing the titanium getters.

The sample manipulator, illustrated in Fig. 4, was developed in this laboratory and was capable of 2.5" vertical motion and  $\approx 360^{\circ}$  rotation (restricted by electrical connections). The tantalum sample holder was mounted on a ceramic insulator and thereby could be electrically isolated from ground potential. It contained an internal heater filament, capable of heating the holder to  $650^{\circ}\text{C}$ , and a Pt-Pt-10% Rh thermocouple. The crystal was mounted to the holder by use of 0.20" Ta tabs fitted to slots cut into the sample. The sample holder cross-section was slightly less than the  $(0.707 \times 0.707)\text{cm}^2$  crystal cross-section so that only the crystal subtended the direct line of sight at each measurement or deposition apparatus in the vacuum system.

The vacuum station was equipped with several gas admission systems, capable of admitting controlled amounts of spectrographically pure oxygen, hydrogen and argon through Granville-Phillips type C valves. The argon was further purified using a cataphoretic procedure described elsewhere.<sup>13</sup> Much use was also made of an EAI-150 quadrupole mass spectrometer for residual gas analysis studies during several phases of the work. Two 36" diameter Helmholtz coils were mounted in the horizontal plane, symmetric about the center sample position to null out the effects of the vertical component of the earth's magnetic field. This was found critical both to the operation of the Farnsworth gun to be described later and in minimizing the effect of magnetic fields, which tended to broaden the inherent energy spread of low-energy electrons.

A schematic top view of the experimental components of the vacuum chamber is shown in Fig. 5. The salient features of each and the experimental techniques used in operation of each component will now be briefly discussed.

### 1.2.2 LEED-Auger Electron Spectroscopy (AES)

The techniques and value of LEED and AES in analysis of surface symmetries and surface chemistry has been well documented.<sup>14,15,16</sup> The applications of low-energy electron diffraction (LEED) in the determination of long and short range surface atomic ordering<sup>17</sup> and for surface structural determinations<sup>18</sup> have been successful to varying degrees. It is assumed in simple kinematical theory that only consideration of the two-dimensional periodicity of the surface is necessary to describe features of the LEED pattern and diffraction intensities. Experimentally, the observation of a "standard" LEED pattern of high intensity with respect to the non-coherent background is used as necessary, but not sufficient, proof that the surface is in a clean, ordered state.

Auger Electron Spectroscopy (AES) has been shown to be complementary to LEED in establishing the condition of chemical purity at a surface. Briefly this technique characterizes the chemical composition of the surface layer, to depths<sup>19</sup> of approximately 10 - 25 Å, by analyzing the energy distribution of electrons emitted from the surface region under the influence of electron bombardment. A certain fraction of the backscattered electrons occur as peaks in the energy distribution at energies (independent of the primary excitation energy) characteristic of inner atomic energy level spacings in the atom. Since these energy level spacings are unique to a particular element, the analysis of the kinetic energy of these discrete peaks gives both qualitative and quantitative information regarding the surface chemical composition. Weber and Peria<sup>14</sup> have demonstrated the compatibility of LEED and AES measurements in a standard LEED-type hemispherical analyzer. A four-grid hemispherical LEED-Auger system, illustrated in Fig. 5, was used in this experiment. The ac modulation-phase sensitive detection method proposed by Harris<sup>20</sup> was used for energy analysis of the backscattered electrons from the surface region. The detection system essentially that described by Palmberg et al.,<sup>21</sup> was capable of detecting  $< 10^{12}$  Cs atoms/cm<sup>2</sup> on the sample substrate.

### 1.2.3 Crystal Cleaning Facilities

The system capabilities for cleaning surface contamination layers from the Si(100) and Ge(100) surfaces consisted of an ion bombardment (sputtering) chamber and a heater, internal to the sample holder, for annealing the surface disorder produced by ion bombardment. The sputtering chamber was of a standard design described by Riach;<sup>22</sup> providing ion bombardment densities up to approximately  $80 \mu\text{A}/\text{cm}^2$  at 50-300 eV energy. The normal operating procedure used for ion-bombardment cleaning was to valve off the pumping well and then to turn off the system ion pumps. The system pressure was then raised to approximately  $1-2 \times 10^{-3}$  Torr of purified argon. The discharge was operated in the temperature-limited emission mode described by Riach, which is characterized by high ion current densities, stable operation and uniform sputtering. In practice, the ion energies were kept  $< 300$  eV to insure uniform ion current densities and to minimize surface damage induced by high energy bombardment.

### 1.2.4 Cesium Ion Deposition-Work Function Measurements

Weber and Cordes<sup>23</sup> demonstrated the feasibility of using ion-exchanged sodium aluminosilicate (Linde type A zeolite) sources to obtain an efficient thermally-activated cesium ion source. The obvious advantage of this ion source over evaporation sources was the ability to determine alkali coverage of a surface by simply measuring the incident ion current. This, of course, assumes a negligible neutral atom output, which would not be measured by this technique. Weber<sup>24</sup> measured the impurity and neutral Cs emission from these sources and found less than 0.3% impurity emission (mainly other alkali ions) and 2% neutral emission at the normal operating temperature of approximately 850°C. The latter was confirmed in this experiment by placing a clean surface in position for ion deposition with the sources at emitting temperature but with the target biased positively with respect to the source. By observing the work function shift of the target with time it could be determined that, within normal deposition times, less than 2% of the total alkali deposition arrived as a neutral species.

The design and construction of the cesium ion gun, shown in Fig. 6, has been previously discussed by Weber.<sup>24</sup> The activation of the cesium ion source prior to insertion into the gun was carried out in a u.h.v. system whose ambient could be

monitored by a mass spectrometer (rather than in a roughing pump system as described by Weber). This was to minimize contamination from the ambient during the melting procedure and to enable a determination of the impurity emission from the zeolite source during and after activation. The mass spectrum showed mainly CO, CO<sub>2</sub>, and H<sub>2</sub>O present, at a temperature slightly below the fusion point, and a large burst of CO and CO<sub>2</sub> accompanying the fusion of the source onto the Pt foil. The operating point of the source was determined from the power input vs. emission current characteristics after activation. The operating temperature was chosen to allow a 1-2  $\mu$ A ion current to be extracted from the source.

The experimental procedures used in operating the ion gun, such as the determination of the operating potentials on the gun electrodes, were dictated by several considerations: uniformity of ion deposition, the need to measure accurately the total number of deposited ions and the desire to operate the gun in a contamination-free mode. The uniformity of deposition was determined by measuring the work function over several areas of the crystal after deposition. Excellent uniformity, corresponding to a variation in work function reduction of less than 5% over the crystal surface, was found when the ion gun was operated in the defocussed mode described by Weber. In this mode the gun potentials were set so that the ratio of the ion current, measured at the rectangular aperture ("A" in Fig. 6), to the target current was in the ratio of the aperture area to the target area. The measurement of the total amount of deposited Cs, as previously mentioned, was dependent upon the neutral emission from the source but was also dependent upon the incident ion energy. The latter arises from the energy dependence of the sticking probability. Using AES, McNeil<sup>25</sup> determined that the sticking probability for 20 eV K<sup>+</sup> ions on Si was only 0.80. At less than 6 eV, which was the upper limit of ion energies used in this experiment, the sticking probability was shown to approach unity.

Ion sources, although used extensively for quantitative alkali deposition, can under certain conditions give rise to contamination. In particular, it was shown in this experiment that, if operated improperly, the zeolite sources

produced sufficient molecular oxygen to significantly affect the experimental results. The supportive evidence for this statement and resolution of this problem will now be discussed in some detail.

#### 1.2.4.1 Oxygen Contamination of Cesium Depositions

It was observed in these experiments, using high sensitivity AES measurements, that, even under uhv ( $1 \times 10^{-10}$  Torr) conditions, there existed oxygen contamination in the ion-deposited cesium layers. Subsequent use of the quadrupole mass spectrometer to monitor the ambient gas during operation of the ion source produced a rather surprising result: a mass peak corresponding to  $O_2^+$  was observed only during the process of extracting ions from the source. No  $O_2^+$  component was observed while outgassing the source above the operating temperature, or by any other means than ion extraction. The oxygen peak in the mass spectrum could be literally switched "on" and "off" by biasing the circular grid "B" (Fig. 6) negatively or at positive potential with respect to the ion source. Further, the magnitude of the oxygen peak was observed to be roughly proportional to the ion current extracted. This observation indicated that either the oxygen component was due to ion-impact desorption of molecular oxygen from the surface of the ion gun electrodes, or it was emanating from the alumino-silicate source. The former was discounted through the following experiment: the ion gun was operated in two modes: (a) the normal operating mode with the approximate potentials shown in Fig. 6 and (b), operated with only circular grid "B" negative with respect to the ion source and all other potentials at  $0^V$  (filament potential). The latter mode, (b), allowed extraction of ions but did not allow ions to strike the gun surfaces. The total pressure of the system was measured by a Bayard-Alpert gauge and gas composition was recorded using the EAI quadrupole mass spectrometer. The filament was kept at a constant temperature (approximately  $850^\circ C$ ) and the potential on grid "B" was varied from 0 to  $-25^V$ , causing variation in the extracted ion current from 0 to  $5 \mu A$ . Figure 7 illustrates the results obtained by operating in each of these modes. Curve A is typical of the rise in pressure observed with increasing ion current operating in mode (a). This was mainly due to a large  $CO^+$  component, as shown by the corresponding partial mass spectrum, resulting from ion-impact desorption from the ion gun electrode surfaces. Operating in the latter mode (curve (b)) and, thereby, suppressing ion-impact gas desorption caused a precipitous

decrease in the  $\text{CO}^+$  peak with essentially no change in the  $\text{O}_2^+$  peak, as shown in the corresponding partial mass spectrum. The slight increase in total pressure in curve B with increasing ion current was due mainly to an increase in the  $\text{O}_2^+$  peak. Biasing grid "B" positive produced an immediate decrease in total pressure and the  $\text{O}_2^+$  peak magnitude. From this evidence, it was clear that the  $\text{O}_2$  partial pressure did not arise from ion-impact gas desorption, but was related to processes at the ion source. The observation of the phenomenon suggested a solid-state electrolysis process i.e., the process of continuous ion extraction from an essentially insulating source (alumino-silicate) proceeded by negative  $\text{O}^{2-}$  neutralization. Subsequent recombination at the Pt foil may liberate  $\text{O}_2$  as observed. There may have been, of course, an intermediate process resulting in oxygen evolution at the filament. The level of contamination resulting from this oxygen evolution was dependent upon the cesium coverage and manner of operating the ion gun. Comparison of photoemission, work function and AES data indicated that during normal deposition runs, typically,  $\sim 10\%$  of oxygen coverage could be inadvertently obtained concurrent with deposition of cesium to maximum coverage. The effect of oxygen contamination at maximum cesium coverage depended upon the total amount of oxygen evolved, but usually resulted in an enhancement of the photoelectric yield and a reduction in the sample work function. The correlation of the oxygen contamination level with cesium coverage was derived by monitoring the intensity of the  $\text{O:KLL}$  and  $\text{Cs: } M_{4,5}N_{4,5}N_{4,5}$  transitions by AES, as will be discussed in Sec. 1.3.4.3 and illustrated in Fig. 29.

The resolution of this dilemma, found by monitoring the ambient gas composition and AES spectrum of the deposited cesium, was to pre-heat the source, for 1-2 minutes at  $50\text{--}100^\circ\text{C}$  above the normal operating temperature (grid B =  $+22.5\text{V}$ ) prior to ion deposition. Subsequently reducing the source temperature and depositing in the normal mode, produced an effective increase in the rate of ion deposition of 3-5 times that obtained without preheating and an oxygen contaminant level (from AES data) at full cesium coverage, amounting to less than 2-3% of the maximum obtainable oxygen coverage. When full Cs coverage was reached in a single deposition, the oxygen AES peak could not be detected at the limit of our detectability.



The preheating procedure may be rationalized in terms of producing a  $\text{Cs}^+$  space-charge region or cesium enriched layer at the zeolite surface, prior to deposition. A cesium surface layer could increase the surface conductivity, and thus, the probability of electron neutralization during ion emission. Whatever the physical process involved, extraction of ions from this source, which was preheated in the above manner, resulted in a larger ion current with little oxygen evolution during deposition.

#### 1.2.4.2 Work Function Measurement Techniques

The sample work function was measured using a gun described by Farnsworth.<sup>26</sup> Measurement of relative shifts in sample work function from the resulting retarding potential curves could be made within approximately 0.02 eV, but an absolute measure of the sample work function could not be determined from these curves. Information regarding the absolute work function was, however, obtained from photoelectric measurements to be described later.

#### 1.2.5 Photoelectric Measurements

The two related photoelectric measurements to be discussed below; viz., the photoelectric yield  $Y(h\nu)$  and the energy distribution of photoelectrons,  $\frac{dY}{dE}$ , were made using a 3-grid hemispherical energy analyzer, shown essentially to full scale in Fig. 8. A stainless steel shield covered the entire grid assembly, eliminating electrostatic pickup from external sources and, as previously mentioned the use of external Helmholtz coils minimized the magnetic field distortions in the analyzer. A hemispherical 304 stainless steel collector with a 1/2" diameter hole on the optical axis was mounted concentrically to the grid structure as shown in Fig. 8. A circular repeller, normally biased -6V with respect to the collector, was used to prevent photoelectrons from escaping through the light beam input hole. An optical grade G.E. sapphire window was mounted on the flange to allow the light beam input from the exterior monochromator.

A double-monochromator optical system of a design used by Fisher,<sup>27</sup> and later modified and described by Riach,<sup>22</sup> was used in this work. The main design consideration, that enabled meaningful photoemission measurements

to be made, was the requirement of spectral purity of the light output. Subject to this constraint, it was desirable to obtain maximum output intensity to enable measurements from low yield photosurfaces, e.g., clean Si. Figure 9 illustrates the basic layout of the photoemission system. The spectral purity was obtained by coupling two monochromators (Bausch and Lomb 33-86-25 and 33-86-40) in series and subsequently filtering out the higher order dispersions, which are characteristic of grating monochromators, at the output of the second monochromator. The output section consisted of quartz-fluorite lenses in the focusing stage and two quartz beam splitters, which shunted a small fraction of the output light to RCA 937 (spectral range 5.5-3.10 eV) and RCA 917 (3.05-1.20 eV) photocells. The focal length of the assembly was variable and provided a well-focussed 2mm x 2mm spot at the center of curvature of the photoanalyzer. To enable determination of the beam size and focus at the sample surface (when positioned at the center of curvature of the photoanalyzer), a frosted-glass target with a rear mounted 45° mirror was mounted on the sample rod (not shown in Fig. 4) at an angle of approximately 90° with respect to the sample. This allowed observation of the size and the degree of focus of the light beam impinging upon the glass, when the latter was positioned in front of the analyzer. Subsequent rotation of the manipulator brought the sample into position for measurements. The output light intensity available at the sample position was dependent upon the light source used, which in turn, depended upon the measurement mode desired. The photoelectric yield measurements were most conveniently made using a Bausch and Lomb 150 watt Xe lamp, which provided a relatively smooth, high intensity spectral output. This lamp, however, was found unsatisfactory for energy distribution measurements due to its disposition toward precipitous changes in output intensity over the time periods (400 secs.) needed to obtain a typical energy distribution curve. This phenomenon was due to the wandering of the position of the arc in the Xe source and appeared to be inherent in the lamp design. Interchangeable with the above lamp, on the input of the first monochromator, was a 1000 watt Xe lamp and housing designed and constructed by P.A. Lindfors of this laboratory. The source gave an extremely stable output over long time periods (within 5% over 8-10 hours). In addition, it provided increased intensity, which was invaluable for energy distribution measurements from low yield surfaces where the total photocurrents, even with the increased intensity, approached  $10^{-15}$  amps.

The photoelectric yield was calibrated in terms of the absolute (photon flux) output of the monochromator by use of an Eppley 4100 vacuum thermopile, calibrated using radiation standard C-631 of the National Bureau of Standards. Thus the monochromator output (photon flux) was related to the 917 and 935 photocell currents at each photon energy in the 1.20 to 5.5 eV spectral region. Using this calibration, it is estimated that errors in the absolute measurement of the yield due to uncertainties in light output were less than 10% over the entire spectral range. The effects of scattered light from the monochromator and analyzer upon the measured yields will be discussed subsequent to presentation of the experiment evidence in Sec. 1.4.

#### 1.2.5.1 Photoelectric Yield

The photoelectric yield at a fixed photon energy i.e., the number of emitted photoelectrons per absorbed photon is defined in terms of observable or calculable quantities, as,

$$Y(h\nu) = \frac{1}{e} \frac{I(h\nu)}{N_p(h\nu)[1-\rho(h\nu)]} \quad (3)$$

where  $e = |e|$  (the electronic charge),  $I(h\nu)$  is the emitted photocurrent,  $N_p(h\nu)$  is the incident photon flux, and  $\rho(h\nu)$  is the sample reflectivity. The calibration of the light output and corresponding photocell response with the Epply vacuum thermopile allowed determination of the absolute photon flux at each photon energy in terms of a calibration factor  $\phi(h\nu)$ , and the observed photocell current,  $I_c(h\nu)$ . Thus at each photon energy, the yield  $Y(h\nu)$  could be expressed in terms of these experimental quantities as

$$Y(h\nu) = \frac{I(h\nu)}{[1-\rho(h\nu)]} \frac{\phi(h\nu)}{I_c(h\nu)} \quad (4)$$

The tacit assumption is usually made that the reflectivity,  $\rho$ , is independent of surface conditions (e.g., the presence of an adsorbate) in the photon energy range used in this experiment. At least it can be shown<sup>2</sup> that the major structure in the reflectivity for clean and cesium-covered Si is characteristic of volume processes (e.g. interband transitions), independent of surface conditions. This follows from the fact that the region of influence of a monolayer of cesium is small compared to the absorption

depth of the incident radiation. However, extremely small changes in reflectivity due to cesium adsorption have been detected by application by ellipsometry techniques. It follows that the applicability of bulk reflectivity corrections for surface state emission processes should be questioned. Evidence supporting this view will be presented in Sec. 1.3.2.2 and discussed in Sec. 1.4.

The operation of the hemispherical analyzer (Fig. 8) in the yield measurement mode was accomplished by biasing the 3 grids ( $G_{1,2,3}$ ) and the collector at +180V with respect to ground. The emitted photocurrent was measured by grounding the target through a Cary Model 31 vibrating reed electrometer. The electrometer remote head was mounted on the vacuum station which was, in turn, mounted on pneumatic cushions. This prevented spurious capacitive signals,  $V_{dc}^{dc}$ , induced by building vibrations or other sources of microphonics, from disturbing the low-signal measuring capabilities of the Cary electrometer. With this arrangement, currents smaller than  $10^{-15}$  amps could be measured with the electrometer in the damped mode.

#### 1.2.5.2 Photoelectron Energy Distribution

The method of measuring the energy distribution of photo-emitted electrons by the retarding potential technique has been previously discussed by Riach<sup>22</sup> and Eden<sup>5</sup> and illustrated in Fig. 1. The collector current,  $I$ , measured as a function of the applied bias potential,  $V_{app}$ , is related to the energy distribution of photoelectrons by:

$$I(E) = \int_E^{\infty} N(E) dE, \text{ where } E = -e V_{app} \quad (5)$$

It is clear<sup>22</sup> that the desired quantity,  $N(E)$  is proportional to the derivative of the retarding potential curve.

Two standard methods of electronically differentiating the retarding potential characteristics were attempted and the results compared. These were: the ac modulation-phase sensitive detection techniques, described by Appelt and Hachenberg<sup>28</sup> - analogous to the detection method used in AES (described in Sec. 1.2.2) and secondly, the dc time-differentiation technique.<sup>2</sup>

Using the ac modulation technique, shown schematically in Fig. 10 (a), a small audio-frequency modulation voltage was superimposed on the retarding potential applied to the inner grids  $G_{2,3}$ . The current reaching the outer collector was amplified by a low-noise,  $10^2$ -gain Ithaco preamplifier and fed into a PAR HR-8 lockin amplifier. It can be easily shown that if the modulation amplitude is small (typically 20 mV) the amplitude of the fundamental frequency detected by the lock-in amplifier is proportional to the energy distribution function of the photoelectrons,  $N(E)$ .

In the dc technique, illustrated in Fig. 10 (b) an accurately linear ramp voltage was applied between the target and  $G_{2,3}$  and the resulting collector current was simultaneously, electronically differentiated. Mathematically, it can be seen from Eq. 5, by implicit differentiation with respect to time, that

$$\frac{dI(V)}{dt} = -N(E) \frac{dV}{dt}, \text{ where } V \equiv V_{app}. \quad (6)$$

Thus if  $\frac{dV}{dt}$  corresponding to the applied ramp voltage, is constant, the differentiated collector current is proportional to the energy distribution of emitted electrons,  $N(E)$ .

A direct comparison of the relative sensitivities of the two techniques was made. Using the ac method, the minimum total photocurrent needed for measuring energy distribution curves (EDCs) was approximately  $5 \times 10^{-12}$  amps, whereas the dc technique allowed measurements to be carried out at nearly  $1 \times 10^{-14}$  amps. These results indicate nothing inherently inferior about the ac technique, rather, they reflect the relative sensitivities of the current-sensing instrumentation available. Interfacing with the Cary vibrating reed electrometer greatly favors the dc technique. Eden<sup>5</sup> has discussed the relative merits of the two techniques in distorting structure in the EDCs and claimed superiority for the ac technique. A direct comparison of the relative distortion in the EDCs was made by depositing cesium onto the crystal (increasing the yield to allow measurement by the ac method) and by subsequently comparing the EDCs taken at constant light intensity and photon energy. The EDCs obtained by the

two methods could be superimposed within a line-width on the recorder trace. For practical purposes the methods gave equivalent structure and thus the large difference in ultimate sensitivity greatly favored the dc technique.

The instrumentation used in the dc method was designed and described by Riach.<sup>22</sup> The requirements for accurate dc measurement of EDCs were met using operational amplifiers; as an integrator which provided the linearly-varying ramp voltage  $V(t)$  and as a differentiator, to measure  $\frac{dI}{dt}$ . The ramp voltage was usually varied at .01 V/sec and could be maintained with 2% of this value over long time periods. The capacitive component of collector current,  $C \frac{dV}{dt}$  (where C is the target-collector capacitance) was nulled using a current bridge, which fed a current to the electrometer input, to cancel the capacitive current. This was important since the capacitive current at  $\frac{dV}{dt} = .01$  V/sec. was on the order of  $10^{-15}$  amps. This was reduced to less than  $10^{-16}$  amps using the capacitance balance.

A shift of approximately 40 mV in the absolute energy of structure in the EDCs, resulting from a low-pass filter in the differentiator section, was observed with a ramp voltage of .01 V/sec. The determination of relative separation in structure could be made more accurately than this, since the filtering tended to broaden peaks in the EDCs rather than to shift them relative to one another.

It may be surmised from this brief discussion that the 3 grids in the analyzer, needed for the ac technique, are unnecessary, and perhaps deleterious, in the dc technique. However, by proper biasing, the grids may be used to some advantage. Biasing the inner grid from 3 to 6V positive with respect to the target (and sweeping it with the target) provided a radial collecting field for photoemitted electrons that was independent of the instantaneous value of the retarding potential. This also minimized the magnetic field distortions in the EDCs by providing greater collection efficiency for electrons which were emitted with near-zero kinetic energy. Biasing  $G_{2,3}$  at 1.6V negative with respect to the collector provided an effective collection "well" that prevented low energy electrons which were initially reflected at the collector surface from escaping collection.

The energy "resolution" of the photoelectric analyzer, may be defined as the system response to a delta function,  $\delta(E)$ , of electrons emitted from the focus of the hemisphere. This function could not be directly measured due to the presence of other factors which broadened the energy distribution of electrons from the real crystal surface. However, an upper bound on the effective resolution; including non-monochromatic incident light, magnetic fields and variations in sample and collector work functions, could be made in several ways. Experimentally, EDCs were obtained near threshold whose width at half-height approached 170 mV. However, due to the low photocurrents at threshold, these were obtained using a 10 sec. damping on the Cary electrometer providing an additional apparent broadening. Estimates of the resolution function, using the high and low energy intercepts of the EDCs characteristic of the clean Si surface, as suggested by T.E. Fisher,<sup>3</sup> corresponded closely to this value.

Calculations of the effects of nonuniform emitter and collector work functions upon EDCs has been previously discussed.<sup>3,22</sup> In brief, it should be noted that nonhomogeneous emitter work function affects only the low energy end of the EDCs. This follows from the use of the retarding potential technique, which measures the energy of the emitted electron with respect to the sample Fermi level (see Fig. 1). Hence, electrons in the high energy region, although emitted with varying kinetic energies (because of work function non-uniformities) appear at the same external kinetic energy in the retarding potential measurement. A nonuniform emitter work function, however, distorts the low energy end of the distribution since the low energy cut-off is determined by the sample work function. The "collector" work function uniformity (in the mode shown in Fig. 10(b) actually grids  $G_{2,3}$ ) contributed a small portion total resolution function.

Since it is impossible to maintain the photon flux constant at various wavelengths, an essential step in the meaningful analysis of energy distributions was their normalization so that the enclosed areas were in the same ratio as the respective yields. The areas under each curve were measured with a planimeter and the spectra normalized using appropriate scaling techniques. However for accurate high energy edge measurements the photon energy

and flux were held constant and great care was taken that the sensitivity of the detection system was kept within a few percent for the duration of the measurements. The high energy edge taken under these conditions was a very reproducible entity and its location could be reliably measured to 0.02 eV. The effect of magnetic fields, emitter nonuniformity, nonideal geometry and collector reflectivity changes tended to broaden the distribution. Such broadening was not serious in this study as the low energy edge was not employed as an experimental parameter because an independent means of measuring work function was available. However, except at very low currents, the extrapolation of the low energy edge to the horizontal axis occurred within 100 meV of the position of zero kinetic energy calculated from  $h\nu - \phi_s$ . No degradation of the high energy edge was ever observed with changing the first grid potential or the magnetic field within reasonable limits.

An average work function of  $G_{2,3}$  was measured using the Fowler technique.<sup>29</sup> Grids 2 and 3 were grounded through the Cary electrometer with grid 1 and the metal collector maintained at +12v with respect to ground. By illuminating the grids with monochromatic light and by fitting the measured yield to a Fowler plot, a work function value of  $\phi_c = 4.30 \pm .05$  eV was derived. This technique is, of course, valid only for metals where the photothreshold coincides with the work function. Determination of the collector work function,  $\phi_c$ , thereby allowed a direct determination of the Fermi level. On each measured EDC, a reference position, corresponding to  $V_{app} = 0$ , was marked. The Fermi level was then located at  $(\phi_c + V_{G_{2,3}} - h\nu)$  on the x (energy) axis. The potential applied to grids 2 and 3 ( $V_{G_{2,3}}$ ) by means of a battery was  $1.60V \pm .02$  as determined by measurement with a Keithley 602 electrometer.

Lastly, a few comments should be made regarding the possible perturbations of photoemissions from grids  $G_{1,2,3}$ . First, it should be recognized that the typical photocurrents from metals are orders of magnitude lower than from semiconductors due to the small absorption coefficients and the strong electron-electron scattering processes in metals. No contribution to the measured yield due to photoemission from  $G_{1,2,3}$  should be observed since the only current leaving the target is measured. In measuring the EDCs, however, the concern is that any contribution from the grids, however small, should not appear in the high energy edge region of the distributions (as will be appreciated later). Biasing  $G_1$  at 4-6v with



respect to the target effectively displayed any contribution from  $G_1$ , at most photon energies, completely below the low energy end of the EDC envelope. Since  $G_{2,3}$  was not swept, it provided a constant current to the collector and contributed nothing to the EDC, wherever it appeared in the retarding potential characteristic.

### 1.2.6 Sample Preparation

The value of the experimental results to be presented depended critically upon a knowledge of the chemical composition and structural order of the surface region. The structural and chemical factors, affecting the externally observed photoelectric emission, existed in the two dimensional surface array and to a depth of a few hundred Å into the crystal. The periodicity and cleanliness of the surface were monitored by LEED and AES, respectively. The problems associated with determining the depth profile of the chemical composition and its effect upon the photoelectric properties was circumvented by using nearly intrinsic high purity material.

The silicon sample was cut from a 100 ohm-cm, n-type Czochralski boule. The boule was mounted in a goniometer and oriented in the  $\langle 100 \rangle$  direction by etching in NaOH to expose  $\langle 100 \rangle$  facets and using an optical back-reflection method to locate the 4-fold symmetric  $\langle 100 \rangle$  direction. The sample was then cut to give an  $0.5 \text{ cm}^2$  surface area ( $0.707 \text{ cm} \times 0.707 \text{ cm} \times 0.40 \text{ cm}$ ), mechanically polished and etched prior to insertion into the vacuum system.

## 1.3 Experimental Results

### 1.3.1 Characterization of the Clean Surface

Extensive<sup>30,31,32,33</sup> studies have been carried out on cleaning techniques for silicon surfaces employing the criteria of a good LEED pattern and a reproducible work function to determine whether the surface was clean. In this study the sample was cleaned by outgassing, sputter-anneal cycles with frequent use of Auger spectroscopy to determine the degree of cleanliness. An Auger spectrum taken of the contaminated surface before any cleaning treatments (Fig. 11) showed oxygen and carbon to be the major contaminants. The anomalous structure on the low energy side of the Si- $L_{2,3}$  VV transition results from a Si-O binding state. Attempts were made to

reduce the surface oxide by exposing the hot (300°C) silicon surface to  $10^{-3}$  Torr sec. of hydrogen while facing a hot tungsten atomizing filament. A subsequent Auger spectrum showed that while no reduction in the oxygen peak had occurred, the carbon signal was dramatically reduced.

Several attempts to produce a clean surface by sputtering with argon ions ( $\sim 200$  eV) and subsequent annealing from 600°C failed to produce a clean surface as evidenced by LEED and Auger spectroscopy (Fig. 12a). The sample exhibited a very weak  $2 \times 1$  pattern and still had substantial oxygen contamination. If electron bombardment heating was employed to supplement the internal heater, sample temperatures of 1200°C could be obtained. During such heating cycles great care was taken to reduce any possibility of "cracking" carbon monoxide on the surface due to the energetic electron beam ( $\sim 1000$  eV). Sputtering with 100 eV ions and subsequent heating to 1100°C removed the surface oxide but subsequent heating at lower temperatures ( $\sim 600^\circ\text{C}$ ) caused the segregation of potassium to the surface (Fig. 12b). The potassium was present in the silicon sample due to a previous study with energetic potassium ions. Further long-term outgassing (24 hours cycles) and sputter-anneal treatments enabled the surface to be cleaned and to remain clean with subsequent heating. The only impurity within the detection limit of the Auger spectroscopy ( $< 1\%$  monolayer for most common contaminants) was trace quantities of tantalum from the sputter unit (Fig. 13a). The LEED pattern was that from a  $2 \times 1$  domain surface structure and exhibited strong half-order reflections. Although the "quarter-order" reflections reported by Lander and Morrison<sup>33</sup> were diligently sought, no such reflections were observed with incident beam energies down to 20 eV. The presence of potassium or oxygen as a impurity caused a severe degradation of the LEED pattern which, while still corresponding to a  $2 \times 1$  domain structure, exhibited only weak, diffuse half-order reflections.

### 1.3.2 Photoemission from Clean Si(100)

#### 1.3.2.1 Photoelectric Yield:LEED

The photoelectric yield (electrons/incident photon) characteristic of the Si(100) surface in varying states of cleanliness is shown in Fig. 14. The correction for reflectivity was not made since its value changed by only 15% over the range of photon energies used. Further, since the reflectivity was constant at a particular photon energy, independent of coverage, direct comparisons of uncorrected yield curves were valid. The surface characterized by curve (C) was produced by low

energy ( $< 300$  eV) ion bombardment and subsequent heating to  $600^{\circ}\text{C}$ . The Auger spectrum was essentially that displayed in Fig. 13 (a) - indicating the presence of a surface oxide, corresponding to  $\sim .05$  monolayers oxygen. Correspondingly, the LEED pattern ( $2 \times 1$ ) was diffuse, suggesting an amorphous overlayer. The effect, upon the photoelectric yield, of potassium contamination, due to the diffusion of potassium to the surface, was to give a large increase in yield and a much lower photothreshold than observed for the clean case (Fig. 14A). The amount of potassium responsible for such a change was estimated to be  $\sim 5\%$  of a monolayer (calibrated from the data of Weber and Peria).<sup>14</sup> Using the Auger spectrum as a gauge of surface cleanliness and the LEED pattern as a monitor of surface order, the Si(100) surface yielding the two sets of data fitting curve (B) in Fig. 14 represents (within our detection limits) the clean surface. The slight deviation in the two data sets in curve B could be caused by a slight trace of K which was well below the quantitative detection limits of the AES spectrometer (approximately  $.1\%$  monolayer). The LEED pattern characteristic of both surfaces was an intense  $2 \times 1$  pattern at 48 eV. These results and the approximate photothreshold shifts relative to the clean surface (curve B), are summarized below:

TABLE 1

## Characterization of Sputtered-Annealed Si(100) Surfaces

Curve	LEED Pattern	Contaminants (From Auger Spectrum)	Photothreshold shift
A	$2 \times 1$ (Weak $1/2$ order)	$.05$ monolayers potassium	$-0.50$ eV
B	Intense $2 \times 1$	Clean	0
C	Weak $2 \times 1$	$.05$ monolayers oxygen + carbon	$+0.10$ eV

The salient feature of the spectral dependence of the photoelectric yield in Fig. 14, independent of the surface condition, is the existence of two distinct regions separated by a "knee" or transition region in the  $\sim 5.0$  eV photon energy range. We shall anticipate a result of this study, discussed in Sec. 1.4.2; that

the spectral yield curves in the low quantum efficiency regions ( $Y(h\nu) < 10^{-3}$ ) for clean and cesium-covered silicon could be fitted by a power law dependence, viz.,

$$Y(h\nu) = C_1 (h\nu - \phi_{ss})^3 \text{ or } 5/2 + C_s (h\nu + \phi_v)^3 \text{ or } 5/2$$

The significance of the subscripts used to denote the photothresholds will become meaningful later in this section. For clean silicon, shown in Fig. 14, the experimental limit in the photon energy (5.5 eV) precluded unambiguous fitting of the data for the higher yield emission process ( $h\nu > 5.0$  eV) and determination of its photothreshold,  $\phi_v$ . However, the lower yield emission process could be fitted closely to a power law dependence (with  $n = 3$  or  $5/2$ ) as shown in curve D (inset) in Fig. 14. Shown in curve D is a straight line fitting to the spectral yield data (curve B) plotted to the  $2/5$ th power. The extrapolation to the abscissa axis indicated an apparent threshold ( $= \phi_{ss}$ ) of  $4.5 \pm .05$  eV. It should be noted that, even without reverting to a particular model to derive the photothreshold, the value of 4.5 eV could have been estimated from examination of the spectral yield (curve B) in Fig. 14.

The effect of reflectivity corrections upon the preceding data is shown in Fig. 15. The clean Si(100) data, from curve (B) Fig. 14, and the data corrected for reflectivity, using the tabulated data of R.C. Eden<sup>5</sup> are shown for comparison in curves A and B, respectively. It should be noted that applying the reflectivity correction to the yield data does not change the qualitative aspects of the spectral yield.

### 1.3.2.2 Photoelectron Energy Distribution

The spectral dependence of the differential yield  $dY(h\nu)/dE$ , for clean Si(100) is shown, for photon excitations in the 5.0 - 5.5 eV energy range, in Fig. 16. In these curves, a linear extrapolation of the rapidly decreasing low energy edge of each EDC to the abscissa was made. This procedure removed electrons from a tail in the experimental curve which extended to negative kinetic energies. This tail, which arises from the finite resolution of the analyzer, is discussed in Secs. 1.2.5 and 1.4.2.2. Subsequent to the extrapolation procedure, the EDCs

in Fig. 16 were scaled so that the areas under each curve were proportional to the spectral yield at the corresponding quantum energy. Since the reflectivity,  $\rho$ , varied by only approximately 5% over this energy range, no correction was made in the normalization. These curves, with the abscissa plotted as  $E - E_f - h\nu$ , display the energy of the initial state, relative to the Fermi energy (0). The Fermi energy was determined within  $\pm 50$  meV using the relationship

$$E_f = -(\phi_c + V_{G2,3} - h\nu) \quad (7)$$

as discussed in Sec. 1.2.5.2. Constraints upon obtaining exact normalization of EDCs in Fig. 16 arose from the indeterminacy in the area under each EDC (due to the linear extrapolation procedure) and by the normalization to the uncorrected yield. The reason for using the latter will become clear when the origin of photoelectric processes observed in Figs. 14-16 is discussed in Sec. 1.3.2.2. However, independent of our ability to obtain exact normalization of the energy distribution curves (EDCs) to the photoelectric yield, several features of the EDCs are quite striking. Comparison of the photoelectric yield (curve B, Fig. 14) and the above EDCs, yields corroborative evidence that two distinct emission processes were responsible for the photoelectric yield from clean Si(100) in the observable energy range. The lower threshold process was clearly indirect as seen from the coincidence of the initial states (high energy edges of the EDCs). Further, it is clear that emission from states occupied up to the Fermi level (0) was observed. Hence, either the clean Si(100) ( $10^2$  ohm-cm, n-type) surface was degenerately p-type at 300°K or emission from filled states lying in the band gap was observed.

EDCs at lower photon energies were not taken due to the detection limitations of the energy analyzer. The clean surface EDCs shown above were measured typically at maximum photocurrents of  $3 \times 10^{-14}$  A. At 4.9 eV the total photocurrent was less than  $1 \times 10^{-14}$ , and the signal levels were comparable to the background noise. However, at  $h\nu \geq 5.0$  eV, the EDCs were reproducible, usually within 10 meV - especially in the region of the high energy edges.

### 1.3.3 Characterization of Cesium-Covered Si(100)

#### 1.3.3.1 Work Function Measurements

Having established, through the use of Auger Electron Spectroscopy, photoemission and LEED, the attainment of a clean Si(100) surface and, (as discussed in Sec. 1.2.4.1), the ability to deposit Cs ions with minimum contamination, the change in work function vs. cesium coverage was measured. In Fig. 17 is plotted the work function vs. cesium coverage,  $\theta$ . The fractional cesium coverage,  $\theta$ , is plotted on the basis of one adsorbate atom per surface atom; thus, for Si(100), full coverage ( $\theta = 1$ ) corresponds to  $7.4 \times 10^{14}$  atoms/cm<sup>2</sup>. The ordinate values must be viewed as tentative since no accurate method for measuring the absolute work function of the clean Si(100) surface was available in the experimental system. The initial value ( $\theta = 0$ ) of 4.6 eV was determined from analysis of the spectral yield photothresholds together with the corresponding sets of energy distributions. This assignment is of secondary importance at this point and will be tested in terms of its consistency with the accumulated photoemission data. However, the total work function change, due to cesium adsorption, could be accurately determined from the retarding potential measurements. Its value of  $\Delta\phi = 3.3$  eV could be reproduced within 2%, independent of the number of deposition steps used in attaining maximum coverage. A work function minimum was reached at approximately  $0.43 \pm .02$  monolayers Cs coverage. Further deposition ( $\theta > .43$ ) resulted in an increased work function, within the normal measurement time after deposition (5-10 minutes). However, if the system was allowed to equilibrate, the work function returned to the minimum value. The transitory effect is indicated by the dotted line in Fig. 17.

Subsequent to the completion of the studies on cesium-covered Si(100), the effects of the addition of oxygen to a fully cesiated surface were investigated. Approximately  $10^{-7}$  Torr-sec oxygen was leaked into the system until the photocurrent at  $h\nu = 2.9$  eV was maximized (the photoemission results are presented in the next section). The effect of oxygen admission was a further reduction of  $\sim 0.200$  eV in the work function, as shown by the triangular point in Fig. 17. Care was taken during oxygen admission to minimize concurrent formation of CO. This was accomplished

by turning off all filaments in the system (including the mass spectrometer filament) during oxygen admission. It has been previously observed using the mass spectrometer, that a hot filament made an efficient oxygen-to-CO converter - probably due to the presence of carbon residues at the filament surface. However, the presence of either oxygen or CO adsorbates on the cesium-covered surface could be easily distinguished: small doses of oxygen invariably increased the photoelectric yield whereas CO adsorption decreased the yield in all coverage ranges. Secondly, the photoelectric yield of the oxygen-cesium covered surface did not change under the influence of electron bombardment whereas the CO could be easily desorbed, causing an increase in the photoelectric yield.

#### 1.3.3.2 Photoelectric Yield from Cesium-Covered Si(100)

The salient features of the spectral yield, resulting from the deposition of submonolayer quantities of cesium, were a precipitous increase in the photoelectric yield and a decrease in the photoelectric threshold, the latter moving from the ultraviolet (4.6 eV) to the near-infrared (1.30 eV), as shown in Fig. 18. Plotted is the spectral yield (uncorrected for reflectivity) as a function of cesium coverage ( $\theta = 1-7.4 \times 10^{14}$  cesium atoms/cm<sup>2</sup>).

Prominent structure appears in the yield curves, mainly for  $\theta > .155$ . A discussion of these features, in terms of features in the reflectivity and joint density of states in silicon will be carried out in Sec. 1.4.2.1. It is only important to note here that these features are associated with volume photoemission processes in silicon.

#### 1.3.3.3 Photoelectron Energy Distributions from Cesium-Covered Si(100)

It is clear from the spectral yield data of the previous section that the adsorption of submonolayer quantities of cesium extends the ability to observe photoemission from deep-lying valence band states, which were previously inaccessible (at our limiting photon energy  $h\nu \approx 5.5$  eV) due to the large clean-surface work function. In the following presentation of photoelectron energy distribution curves (EDCs), several methods of plotting the raw data will be used to emphasize a particular aspect of the information gained from the EDCs. In the regions of high photoelectric yield (approximately  $Y > 10^{-3}$  for  $\theta \geq .155$  monolayers) our main interest will be characterization of the dominant emission processes (direct or indirect) which

are related to the energy band structure of the solid. Correspondingly, the data will be plotted without normalization to yield, on an energy scale that emphasizes the movement of structure in the EDCs with photon energy.

It was of greatest interest in this work to characterize the emission processes prevalent in the threshold region (approximately  $Y < 10^{-4}$  for  $\theta < .155$  monolayers). The EDCs from the threshold region will usually be plotted with the ordinate normalized to the yield/absorbed or incident photon and the abscissa (energy) plotted as  $E - E_f - h\nu$  (to reveal the energy of the initial state).

The seeming uncertainty concerning normalization of the EDCs to the corrected (for reflectivity) or uncorrected yield should be briefly discussed since it involves a predisposition toward an interpretation of the origin of the threshold emission processes. Normalization of the EDCs to the absorbed photon flux using tabulated reflectivity values, obviously presupposes that the total yield originates in bulk processes. This assumption is certainly valid over the high yield spectral regions. However, the compilation of our evidence will reveal that the threshold emission process in Si(100) is characteristic of emission from localized surface states, lying in the forbidden band gap. Hence, a bulk reflectivity correction to the normalized yield is incorrect. The approach followed in normalization was to correct for reflectivity where the surface state emission was a small portion of the total yield and to normalize to the uncorrected yield where the surface state emission dominated. The latter followed from the experimental observation that the EDCs characteristics of surface state emission formed within experimental error, a common envelope when normalized to the uncorrected yield. This suggested that the "reflectivity" characteristic of the surface state emission is essentially constant in the optical energy range. The only difficulty in normalization arises when the yield from the bulk and surface processes are comparable in magnitude as for clean Si in Fig. 16. However, this will be of no practical importance since, for  $\theta > 0$ , the photoemission processes can be well characterized without use of the information available from this transition region.

Shown in Figs. 19-22 are the normalized EDCs characteristic of silicon at  $\theta = 0.155$ ,  $\sim 0.25$  and  $0.43$  monolayers cesium coverage. The data for  $\theta = 0.25$  is subject to uncertainty in that oxygen could also be detected on this surface. This contamination however does not effect the generalized discussion for which such distributions were employed. Distributions from surfaces which were slightly contaminated



with oxygen were not employed for surface sensitive studies such as surface potential determinations or work function changes. The photon energies used at a particular coverage were chosen to span regions of the photoelectric yield dominated either by volume or by surface emission processes. The energy scale  $E - E_f - h\nu$  was established, as discussed in Sec. 1.2.5.2, by measurement of the collector work function.

EDCs:  $\theta = 0.155$

Figures 19 and 20 show normalized EDCs from 2.80 to 5.0 eV photon energies for a cesium coverage of 0.155 monolayers. The high energy edges of the EDCs at 5.0 and 4.0 eV in the volume emission region of Fig. 19(a) show close correspondence. The slight divergence of the curves in the surface state emission region was probably due to, as previously discussed, the non-applicability of the reflectivity correction in this region. The division of the EDCs into volume and surface state emission showed by the dotted lines is intended to be only qualitative. Also shown in Fig. 19(a) is an expansion ( $\times 10/3$ ) of the volume-surface emission threshold region, clearly showing the agreement in the volume emission high energy edge. The EDCs at  $h\nu = 3.85$  and 3.70 eV (where volume emission processes start dominating), uncorrected for reflectivity, shows good agreement in the surface state emission region. To illustrate the coincidence (within experimental error) of the surface state emission EDCs, a direct trace of the experimental data from the X-Y recorder output (not scaled or replotted) is shown in Fig. 20(a). Prior to each run the recorder X axis was shifted by the change in photon energy  $\Delta h\nu$ , otherwise the experimental conditions were identical for each run. The experimental correction factor,  $\beta(h, \nu)$  in Eq. 4 varied by only  $10^4$  over the photon energy range used. Thus the data shown is approximately normalized to the uncorrected yield. Interesting features of these curves are; the coincidence of the high energy edges, indicating convincingly the indirect nature of surface state emission, and, the structure in the EDC taken at 3.70 eV, showing the distinct contribution of the more efficient volume processes. Further decreasing the photon energy and normalizing to the uncorrected yield, which lies in the range  $10^{-6} < Y < 10^{-5}$ , provides EDCs characteristic of the surface state emission region, as illustrated in Fig. 20(b) for  $h\nu = 3.00$  and 2.80 eV. The effect of the photoemission analyzer limitations, which contributes electrons below the apparent zero of kinetic energy is

shown by the dotted line extending as a tail on the  $h\nu = 2.80$  eV distribution. This phenomenon was found to contribute substantial uncertainty in the low energy cutoff only near the surface state threshold, where the total photocurrent was  $< 10^{-13}$  amps.

EDCs:  $\theta = 0.25$  (+ oxygen)

The existence of an oxygen-containing surface contaminant should not affect the characteristic volume photoemission processes, other than by altering the range of accessible initial states through alteration of the work function. Figure 21 shows the relationship between EDCs at 5.0 and 4.5 eV photon energies and an expansion of the threshold region. The latter shows similar behavior to the surface state emission region for  $\theta = 0.155$  monolayers. The EDCs shown give clear indication of neither direct nor indirect optical transitions. Similar behavior in the volume emission processes is also seen for  $h\nu = 4.25$  and 4.1 eV, as shown in Fig. 22(a). However, the high energy edges near the surface state threshold show convergence as clearly demonstrated by the  $\times 10/3$  expansion. An interesting feature of these EDCs is the sharp onset for surface state emission, as shown by the  $\times 100$  expansion. For photon energies  $h\nu = 4.0$  eV ( $Y < 7 \times 10^{-4}$ ), the correspondence of the high energy edges was excellent, as shown in Fig. 22(b). This result indicates more clearly than for the  $\theta = 0.155$  EDCs, the indirect nature of the volume emission at photon energies approaching the valence band emission threshold. The surface-state-emission EDCs showed similar behavior to those for  $\theta = 0.155$  (indirect threshold) and would only add redundancy to this presentation.

EDCs:  $\theta = 0.43$  (Full Coverage)

At full coverage the maximum capability to probe the initial valence band states, determined by  $h\nu - \phi$ , was reached. Energy distribution curves, taken near the photon energy limit of the probing capabilities for deep-lying valence band states, are shown in Fig. 23 for  $h\nu = 5.4$ , 5.1 and 4.8 eV. This high yield region cannot be characterized in terms of indirect transitions from the same initial state nor direct transitions (unless the conduction bands are flat over the range of interest). Figure 24(a) shows a slightly truncated set of EDC's at  $h\nu = 4.8$  (for comparison). 4.2 and 3.9 eV:

It can be observed that as the photon energy decreased, the high energy edges of the EDC's tended to merge. Figure 24(b) illustrates, rather convincingly, the onset of the indirect emission threshold and the mixed (indirect and direct) nature of the optical transitions in this region. The transition between direct and indirect processes is particularly evident in the  $h\nu = 3.9$  eV curve in (b). As can be seen from both the EDCs and the spectral yield curve, the influence of the surface state emission in this region is minimal. Additional EDCs at lower photon energies will be introduced where appropriate to the discussion in Sec. 1.4.2. However, their qualitative behavior (indirect) was identical to those obtained at lower cesium coverages.

In Figs. 25 and 26 are plotted, on a horizontal energy scale corresponding to the external kinetic energy, the unnormalized EDCs for Si(100) at full cesium coverage. The relative magnitudes of the curves are arbitrarily assigned, to provide maximum clarity. Figure 25 illustrates the invariance with photon energy of a prominent peak (labeled I) in the EDCs measured at  $h\nu = 5.8, 5.4$  and  $5.1$  eV. Also appearing is a peak (or dip), III, on the high energy edge of the EDC at  $h\nu = 5.85$  eV. The latter photon energy could be utilized only for measurements on high yield surface (i.e. fully cesiated), due to the rapid decrease in intensity at  $h\nu < 5.5$  eV. At lower photon energies, an additional feature, peak II became prominent and appeared stationary in energy independent of the photon energy for  $h\nu > 3.9$  eV. However, due to its location near the emission threshold (at zero kinetic energy), its assignment as a true peak must await further verification.

#### 1.3.3.4 Determination of $|E_v - E_f|$ vs. Cesium Coverage

The establishment of an indirect threshold for valence band emission, Sec. 1.3.3.3, assures us that the highest emitting valence band state observed was characteristic of the valence band maximum at the surface (with qualifying assumptions discussed in Sec. 1.4.2). Thus, in principle, the determination of the separation of the highest emitting valence band state and the surface Fermi level could be determined by direct measurement in the high energy threshold region of the EDCs. In practice, only shifts of the Fermi level relative to a fixed reference could be measured. This reference may not have corresponded to the highest-emitting valence band state but certainly was stationary with respect to the true maximum. This fixed reference was chosen to be

the linear extrapolation of the high energy edge of the valence band emission as denoted by  $E_V'$  in Fig. 27. Shown in Fig. 27, for illustration, is an experimentally observed EDC in the valence band-surface state emission transition region taken at  $h\nu = 5.2$  eV and at a cesium coverage of  $\theta = 0.144$  monolayers. Similar data was taken at this fixed photon energy and constant incident photon flux at cesium coverages of  $\theta = 0, 0.031, 0.062, 0.093, 0.124, 0.155, 0.186, 0.248, 0.310, 0.372, 0.435$  and  $0.497$  monolayers. The relative yield ( $\propto$  area) of this surface emission region with respect to the region of efficient volume processes in the EDCs is, of course, a function of cesium coverage and can be estimated from the data in Figs. 19(a), 21 and 22. The relative shift in the Fermi level with respect to  $E_V'$  upon fully cesiating the silicon crystal was found to be  $0.35 \pm 0.050$  eV. This shift was measured from the above data and from previous data taken at various photon energies (under less stringent experimental conditions) as a secondary check. This check consisted of taking an EDC from clean and cesiated surfaces at photon energies of the order of 1 eV above the photoelectric threshold. The results were in good agreement with the calibrated run plotted in Fig. 28. The data is plotted normalized to a clean surface value ( $E_V - E_F$ ) of 0.300 eV (which is within 0.020 eV of  $E_V'$ ), a value consistent with the photoelectric data from the clean surface as will be discussed in Sec. 1.4.3. From Fig. 28 it can be seen that the difference between the Fermi level and the valence band edge increases with initial depositions of cesium, passing through mid-gap at  $\theta = 0.05$  monolayers, reaching a saturation value of  $\sim 0.650$  eV at  $\theta = 0.08$  monolayers. Further cesium deposition causes no further band bending.

#### 1.3.4 Gas Adsorption on Clean and Cesium-Covered Si(100)

A rather cursory examination of the effects of the adsorption of  $O_2$  and CO upon the photoemissive properties of clean and cesium-covered silicon was carried out.

##### 1.3 4.1 CO Adsorption

It has been postulated previously<sup>39</sup> that CO adsorption has deleterious effects upon the photoelectric yield from cesium-covered gallium arsenide. It was also observed that electron beam impact on the CO contaminated surface effected a return to the original yield. Similar results were found

for the cesium-silicon system. The photocurrent from a fully cesiated silicon surface at  $h\nu = 2.50, 2.90$  and  $3.5$  eV was monitored before and after a CO exposure of approximately  $10^{-4}$  Torr secs. The CO was produced by outgassing a Bayard-Alpert gauge present in the system. Mass spectrometry showed that ambient produced from such a procedure was 99% CO with slight amounts of  $\text{CO}_2$  and  $\text{CH}_4$ . The results are shown in Table II in terms of the sample photocurrent,  $I_C$ : at a constant reference photocell current; hence the ratios are proportional to the ratios of the absolute yields. The photocurrents after electron beam impact with the surface (as a result of an Auger spectrum being recorded) are shown in the last column on Table II. It is seen that the results are similar to those observed previously on GaAs. Monitoring the ambient gases with a mass spectrometer during the desorption processes confirmed the correlation between the recovery of the photoelectric yield and the desorption of CO (and a smaller quantity of  $\text{CO}_2$ ).

#### 1.3.4.2 Oxygen Adsorption

As previously discussed in Sec. 1.3.3.2 an oxygen exposure of approximately  $10^{-8}$  Torr-sec produced an increased photoelectric yield (Fig. 18) and a reduction of approximately 0.20 eV in work function (Fig. 17) when adsorbed onto the cesiated silicon surface. No additional lowering of the work function, or increase in the photoelectric yield, was observed after 4 additional cesium/oxygen cycles. However, due to experimental limitations (obvious from Fig. 5), the photoelectric yield could not be monitored simultaneously with cesium deposition; thus, the photoelectric yield could not be optimized with cesium coverage as was done with oxygen. No measurable shift in the surface Fermi level using the techniques of Sec. 1.3.3.4, could be detected after oxygenation of the cesium-covered surface. The effect of oxygen adsorption onto the clean silicon surface was manifested by an increase in photocurrent by a factor of  $10^2$  at a fixed photon energy ( $h\nu = 5.4$  eV), however, only while maintaining an oxygen partial pressure of  $> 10^{-7}$  Torr. Closing the oxygen source caused a rapid decrease in photocurrent to within 5% of its original value. This increase in current may have been associated with electrons excited by the energy released by the oxygen-silicon reaction i.e. Chememission<sup>40</sup> or released by photon absorption. Unfortunately no measurements were taken in the absence of the external photoexcitation.

TABLE II  
EFFECT OF CO ADSORPTION UPON CESIUM COVERED SILICON

<u>Photon Energy</u>	<u>Photocurrent, <math>I_c</math> (a)</u>		
	<u>Full Cs Coverage</u>	<u>After CO Adsorption</u>	<u>After <math>e^-</math> Bombardment</u>
2.50 eV	$7.0 \times 10^{-11}$	$4.7 \times 10^{-12}$	$5.5 \times 10^{-11}$
2.90	$2.5 \times 10^{-10}$	$2.1 \times 10^{-11}$	$2.0 \times 10^{-10}$
3.50	$1.54 \times 10^{-9}$	$2.7 \times 10^{-10}$	---

1.3.4.3 Auger Spectroscopy of Si(100) - (Cs + O<sub>2</sub>)

An observation of practical and perhaps theoretical interest was made from the comparison of the Auger spectra characteristic of cesium-covered and cesium-oxygen-covered silicon. In Sec. 1.2.4 it was noted that, by monitoring the characteristic high energy O:KLL and Cs: M<sub>4,5</sub>N<sub>4,5</sub>N<sub>4,5</sub> Auger transitions, important information relative to the oxygen contamination emanating from the cesium zeolite source, or from the ambient, could be gained. It is well known, that the most prominent cesium Auger transition, an O<sub>1</sub>N<sub>4,5</sub>N<sub>4,5</sub> doublet (2 eV separation), occurs in the low energy region, near 47 eV. Its relationship in energy and its relative magnitude in comparison to the Si:L<sub>2,3</sub>VV transition, at full cesium coverage is shown in Fig. 27(a), curve B (amplified x 100). It should be noted that the ratio of Cs/Si peak heights (as measured by their peak-to-peak deflection) was  $.88 \pm .01/1.0$ . This ratio was found in all cases, within experimental error, for full cesium coverage on silicon. The absence of oxygen contamination on the surface can be seen by the lack of a recognizable O:KLL transition in the 500-520 eV energy range of curve B. However, the addition of approximately 10<sup>-8</sup> Torr-sec. oxygen, in the process of obtaining maximum photoyield, produced a rather startling result, as shown in Fig. 29(b), curve A'. The final Cs/Si peak ratio in this case was approximately 1.1/1.0. The presence of oxygen on the surface was verified by the O:KLL transition prominent in curve B'. This experimental evidence was repeatable and followed, without exception, the trend that the Cs/Si peak ratio increased monotonically with oxygen coverage. The amplification specified on each curve is relative to that used for curve A. From the comparison of the amplification factors and the magnitude of the peaks, it can be seen that the Si:L<sub>2,3</sub>VV peaks in A and A' remained essentially constant and that the relative magnitude of the high energy cesium doublet in curve B' decreased relative to that in B. The latter perhaps was subject to 10% error in determining the relative gains. The consequence of this observation is that, care must be taken to determine the interactions of the entire adsorbate-substrate system before determining adsorbate densities from peak magnitudes.<sup>15</sup>

## 1.4 Discussion

### 1.4.1 Attainment of Clean Si(100)

As previously mentioned (Secs. 1.2.6 and 1.3.1) the analytical techniques for the determination of a clean, well-ordered surface were Auger electron spectroscopy and low energy electron diffraction (LEED). The detection limits of the present spectrometer were  $< 0.005$  monolayers for oxygen, sulphur, carbon and the alkali metals. The detection limits for tantalum and tungsten (possible contaminants arising during sputtering) were not quantitatively known but from existing data<sup>36</sup> it was felt that  $< 0.005$  monolayers was also a fair estimate for such elements. The conclusion of this study was that a clean, well ordered surface of Si(100) can only be obtained after long outgassing treatments ( $\sim 1000^\circ\text{C}$ ) followed by sputter annealing cycles employing 100 eV argon ions and annealing temperatures of  $1000^\circ\text{C}$ . After such treatments the silicon surface had no impurities greater than 0.005 monolayers and remained clean with typical experimental procedures. The LEED pattern was that from a  $2 \times 1$  domain surface<sup>33</sup> and did not exhibit any other reflections. This is contrary to the work of Lander and Morrison who also observed incomplete quarter-order reflections at incident beam energies below 70 eV. The existence of such reflections was explained by Lander as the result of two classes of sites along the  $\langle 11 \rangle$  direction, one producing quarter-order reflections, the other only half-order reflections (see Fig. 2, Ref. 33). As quarter-order reflections were never observed in this study it is impossible to state whether such reflections result from impurities or from another mode of ordering at the clean surface. It can only be stated that the Si(100) surface, shown to be clean by Auger electron spectroscopy exhibited only reflections characteristic of a  $2 \times 1$  domain surface structure.

### 1.4.2 Characterization of Optical Transitions in Silicon

Although the principal interest in this work was to characterize the emission processes from clean and cesiated silicon in the low photoelectric threshold region, and thus to determine the change in surface potential of silicon (100) upon cesiation, it was previously noted that the structure in the high spectral yield region and the corresponding EDC's contains information regarding the nature of the dominant optical transitions. The photoemission data presented in Sec. 1.3 will be discussed in two sections.



The first will attempt to correlate the high yield data in terms of optical transitions and band structure while the second will discuss the transitions responsible for the threshold emission.

#### 1.4.2.1 Interpretation of the High Yield Photoemission Data

Prominent structures in the photoemission data (spectral yield and energy distributions) of silicon have previously been attributed<sup>2,5,42</sup> to direct optical transitions between states with a high joint density. Briefly this follows from a completely classical description of the optical properties of the solid in terms of the complex dielectric constant  $\epsilon(\omega) = \epsilon_1(\omega) + i\epsilon_2(\omega)$ . The prominent loss (or absorption) mechanisms in the optical frequency range described by the imaginary part,  $\epsilon_2(\omega)$ , is due mainly to interband transitions between filled (valence band) and empty (conduction band) states. It was shown<sup>40,42,43</sup> that maxima in the optical absorption data occur due to the onset of direct transitions ( $\nabla_k[E_C(K) - E_V(K)] = 0$ ) between states with high joint densities. Phillips<sup>44</sup> has shown that such conditions are frequently found in the high symmetry directions in  $E$  vs.  $k$  space. Structure in  $\epsilon_2(\omega)$  can be shown to be directly related to structure in the reflectivity,  $R$ , the parameter relating incident flux to the absorbed flux. Thus, in principle, the characterization of the optical transitions in silicon and the relationship of these transitions to the structure observed in photoemission data can be accomplished by correlating such data with the  $E$  vs.  $k$  topography and the optical constants.

Unfortunately there are considerable discrepancies in the numerous<sup>45,46,47,67</sup> energy band calculations that exist for silicon. The dominant discrepancy is the separation between the valence and conduction band at the high point density of states around the  $\Gamma$  symmetry joint. Herman assigns the direct gap ( $\Gamma_{25'} - \Gamma_{15}$ ) to have a separation of  $\sim 2.4$  while the other calculations set the separation to be  $\sim 3.5$  eV. The  $E$  vs.  $k$  diagram calculated by Cohen and Bergstresser<sup>67</sup> was employed in this discussion with a direct gap of 3.5 eV and is illustrated in Fig. 30, together with that of Herman<sup>45</sup>. The choice of this representation was that of consistency with previous authors<sup>2,5</sup> and that it represented the most widely used band structure. The accessible final states lying above the vacuum level for clean and fully cesiated silicon are shown by the intersection of the  $E$  vs.  $k$  diagram with dotted lines  $E_{vac}(Cs)$  and  $E_{vac}(clean)$ .

For photon energies less than the direct gap (3.5 eV) the optical absorption length is very long and the only energy loss mechanism of significance is that of electron-phonon interaction. Because the vacuum level was well above the conduction band minimum, thermalized electrons diffusing in the conduction band minimum could not escape and thus only "hot" electrons were externally observed. Since the mean free path for electron-phonon scattering<sup>5</sup> is  $\sim 60\text{\AA}$  an electron escaping from one absorption depth would undergo many collisions and lose a considerable amount of energy. Eden<sup>5</sup> has employed a simple model employing phonon-electron scattering and shown that the spectral yield should have a cubic energy dependence and the corresponding EDC's should be parabolic. The experimental data observed in this region, neglecting the surface state contribution (see Sec. 1.4.2.2), were consistent with such a model.

As the photon energy is increased to beyond the direct gap separation then direct transitions can occur. The absorption depth for photons becomes much smaller and at high photon energies electron-electron scattering can occur. As the loss of large amounts of energy by the inefficient phonon electron interactions becomes less probable the energy distribution of emitted electrons represents more directly structures in the excited electron energy distributions. The use of energy distributions to determine the nature of optical transitions has been briefly discussed in Sec. 1.1.3 where it was demonstrated how such data should allow one to distinguish between direct and indirect transitions. If only direct transitions are allowed then, in general, energy distributions will not extend up to  $E_{\text{int}} = h\nu$  (Fig. 1) since such transitions are only possible if there exists a final state at an energy of  $h\nu$  above the valence band maximum, having the same  $k$  value as does the valence band maximum. Similarly, structure in the energy distributions will tend to move with changing photon energy by an amount, depending on the  $E$  vs.  $k$  topography, but usually less than  $\Delta h\nu$ . Indirect transitions however will be characterized by energy distributions that always extend up to  $E_{\text{int}} = h\nu$ . Structure in energy distributions due to indirect transitions will move with increments equal to the change in photon energy if the initial state remains constant, while structure due to a given final state will remain fixed as the photon energy is varied. Of course such behavior could also result from direct transitions if the respective energy bands were very flat over a wide range of  $k$  space.

The photoemitted electrons are collected and sorted as to their kinetic energy. The zero point is determined by the low energy cut off and is thus subject to any error in such a determination. Furthermore, in order that a meaningful interpretation can be made, the external kinetic energy must be converted to an electron energy above the valence band maximum so that the final state can be ascertained. Thus a knowledge of both the work function and  $|E_F - E_V|$  is imperative. The combination of these uncertainties with the inherent unreliability in the knowledge of the band structure makes any interpretation necessarily qualitative. Previous workers<sup>2,5</sup> have assumed that the cesiated surface is degenerately n-type and thus  $|E_F - E_V|$  is equal to the band gap and the work function equal to the photoelectric threshold. Both the work function and  $|E_F - E_V|$  were measured in this experiment. The values 1.3 eV and 0.65 eV respectively were obtained for fully cesiated silicon.

The photoelectric energy distributions from fully cesiated silicon (100) are shown in Figs. 23, 24, 25 and 26. The dominant structures are peaks at a kinetic energy of 2.2 eV, observed only at high photon energies, and at 1.6 eV observed at all photon energies above 3.8 eV. The latter was invariant in its energy position over a wide photon energy range. Very little can be said about the high energy peak at 2.2 eV as the threshold for the appearance of the structure was very near the high energy limit of our photon energy range. However its threshold and its position above the valence band maximum of 4.2 eV is consistent with the onset of direct transitions of the nature  $L_3 \rightarrow L_3$ . By far the more prominent structure is the peak at a kinetic energy of 1.6 eV. This peak has been observed by Gobel and Allen,<sup>2</sup> and Eden<sup>5</sup> and has, together with the photoelectric data in general, been assigned to from direct transitions. The reassignment of this peak to 3.5 eV above the valence band maximum (compared to the values of  $\sim 4.0$  eV previously employed) due to definite knowledge of  $|E_F - E_V|$ , and the observed invariance of this structure in kinetic energy with changes in photon energy makes the interpretation of such data solely in terms of direct transitions questionable. That indirect transitions can occur with cesiated silicon is demonstrated by the high yield ( $\sim 10^{-2}$  electrons per absorbed photon) at energies below the

direct gap separation. Similarly it will be shown that the high energy regions of energy distributions from cesiated silicon are characteristic of indirect processes (Sec. 1.4.2.2). Thus it does not seem unreasonable to determine whether indirect transitions can explain the peak at 1.6 eV. As mentioned previously the final state responsible for the peak remained constant as photon energy was varied and lay 3.5 eV above the valence band maximum. This is the position of the conduction band minimum at  $\Gamma_{15}$ .<sup>67</sup> Thus possible interpretation is that indirect transitions occur from initial states to  $\Gamma_{15}$ . Such an assignment is far from unambiguous and it is quite feasible that such anomalous structures can be entirely explained by direct transitions. However, until accurate band structure and density-of-state data is available, the possibility of indirect transitions giving rise to such structure in the EDC's cannot be dismissed.

The spectral yields from a partially cesiated and near fully cesiated surface are shown in Figs. 31 and 32. The prominent features were a sharp rise in yield at  $\sim 3.3$  eV and a valley at 4.4 eV. The optical transition strength ( $[h\nu]^{2p_2}$ ) showed similarly a sharp increase at 3.3 eV, a dip at 3.6 eV followed by a sharp maximum at 4.3 eV. The sharp increase in yield is consistent with the onset of direct (with possibly indirect) transitions between  $\Lambda_3 \rightarrow \Lambda_1$  around the  $\Gamma$  symmetry point. As the final states were above the vacuum level the photoexcited electrons could escape and be externally counted. The maximum at 4.3 eV in the optical transition strength is consistent with the onset of  $X_4 \rightarrow X_1$  transitions. As the final state was below the vacuum level such photoexcited electrons could not escape and thus produced a minimum in the spectral yield and no corresponding structure in the EDC's.

To conclude, the ambiguity in the knowledge of the band structure and the limitation of photon energies available precludes anything other than a qualitative discussion of the high yield region of the spectral yield of silicon. As such ambiguities do not in anyway detract from the purpose of this study and the use of optical parameters and band structure to interpret photoelectric data from silicon has been thoroughly discussed by Eden,<sup>5</sup> any further discussion at this point

would be redundant. The interpretation of the available data is consistent with that of previous workers, within the limitations discussed, with the exception that indirect transitions cannot be neglected as contributing to the spectral yield.

#### 1.4.2.2 Threshold Emission Processes

The remainder of this discussion will be restricted to the threshold region of the spectral yield. The sensitivity of the photoelectric analyzer allowed distributions to be taken over the entire threshold region, allowing unambiguous interpretation of the emission processes without recourse to any band structure model.

It has been previously observed for group IV<sup>9,22</sup> and groups III-V<sup>7,47,48,49</sup> semiconductors that the photoelectric spectral yield near threshold could be fitted to a power law, i.e.,

$$Y(h\nu) = C(h\nu - \phi)^n \quad (8)$$

where  $n = 5/2$  or  $3$ . Experimentally the difference between a  $3$  or  $5/2$  exponent plot could not be determined within the limits of experimental error. Neither could it be determined whether the process yielding the cubic (or  $5/2$ ) dependence was due to surface states,<sup>49</sup> indirect,<sup>9,50</sup> or direct<sup>51,52</sup> transitions. Thus determining the nature of the emission processes by fitting the spectral yields to Eq. (8) yielded non-unique interpretations due to the existence of many, distinctly different, indirect processes having a cubic (or  $5/2$ ) energy dependence near threshold.

It was found in this study that the spectral yield curves in the region of low quantum efficiency could be fitted by assuming a power law dependence viz.

$$Y(h\nu) = C_1(h\nu - \phi_1)^{5/2} + C_2(h\nu - \phi_2)^{5/2} \quad (9)$$

In the following discussion it will be shown that, by the examination of the spectral yield together with the corresponding EDC's, an unambiguous interpretation of the nature of these threshold photoemission processes and the significance of the photothresholds  $\phi_1$  and  $\phi_2$  could be determined.

### Clean Silicon (100)

As previously observed in Sec. 1.3.2.1 the spectral yield exhibited a distinct knee (Fig. 14), suggesting the existence of two contributions to the yield curve. The lower threshold contribution could be fit to a cubic (or  $5/2$ ) photon energy dependence. The limitation of available photon energies to those less than 5.5 eV precluded the unambiguous fitting of the higher threshold region to such a plot and thus the identification of the emission process and the photoelectric threshold were also precluded. However the limited data was certainly consistent with two indirect processes with photoelectric thresholds at 4.55 eV and  $\sim 4.90$  eV.

The corresponding EDC's (Fig. 16) gave additional evidence of the existence of two distinct emission processes contributing to the observed spectral yield. There is no doubt that the lower threshold process is indirect, due to the coincidence of the initial states responsible for the high energy edge in the EDC's. However, the assignment of the higher threshold to indirect processes is ambiguous. This ambiguity, as mentioned previously, would indeed occur if the emission was due to contributions from both bulk and surface transitions, due to the difficulty in accurate normalization of the surface state emission (non-applicability of the bulk reflectivity corrections). As the lower threshold contribution, in the case of clean silicon, was a very sizeable fraction of the total yield, if the lower region were due to a surface process, then it would not be expected that an indirect valence band edge would form an "envelope" when the EDC's were displayed as to show the initial states. Although neither the spectral yield analysis nor the EDC's allowed an unambiguous assignment of the two processes to surface state emission and indirect valence band emission, the overall analysis of the photoelectric data favored very strongly such an interpretation. The model proposed is that the clean Si(100) surface, produced by sputter-annealing techniques, has a work function of 4.55 eV and that the valence band at the surface lies 300 meV below the Fermi level, with surface states filled up to the Fermi level. The evidence for such an interpretation is summarized below:

(a) As the voltage drop across  $1000 \text{ \AA}$  of the doped crystal is only 21 meV and the escape depths for photoelectrons are less than this the silicon crystal can be considered as "flat-band". Thus the data must be explained by a model employing direct or indirect emission processes from an essentially flat-band surface.

(b) As the spectral yield showed a photoelectric threshold of 4.55 eV and the corresponding distributions showed that emission was observed from states extending up to the Fermi level then the lower threshold must be equal to the work function.

(c) If the lower energy contribution in the EDC is not that of surface state emission then Si(100) must be, and must remain with cesium coverage, degenerately p-type. Such a model would be entirely consistent with previous work. The only reported case of degenerately p-type Si(100) was that of Allen<sup>30</sup> who measured specimens cleaned in glass apparatus and contaminated with boron. Since the present experiment was conducted in a metal bell-jar and constant use was made of Auger spectroscopy, no such contamination was present on the clean surface.

(d) Both the spectral yield and the EDC's are consistent with the proposed model especially if the reflectivity correction for bulk processes is taken into account.

(e) It will be shown that as cesium coverage extends the ability to probe into the valence band that two distinct indirect processes definitely exist. As the bulk (valence band) contribution gradually outweighed the surface state contribution, at accessible photon energies, then the high energy edges of the EDC's (e.g. Fig. 19a) formed an envelope when the distributions were displayed to show the initial state. Although cesiation can change the position of the valence band and alter surface state distributions it should not change the emission processes responsible for the high energy edge of the distribution at a fixed photon energy. Thus the unambiguous assignment of the two threshold emission processes from silicon with small quantities (e.g., 3%) of cesium to indirect processes is strong evidence that the two similar processes observed with clean silicon are also due to indirect processes.

#### Cesiated Silicon

As previously mentioned the lowering of the vacuum level through the conduction band by deposition of cesium caused a precipitous increase in the spectral yield (Fig. 18) of silicon. The spectral yield in the threshold region could be fitted to a cubic or  $5/2$  energy dependence of the type described by Eq. (9). This fitting was generally more reliable

with increasing cesium coverage due to the availability of data from the threshold region (photon energy limitations no longer being a problem as in the case of clean silicon). Also the separation between the two threshold emission processes increased (Sec. 1.4.3) with cesium coverage thus reducing the effective region of overlap of the two processes in the  $y^{2/5}$  plot. The plots showed two distinct linear regions (e.g., Figs. 31 and 32) allowing the linear extrapolations to the axis of the abscissa to be made with relative certainty. Corresponding EDC's in the threshold region (Figs. 19, 20, 22 and 24) showed that there were indeed two distinct processes. If such distributions were plotted to display the initial states then the coincidence of the high energy edges of both processes were very evident. This, together with the  $5/2$  energy dependence of the spectral yield, is strongly suggestive of two indirect processes being responsible for the threshold emission from silicon. The lower threshold must be surface state emission, unless the surface is degenerately p-type, and coincides with the work function of the sample. Also the EDC's in this region were invariant with photon energy and formed a common envelope when normalized to the uncorrected yield (see Figs. 19, 20, 22 and 24). This invariance is shown as a dotted line beginning in the surface state region and extending parallel to the abscissa axis in Fig. 31. The second threshold process, with a higher photoelectric threshold, also formed an envelope when the EDC's were displayed to show the initial state. Before this threshold can be definitely assigned to indirect transitions from the valence band maximum it must be ascertained that direct transitions cannot explain such behavior.

The fitting of the spectral yield to a  $5/2$  plot does not unambiguously preclude direct transitions. Gobeli and Allen<sup>50</sup> have suggested that the cubic part of the yield close to threshold could be due to the excitation of electrons from the top of the valence band with simultaneous exchange of normal momentum with the surface. The ability of adsorbed cesium to scatter emitted electrons has been demonstrated by Gobeli et. al.<sup>68</sup> Similarly the coincidence of the high energy edge of the threshold process in the EDC's does not allow the unambiguous assignment of the process arising from indirect transitions. As mentioned previously, direct transitions could display this type of behavior if such transitions arise from a region of the valence band which is at a constant energy over the



photon energy range investigated. However as the coincidence of the high energy edge was observed over photon energy ranges of 2.0 to 5.0 eV such an interpretation is certainly dubious. Hence the second threshold process can be ascribed to the indirect valence band threshold with little ambiguity.

To conclude, through the correlation of spectral yield and energy distribution, the characterization of the threshold photoemission processes from clean and "cesiated" silicon (100) could be made with a high degree of certainty. It was shown that the indirect surface state emission dominated the yield in the threshold region with the onset, at increasing photon energies, of indirect valence band emission. The two photoelectric thresholds, evident from the spectral yield, were thus assigned as the surface state threshold [ $\phi_{ss}$ ] and indirect valence band threshold [ $\phi_v$ ].

#### 1.4.3 Band Bending at the Clean and Cesium Silicon Surface

In Sec. 1.3.3.4 the parameter  $|E_F - E_v|$  was determined for silicon (100) as a function of cesium coverage. This determination was made by studying the separation of the highest emitting valence band state and the surface Fermi level in the high energy threshold region of the EDC's. However, because of the difficulty in locating  $\phi_v$  from the distributions a fixed reference point (Fig. 27) was chosen and relative shifts in  $|E_F - E_v|$  measured. The resultant data is plotted as a function of cesium coverage in Fig. 28. As previously mentioned these data were taken under stringent experimental conditions such that the photon energy and the analyzer sensitivity were held constant for the duration of the measurements. As  $E_v$  was determined by an extrapolation to the abscissa, any error in this extrapolation is an error in the determination of  $|E_F - E_v|$ . Although an error of  $\pm 50$  meV could be ascribed to this measurement (Fig. 28) depending upon which portion of the slope was extrapolated, it is believed that with careful choice of the region to be extrapolated, the error in the determination was less than this value. As only a relative shift was measured, any discrepancy between  $E_v$  and the valence band maximum was not an error in this measurement as long as the choice of  $E_v$  was maintained for the duration of the measurements. Similarly the relative measurement was independent of any error in the Fermi level determination as long as the work

function of the repeller grids remained constant for the duration of the measurements. The use of an ion source for cesium deposition (limiting cesiation to only the silicon surface) and frequent checks on the repeller grid work function assured that the grid work function did indeed remain constant. The validity of the data in Fig. 28 was checked by measuring  $|E_F - E_V|$  in a completely independent run in which the distributions taken near threshold were examined as a function of cesium coverage. The results were in very good agreement with the data presented in Fig. 28.

As previously mentioned the work function of the clean silicon (100) could be fixed at  $4.55 \pm 0.05$  eV by the observation that emission was occurring up to the Fermi level and thus  $\phi_{ss}$  was equal to the work function. The assignment of  $\phi_V$  to the indirect valence band threshold should allow the absolute determination of  $E_V$ . However as indicated in Sec. 1.3.2 (Fig. 14) and Sec. 1.4.2.2 the value of  $E_V$  for the clean surface is subject to experimental uncertainty due to the limitation of maximum photon energy (5.5 eV) in the present apparatus. A careful fitting of the yield data corrected for reflectivity above  $h\nu = 5.0$  eV gave an extrapolated value of  $E_V = 4.85 \pm 0.1$  eV. This value was within 40 meV of the value chosen by determination of  $E_V$  by extrapolation techniques. Thus a value of  $|E_F - E_V|$  for the clean surface of 300 meV is not unreasonable. However, as previously mentioned, the deposition of cesium enabled greater accuracy in the determination of  $E_V$ . At cesium coverages above  $10^4$ ,  $|E_F - E_V|$  should remain a constant and thus could be employed to determine the absolute scale for Fig. 28. Examination of yield data at coverages above  $10^4$  gave a value of  $\phi_V - \phi_{ss}$  of  $650 \pm 50$  meV (e.g. Figs. 31 and 32). This value is totally consistent with the clean surface value of 300 meV.

Thus by analysis of the photoelectric energy distributions, spectral yields and work function data an entirely consistent model can be developed for the band bending at the surface of clean and cesiated silicon (100). At the clean surface the separation between the valence band and the Fermi level is 300 meV. This separation increases with cesium deposition until at  $\sim 10^4$  of a monolayer of cesium it has reached 650 meV. No further band bending occurs even though cesium deposition continues up to  $\sim 45^4$  of a monolayer.

There now exists sufficient self-consistent data to discuss the correlation between the photoelectric yield, energy distributions and work function data as cesium is adsorbed on the (100) face of silicon. Since the first ionization potential of cesium is 3.98 eV and the work function of clean silicon is  $4.55 \pm 50$  eV, it can be expected that cesium adsorbs at least initially, as a  $\text{Cs}^+$  ion. The observed work function reduction due to cesium adsorption can, in a simple model, be divided into two components:

$$\Delta\phi = \Delta\phi_{\text{dipole}} + \Delta|E_V - E_F| \quad (10)$$

The latter component,  $\Delta|E_V - E_F|$ , represents a displacement of the conduction band edge towards the Fermi level due to the filling of previously unoccupied surface states by electrons from the adsorbed cesium "donors". A reduction in work function ( $\Delta\phi_{\text{dipole}}$ ) can also occur upon Cs adsorption due to a reduction in electron affinity by the formation of an electric dipole layer at the surface.

The relative contributions of each of these components to the total work function reduction can be seen from comparison of Figs. 17 and 28. In comparing these figures, it should be noted that the work function is plotted on a logarithmic scale, whereas the  $|E_V - E_F|$  shift is plotted linearly. An initial rapid, downward movement of the energy bands at the surface, with respect to those in the bulk, occurs at increasing cesium coverage  $0 \leq \theta \leq 0.08$ . The corresponding effective work function reduction is equivalent to approximately 20 eV monolayer.<sup>-1</sup> The saturation of the  $|E_V - E_F|$  curve above 10% of a monolayer and the continuing work function reduction indicates that the latter must be due entirely to the dipole component in Eq. (10). Topping<sup>55</sup> has proposed a model to account for the work function reduction produced by the formation of a surface dipole layer. Weber and Peria<sup>14</sup> found in their experiment on Si(100) that the Topping model could only be fitted for cesium coverages  $\theta > 0.125$ . The availability of  $|E_V - E_F|$  data in this experiment allows an explanation for this discrepancy. The work function reduction in the region below 10% monolayer is strongly influenced by the large change in  $|E_V - E_F|$ . Further, for Si(111), Weber and Peria

were able to fit the Topping model from essentially zero cesium coverage. Correspondingly Monch<sup>56</sup> has shown from surface conductivity measurements that for Si(111) -Cs rapid band bending occurred at less than 0.01 monolayers with a saturation in  $|E_v - E_f|$  at approximately 0.013 monolayers of cesium. This would have had no effect upon the fitting of the Topping model on the comparatively coarse coverage scale of Weber and Peria.

#### 1.4.4 Surface States on Clean and Cesiumated Si(100)

In the preceding section, an examination of the surface parameters describing the band bending as a function of cesium coverage was made. There, of course, exists a causal relationship between the observed band bending and the surface state density and energy distribution. This relationship will now be investigated.

The surface states observed in the present experiment were; the intrinsic states due to the termination of the periodic lattice, and surface states introduced by the adsorption of cesium onto the silicon surface. The influence of bulk impurities upon the observed emission may be neglected since, for the near intrinsic sample used, the bulk donor and acceptor concentrations were  $< 10^{14} \text{ cm}^{-3}$  and the uncompensated donor concentration  $< 5 \times 10^{13} \text{ cm}^{-3}$ . The relative emission from surface states and impurity atoms may be estimated as follows: assuming an impurity concentration of  $10^{15} \text{ cm}^{-3}$  and an absorption/escape length of 100 Å, there are approximately  $10^9$  impurity atoms per  $\text{cm}^2$  in the layer contributing to photoemission. Assuming equivalent photoelectric cross sections, the ratio of emitting surface states/impurity atoms in the surface layer will be at least  $10^6$ . Thus impurity emission can be ignored.

The determination of surface state energy distributions for semiconductors has been attempted by numerous methods (see Chapter 6, Ref. 59). These techniques have invariably measured the effects of the presence of surface states and the results were thus subject to formidable interpretative (as well as experimental) limitations. In contrast, the direct observation of surface state emission reported here presents a considerably simpler conceptual insight into the density and energy distribution of surface states. It should be noted that the observation of surface state emission

has also been recently reported from cleaved Si(111) by R.C. Eden<sup>60</sup> and as early as 1964 by Allen and Gobeli<sup>8</sup> from cleaved and heated Si(111). The similarity between the "toe" in the high energy edge of the EDC's reported by Eden and that reported here indicates very strongly that the observed emission is related to physical processes on the silicon surface and not to anomalous emission.

#### 1.4.4.1 Intrinsic Surface States

To enable correlation of the observed band bending and the intrinsic surface state density and energy distribution, one must make two basic assumptions: (a) at small cesium coverages, the intrinsic surface state density is unaltered by cesium adsorption and, (b) cesium adsorbs as an ion, resulting in the initial stages of adsorption, in the filling of previously unoccupied intrinsic surface states. Experimental evidence exists to support both assumptions:

Monch<sup>56</sup> has shown, through the correlation of field effect and surface conductivity results on Si(111), that, at low coverages, the influence of cesium adsorption is analogous to inducing charge in surface states by applying an electric field normal to the semiconductor surface (field-effect experiment). Thus, the adsorbate does not perturb the intrinsic surface state distribution. This correlation also showed that cesium adsorbs as an ion, since the adsorbed Cs decreased the surface conductivity, in Monch's work, in the same manner as in the field effect experiments carried out by Henzler<sup>61</sup> i.e., cesium adsorption supplies negative charge to the surface states.

#### Intrinsic Surface State Densities

In Sec. 1.3.3.4 was described the experimental procedures used in determining  $|E_V - E_F|$  (or essentially the band bending) vs. cesium coverage. The data was taken at constant photon energy ( $h\nu = 5.2$  eV) and incident photon flux, as well as with constant detector sensitivity. Thus, in addition to using the data to determine the effective band bending, it can be seen that the measurement of the areas under the surface state distributions (see Fig. 27) as a function of cesium coverage gave a direct measure of the relative surface state yields. The latter were, of course, proportional to the number of occupied surface states lying between the valence band maximum and the Fermi level (any surface states

lying below the valence band maximum would be masked by the onset of the relatively efficient valence band indirect transitions). This assumes that the factors contributing to the spectral yield, e.g., excitation cross section and barrier transmission did not vary over the energy span of occupied states ( $\sim 0.65$  eV).

The surface state EDC area was taken to be approximately that bounded by the experimental curve and the dotted extrapolation of the valence band high energy edge as shown in Fig. 27. Several shapes of the valence band edges were assumed, but the results were invariably the linear dependence shown in Fig. 33. In order to interpret this curve, account must be taken of the simultaneous changes which occur in the space charge layer. The change in the band bending which does occur implies that negative charge is added to this layer as Cs is adsorbed. Some very simple calculations show, however, that the amount of this charge (expressed in terms of electronic charges) is negligible compared to the number of added Cs atoms. Stated differently, the number of electrons added to the surface states is, to a very good approximation, equal to the number of Cs atoms adsorbed. Thus, if the area under the surface state portion of the EDC is indeed proportional to the number of occupied surface states (above the valence band maximum) the linear dependence (Fig. 33) is to be expected. The occupied surface state density corresponding to the clean surface can therefore be determined by linear extrapolation of the curve to the abscissa, shown by the arrow in Fig. 33. This value, of course, depended upon the assumed form of the valence band contribution to the EDC in the overlap region and varied from  $1.2$  to  $1.5 \times 10^{13}$  states/cm<sup>2</sup> for the trial envelopes used.

By assuming that only the intrinsic surface states are being filled, up to the coverage corresponding to Fermi level stabilization ( $\theta \sim 0.10$ ), the surface state density in the interval  $E_v \leq E \leq (E_v + 0.65 \text{ eV})$  can be calculated. This density turns out to be  $7$  to  $8 \times 10^{13} \text{ cm}^{-2}$ , again depending somewhat on the extrapolation method used to remove the valence band contribution in the region of overlap.

#### 1.4.4.2 Energy Distribution of Surface States

The relationship between the energy distribution of surface states,  $N_{ss}(E)$ , and the external energy distribution of photoelectrons,  $N_0(E)$ , has been theoretically derived by Pikus.<sup>65</sup> By solving Schrodinger's equation for the eigenstate

or an electron,  $\psi = \psi(k_y, k_z)$ , in a two-dimensional periodic array (y-z axes parallel to the surface) and a potential function,  $V = V(x)$ , Pikus derived the general criteria for relating  $N_{ss}(E)$  and  $N_0(E)$ . Under the assumption that the potential function,  $V(x)$ , was not determined by the periodicities in the y-z directions, he found that the probability of ejection did not depend upon the energy of the initial state or upon the photon energy (assuming  $h\nu$  was above the photothreshold). The energy of the electron in the final state,  $E$ , is simply related (as for volume processes) to the initial energy,  $E_{ss}$ , by energy conservation, viz.

$$E = E_{ss} + h\nu \quad (11)$$

where  $h\nu \geq (E_{ss} - E_{vac})$ . It follows that the energy distribution of ejected electrons,  $N_0(E)$ , is simply related to the initial surface state distribution,  $N_{ss}(E)$  by

$$N_0(E) = \tau(E, h\nu) \cdot N_{ss}(E) \cdot f(E). \quad (12)$$

The function  $f(E)$  is the Fermi-Dirac distribution for electrons and  $\tau(E, h\nu)$  describes the transmission characteristics of the potential barrier,  $V(x)$ . For final energies,  $E \gg (E_{ss} - E_{vac})$ , the barrier transmission will have little effect upon the external distribution, while near threshold,  $E \approx (E_{ss} - E_{vac})$ , the distortion of the observed energy distributions will depend upon the form of  $\tau(E, h\nu)$ . In general  $\tau$  will depend upon  $h\nu - (E_{ss} - E_{vac})$ , where the last term is dependent upon the work function,  $\phi$ . It was observed in Sec. 1.3 that normalization of the EDC's to the yield/incident photon caused the surface state region of the EDC's to form a common envelope-independent of photon energy. This in a direct manner, corroborates the theory of Pikus, viz., the probability of ejection does not depend upon the energy of the initial state or upon  $h\nu$ . This theory thus provides some justification for using the uncorrected yield ( $\rho = 0$ ) in normalization of the surface state EDC's and in the  $Y^{2/5}$  extrapolation in the surface state region.

The greater uncertainty in relating the observed EDC's (for example, Fig. 27) to the initial surface energy distribution is the result of the distortion of the EDC's by the finite time constants of the measuring system. Nevertheless, in energy regions where the actual EDC is not changing too rapidly, the observed EDC's are probably a reasonable estimate of the gross features of the intrinsic surface state distributions, but modified in the vicinity of  $E_F$  by the Fermi function. In all cases, as  $|E_V - E_F|$  increased, the EDC's exhibited a linear decrease towards midgap.

#### 1.4.5 Model for Cesium Adsorption on Si(100)

At coverages less than  $10^4$  the model commonly proposed<sup>69</sup> for the adsorption of cesium on semiconductors holds. The adsorbed cesium forms a donor-like state at the surface, above the Fermi level, and is ionized, contributing its electron to the acceptor-like intrinsic surface states of the silicon. The bands are thus bent downwards (Fig. 28) and the occupied intrinsic surface state density increases (Fig. 33).

While the adsorption of Cs up to  $\theta = 0.12$  was accompanied by a 10-fold increase in the measured surface-state yield, the adsorption of an equal amount of Cs up to  $\theta = 0.25$  brought on no further increase. Correspondingly, the Fermi level was stabilized for coverages greater than  $10^4$ .

Similar stabilization on the cesiated silicon (111) surface has been reported by Monch<sup>56</sup> and was explained as an encounter of the Fermi level with adsorption-created states. Further complexities of the Monch model, such as annihilation of intrinsic states by adsorbed Cs do not seem to be necessary for our purposes. We can interpret the results by the following simple picture:

At small coverages the intrinsic surface state distribution is unaffected by the Cs and one electron is added to the surface states for each Cs adsorbed. The valence band edge therefore moves away from the Fermi level until the latter encounters the adsorption-created states whose density is equal to the surface density of Cs. One difficulty with the simple model is that one might expect to detect photoemission from the adsorption-created states. This would occur as a rather narrow-peak at the high energy limit of the distributions of Fig. 22, for example. Details such as these were never observed. Perhaps this



situation can be qualitatively understood in terms of a property of photoelectric processes viz. the photoelectric effect cannot occur for free electrons, since energy and momentum conservation cannot be simultaneously satisfied.<sup>62</sup> This suggests that the efficiency of the photoelectric processes depends upon the degree of coupling to a momentum absorber. The intrinsic surface states, which result from a rearrangement of binding states (which lie outside the band of allowed bulk states) of the substrate atoms, are coupled to the crystal lattice, i.e., the surface state electronic wavefunctions extend several atom layers deep into the crystal.<sup>63</sup> Hence the lattice provides an efficient momentum absorber for photoelectric emission. If indeed adsorption-created states were responsible for Fermi-level stabilization and such states were localized to cesium adatoms, then the lack of coupling to the crystal lattice could result in a decreased efficiency of such states for the photoemission process. This could explain the absence of any structure in the photoemission data from the adsorption created states. Our hesitancy in making a definitive explanation for the stabilization of the Fermi level lies in the present lack of available theoretical treatments for the adsorption of cesium on semiconductors.

#### 1.4.6 Conclusion

Perhaps the most significant result of this work was the determination of the electrostatic potential profile of the clean and cesium-covered Si(100) surface, (Fig. 34). In particular, direct evidence of Fermi level stabilization well below the conduction band was observed. While no definite explanation could be presented for such stabilization, it is of interest that although the intrinsic surface state density for the Si(100) surface derived from this work is at least an order of magnitude greater than that for the Si(111) surface derived by Monch,<sup>56</sup> the potential profiles of the cesium-covered surfaces were nearly identical. This suggests that such stabilization results from adsorbed cesium binding states rather than from the intrinsic surface states, as has been frequently assumed.

The direct observation of photoemission from surface states, although not adding further knowledge with respect to their origin, provided a direct determination (within the limitations of the energy analysis technique) of the energy distribution and density of intrinsic surface states lying in the forbidden gap.

## 2. LOW ENERGY ELECTRON SCATTERING STUDY OF GERMANIUM(100)

### 2.1 Introduction

In order to use a low energy electron beam as a probe for studying electronic properties of a solid surface with adsorbed overlayers, it is important that the interaction of low energy electrons with a clean solid surface are first understood. This study was directed toward obtaining some understanding of such interactions. Low energy electron interactions are of interest because the penetration of the solid is small thus giving information related to the first few atom layers. This experiment involved the measurement of energy and angular distributions of low energy backscattered electrons from a Ge(100) single crystal. Such measurements are generally classified as secondary electron measurements.

Most of the secondary electron measurements that have been made in the past were concerned with secondary emission at relatively high primary energies, and were generally made with a small solid angle detector in a fixed scattering direction or with a large solid angle detector. Such measurements have been discussed in review papers.<sup>70,71</sup> In the present experiment measurements were made for primary energies below 50 eV, a range which has not had much study. A high resolution, movable, small solid angle detector was used. Because of the lower energy and smaller penetration of the primary electrons, it was hoped that band structure effects would be more evident and that small energy interband or intraband Auger transitions might be detected.

Inelastic backscattering measurements can also give information about the types of electron excitations that take place near the surface. The low energy inelastic scattering differs from the characteristic loss measurements at high energies in that the penetration is small, making surface excitations more important; also the lower energy can give information on excitations which cannot be measured at the higher energies. The high-energy characteristic-loss work has been well reviewed.<sup>72,73</sup> It is implicit in the low-energy inelastic backscattering measurement, that the electrons undergo an elastic scattering event as well as being inelastically scattered, since the probability is small of transferring enough momentum to turn the primary electron around and backscatter

it in an inelastic electron-electron collision. This relationship between inelastic scattering and low energy electron diffraction (LEED) has recently been explored by several workers,<sup>74-79</sup> but was first suggested in 1927 by Davisson and Germer,<sup>80</sup> and later was considered by Turnbull and Farnsworth in 1938<sup>81</sup> and Reichertz and Farnsworth in 1949.<sup>82</sup>

Simple two-step processes of combined elastic and inelastic scattering can be proposed. An electron can be elastically backscattered and then suffer an inelastic collision before leaving the crystal; this will be termed an EIS (elastic-inelastic scattering) process. Such a process is characterized by a maximum in the inelastic intensity when the elastic intensity reaches a maximum, and all loss peaks maximize simultaneously. In the second type of process an electron is inelastically scattered and is then elastically backscattered from the crystal; this is called an IES (inelastic-elastic scattering) process. For this type of process, a particular loss peak would attain its maximum intensity when its secondary energy corresponded to the energy for a maximum in the elastic scattering. Only one particular value of energy loss would satisfy this condition at one time so the loss peaks would maximize independently. For the EIS process the scattering angle for maximum inelastic intensity is the same as that of the elastic peak whereas, in the case of an IES process, a maximum in intensity occurs at an angle for which the LEED beam would occur if its energy were equal to that of the inelastic electron.

## 2.2 Experimental Apparatus

### 2.2.1 Vacuum System

Figure 35 shows a schematic view of the main chamber of the ultra-high vacuum system and the experimental components inside. The main chamber itself is 8.65 inches in diameter and has four 4.0 inch side ports and four 2.0 inch side ports alternated every 45° around it. All the parts of the vacuum system were made of 304 stainless steel and gold gaskets were used for flange seals. A 50 liter/sec. sputter-ion pump was used as the main pump and was connected to one of the 4.0 inch side ports by about 3 feet of 4.0 inch pipe, leaving the entire base plate available for apparatus construction. A titanium sublimation pump was housed inside

the pipe going to the sputter-ion pump and provided additional pumping of active gases. For rough pumping two zeolite sorption pumps were used with liquid  $N_2$  cooling and these were connected to the system by a Granville-Phillips 1.0 inch ultra-high vacuum valve.

Two windows were mounted on the system; one, a 4.0 inch window, was used as a viewing port for observing sample and energy analyzer positions, and the other was a 2.0 inch quartz window which provided a direct view of the sample face for visual checks of sample temperature and was available should photoelectric measurements be desired.

A gas admission system was coupled to the vacuum system by a 1/2 inch Granville-Phillips type C valve. This was used to admit pure argon for ion bombardment cleaning of the sample.

### 2.2.2 Electron Gun and Scattering Chamber

A schematic view of the electron gun and scattering chamber is shown in Fig. 36; also shown is the energy analyzer and related biasing configurations. The electron gun is a three-electrode device machined from 304 stainless steel. Focusing is controlled primarily by the voltage between the second and third anode; the first anode voltage has almost no effect on the focus but acts mainly to control the amount of current. A tungsten ribbon filament was used as the electron source and was heated by direct current flow. At the desired emitting point of the filament, the .040 inch by .001 inch ribbon was etched to about half its initial size to permit smaller filament currents to be used. This was desirable because magnetic fields needed to be minimized. About 1.0A of filament current was used and this gave beam currents of about  $1.0 \times 10^{-8}A$  for 10 eV primary energy and about 1.0  $\mu A$  at 100 eV.

To obtain good focusing properties and a stable beam position for electron energies in the range 5-1000 eV, it was necessary to vacuum anneal the electron gun at 1050° C and then quench it with a flow of argon. This procedure removed residual magnetization induced in the gun parts by machining. Regions where the metal was machined to small dimensions, such as near the apertures of the electrodes, had magnetizations of up to several gauss; spot welding also caused excessive localized magnetization in the stainless steel. A beam size of about 1.5 mm was obtained

at the target position and its position was stable with changes in energy when good cancellation of the Earth's magnetic field was provided by Helmholtz coils. A voltage divider was used to bias the second anode and the voltage ratio for best focus was found to be constant so that the energy could be changed continuously without affecting the beam focus.

A 3.0 inch spherical scattering chamber was formed from two hemispheres of 304 stainless steel. From these were supported the internal grids and collector plates. Surrounding the target, which during measurements was positioned at the center of the scattering chamber, was a spherical grid,  $g_1$ , constructed of 100 line/inch chromium plated stainless steel woven mesh. This grid was kept at target potential thus maintaining a field free region about the target to minimize trajectory distortion. A battery in the target lead, allowed for correction of a contact potential difference between the target and  $g_1$ . A hemispherical collector was placed behind  $g_1$  on the back half of the scattering chamber and was biased at  $22\frac{1}{2}$  V to help remove electrons from the central region.

On the other half of the scattering chamber, a second hemispherical grid,  $g_2$ , was mounted concentric to the first grid with 0.1 inch spacing and was used as a retarding grid for energy analysis of the scattered electrons. This grid was connected to a nearly complete hemispherical collector which was used for large solid angle measurements. To permit measurements of energy distributions at specific angles a slot was cut in this collector and a drift channel was welded in to provide an electrically shielded drift space, extending beyond the outer hemisphere, in which an entrance tube for the energy analyzer moved. All these parts were also chromium plated.

### 2.2.3 Energy Analyzer

Figure 36 shows a schematic view of the  $127^\circ$  cylindrical, electrostatic energy analyzer that was used in the experiment. The analyzer was mounted on a cart which rode in a slotted track providing  $60^\circ$  rotation about the scattering chamber in the horizontal plane. A rotary feedthrough coupled to the cart by a radial arm served as the driver.

The energy analyzer was constructed from 304 stainless steel and as in the case of the electron gun it was necessary to vacuum anneal the entrance and exit aperture plates to eliminate magnetization caused by machining. Chromium plated stainless steel grids with about 75% transmission (100 lines/inch) formed the deflecting electrodes inside the energy analyzer. These were used in conjunction with cylindrical collectors placed directly behind them to prevent the creation of secondary electrons inside the analyzer which could reach the exit aperture. On the exit plate a knife edge, circular aperture .020 inch in diameter was used, while on the entrance plate a .020 inch by .20 inch knife edge slit was used. A slit was necessary because this type of analyzer does not have refocusing properties along the direction of the cylindrical axis. With a circular aperture instead of the slit, small misalignment of the transmitting plane of the analyzer with the trajectory of the electrons entering the analyzer caused loss of signal. A slit provided enough leeway to eliminate this problem.

An analysis of the properties of this type of electrostatic velocity analyzer was given by Hughes and Rojansky.<sup>83</sup> From this analysis, if the angular broadening is neglected, the resolution,  $\Delta E/E$ , is given by

$$\frac{\Delta E}{E} = \frac{2\Delta R}{R_0}$$

where  $\Delta R$  is the aperture width and  $R_0$  is the mean radius of the analyzer. This gives a value of 4.5% for  $\Delta E/E$ . A value of about 5° was estimated for the half angle of acceptance of the analyzer from the approximate orbit equations given by Hughes and Rojansky; however, the geometrical angle of acceptance for a point source at the target with radial trajectories is less than 0.5 degrees. The operating characteristics of the analyzer were in good agreement with calculations, the energy passing relationship,  $E_{\text{pass}} = 3.52 \Delta V$ , where  $\Delta V$  is the potential between the deflecting grids was measured to be less than 3% in error for pass energies from 1.0 eV to 60 eV.

There are two modes of operation for this analyzer. In the first mode, the pass energy is fixed and the electrons are retarded before they enter the analyzer by grid  $g_2$ . Since the resolution is a fixed percentage of the pass energy, this mode leaves the resolution of the analyzer fixed over the entire energy range of the measurement; this method was used almost exclusively. The second mode of operation consisted of setting  $g_1$ ,  $g_2$  and the analyzer case at the same potential and then obtaining the energy distribution by sweeping  $\Delta V$ . Energy distributions obtained this way had to be corrected by a resolution factor to give their true shape. The true energy distribution is related to the measured distribution by a factor proportional to  $\frac{1}{E}$ . In Fig. 37 a single energy distribution is shown as measured by the two methods. Curve B was taken by sweeping  $\Delta V$ . Also shown is a  $\frac{1}{E}$  curve and the calculated points obtained by dividing one distribution into the other. There was about a 0.5 eV shift to higher energies for curve B, so that its resolution factor of  $\frac{1}{E}$  was calculated for the span of 0.5-10.5 eV and it was then shifted in the figure to coincide with the energy scale of curve A. This agreement is quite good, and indicates that the two methods are equivalent. This second mode of operation was sometimes useful in detecting small peaks on the large secondary background, since the energy dependence of the resolution discriminated against the large secondary peak thereby reducing its magnitude.

#### 2.2.4 Apparatus Alignment

Mechanical alignment of the parts of the apparatus was a critical factor for obtaining reliable energy and angular distributions. A procedure utilizing a laser beam was developed to align the parts accurately. A jig was constructed that supported a front surface mirror at the sample position such that it could be rotated about the same axis as the energy analyzer with accurate control of the angle. With the mirror set for normal incidence the laser beam was directed down the axis of the electron gun and reflected back from the mirror to the laser and back again to the electron gun. If there was some misalignment, the reflected beam back to the gun could be seen displaced from the originally transmitted beam. The electron gun position was then adjusted until all the beams were coincident, this was the condition for having the electron gun properly aligned. Next the mirror was rotated so that the

laser beam was reflected onto the energy analyzer. A mirror was mounted on the entrance plate of the analyzer and the aperture position was marked with cross hairs. The reflected laser beam from the target mirror was kept between the cross hairs of the analyzer mirror and the analyzer position was adjusted until the laser beam doubled back upon itself. When this condition was reached the electron gun and energy analyzer were in mutual alignment with the proper target position.

#### 2.2.5 Target Assembly and Manipulator

The target was mounted at a fixed  $45^\circ$  angle to the incident beam on the end of a manipulator shaft as shown schematically in Fig. 35. The main rotary axis of the manipulator was coincident with the electron beam axis, so that rotations of the target left the incident angle unchanged, such rotations are equivalent to rotating the energy analyzer about the target. Besides the rotary motion, the manipulator allowed the crystal to be translated 6 mm in two directions perpendicular to the rotary axis and the rotary axis itself could be tipped. A translation stage permitted the target to be withdrawn from the scattering chamber where it could be cleaned by ion bombardment.

The Ge crystal was mounted on a tantalum block which was machined to fit the crystal. Tantalum tabs which fit into slots cut in the sides of the crystal were welded to the tantalum block and held the crystal in place. A 150 watt projection lamp filament, mounted inside the tantalum block, was used to heat the block and sample by radiation.

#### 2.2.6 Ion Bombardment Cleaning Apparatus

An ion bombardment method was used for cleaning the target and a schematic of the apparatus is shown in Fig. 38. This method consists of bombarding the surface to be cleaned with ions which "sputter" the surface away, i.e. surface atoms are ejected due to the impact of the ions; in this experiment argon ions were used. This apparatus is nothing more than an ionization chamber from which the ions can be drawn to the target surface. It consists of a cylindrical tantalum enclosure with a square hole at one end where the target is positioned. Inside a double



filament of .005 inch tungsten wire provides a source of electrons and a sinusoidally shaped .030 inch tungsten wire forms the anode used for accelerating the electrons to ionize the argon.

This apparatus was used at a pressure of  $1.0 \times 10^{-3}$  Torr of argon which had been cataphoretically cleaned<sup>84</sup> prior to admission to the vacuum system. A gas discharge was struck inside the ion bombardment chamber by running the filament at about 5.0 A and setting the anode voltage at about 30 V. Ions were then drawn to the target by applying a negative potential to the target with respect to the anode. Two modes of discharge were encountered with this apparatus, the one was characterized by low target currents and nonuniform sputtering and the other by large target currents and quite uniform sputtering. The high current mode was the one used and was obtained by raising the anode voltage up to about 80 volts momentarily, thus striking the high current mode, and then reducing the anode voltage to the desired operating voltage of about 27-30 V; at an anode voltage of about 25 V the discharge usually reverted to the low current mode. The anode voltage was kept as low as possible to minimize sputtering of the filament and tantalum enclosure. For typical operating conditions, i.e. using 4.8 A filament current, 30 V anode potential and 50 V target potential, an ion current density of about  $100 \mu\text{A}/\text{cm}^2$  was obtained.

## 2.3 Experimental Procedure

### 2.3.1 Vacuum Processing

Working pressures used in this experiment were typically  $1.0 \times 10^{-10}$  Torr or lower as determined by a calibration of ion pump current and a Bayard Alpert gauge. Processing started with ultrasonically cleaning every part in methyl alcohol or boiling Freon prior to assembly. After assembly the system was rough pumped to about  $1.0 \times 10^{-3}$  Torr using zeolite sorption pumps with liquid nitrogen cooling. At this pressure the titanium getters were outgassed and the ion pump was baked into the sorption pumps for several hours. The sorption pumps were then valved off and the sputter-ion pump was started with the aid of the titanium sublimator. Once the pressure reached about  $1.0 \times 10^{-8}$  Torr a brief

outgassing was given to all the filaments in the system and then the entire system was baked at 275°C. After the pressure dropped to about  $5 \times 10^{-7}$  Torr while hot the system was cooled slowly and a thorough outgassing was given to all the filaments and to the titanium sublimators. To remove gases readsorbed on the walls during this outgassing the system was rebaked at 275°C. This procedure typically produced total pressures of about  $1.0 \times 10^{-10}$  Torr or less.

### 2.3.2 Secondary Electron Energy and Angular Distribution Measurements

Measurements of the secondary electron energy and angular distributions were carried out in two ways, the apparatus for the first method is shown schematically in Fig. 39. For these and all other measurements, a set of Helmholtz coils was used to null out the external magnetic fields to within 10 milligauss. In this technique, those secondary electrons which arrive into the solid angle accepted by the energy analyzer are retarded by grid  $g_2$  prior to entering the energy analyzer and those whose kinetic energy is correct, pass through the energy analyzer and reach the electron multiplier. A Channeltron electron multiplier was used in its pulse-saturated mode so that the detection technique was one of pulse counting. The amplified pulses were fed into an integral discriminator whose output went to a ratemeter which provided an analog signal in counts/sec. By sweeping the target and inner grid potential a direct plot of the energy distribution of secondary electrons was obtained.

It was important to maintain a field free region between the target and the inner grid,  $g_1$ , so that the electron trajectories were not unduly distorted and so that the zero of kinetic energy could be established. The condition for no potential difference between the target and inner grid could be determined by varying the target potential with  $V_{tg}$ . With  $V_{tg}$  set so that the target was negative with respect to  $g_1$ , including the contact potential contribution, electrons originating at the target with zero kinetic energy would be accelerated to the analyzer by the potential difference, and the zero point of the energy distribution plot would show a shift along the retarding potential axis. As the bias  $V_{tg}$  was increased then the zero point of the

energy distribution would shift to lower retarding voltages, until the point was reached where no potential difference existed between the target and inner grid. Further increases in  $V_{Tg}$  would result in an overall shift of the energy distribution, but the low energy cutoff would remain fixed since only electrons whose kinetic energy was large enough to overcome the potential barrier established could reach the energy analyzer. Thus by carefully adjusting  $V_{Tg}$  from some negative value towards positive values, the condition where the low energy threshold of the energy distribution just stopped moving could be determined and this was the condition for no potential difference between target and inner grid. Since the clean Ge target is assumed to have a work function of 4.75 eV, the +0.6 eV value necessary for  $V_{Tg}$  means that the work function of the chromium plated grid,  $g_1$ , was about 4.15 eV. This agrees well with a value determined by photoemission measurements from similar grids using the Fowler technique.

The second method of measurement was basically quite similar, but utilized a FabriTek model 1064 signal digitizer for data accumulation and manipulation; the schematic is shown in Fig. 40. In this type of measurement, an output ramp which was synchronized to the memory advance of the signal digitizer was amplified and used as the retarding voltage. Pulses from the integral discriminator were then fed directly into the signal digitizer where the information was stored. Typically, counts from about a thousand sweeps would be accumulated in the memory for a single energy distribution. Only one fourth of the memory was used to accumulate an energy distribution so that the rest of the memory could be used to store other distributions or for the purposes of scaling, adding or subtracting distributions or integrating the data.

### 2.3.3 Auger Measurements

In a secondary electron energy distribution there is generally fine structure at fixed secondary energies independent of the primary energy. These peaks are usually due to excitation of electrons through Auger processes<sup>14,20</sup> and a correlation can be made between the energies of these peaks and atomic energy levels listed in x-ray tables. Such correlations provide an identification of the atomic species present in the first few atom layers at the surface.<sup>19</sup>

Figure 41 shows the schematic of the apparatus as used to measure Auger spectra. The ac modulation technique for differentiation of the collector signal has been described elsewhere.<sup>19</sup> Briefly, the target, third anode and grid,  $g_1$ , are modulated by a sinusoidal voltage of 3-6 V, which produces an ac signal at the collector versus retarding voltage which is proportional to the energy distribution of the secondary electrons. For this apparatus the collector is connected to the retarding grid,  $g_2$ , hence a large capacitive signal was produced, due to the capacitance between  $g_1$  and  $g_2$  which was sufficient to overdrive the detection apparatus. To correct this, a capacitance bridge circuit was formed by the variable capacitor,  $C_n$ , and a center-tapped modulation transformer. By tuning  $C_n$  it was possible to effectively null out the capacitive signal. After preamplification, the ac signal went to a lock-in amplifier where the second harmonic was measured. It can be shown,<sup>19</sup> that this is proportional to the derivative of the energy distribution. This is more desirable than the energy distribution itself, because small peaks and shoulders on a large background in the energy distribution are shown up as quite prominent features in the differential curve making observation and identification much easier.

#### 2.3.4 Electron Diffraction, Characteristic Loss and Inelastic Diffraction Measurements

Measurements of low energy electron diffraction (LEED), characteristic losses and inelastic diffraction were taken with the apparatus as shown in Fig. 39. To measure the LEED patterns or beam intensities, the retarding voltage was set so that elastic electrons passed through the energy analyzer. By rotating the target and energy analyzer it was then possible to map out the LEED pattern or to obtain an elastic intensity profile. Elastic intensity versus primary energy measurements were taken in a point by point fashion since each energy change moved the LEED beams which necessitated moving the energy analyzer.

Characteristic losses were measured by sweeping the retarding voltage through a range of energies near the elastic peak and plotting the energy distribution; these were done at specific scattering angles. Variations in the loss peak intensities with angle and primary energy were also measured and these gave information about inelastic diffraction events. Either a series of energy

distributions would be taken at increments in scattering angle, or the retarding voltage was set to allow electrons from a particular loss peak to pass through the energy analyzer and the angle of scattering was varied.

### 2.3.5 Target Preparation and Cleaning

A (100) face of Ge was chosen as the surface to be studied because Ge has been well studied in this laboratory by other techniques and the (100) face gives a simple LEED pattern thus making inelastic diffraction measurement simpler. The sample was cut from a commercial single crystal of 45  $\Omega$ -cm germanium to a square face .7 cm on a side. This sample was oriented to within  $\pm 0.5^\circ$  by a technique using a preferential etch and optical reflection patterns.<sup>85</sup> After orientation it was mechanically polished to an optically flat mirror finish.

Prior to mounting the sample it was etched in concentrated hydrofluoric acid to remove the oxide layer and was ultrasonically cleaned in methyl alcohol. Once in vacuum, the sample was cleaned by ion bombardment and heating. Initial sputter cleanings removed about one thousand atom layers each; these were followed by lengthy heatings at about 600°C. At first, this procedure left the surface with some carbon contamination as determined by an Auger spectrum, and this was the only contaminant observed. After several of the sputter-anneal cycles the carbon contamination disappeared and it is suspected that the carbon was migrating onto the surface from the sample holder and sample edges during the anneal stage until it was depleted. After a clean surface was established, the sample was annealed each day prior to making measurements. This was done to desorb any CO or other contaminants, which might have been adsorbed, to prevent their being cracked by the electron beam. Periodically, a significant amount of carbon could be detected by measurement of an Auger spectrum as shown in Fig. 42; this seemed to be accompanied by some degradation of the LEED beam intensities also. This could have been due to further surface migration during the many anneals or some cracking of CO could have taken place. A light sputtering of the surface ( $\sim 100$  atom layers) was sufficient to reestablish a clean surface as demonstrated by the Auger spectrum of Fig. 43. In the figure, each section of the Auger spectrum is labeled with the relative attenuation, A, the

time constant used,  $\tau$ , the peak to peak modulation voltage,  $V_m$ , and the primary electron current,  $I_p$ ; where they have been omitted they are the same as the previous section of the spectrum. To reduce the depth of damage during sputtering and make annealing easier, the ion energy was kept at 80 eV for all but the initial sputtering when 200 eV ions were used.

## 2.4 Results and Discussion

### 2.4.1 Secondary Electron Energy Distributions

Nearly all of the secondary electron energy distribution (SED) measurements were made for primary energies below 30 eV, since the most pronounced structure was obtained under these conditions. This structure can be generally described as peaks which occur at about 3.5 eV, 6.0 eV and 11.0 eV although the energy at which they occur is somewhat dependent on the scattering angle. This structure is shown in Fig. 44 for a typical energy distribution taken at the specular scattering angle with 45° angle of incidence and a primary energy of 21 eV. Also evident are two energy loss peaks which will be discussed later. For greater primary energies the 6.0 eV peak is degraded to a shoulder on the background but the structure near 11.0 eV becomes more prominent as shown in Fig. 45. In Fig. 46 three curves taken at different scattering angles are shown; the primary energy is 12 eV. There are definite shifts of the peak positions, especially the peak near 6.0 eV, with scattering angle. A detailed study of the angular behavior has not been made as yet so these observations are not definitely understood. Near the elastic peak the structure could be a combination of loss peaks and the secondary peak which occurs near 11 eV. As for the origin of the structure at 3.5 eV and 6.0 eV, two possibilities have been ruled out for the present. The first of these is the possibility that intraband Auger processes are taking place in the valence band. Energy values can be obtained that are reasonable only by assuming the ionized level is at a maximum in the density of states of the valence band and that the neutralizing electron as well as the ejected electron come from the top of the valence band. This seems unlikely and furthermore these peaks are not evident for the sputtered (and unannealed) surface. The second possibility is that these peaks are due to electrons from maxima in the density of states for the conduction band along symmetry directions; however, this does not agree very well with band structure curves available. The best explanation that can be given at present, is that this structure is due to diffraction

of secondary electrons out of the crystal. Secondary electrons created in the crystal whose momenta are directed in the proper direction can be diffracted out to the detector. If the energy of the secondary corresponds to the energy for strong diffraction then the signal at the detector will be enhanced. This would lead to fine structure on the secondary energy distribution curve. To check on this, the elastically scattered intensity in the specular beam was measured and is shown in Fig. 47. There is a good correlation between the energy for maxima in the elastic intensity plot and the energies where peaks occur in the SED. As a check on this, the crystal was sputtered with 80 eV ions, resulting in a disrupted surface which showed no diffraction. A SEE curve was measured for this condition and then the sample was annealed and the SED remeasured; this data is shown in Fig. 48. The broad hump near 4.5 eV in the sputtered crystal SED is not understood as yet, but the dependence of the fine structure upon surface order is clearly shown by the annealed crystal SED. This model could also explain the shift in the peak positions with angle, since electrons diffracted into a different angle would be expected to have maxima at a different energy. Since the angle of incidence could not be changed this could not be checked.

The structure which occurs near 11.0 eV does not correlate with any maxima in the elastic intensity, so it must be due to another mechanism. Even in the Auger spectrum taken at a primary energy of 1000 eV there is a peak evident near 11.0 eV, as shown in Fig. 43. For the present this peak will be considered as due to an Auger process, but the levels involved cannot be identified.

#### 2.4.2 Inelastic Scattering Measurements

Most of the characteristic loss measurements were taken for primary energies below 100 eV; a typical spectrum is shown in Fig. 49 for a primary energy of 70 eV. This spectrum was taken in the specular scattering direction where the largest amplitude loss peaks were obtained; they are shown indicated by arrows at energies of 1.5, 3.0, 10.0, 16.0 and 32.0 eV. The peaks at 16.0 eV and 32.0 eV are the bulk plasma loss peaks; the 16.0 eV peak is not very evident in this spectrum because of the low primary energy and the dominance of the surface plasma loss peak, at 10 eV, in this scattering direction. These three losses agree well with other measurements. All three of the smaller energy

loss peaks are felt to be due to interband transitions and correspond fairly well to some of the principal gaps found for optical transitions. However, since direct transitions are not required as in the case of photon excitation, this correspondence is not necessarily of any importance, but nondirect transitions between maxima in the density of states could also give values close to those observed. These peaks have not been cited in the literature previously, thus no comparisons can be made.

Several energy distributions at different primary energies in the specular direction are shown in Fig. 50. All the curves are shown for the same sensitivity, but a vertical displacement has been made between each set of two curves to avoid confusion. At the lower primary energies it is especially noticable, that the inelastic signal is increased when the elastic scattering is increased and this is more true the smaller the energy loss. This is what would be expected for a process of diffraction followed by inelastic scattering. Another noticeable feature is that the surface plasmon peak for the 80 eV curve is shifted from about 10 eV to 9 eV, and the increase in the inelastic signal is greater than the increase in elastic signal. This could be due to a superposition of electrons from both an EIS and an IES process. Since the elastic intensity exhibits a maximum centered at 75 eV, then the IES process would show increased signal centered about a loss of 5 eV. This could account for the large inelastic signal as well as the shift toward lower energy of the surface plasmon peak. The change in the relative sizes of the 16.0 eV and 10 eV peaks with primary energy, is considered to be due to changes in cross-sections with primary energy.

As was mentioned already, the inelastic signal was increased in or near the direction of diffraction maxima. For the measurements made so far, it would appear that there is little or no shift in angle between the maximum for a loss peak and that of an elastic peak. One exception has been found. This occurs for the scattering, near the 01 diffraction beam. A sharp maximum in elastic intensity of the 01 beam was obtained at 60 eV. Thus by setting the primary energy at 70 eV any IES process involving a surface plasmon of 10 eV would be enhanced.



Leaving the primary energy fixed, energy distributions were taken at a series of angles about the 01 beam in the 01 azimuth. A plot of the intensities of the elastic peak and 10 eV loss peak are shown in Fig. 51. Due to difficulty in deciding what background to subtract, the shape of the inelastic curve is somewhat uncertain but the shift in maxima is definite. As can be seen the LEED beam is rather wide; this is felt to be due to a carbon build-up on the surface, but does not affect these results. The angular shift is just that which would be expected for the elastic peak if the primary energy were changed from 70 eV to 60 eV. This seems to be a clear demonstration that the IES process is active.

## 2.5 Conclusions

An apparatus was constructed to measure the energy and angular distributions of secondary electrons from the (100) face of a Ge single crystal. Two types of measurement were made with the apparatus. One concentrated on peaks fixed in secondary energy and was made for primary energies below 30 eV. The second type of measurement dealt with the characteristic loss peaks in the near elastic region of the spectrum and was done for primary energies mostly in the 50-100 eV range.

Structure observed in the secondary electron energy distribution, was most pronounced at primary energies below 30 eV, and consisted of peaks at secondary energies of 3.5, 6.0, 11.0 eV, independent of the primary energy. These were at their maximum intensity in the specular scattering direction and were only evident when the crystal was well ordered and exhibited a diffraction pattern. The peaks at 3.5 and 6.0 eV occur at the same energy as maxima in the elastic intensity spectrum for the 00 beam. It is felt, therefore, that these secondary electron peaks are due to diffraction of secondary electrons.

Characteristic loss peaks were measured for energies of 1.5, 3.5, 5.5, 10.0, 16.0 and 32.0 eV. The three lowest energy losses are considered to be due to interband transitions while the larger three are due to plasmon excitations, the 10 eV peak being the surface plasmon, and the 16.0 and 32.0 eV peaks being the first and second bulk plasmons. By varying the angle of detection and primary energy, evidence was found for two types of double scattering events.

### 3. STUDY OF GALLIUM ARSENIDE THIN FILM SAMPLES

#### 3.1 Experimental Results and Discussion

A belljar vacuum system and electronics apparatus were constructed as a photocathode activation system. This system was successfully tested for ultra high vacuum conditions and production of the following measurements on installed samples: photoelectric yield, energy distribution of photoelectrons, Auger spectroscopy and sample temperature.

Two GaAs thin film samples were obtained from the Night Vision Laboratory, U.S. Army Research and Development Laboratories at Fort Belvoir, Virginia (Samples R64A and R62). These samples were installed in the photocathode activation system with the following results which were the similar for both samples: Peaks in the Auger data were found at  $\sim 150$ , 265 and 510 eV and these peaks were ascribed to the presence of sulfur, carbon and oxygen respectively. No peaks ascribed to either gallium or arsenic or the doping element, zinc, were found. No measurable photoemission was obtained from the samples either before or after heating to temperatures  $\sim 700^\circ\text{C}$ . Heating did result in evaporation of material from the sample surfaces. Auger spectra taken before and after cesiation of the sample surface showed cesium had a residence time of less than ten minutes on the surface. No photoemission measurements were made during the short cesium residence time, and no measurable photoemission was obtained in tests made  $\sim 15$  minutes after cesium deposition. The Auger spectra obtained  $\sim 15$  minutes after cesiation were identical with those obtained before cesiation. This situation was repeatable with cesium coverage from 1/10 to greater than one monolayer.

#### 3.2 Conclusions

The two GaAs thin film samples examined in the photocathode activation system were very poor photoemitters. Continuing work in the photocathode activation system was subsequently supported by other funds and will be reported elsewhere.

#### 4. STUDY OF GALLIUM ARSENIDE-CESIUM

##### 4.1 Introduction

The efficiency of cesiated GaAs  $p^{++}$  single crystals as high yield visible-infrared photocathodes is well known.<sup>1</sup> Research has been directed toward a better understanding of two aspects of such a photoemitter: 1) The instability of the photoelectric yield with time subsequent to cesium deposition and 2) the effect of surface treatment of the GaAs substrate (prior to cesiation) upon the final photoelectric yield. The former point was studied under the previous contract<sup>2</sup> employing Auger electron spectroscopy and photoemission measurement techniques. It was concluded that the decay in photoelectric yield with time was due to the adsorption of the gaseous ambient (mainly CO) and not to the desorption of cesium. The effect of the adsorption process was to decrease the effective GaAs-Cs dipole layer and shift the photoelectric threshold to higher photon energies.

The latter aspect has not been carefully studied except to note that a GaAs(110)-Cs photosurface cleaned by heating to 680°C possessed a photoelectric yield inferior to that of the cleaved surface and that such a thermally treated surface was gallium rich.<sup>39</sup> During this interval the program was extended to study the effect of surface treatments upon the final photoelectric yield of uncleaned GaAs(110).

##### 4.2 Experimental Techniques

These studies were directed toward monitoring the work function of the uncleaned GaAs(110) surface under cesiation and heating cycles. The basic experimental apparatus has been described previously.<sup>39</sup> The work function data were obtained by analysis of the I-V retarding potential characteristic acquired with the 3-grid LEED electron optics. Weber and Peria<sup>34</sup> have shown that other information than the change in work function can be obtained from the retarding potential characteristic.

The sample was heated by focussing the energy from an external radiation source upon the sample while the temperature was monitored with a Therm-dot optical pyrometer capable of 3°C resolution in the range 100°C to 700°C. To circumvent the difficulty encountered by use of a

radiation source with a pyrometric determination of temperature, a time-base recorder was used to monitor the rate of decay of temperature after the radiation source had been extinguished. The equilibrium temperature of the sample was determined by extrapolation of the decay curve back to that instant.

Cesium ions were deposited upon the thermally treated surface by means of an aluminosilicate source and the associated ion optics. Accurate coverage could be obtained by integrating the ion current by means of a capacitor. The use of such sources has been discussed previously (see Sec. (1.2.4)).

#### 4.3 Results and Discussion

A GaAs(110) crystal surface, obtained by roughly cleaving in air was employed in these studies. In the initial study the surface was cleaned by heating to 680°C and the cesium was deposited in 0.1 monolayer increments. This cycle was repeated (removing the previous Cs deposit) until 0.9 monolayer coverage was reached. As will be shown later, the nature of the I-V curve at 0.9 monolayer made further deposition meaningless. The plot of work function vs. cesium coverage is shown in Fig. 52(a). It is evident that the surface is considerably altered from the cleaved surface, where a w.f. minimum of  $\leq 1.5$  eV is reached at less than one monolayer coverage. Assuming that the w.f. at zero coverage is 4.5 eV, the minimum, reached at 0.9 monolayer, was 2.85 eV. This result will become plausible after some further observations are discussed.

A second important parameter measured from the I-V characteristics was the total width and shape of the curve from  $I=0$  to  $I=I_{\text{max}}$ . The retarding potential technique measures a true average work function if the spatial extent of the work function variation is small compared to the beam diameter or if the magnitude of the variation is small. However as the patch size increases and/or the work function variation on the surface becomes large, the I-V curve represents a composite of the characteristics of each distinct surface area. This is shown graphically in Fig. 52(b) for a heated GaAs(111)A + Cs surface. This delineation of the surface patch structure is not clearly observed in the GaAs I-V characteristic until Cs is deposited, suggesting

that the initial w.f. difference between the gallium-rich<sup>39</sup> and GaAs areas is small and that the adsorption of cesium on the inhomogeneous surface is strongly dependent upon the substrate atoms.

Experimentally it was observed that the width of the I-V curve increased with increasing cesium deposition. At coverages near 1 monolayer the structure illustrated in Fig. 52(b) appeared. The width of the I-V curve prior to cesium deposition was found to increase after the first few heating cycles and to remain essentially constant thereafter (Fig. 53(a)). The scattering of points at .6 and .9 monolayers may indicate the presence of a gradient in gallium concentration across the surface due to non-uniform heating. However the apparatus was such that it was not possible to sample precisely the same area of the crystal after each heating cycle so that non-uniformities may be reflected in the data. The width of the I-V curve after cesium deposition is also shown as a function of coverage in Fig. 53(a). It is clear that the presence of cesium on the surface greatly accentuated the work function difference between the GaAs and Ga areas of the composite surface.

The preliminary conclusion reached from these observations was that the Ga-rich areas of the surface were, at the very least, inactive in increasing the photoelectric response. Furthermore, investigation of another phenomenon which occurred subsequent to cesium deposition indicated that the gallium-rich areas acted as a "sink" for cesium ions. This phenomenon was the migration of alkali ions in the first few minutes after deposition. This was first studied by L. Cordes<sup>86</sup> employing  $\text{Na}^+$  on Ge. Cordes found, by depositing Na on 1/2 of a Ge(111) web crystal and probing the Na distribution by scanning the work function over the surface, that the Na migrated over distances of 2 to 5 mm depending on initial coverage. He also found that the final distribution was non-uniform and was attained in  $\leq 10$  minutes. No further change in Na distribution was observed in 24 hours. Cordes showed that this process could not be explained in terms of a simple diffusion process but was a result of electrostatic repulsion between  $\text{Na}^+$  ions. This migration phenomenon was also observed in the present study by monitoring the change in work function in a particular surface area as a function of time. The I-V characteristic was measured as quickly as

possible (typically 1-2 minutes after Cs deposition) and at 2-3 minute intervals until the curve became stabilized. Typical curves illustrating the shift in work function at .1 monolayer coverage are shown in Fig. 53(b). At higher coverages however the shift in work function due to  $\text{Cs}^+$  migration occurred in a manner that suggested the role of Ga as an effective Cs sink. In Fig. 54 is shown the nature of the work function change with time on a patchy surface with a 0.9 monolayer Cs deposit. If the migration of  $\text{Cs}^+$  ions were from Cs-rich (low w.f.) to low density (high w.f.) areas one would expect an equilibrium I-V characteristic as shown by the dotted curve in Fig. 54. On the contrary we observed a further depletion (increase in w.f.) in the high work function areas (upper portion of the curve) and little shift in the lower work function areas (lower portion of the curve). This suggests that  $\text{Cs}^+$  ions within a migration length of a gallium island may be captured, perhaps by alloying. The non-uniform equilibrium  $\text{Cs}^+$  distribution then is a maximum between the gallium islands and is small surrounding the Ga-rich areas. The plausibility of this hypothesis is strengthened by the observation that the low work function areas in Fig. 54 do not shift appreciably, indicating little  $\text{Cs}^+$  loss in the initially high  $\text{Cs}^+$  concentration areas.

As an additional check on the above hypothesis the cesiated GaAs surface was exposed to  $5 \times 10^{-8}$  Torr-minutes of oxygen. If the higher w.f. areas in the I-V curve are due to Ga-rich (Cs-deficient) areas then little shift in w.f. should be observed. Conversely the active Cs-rich interstitial areas would shift in w.f. due to reduction of the Cs-GaAs dipole by oxygen absorption. The results, shown in Fig. 55, do indeed show that only a portion of the surfaces is active since only the lower w.f. areas were shifted.

#### 4.4 Conclusion

The effect of cleaning the GaAs surface by heating prior to formation of the GaAs-Cs photocathodes was evaluated by monitoring the work function during the activation process. By observing the characteristics of the I-V retarding potential curves from GaAs-Cs during heating-Cs deposition cycles, evidence of a gallium rich surface<sup>2</sup> has been obtained. The small work

function reduction due to cesium adsorption can be understood by the assumption that gallium acts as a cesium "sink" for adsorbed species within a migration length. It appears that, in equilibrium, the stoichiometric GaAs areas have perhaps an effective coverage of 0.3 monolayers for an apparent 0.9 monolayer deposition. This effect precludes attainment of high photoelectric yield cathodes. This study has implications as to the feasibility of non-epitaxial GaAs film photocathodes, where variations in surface stoichiometry may occur over micron distances.

It was the intention of this study to continue the GaAs work in a stainless steel ultra-high vacuum system as described in Sec. 1.2. A cleavage apparatus was designed and constructed and appropriate GaAs samples were cut. However at this time it was decided that silicon would be a more useful material to study and the GaAs research was terminated.

## 5. DECONVOLUTION TECHNIQUES IN AUGER ELECTRON SPECTROSCOPY

### 5.1 Introduction

The effectiveness of a LEED (low-energy electron diffraction) apparatus for energy analysis of Auger electrons from a solid surface, as well as for structural studies of the surface, has been amply demonstrated.<sup>14,15</sup> The correlative study of the chemical and structural nature of the surface thus made possible removes considerable ambiguity in the interpretation of surface phenomena.<sup>19,87</sup>

However, certain limitations have arisen in the use of Auger Electron Spectroscopy (AES) due to the inherent lack of resolution in the LEED analyzer and to an incomplete understanding of Auger processes and Auger electron interactions in the solid. The resolution of the LEED-Auger spectrometer is limited by the static characteristics of the LEED chamber and by the dynamical broadening inherent in the ac modulation, phase-sensitive detection techniques used in AES.<sup>20</sup> In addition to limiting resolution, the retarding grid field penetration also produces a shift in the apparent Auger transition energy which, in some cases, causes uncertainties in the identification of the parent atom. Misinterpretation of Auger spectra can also arise from neglecting the effects of Auger electron interactions of a single-particle (e.g., ionization losses) and collective (e.g., plasma losses) nature.<sup>88</sup> The study of more fundamental problems involving Auger processes in solids, such as the effects of variations in chemical bonding upon the Auger spectra or band structure studies, are also limited due to the poor resolution and extraneous energy loss structure observed in AES data.

It has been found that by using the energy loss and analyzer resolution information contained in the nearly elastically-backscattered primary electron energy distribution in a deconvolution technique, the complexity of the Auger data (resulting from Auger electron interactions) and the energy broadening can be greatly reduced. The main purposes of this work are to describe the deconvolution technique



and its applicability to AES and to present experimental evidence supporting its viability. Although of secondary importance in this report, the more obvious features of the deconvoluted data will be discussed whenever they appear to be significant.

## 5.2 Formulation of the Deconvolution Technique

### 5.2.1 Mathematical Procedure

To recover the unbroadened Auger electron energy distribution  $A(\epsilon)$ , from the measured distribution,  $N(\epsilon)$ , we must describe in functional form,  $B(\epsilon)$ , the cumulative effects of finite instrument resolution and inelastic interactions in the solid upon an ejected Auger electron. If such a function  $B(\epsilon)$  can be obtained, then  $A(\epsilon)$ ,  $N(\epsilon)$  and  $B(\epsilon)$  can be related by the convolution integral,

$$N(\epsilon) = \int_{-\infty}^{\infty} A(\epsilon') B(\epsilon - \epsilon') d\epsilon' \equiv A(\epsilon) * B(\epsilon). \quad (1)$$

This relationship has been widely used in many forms of spectroscopy<sup>89,90</sup> to compensate for the effects of instrument broadening. Two problems appear in obtaining the unbroadened spectrum  $A(\epsilon)$ : the specification of the functional form of the broadening function  $B(\epsilon)$  and the solution of the convolution integral, Eq. (1), for the unknown function,  $A(\epsilon)$ , in the integrand. The latter is most easily accomplished by use of the well-known operational property of Fourier transforms (F), viz.,

$$F[N(\epsilon)] = F\left[\int_{-\infty}^{\infty} A(\epsilon') B(\epsilon - \epsilon') d\epsilon'\right] = F[A(\epsilon)] \cdot F[B(\epsilon)] \quad (2)$$

Then the unknown function,  $A$ , is simply

$$A(\epsilon) = F^{-1}\left[\frac{F[N(\epsilon)]}{F[B(\epsilon)]}\right]; F^{-1} = \text{Inverse Fourier Transform} \quad (3)$$

A further property of the convolution integral which is of practical importance in the deconvolution technique is

$$N'(\epsilon) = A'(\epsilon) * B(\epsilon) = A(\epsilon) * B'(\epsilon) \quad (4)$$

i.e., the derivative of the convolution integral is the convolution of either of the functions in the integrand with the derivative of the other. This relationship is

useful since the experimentally measured quantities in AES are usually the derivatives of the respective electron energy distributions.

It follows then that Eq. (3) can be rewritten as

$$A(\epsilon) = F^{-1} \left[ \frac{F[N'(\epsilon)]}{F[B'(\epsilon)]} \right] \quad (5)$$

It should be emphasized that the use of either the derivatives ( $N'(\epsilon)$ ,  $B'(\epsilon)$ ) or the energy distributions ( $N(\epsilon)$ ,  $B(\epsilon)$ ) in the deconvolution technique yields the debroadened Auger electron energy distribution.

### 5.2.2 Specification of the Broadening Function, $B(\epsilon)$

The success of the deconvolution technique in obtaining higher resolution spectra is dependent upon the accuracy to which we can functionally describe the apparent energy broadening which an Auger electron distribution experiences through interactions within the solid and by subsequent instrumental broadening. The interactions experienced by fast ( $> 30$  eV) electrons within an electron mean-free path of the surface are mainly: (a) electron-phonon scattering, which contributes typically  $< .1$  eV energy broadening and (b) discrete characteristic losses of 5-30 eV due to single-particle interactions (e.g., ionization losses) and collective interactions of the electron with the electron density of the solid (plasma losses). Much information regarding characteristic losses in solids has been obtained by monitoring the energy distribution of nearly elastically-backscattered primary electrons from solid surfaces.<sup>91</sup> This "elastic peak" ( $\approx EP(\epsilon)$ ) distribution, which is readily obtained in AES, reflects the cumulative effects of electron interaction within the solid as well as the subsequent instrument energy broadening.

It has been shown<sup>88</sup> that certain satellite structures appearing on the low energy tail of Auger electron distributions can be correlated in energy with the characteristic loss features of the  $EP(\epsilon)$  spectrum (recorded at the Auger transition energy). This qualitative agreement suggests that the total energy broadening experienced by Auger electrons may approximate that experienced by nearly elastically-backscattered primary electrons. Thus, in the present work, the elastic peak spectrum  $EP(\epsilon)$ , was assumed to describe the form of energy

broadening,  $B(\epsilon)$ , pertaining to the Auger electron energy distributions. The  $EP(\epsilon)$  spectrum was recorded at the Auger transition energy to eliminate the effects of the energy dependences of the electron interaction cross-section and subsequent instrument broadening.

A simple, phenomenological model illustrating the energy broadening affecting the Auger and elastically-scattered primary electrons is shown in Figs. 56 and 57. Figure 56 illustrates schematically the LEED-Auger measurement apparatus, which will be briefly discussed in Sec. 5.4.1, and the phenomenological energy broadening and scattering parameters acting upon each electron species. Figure 57 illustrates a hypothetical interaction and broadening process resulting in the experimentally measured energy distribution  $EP(\epsilon)$  and  $N(\epsilon)$ . In Fig. 56 it is assumed that a primary electron beam with a small energy spread ( $= \delta(\epsilon)$ ) interacts with the solid and produces a certain number of electrons which are backscattered with essentially no energy loss. The interactions with the solid for this group are mainly discrete characteristic losses (with a small electron-phonon broadening) - described functionally by the scattering function,  $S_p(\epsilon)$  as shown in Figs. 56 and 57. Upon ejection from the crystal this electron distribution is instrument-broadened, according to  $IB(\epsilon)$ , and is recorded as  $N(\epsilon)$ . A similar argument follows for the internally generated Auger electron distribution,  $A(\epsilon)$ , shown in Figs. 56 and 57. The major assumptions to be made in equating the elastic peak spectrum,  $EP(\epsilon)$ , to the broadening function,  $B(\epsilon)$ , in Eq. 1 are: (a) the Auger primary electrons interact with the solid in an identical manner, i.e.,  $S_A(\epsilon) = S_p(\epsilon)$  and (b) the instrument broadenings experienced by equally energetic ejected Auger and primary electrons are identical ( $IB(\epsilon)$ ). These assumptions will now be discussed briefly.

### 5.3 Physical Basis for the Deconvolution Technique

#### 5.3.1 The Equivalence of Auger and Primary Electron Scattering

As mentioned previously, the qualitative similarity between inelastic interactions of the primary and Auger electrons in solids has been demonstrated.<sup>86</sup> A quantitative

measure of the relative scattering probabilities can, in principle, be made by measurement of the relative areas under the main Auger or elastic peaks and the subsequent energy-loss peaks. The ratio of areas under successive peaks then is a measure of the relative probability for inelastic scattering of the Auger and primary electron.<sup>72</sup> Although this procedure involves a certain arbitrariness, due mainly to the uncertainty in the main emission bandwidth and shape, it can be shown that the apparent scattering probability is higher for Auger electrons than for back scattered primaries.<sup>93</sup> This difference arises from the fact that the primary electron elastic peak spectrum contains a large non-interacting specular component. The implication of these results is that the use of the elastic peak spectrum,  $EP(\epsilon)$ , as the broadening function,  $B(\epsilon)$ , in the deconvolution procedure will tend to underestimate the inelastic structure present in the Auger emission spectrum. We shall see, however, in Sec. 5.4.1, that the "residue" remaining after deconvolution can usually be identified and thus does not detract greatly from the interpretation of the final spectrum.

### 5.3.2 The Effects of Instrument Broadening

The second assumption made in the deconvolution procedure is that the energy broadening inherent in the Auger electron spectrometer acts identically upon ejected Auger and backscattered primary electrons of equal energy. The accuracy of this statement will now be discussed briefly.

It is clear that the static resolution limitations of the hemispherical analyzer will affect the ejected Auger and primary electron in the same way. The energy broadening and shift in the apparent external kinetic energy due to the nonspherical equipotential retarding surfaces will affect each electron specie identically. The deconvolution technique will clearly account for the energy broadening in this case. It will also account for the shift in apparent transition energy as can be seen from Eq. (1): since the convolution

integral is a linear functional, a shift in energy of a primary peak spectrum (recorded at an energy  $\epsilon$ ) to  $\epsilon + \Delta E$  will cause a corresponding energy shift to  $(\epsilon - \Delta E)$  in the deconvolved spectrum,  $A(\epsilon)$ .

Dynamical broadening arises from the measurement technique used in Auger electron spectroscopy. This technique superimposes an ac signal,  $V_1 \sin \omega t$ , onto the dc retarding potential,  $V_0$ , of the suppressor grids. A Taylor series expansion of the collector current yields

$$i(V_0 + V_1 \sin \omega t) = i(V_0) + i'(V_0) \sin \omega t + \frac{V_1^2}{2!} i''(V_0) \sin^2 \omega t + \dots \quad (6)$$

Expanding the terms involving  $\sin^n \omega t$  in terms of  $\cos m \omega t$ ,  $\sin m \omega t$  ( $m = 1, 2, 3, \dots$ ) one obtains

$$\begin{aligned} i(V_0 + V_1 \sin \omega t) = & \left[ i(V_0) + \frac{V_1^2}{2} i''(V_0) + \dots \right] \\ & + \left[ V_1 i'(V_0) + \frac{V_1^3}{8} i'''(V_0) + \dots \right] \sin \omega t \\ & - \left[ \frac{V_1^2}{2} i''(V_0) + \frac{V_1^4}{48} i^{(4)}(V_0) + \dots \right] \cos 2\omega t - \dots \end{aligned} \quad (7)$$

It is clear from Eq. (7) that, if  $V_1$  is small, the coefficient of the  $m$ th harmonic frequency is proportional to the  $m$ th derivative of the collector current characteristic. As  $V_1$  increases the higher order terms of the coefficients in the Taylor expansion (Eq. (7)) become appreciable with respect to the first. It is evident that the form and magnitude of the harmonic distortion depends upon the magnitude of the modulation,  $V_1$ , and upon the shape of the electron energy distributions. Thus the dynamical broadening arising from the ac modulation technique can be accounted for in the deconvolution procedure only (a) if the respective  $EP(\epsilon)$  and  $A(\epsilon)$  distributions are identical or (b) in the limit when the modulation amplitude approaches zero. Practically, the influence of modulation distortion can be seen by deconvolution of the data at several modulation amplitudes. The erroneous structure due to harmonic distortion can be seen to disappear at low modulation amplitudes.

## 5.4 Experimental Techniques and Results

### 5.4.1 Experimental Technique

The Auger Electron Spectroscopy instrumentation used in recording the experimental electron energy distributions was essentially that developed by Weber and Peria,<sup>14</sup> using a LEED chamber (shown schematically in Fig. 56). The measured quantities in all data which will be shown were the derivatives of the electron energy distributions,  $dN/d\epsilon$  and  $dEP(\epsilon)/d\epsilon$  obtained by the ac modulation, phase-sensitive detection scheme proposed by Harris.<sup>20</sup> This technique allows Auger spectra, which appear superimposed upon the secondary electron background, to be recorded at higher sensitivity. This background in most cases was assumed to be constant in the derivative spectra. The energy distributions of the raw data,  $N(\epsilon)$  and  $EP(\epsilon)$  shown in the following text were obtained by computer integration of the derivative spectra using a FabriTek 1064 instrument computer. In the following presentation of data, emphasis will be placed upon the viability of the deconvolution technique for AES and, wherever possible, upon the significance of the resultant data. Some deconvoluted spectra will be compared with available published electron emission spectra - notably the data collected by K. Siegbahn, et al.<sup>94</sup> using the ESCA spectrometer. In the latter technique, a high resolution, double-focussing magnetic spectrometer is used to energy-analyze Auger and photoelectrons emitted from a specimen excited by X-radiation or electron impact.

### 5.4.2 Experimental Results

#### 5.4.2.1 Inner Level Transitions

The interpretation of the final deconvoluted spectra  $A(\epsilon)$  is perhaps simplest in the case of Auger processes involving inner atomic levels. In particular it is advantageous to examine transitions involving energy level doublets with, typically, 3-10 eV separations. This allows comparison of the peak separations of the deconvoluted data with tabulated data and allows comparison of the relative intensities of each component of the doublet with photoelectron emission (ESCA) data.

In:  $M_{4,5}N_{4,5}N_{4,5}$

A prominent Auger doublet occurs from  $M_{4,5}N_{4,5}N_{4,5}$  transitions in the elements 2d through Te.<sup>95</sup> The notation used above indicates, in sequence; the initial ionized state, the origin of the neutralizing electron and the initial level of the externally observed electron. Actually the ejection level for this In Auger transition cannot be specified due to the near energy coincidence of the  $N_{4,5}(4d)$  levels. For simplicity we shall retain only a single subscript.

Shown in Fig. 58(a) is the experimentally observed Auger electron energy distribution,  $N(e)$ , and a schematic energy level diagram indicating the origin of the  $M_{4,5}N_5N_5$  spectral lines from In. The distribution was obtained from a sputtered In sample using a primary energy of 2000 eV and 1V rms modulation amplitude. As can be seen, the apparent bandwidth extends over nearly 50 eV. The corresponding elastic peak spectrum,  $EP(e)$ , recorded from In in the energy range of the  $M_{4,5}N_5N_5$  transitions (410 eV) is shown in Fig. 58(b). It should be noted that In displays rather prominent characteristic energy-loss peaks whose spacing below the main elastic peak corresponds quite closely to the calculated bulk plasma-loss energy of 11 eV. Not evident in Fig. 58(b), although easily seen in the derivative ( $\frac{d}{de} EP(e)$ ) spectrum (not shown), is a surface plasma-loss at approximately 8-9 eV below the elastic peak. The deconvolution of  $N(e)$  and  $EP(e)$  was initially carried out using only the elastic peak portion of the  $EP(e)$  spectrum in Fig. 58(b). This, in effect, presumes that Auger electrons experience only a "smearing" only in energy due to instrument broadening and neglects the inelastic interactions encountered by the Auger electrons in the solid. The result of this deconvolution, shown in Fig. 59(a), shows greater resolution of the main  $M_{4,5}N_5N_5$  peaks but retains an appreciable, structured, low energy tail. Conversely, the results of the deconvolution of  $N(e)$  with the entire  $EP(e)$  function, shown in Fig. 59(b) indicates that inelastically scattered electrons contribute significantly to the low energy tail. The remaining structure in Fig. 59(b) can be easily identified. As was discussed in Sec. 5.3.1, the deconvolution technique tends to underestimate the inelastic scattering cross-section of Auger electrons due to the effect of specular backscattering of the primary electron beam. The "residue" in the In spectrum can be identified as arising from bulk and surface plasma losses

NOT REPRODUCIBLE

experienced by ejected  $M_{4,5}N_5N_5$  Auger electrons. Identified in Fig. 59(b) are the bulk plasma losses ( $\hbar\omega_p$ ) at 11 eV separations from the  $M_4N_5N_5$  and  $M_5N_5N_5$  peaks. The corresponding surface plasma loss ( $\hbar\omega_p/2$ ) from the  $M_5N_5N_5$  transition can also be readily identified. The expected energy position of the surface plasma loss peak at approximately  $\hbar\omega_p/2$  below the  $M_4N_5N_5$  peak is indicated by the arrow in Fig. 59(b). This contribution could account for the larger apparent half-width of the  $M_5N_5N_5$  peak (4.7 eV) compared to the  $M_4N_5N_5$  peak (3.2 eV). The relative intensities of the peaks (from ordinate values) closely correspond to the 3:2 ratio expected from the statistical electron populations of the  $M_5$  ( $j = 5/2$ ) and  $M_4$  ( $j = 3/2$ ) levels. (Under the influence of electron bombardment the numbers of vacancies in the  $M_4$  and  $M_5$  levels will be proportional to  $(2j + 1)$ ).

Perhaps the most important result of the deconvolution of the In spectrum is the direct evidence of the existence, and an estimate of the magnitude, of inelastic scattering of Auger electrons within the solid. The almost complete disappearance of the structured low energy tail argues more strongly than simply by comparing the energy separations of structure in the Auger and elastic peak spectra,<sup>88</sup> that Auger electrons undergo discrete inelastic losses of energy prior to ejection into vacuum.

Cd:  $M_{4,5}N_{4,5}N_{4,5}$

The deconvolution of the  $M_{4,5}N_{4,5}N_{4,5}$  doublet ( $N_{4,5}$  not resolved) of Cd from CdS (0001) provides a clearer indication of the usefulness of the deconvolution technique than that of the In spectrum discussed above. This is due principally to the absence of prominent characteristic losses for electrons in CdS. Thus the experimental data could be recorded on a smaller energy interval to include essentially only the region of interest, i.e. the doublet  $M_{4,5}N_5N_5$ . As was indicated in Sec. 5.2.1 (Eq. 5) the linearity of convolution allows the direct use of the derivative data,  $\frac{d}{de}(EP(e) \cdot N(e))$  in obtaining the Auger energy distribution,  $A(e)$ . The respective derivatives of the electron energy distributions measured from Cd- $M_{4,5}N_5N_5$  are shown in Fig. 60. The shift in the point of maximum negative deflection in the  $\frac{d}{de} EP(e)$  spectrum from its expected values at 396 eV to 402 eV is due principally to field penetration effects in the analyzer. A comparison of the

NOT REPRODUCIBLE



resultant deconvoluted Auger distribution,  $A(e)$ , with the experimentally measured distribution,  $N(e)$ , (the latter obtained by computer integration) is shown in Fig. 61. The data was scaled by approximately normalizing to the intensity of the  $M_5N_5N_5$  peak. It is clear from the data shown that the deconvolution technique has yielded a substantially improved spectrum.

Comparison of the final spectrum,  $A(e)$ , can also be made with photoelectron data obtained from the ESCA technique. Shown in Fig. 62 is a superposition of the Cd- $M_{4,5}N_5N_5$  data with the energy distribution of photoelectrons from the  $M_{4,5}$  levels of Cd ( $CdCl_2$ ) excited by  $MgK\alpha$  (1253.6 eV) radiation.<sup>64</sup> The abscissa refers to the Auger electron energy. The ESCA data was shifted along the energy axis to coincide with the Auger transition energy. The kinetic energy of the photoelectrons was in the range 837-850 eV, from which the binding energies of the  $M_{4,5}$  levels were determined by energy conservation, viz:

$$E_{\text{BINDING}} = E_{K\alpha} - E_{\text{KINETIC}} - \phi$$

where  $\phi$  is the spectrometer work function. These binding energies, positive with respect to the Fermi level, are indicated in a schematic diagram of the photoelectron process observed in ESCA.<sup>96</sup> The relative intensities of the  $M_{4,5}N_5N_5$  peaks in the ESCA and Auger distributions show good agreement within the errors involved in determining the ordinate zeros and the high energy cutoff of the  $M_4N_5N_5$  transition. As for the In  $M_{4,5}N_5N_5$  transition, the intensity ratio between the  $M_5N_5N_5$  and  $M_4N_5N_5$  transitions are in good agreement with the 3:2 ratio expected. In this case the areas were measured with a planimeter for intensity comparison rather using the ordinate values as in the In spectrum.

No meaningful comparison can be made between the ESCA and Auger peak widths in Fig. 62 since the energy distributions reflect different final states.

#### 5.4.2.2 Adsorbate Transitions

A particularly prevalent group of adsorbate transitions are those arising from the common surface contaminants C, O and S. There exists much uncertainty about the influence of the substrate upon the adsorbate Auger emission spectra,

NOT REPRODUCIBLE

as well as uncertainty about the origin of the structure in the low energy tail of the emission spectrum. A rather cursory examination of some oxygen emission spectra will provide some answers to the above questions and will further demonstrate the usefulness of the deconvolution procedure.

#### Oxygen: KLL

Oxygen Auger spectra were obtained from adsorbed oxygen on Ti and Mo. Figure 63 shows a direct comparison of the oxygen KLL Auger spectrum from  $\text{TiO}_2$  using the ESCA technique (p. 163, Fig. VI-12, Ref. 94) and the corresponding spectrum from oxidized Ti using the AES deconvolution technique. The spectra were normalized to equal  $\text{KL}_2\text{L}_3$  peak heights. The background and inelastic scattering in the ESCA spectrum has not been compensated for - hence it appears skewed with respect to the AES spectrum. There are obvious structural similarities between the curves but the AES spectrum shows greater detail than the uncorrected ESCA spectrum. The labeling of the transitions follows from the work of Asaad<sup>97</sup> and Siegbahn (Chapt. VI, Ref. 95). It is shown in these references that the number of expected KLL lines using intermediate coupling theory is 9. However, the energy degeneracy of the  $2s12p^5(^3P_{0,1,2})$  and  $2s22p^4(^3P_0, \sim)$  states in oxygen, where pure LS coupling theory is applicable, reduces the observable number to 6. As a result the labeling on some of the peaks in Fig. 63 is not unique. The arrows in Fig. 63 indicate the position of possible characteristic loss residues ( $\Delta\omega_p = 12, 26 \text{ eV}$ ) which appear in the  $\frac{d}{dE}\text{EP}(\epsilon)$  spectrum (not shown). The KLL spectrum from oxidized Mo (Fig. 64) shows similar structure to the O-Ti spectrum, with the exception of the absence of the structure identified in Fig. 63 as the  $\text{KL}_2\text{L}_2$  transition. The characteristic losses in oxidized Mo which appear in the  $\frac{d}{dE}\text{EP}(\epsilon)$  spectrum occur at 12 and 27 eV. The former is nearly coincident with the  $\text{KL}_1\text{L}_3$  transition - the latter is indicated by the arrow in Fig. 63. Similar structure was also found in the oxygen KLL spectrum of oxidized Al and  $\text{Al}_2\text{O}_3$  (Fig. 65). Two conclusions can be reached from the preceding: (a) the principal structure observed on the low energy tail of the oxygen KLL spectrum (in contrast to that of  $\text{In-N}_4, \text{N}_5\text{N}_5$ ) arises from the KLL Auger transitions, and (b) the gross features of the KLL emission spectra are characteristic of the oxygen atom and independent of the substrate or oxidation state.

NOT REPRODUCIBLE

#### 5.4.2.3 Chemical Effects in O:KLL Spectra

As can be seen from Figs. 63 and 64 the KLL transition energies of oxygen in Ti-O are 1.2 eV lower than the corresponding transitions from Mo-O. Although it is possible that the observed shift might result from the existence of a non-zero surface potential on an insulating oxide (the irradiation of the oxide layers with 2000 eV primary electrons could result in a surface potential whose magnitude depended upon the secondary emission ratio of the oxide) such shifts can also be interpreted as changes in the binding energies of the inner (K shell) electrons with respect to the Fermi level. From simple electronegativity differences, which are an indication of the ionicity of the bond, the binding energy of the K shell (hence Auger electron transition energies) should increase with decreasing cation electronegativity, as observed.

In the previous section, the emphasis was placed upon the similarities in the oxygen KLL structures independent of the cation (Ti, Mo, Al). However it is obvious from examination of Figs. 63-65 that differences in the spectra do exist. As stated previously, the expected number of KLL lines for  $Z = 8$  is 6 on the basis of pure LS coupling theory. However, in contrast to the KLL spectra calculated by Asaad and Burhop ( $Z \geq 12$ ), the  $L_{2,3}$  shells ( $2p$ ) of the oxygen  $1s^2 2s^2 2p^4$  configuration are incomplete. Thus the influence of chemical binding upon the KLL spectra for oxygen ( $1s^2 2s^2 2p^4$ ) should be observable.

It should be noted that the available final states for Auger transitions, shown in Figs. 63-65, assumes complete ionic bonding. Although this is not strictly correct, the ionic character of the bonds from simple electronegativity differences, indicates a  $> 60\%$  ionic character for the oxides studied - hence the labeling is, to some extent, justified.

Siegbahn (ref. 94, p. 163) has observed a variation in linewidth in the KLL spectrum of fluorine ( $1s^2 2s^2 2p^5$ ) in  $LiF$  and  $MgF_2$  but did not observe additional KLL lines or variations in transition probabilities due to chemical bonding. Although it cannot be determined from the ESCA O:KLL spectrum (Fig. 63), Siegbahn does correctly anticipate a more complex Auger spectrum for oxygen in  $TiO_2$  than pure LS coupling predicts due to the availability of more final state configurations arising from oxygen bonding. As previously stated, Asaad and Burhop have predicted using intermediate coupling, a nine line KLL spectrum for elements with atomic numbers in the range approximately  $25 < Z < 80$ . This prediction has been experimentally confirmed, with good agreement between theoretical and experimental relative line intensities and separations. A comparison of the O:KLL spectra from O: $Al_2O_3$  and O:AlO which has been shifted to allow coincidence of the  $KL_1L_1(^1S)$  and the  $KL_1L_2(^1P)$  peaks, is shown in Fig. 65. It is obvious that the variations in peak width and structure occur in the configurations involving principally the  $L_{2,3}$  final state i.e., the bonding orbitals of the oxide. For closed L shell configurations ( $n \geq 10$ ) one observes similar final state splitting in the configurations involving the  $L_{2,3}$  states; the magnitude and separation being a function of atomic number. However it is clear that the relative peak separations in the KLL spectra in Fig. 65 do not change appreciably with variations in the cationic or valency state. Rather, the structure differences in the spectra can be mainly ascribed to variations in the relative transition probabilities for the  $2s^1 2p^5$  and  $2s^2 2p^4$  final state configurations. This implies that the energy broadening observed by others in the KLL spectrum of low Z elements (e.g., F:KLL Ref. 94) may not be due to "solid state effects" (e.g., the ordinary broadening of discrete electron energy levels due to orbital overlap from neighboring atoms) but may be explicable in terms of variations in transition probability as suggested by Fig. 65. By comparing the line-widths and intensities of the  $KL_1L_1(^1S)$  and  $KL_1L_2(^1P)$  transitions with the final states of the  $2s^2 2p^4$  configuration, i.e.,  $KL_2L_2(^1S)$ ,  $KL_2L_3(^1D)$ ,.....significant variations in transition probability can qualitatively be seen to occur most noticeably in comparing the AlO and  $Al_2O_3$  spectra in Fig. 65. The O:KLL spectrum of  $Al_2O_3$  appears, to a greater extent than the others, energy broadened. This however can as well be ascribed to increased transition probabilities for the  $KL_3L_3(^3P_{0,2})$  and  $KL_2L_2(^1S_0)$  configuration with respect to the main  $KL_2L_3(^1D_2)$  peak. Also the asymmetry in the

$KL_1L_2(^1P_1)$  peak in  $Al_2O_3$  and the additional structure on the high energy side of the  $KL_1L_3(^3P_1)$  peak suggests the increase in transition probability of the  $KL_1L_2(^1P_0)$  and  $KL_1L_3(^3P_2)$  respectively. The general trend in the  $Al_2O_3$  spectrum is an increase in intensity of the  $P(J = 0)$  states relative to the others; perhaps partially at the expense of the decreasing  $KL_1L_1(^1S_0)$  intensity through interconfiguration interactions of the  $J = 0$  states as suggested by Asaad. Conversely the  $AlO$  spectrum does not display a large intensity increase in the  $2s^12p^5$  or the  $KL_2L_3$ ,  $KL_3L_3$  states, as seen from Fig. 65, and correspondingly displays a larger  $KL_1L_1(^1S_0)$  intensity than  $Al_2O_3$  which lends credence to the interconfiguration interaction theory.

From the examination of the deconvoluted oxygen KLL spectra it is apparent that the main satellite features arise from Auger transitions characteristic of the oxygen atom, independent of the particular oxide studied. This is in marked contrast to the structured low energy tail of the  $In:M_4,5N_5N_5$  spectrum arising from inelastic scattering of the Auger electrons prior to ejection into vacuum.

Relative shifts of the apparent Auger transition energies due to variations in chemical bonding of the oxides cannot be unambiguously determined since the existence of a non-zero surface potential on the oxide surfaces cannot be discounted. However the deconvoluted oxide data exhibits a more prominent chemical effect than relative level shifts i.e., the strong dependence of relative KLL transition probabilities upon the chemical binding state. In the central field, one-electron model, the energy of an electron in the Coulomb field is given by

$$V(r) = \frac{\bar{Z}(r)e^2}{r}$$

where  $\bar{Z}(r)$  is the effective nuclear charge seen by an electron at a distance  $r$ . This effective nuclear charge is modified both by the presence of outer electrons (external screening) as well as by the amount of charge closer to the nucleus (internal screening). The perturbation to the binding energies and correspondingly the shift in apparent Auger transition energy due to chemical bonding depends linearly upon the effective nuclear charge  $\bar{Z}$ . However the relative KLL transition

probabilities can vary greatly with changes in the effective nuclear charge  $\bar{Z}$  as shown by Callan<sup>98</sup> and Asaad.<sup>97</sup> For example, the strength of the  $KL_3L_3(3P_2)$  for low  $\tau$  was calculated to vary roughly as the eighth power of  $\bar{Z}$ . Chemical effects due to charge transfer in bond formation are thus more discernible in the structural features of the KLL spectra than in the more ambiguous shifts in Auger transition energy.

### 5.5 Conclusions

It has been demonstrated that the application of the deconvolution technique to Auger Electron Spectroscopy (using conventional Auger electron spectrometers) yields spectra which agree well with those obtained using a higher resolution spectrometer (ESCA). In addition to increasing resolution, the application of the deconvolution technique also eliminates much extraneous structure which arises from inelastic interactions of Auger electrons within the solid. Although explicit reference has been made to conventional LEED-AUGER analyzers, the deconvolution technique is applicable to any electron spectrometer where primary ionization is produced by electron beam excitation.

6. References

1. J.J. Scheer and J. Van Laar, Solid State Commun, 3, 189 (1965).
2. F.G. Allen and G.W. Gobeli, Phys. Rev. 144, 558 (1966).
3. T.E. Fischer, Surface Sci. 13, 30 (1969).
4. J.J. Scheer and J. Van Laar, Surface Sci. 18, 130 (1969).
5. R.C. Eden, Thesis, Stanford University, May 1967.
6. E.O. Kane, Phys. Rev. 127, 131 (1962).
7. G.W. Gobeli and F.G. Allen, Phys. Rev. 137, A245 (1965).
8. F.G. Allen and G.W. Gobeli, J. Appl. Phys. 35, 597 (1964).
9. G.W. Gobeli and F.G. Allen, Phys. Rev. 127, 141 (1962).
10. F.G. Allen and G.W. Gobeli, Phys. Rev. 144, 558 (1966).
11. L. Tamm, Physik Z. Sowjetunion 1, 733 (1932).
12. W. Shockley, Phys. Rev. 56, 317 (1939).
13. R. Riesz and C.H. Dicke, J. Appl. Phys. 25, 196 (1954).
14. R.E. Weber and W.T. Peria, J. Appl. Phys. 38, 4355 (1967).
15. R.E. Weber and A.L. Johnson, J. Appl. Phys. 40, 314 (1969).
16. E.N. Sickafus and H.P. Bonzel, Recent Progress in Surface Science, Edited by J.F. Danielli, K.G.A. Pankhurst, and A.C. Riddiford, Academic Press, New York, 1970.
17. P.W. Palmberg, Surface Sci. 25, 598, 1971.
18. C.B. Duke, and C.W. Tucker, Jr., Surface Sci. 19, 117 (1970).
19. P.W. Palmberg and T.N. Rhodin, J. Appl. Phys. 39, 2425 (1968a).
20. L.A. Harris, J. Appl. Phys. 39, 1419 (1968a).
21. P.W. Palmberg, G.K. Bohn and J.C. Tracy, J. Appl. Phys. Letters, 15, 254 (1969).

22. G.E. Riach, Thesis, University of Minnesota (1969).
23. R.E. Weber and L.F. Cordes, Rev. Sci. Instr. 37, 112 (1966).
24. R.E. Weber, Thesis, University of Minnesota (1967).
25. W.D. McNeil, Private Communication.
26. H.E. Farnsworth, Rev. Sci. Instr. 21, 102 (1950).
27. D.G. Fisher, Thesis, University of Minnesota (1968).
28. V.G. Appelt and O. Hachenberg, Ann. Physik 6, 67 (1960).
29. R.H. Fowler, Phys. Rev. 32, 45 (1961).
30. F.G. Allen, J. Phys. Chem. Solids 6, 119 (1959).
31. F.G. Allen, J. Eisinger, H. L. Hagstrum and J.T. Law, J. Appl. Phys. 30, 1563 (1959).
32. F. Jona, Appl. Phys. Letters 6, 205 (1965).
33. J.J. Lander and J. Morrison, J. Appl. Phys. 34, 1403 (1963).
34. R.E. Weber and W.T. Peria, Surface Sci. 14, (1969).
35. R.E. Schlier and H.E. Farnsworth, J. Chem. Phys. 30, 917 (1959).
36. F. Jona, IBM J. of Res. and Development 9, 375 (1965).
37. J.A. Dillon and R.H. Oman, Proc. Int. Conf. Semiconductor Physics, Prague, 533 (1960).
38. J.T. Law, J. Appl. Phys. 32, 600 (1961).
39. W.T. Peria, Studies of Photoemitters, Final Report, Contract DA-44-009-AMC-1348(T), June 1970.
40. W.E. Spicer, Fundamental Investigations of Photoemission, Quarterly Report No. 5, Contract DAAK02-69-C-0237, August 1970, p. 3.



41. R.E. Weber and A.L. Johnson, J. Appl. Phys. 40, 314 (1969).
42. H.R. Phillips and H. Ehrenreich, Phys. Rev. 129, 1550 (1963).
43. D. Brust, Phys. Rev. 134, A1337 (1964).
44. J.C. Phillips, Phys. Rev. 104, 1263 (1956).
45. F. Herman, Proc. IRE 43, 170s (1955).
46. E.O. Kane, Phys. Rev. 146, 558 (1966).
47. M. Cardona and F.H. Pollak, Phys. Rev. 142, 530 (1966).
48. H.R. Phillips and E.A. Taft, Phys. Rev. 120, 37 (1960).
49. J.J. Scheer and J. Van Laar, Phys. Letters 3, 246 (1963).
50. G.W. Gobeli and F.G. Allen, Surface Sci. 2, 402 (1964).
51. T.E. Fischer, Surface Sci. 13, 30, (1969).
52. T.E. Fischer, F.G. Allen and G.W. Gobeli, Phys. Rev. 163, 703 (1967).
53. G. Heiland and H. Lamatsch, Proc. Int. Conf. Physics and Chemistry of Solid Surfaces, H.C. Gatos (Editor) 1964; Surface Sci. 2, 18 (1964).
54. J. Eisinger (see Ref. 30).
55. J. Topping, Proc. Roy. Soc. (London) A114, 67 (1927).
56. W. Monch, Phys. Stat. Sol. 40, 257 (1970).
57. V.O. Mowery, J. Appl. Phys. 29, 1753 (1958).
58. C.E. Young, J. Appl. Phys. 32, 329 (1961).
59. A. Many, Y. Goldstein and N.B. Grover, Semiconductor Surfaces, North-Holland Publishing Co., Amsterdam (1965).
60. R.C. Eden, Submitted to 10th International Conference on Semiconductor Physics, July 1970.

61. M. Henzler, Phys. Stat. Sol. 19, 833 (1937).
62. R.E.B. Makinson, Proc. Roy. Soc. (London) **162**, **367** (1937).
63. J. Koutecky, J. Phys. Chem. Solids 14, 233 (1960).
64. T.B. Grimley, J. Phys. Chem. Solids 14, 227 (1960).
65. G.E. Pitus, J. of Exp. and Theoretical Phys. USSR 27, 369 (1954).
66. T.W. Haas, J.T. Grant and G.J. Dooley, Phys. Rev. B1 1449 (1970).
67. M.L. Cohen and T.K. Bergstresser, Phys. Rev. 141, 789 (1966).
68. G.W. Gobelt, F.G. Allen and E.O. Kane, Phys. Rev. Letters 12, 94 (1964).
69. J. van Laar and J.J. Scheer, Phillips Res. Repts, 17, 101 (1962).
70. O. Hachenberg and W. Brauer, Advan. Electronics and Electron Phys. 11, 413 (1959).
71. A.J. Dekker, Solid State Phys., 21, 232 (1958).
72. L. Marton, L.B. Leder and H. Mendlowitz, Advan. Electronics and Electron Phys. 7, 183 (1955).
73. O. Klemperer and J.P.G. Shepherd, Advan. Phys. 12, 355 (1963).
74. J.O. Porteus, "The Structure and Chemistry of Solid Surfaces," edited by G. Somorjai, (Wiley: New York, 1969), p. 12.
75. W.H. Weber and M.B. Webb, Phys. Rev. 177, 1103 (1969).
76. M.P. Seah, Surface Sci. 17, 161 (1969).
77. E. Bauer, Z. Physik 224, 19 (1969).
78. C.B. Duke, G.L. Laramore and V. Metne, Solid State Communications 8, 1189 (1970).

79. J.O. Porteus and W.N. Faith, Phys. Rev. B2, 1532 (1970).
80. C. Davisson and L.H. Germer, Phys. Rev. 30, 705 (1927).
81. J.C. Turnbull and H.E. Farnsworth, Phys. Rev. 54, 509 (1938).
82. P.P. Reichertz and H.E. Farnsworth, Phys. Rev. 75, 1902 (1949).
83. A.L. Hughes and V. Rojansky, Phys. Rev. 34, 284, (1954).
84. R. Riesz and G.H. Dicke, J. Appl. Phys. 25, 196 (1954).
85. G.H. Schuttke, J. Electrochem. Soc. 106, 31 (1959).
86. L.F. Cordes, Ph.D. Thesis, University of Minnesota (1967).
87. N.J. Taylor, Surf. Sci. 15, 169 (1969).
88. W.H. Mularie and T.W. Rusch, Surf. Sci 19, 469 (1970).
89. P.H. van Cittert, Z. Physik, 69, 298 (1931).
90. M.S. Patterson, Proc. Phys. Soc. (London) A63 477 (1950).
91. J.L. Robins, Proc. Phys. Soc. (London) 78, 177 (1961).
92. Blackstock, Ritchie and Birkhoff, Phys. Rev. 100 1078 (1955).
93. W.T. Peria, Private communication.
94. K. Siegbahn et. al., Atomic, Molecular and Solid Structure Studies by Means of Electron Spectroscopy (Royal Society of Sciences Uppsala 1967).
95. R.C. Oswald, M.S. Thesis, University of Minnesota (1969).
96. The discrepancy between the  $M_{4,5}$  separation from both the ESCA and Auger data (6 eV) and the tabulated data (7 eV) of Siegbahn<sup>94</sup> is rather surprising. However examination of the latter data reveals that only the L spectrum was measured, the other levels were derived using x-ray energy separation data.
97. W.N. Asaad, Nuc. Phys. 44, 399 (1963).
98. E.J. Callan, Phys. Rev. 124, 793 (1961).

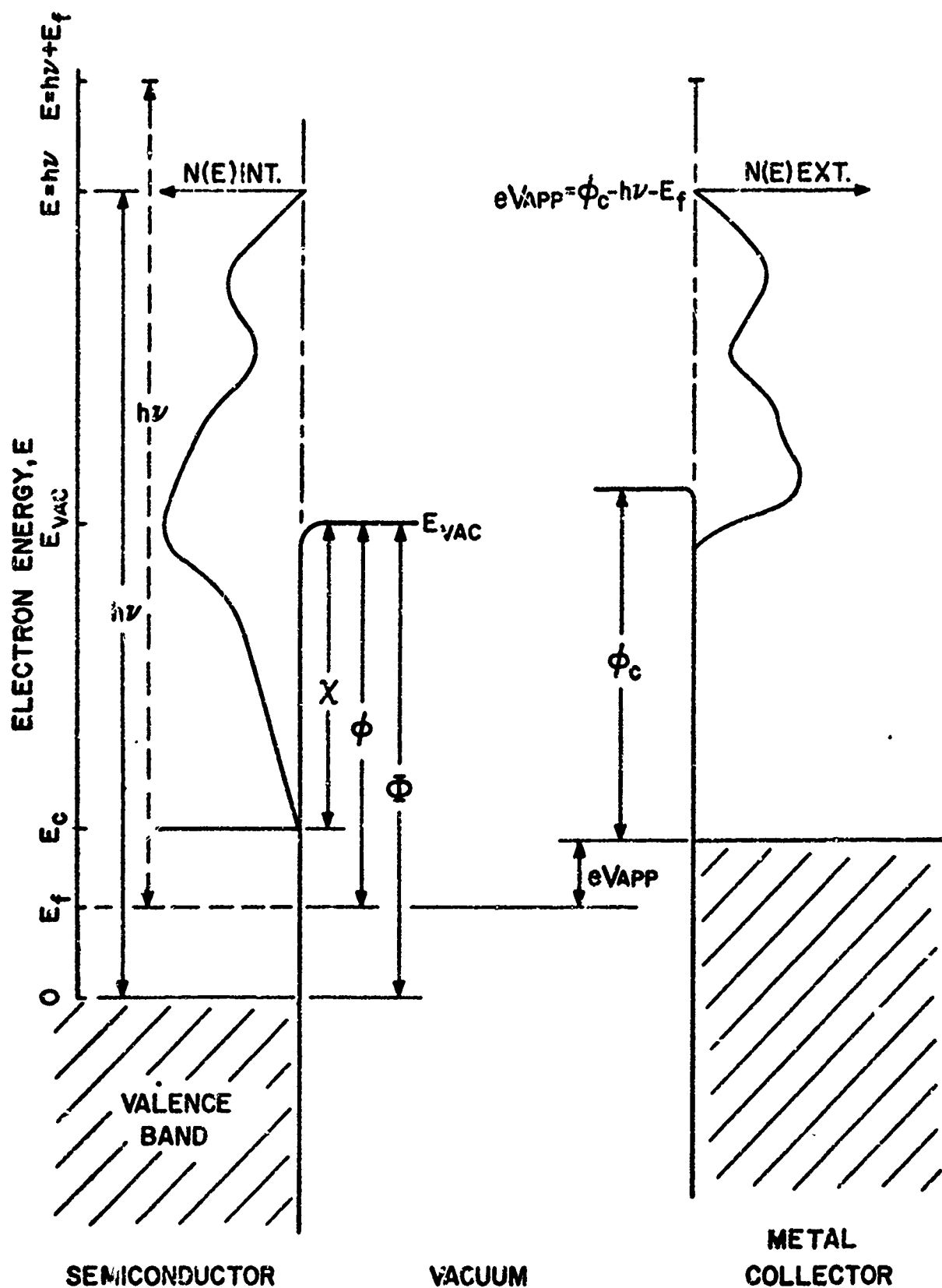


FIG 1 PRINCIPLE OF PHOTOELECTRIC RETARDING POTENTIAL TECHNIQUE

197160

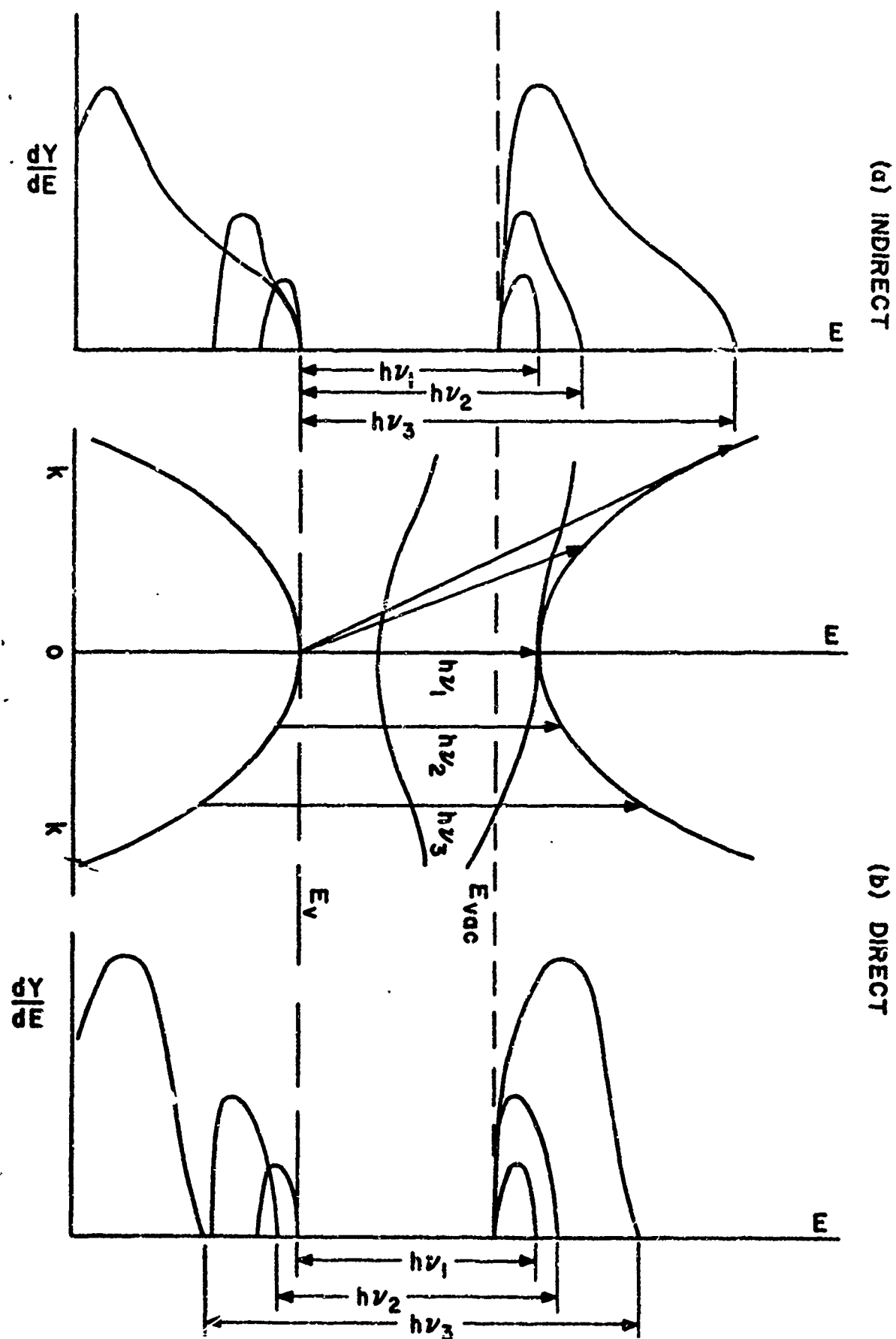
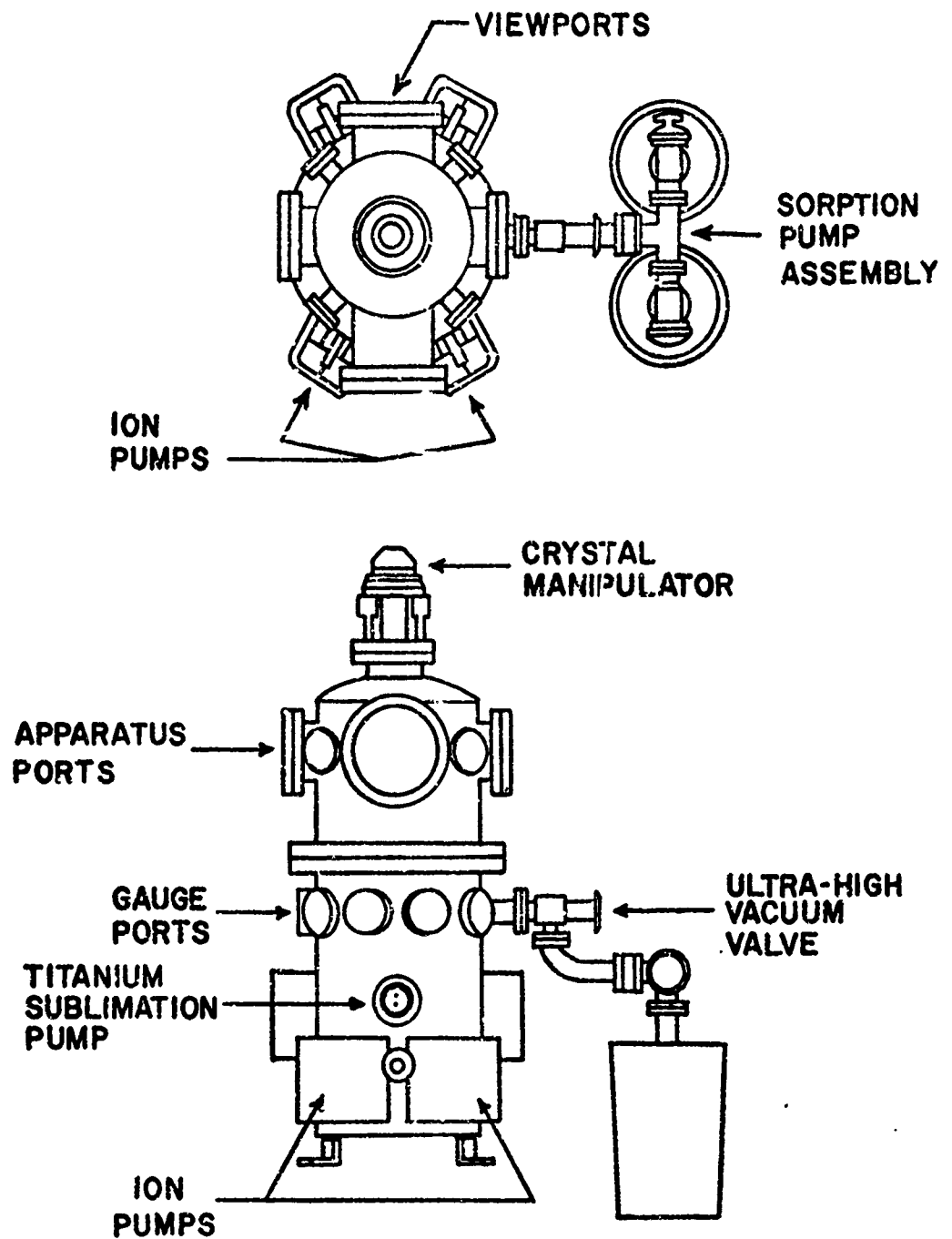


FIG 2 EXPECTED BEHAVIOR OF THE ENERGY DISTRIBUTION CURVES FOR EMISSION DOMINATED BY (a) INDIRECT and (b) DIRECT TRANSITIONS



**FIG 3 TOP AND FRONT VIEWS OF ULTRAHIGH  
VACUUM SYSTEM**

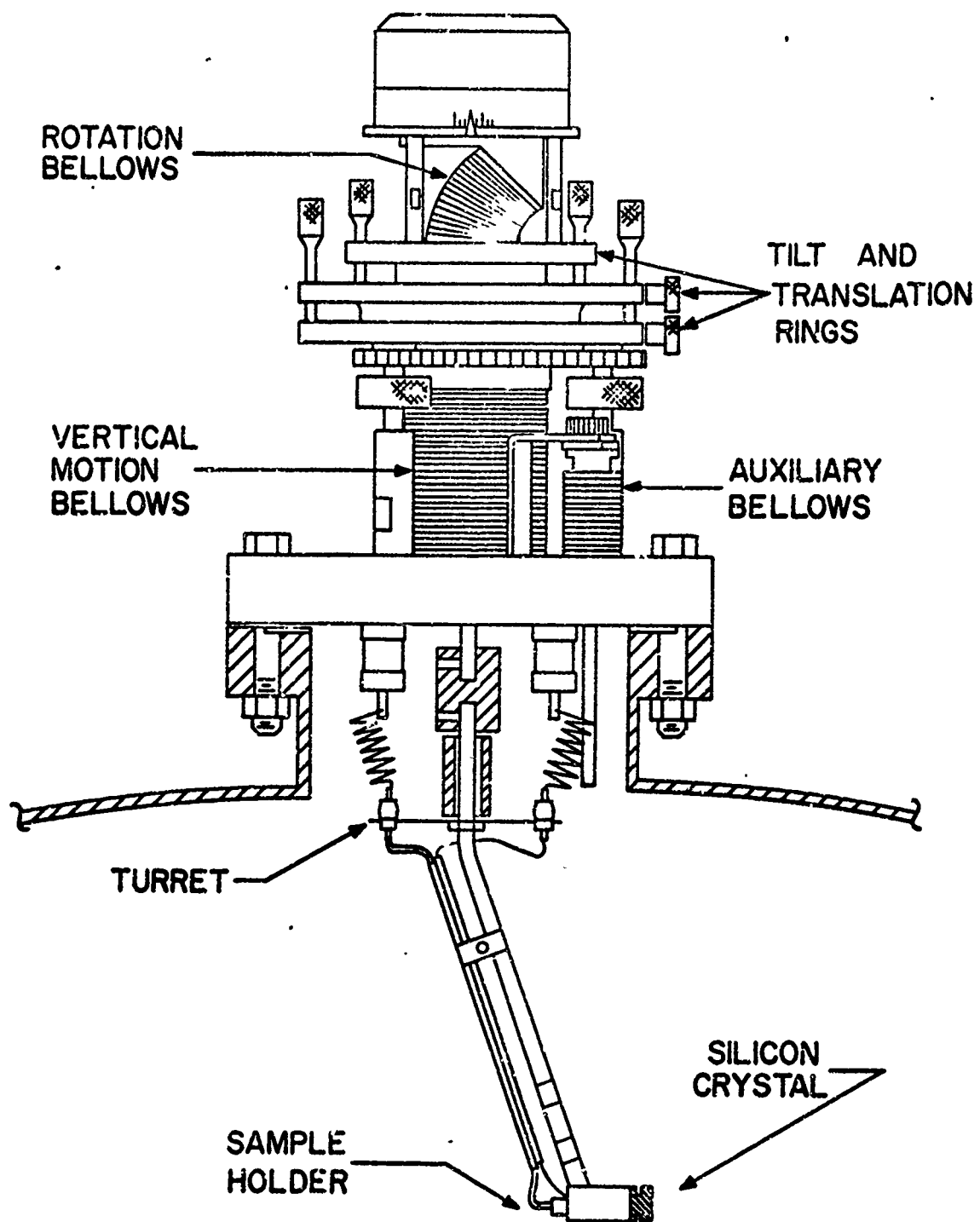


FIG 4 MANIPULATOR AND SAMPLE HOLDER  
ASSEMBLY

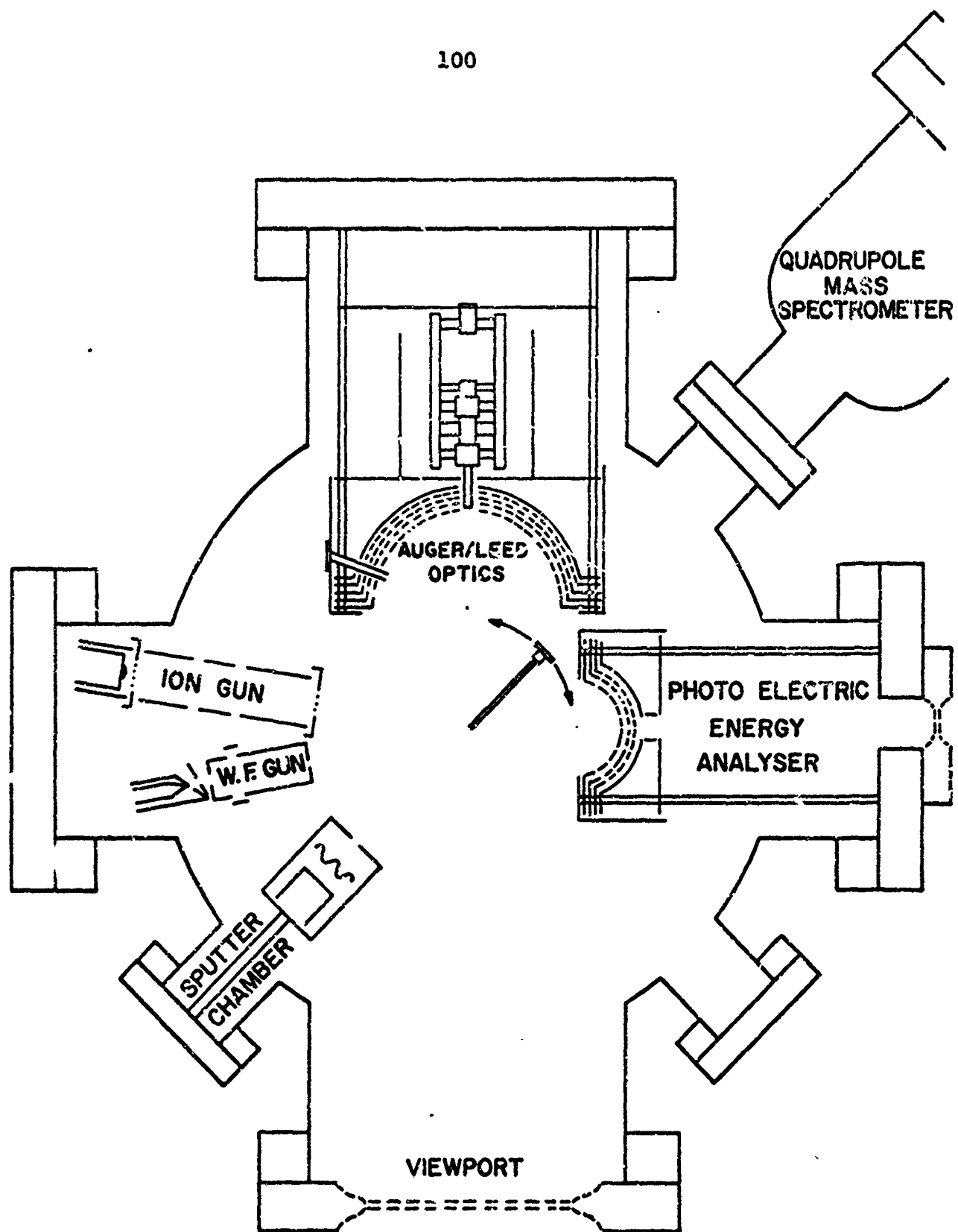


FIG. 5 VACUUM SYSTEM FOR PHOTOEMISSION STUDIES



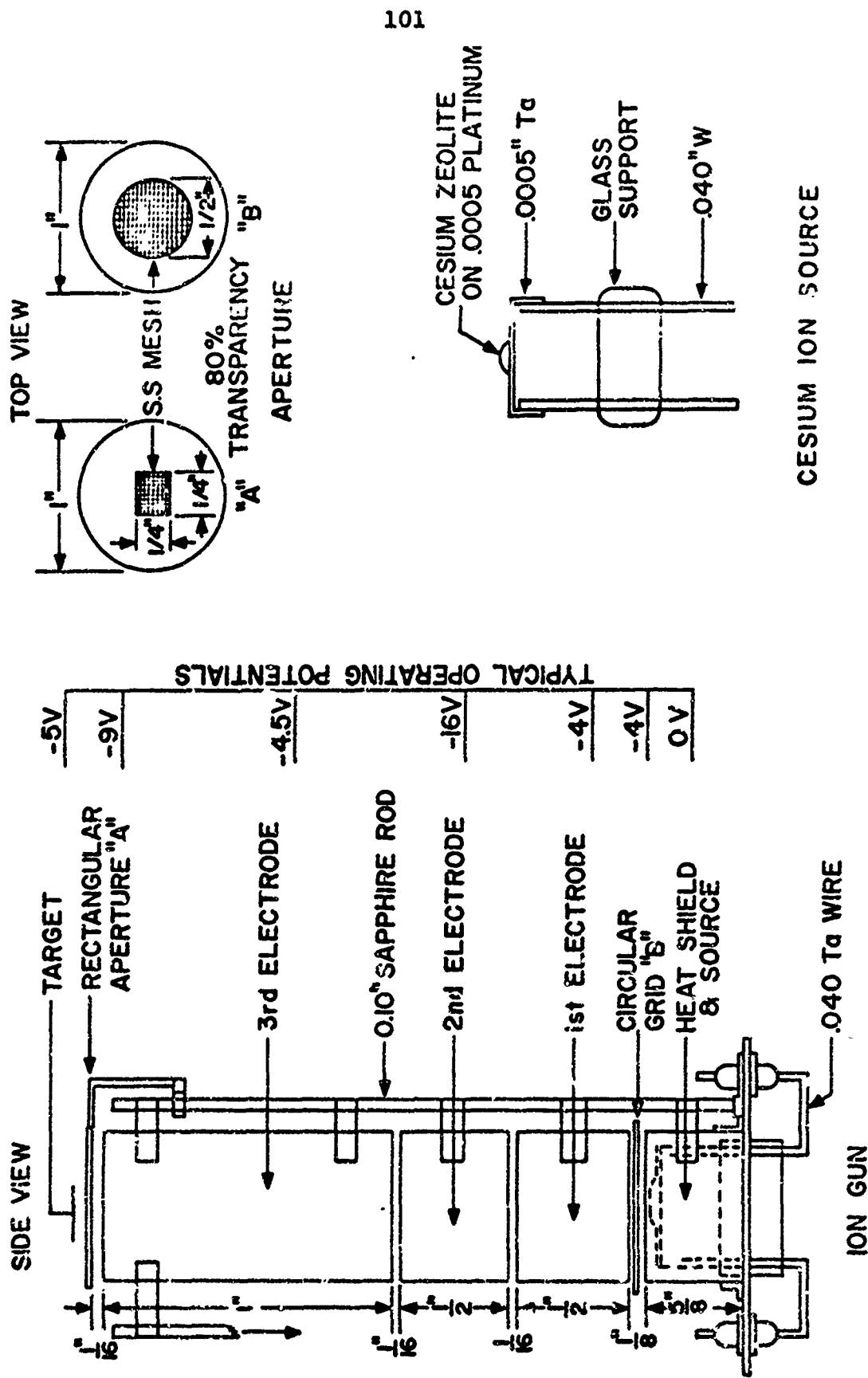


FIG 6 CESIUM ION GUN AND ZEOLITE ION SOURCE USED FOR OVERLAYER STUDIES

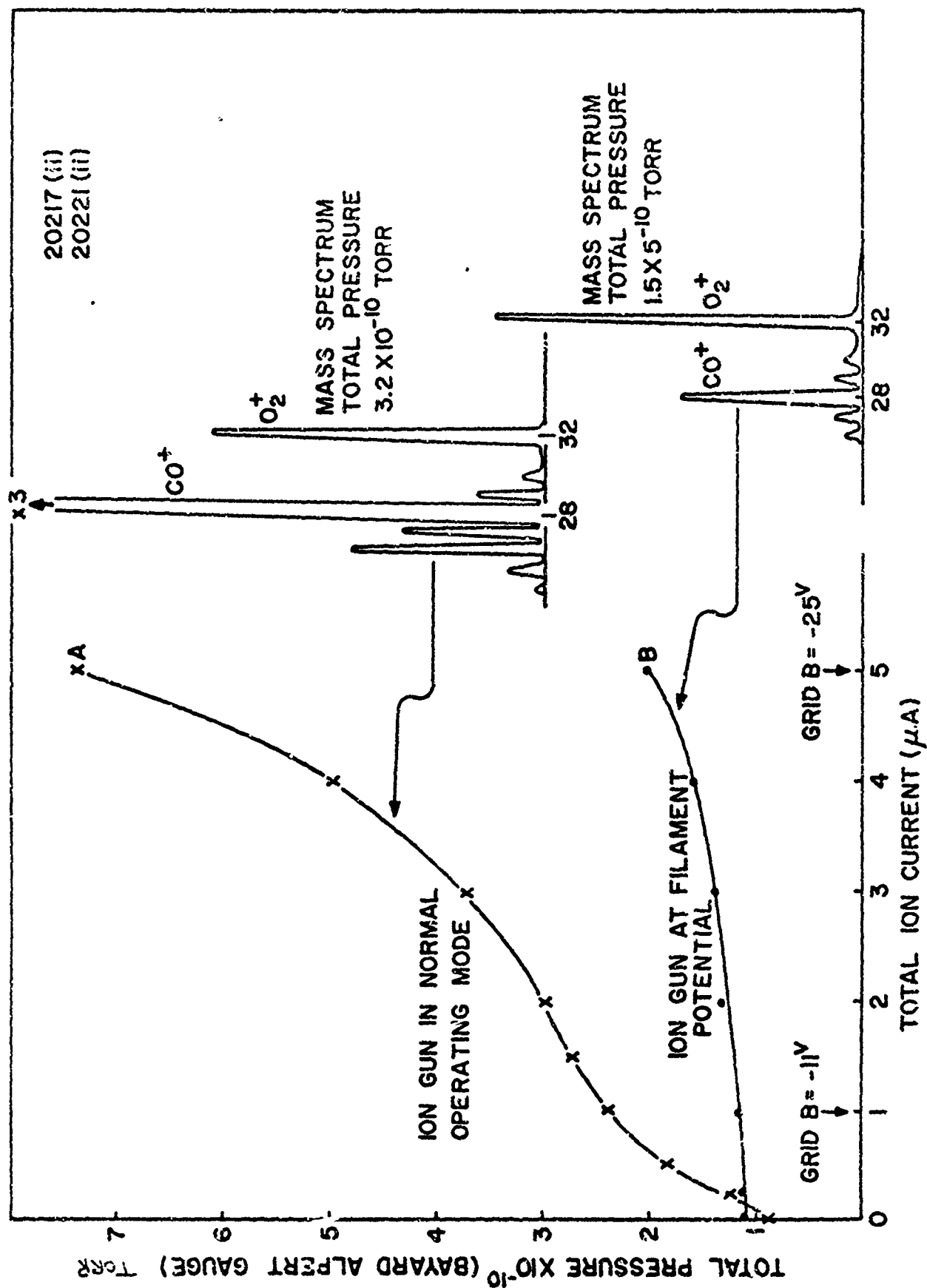


FIG 7 TOTAL PRESSURE AND PARTIAL MASS SPECTRUM, ION GUN, (A) OPERATED IN NORMAL MODE, (B) BIASED TO SUPPRESS ION IMPACT DESORPTION

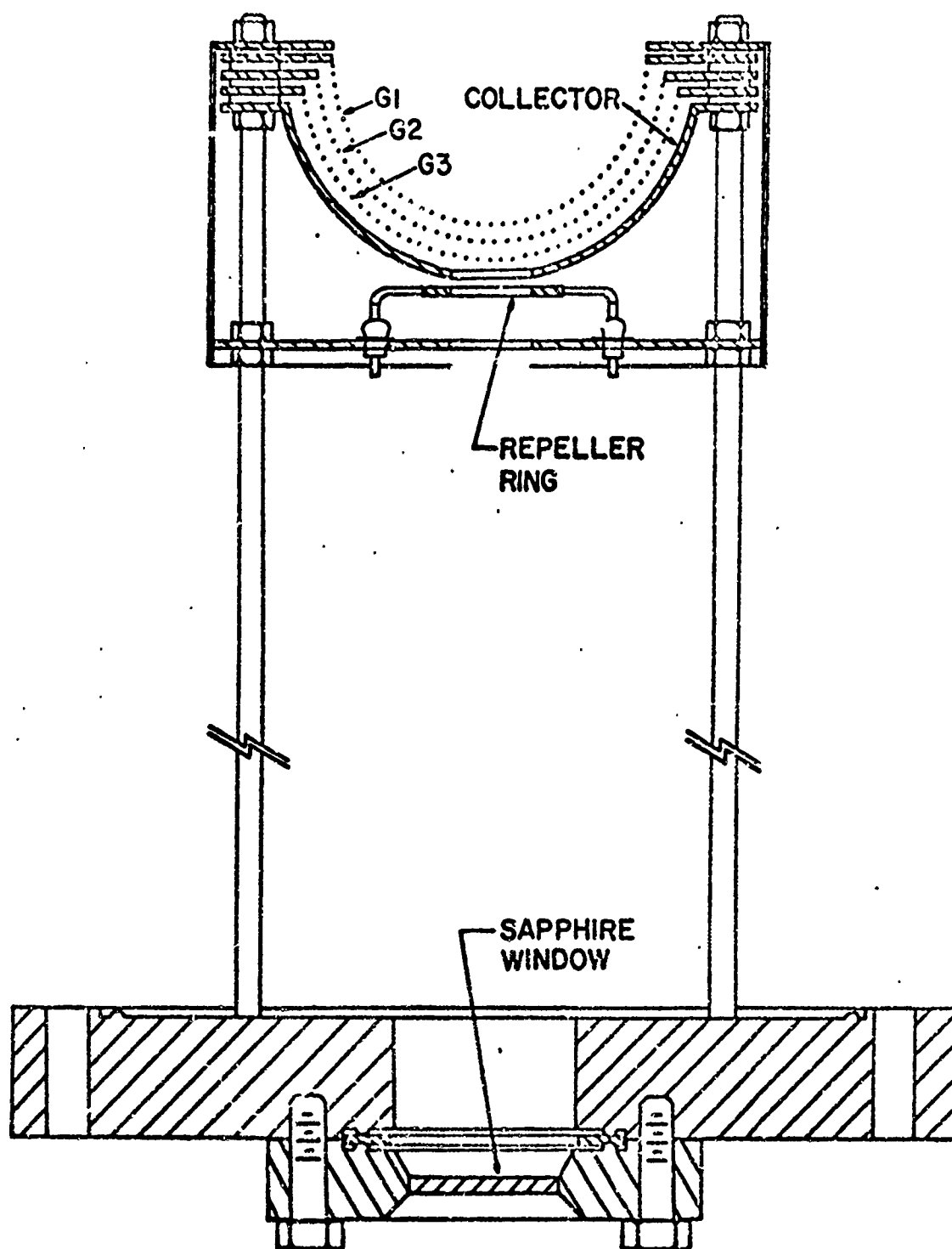


FIG 8 HEMISPHERICAL PHOTOELECTRIC ANALYZER

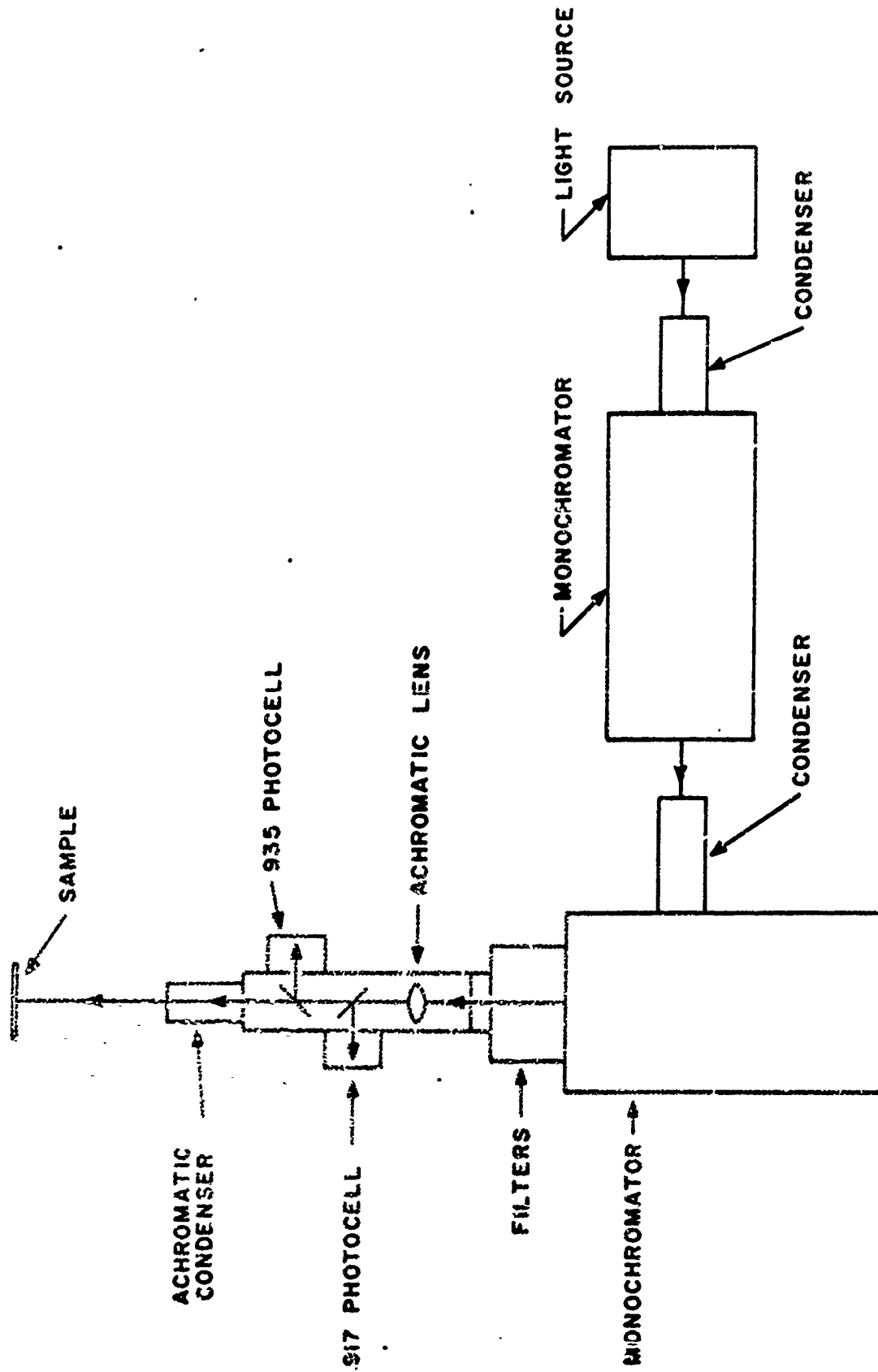
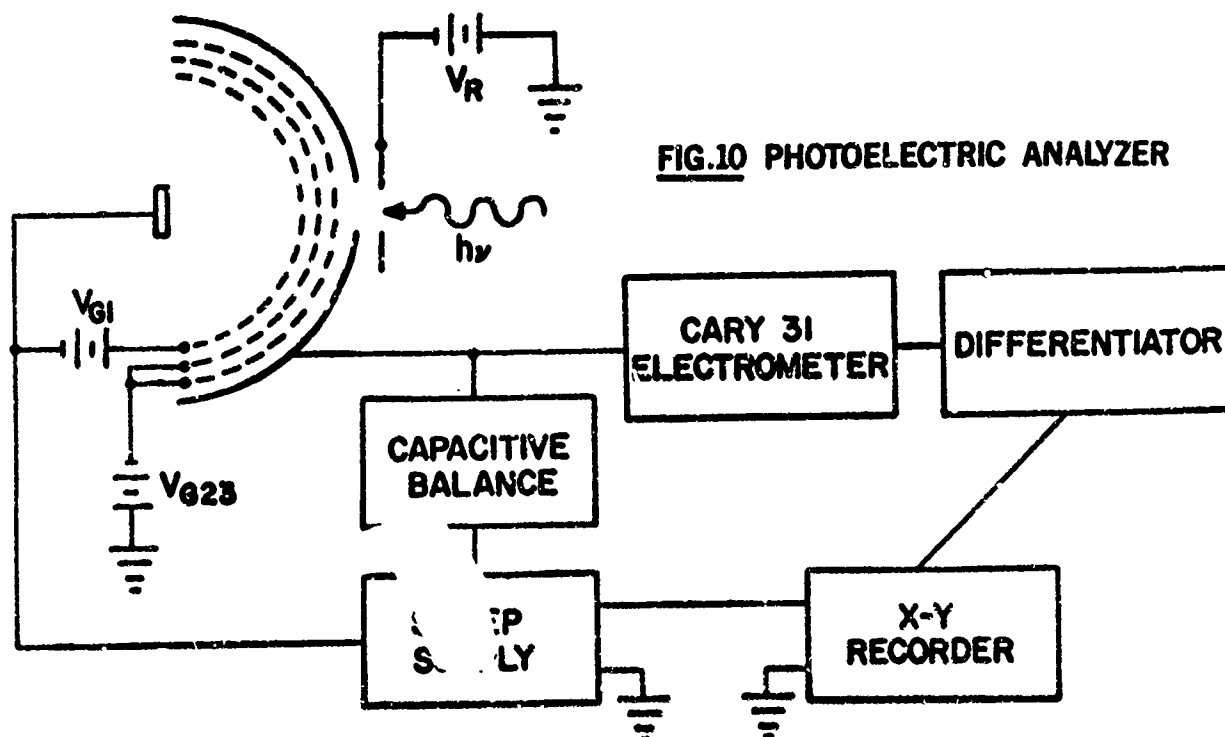
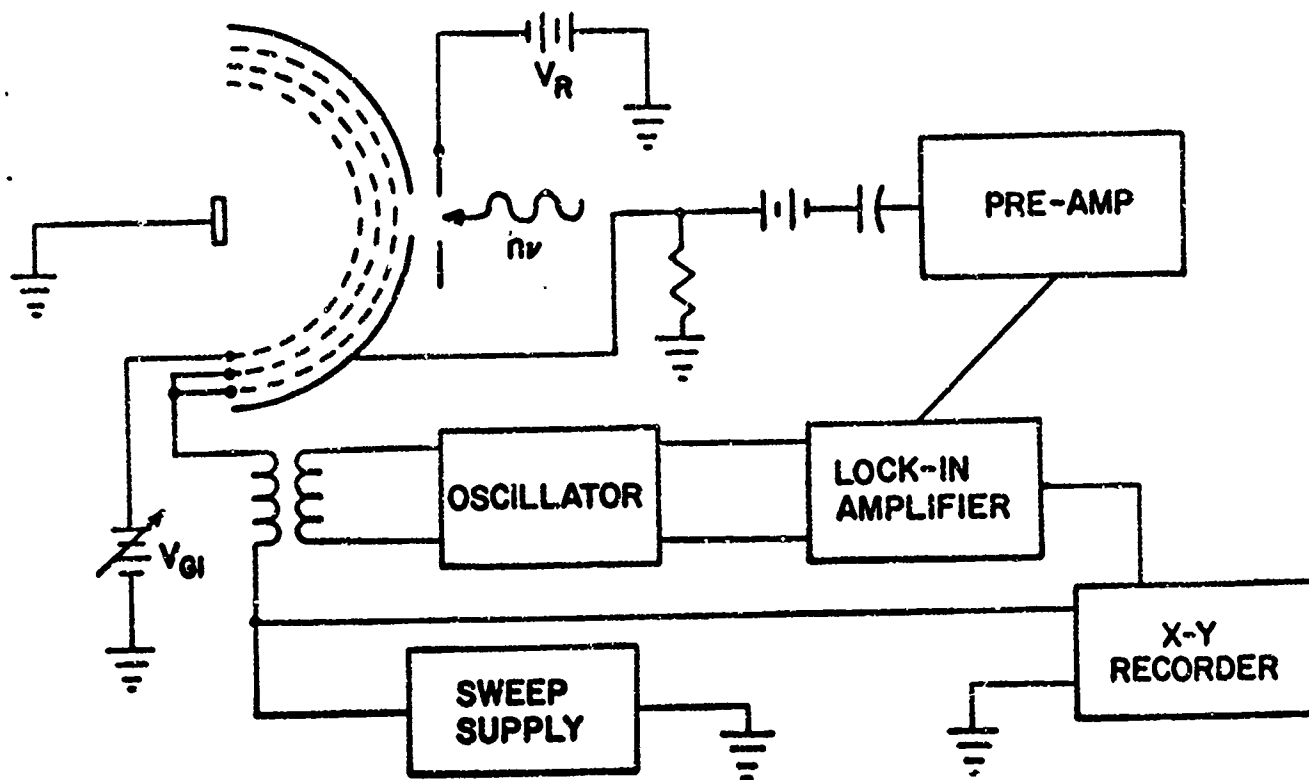


FIG 9 BLOCK DIAGRAM OF PHOTON SOURCE



**FIG.10 PHOTOELECTRIC ANALYZER**

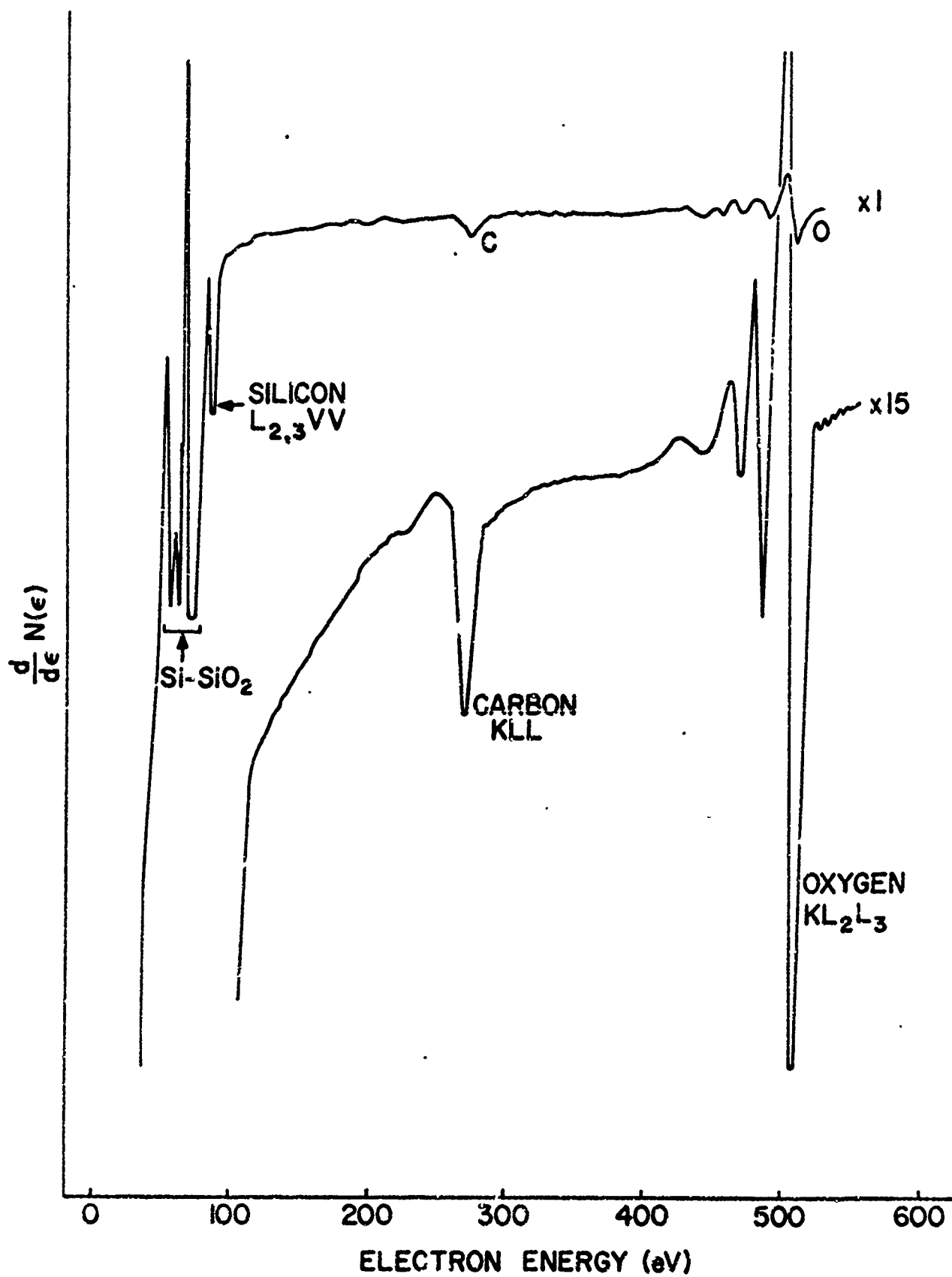


FIG 11 AUGER SPECTRA OF CONTAMINATED SI(100)

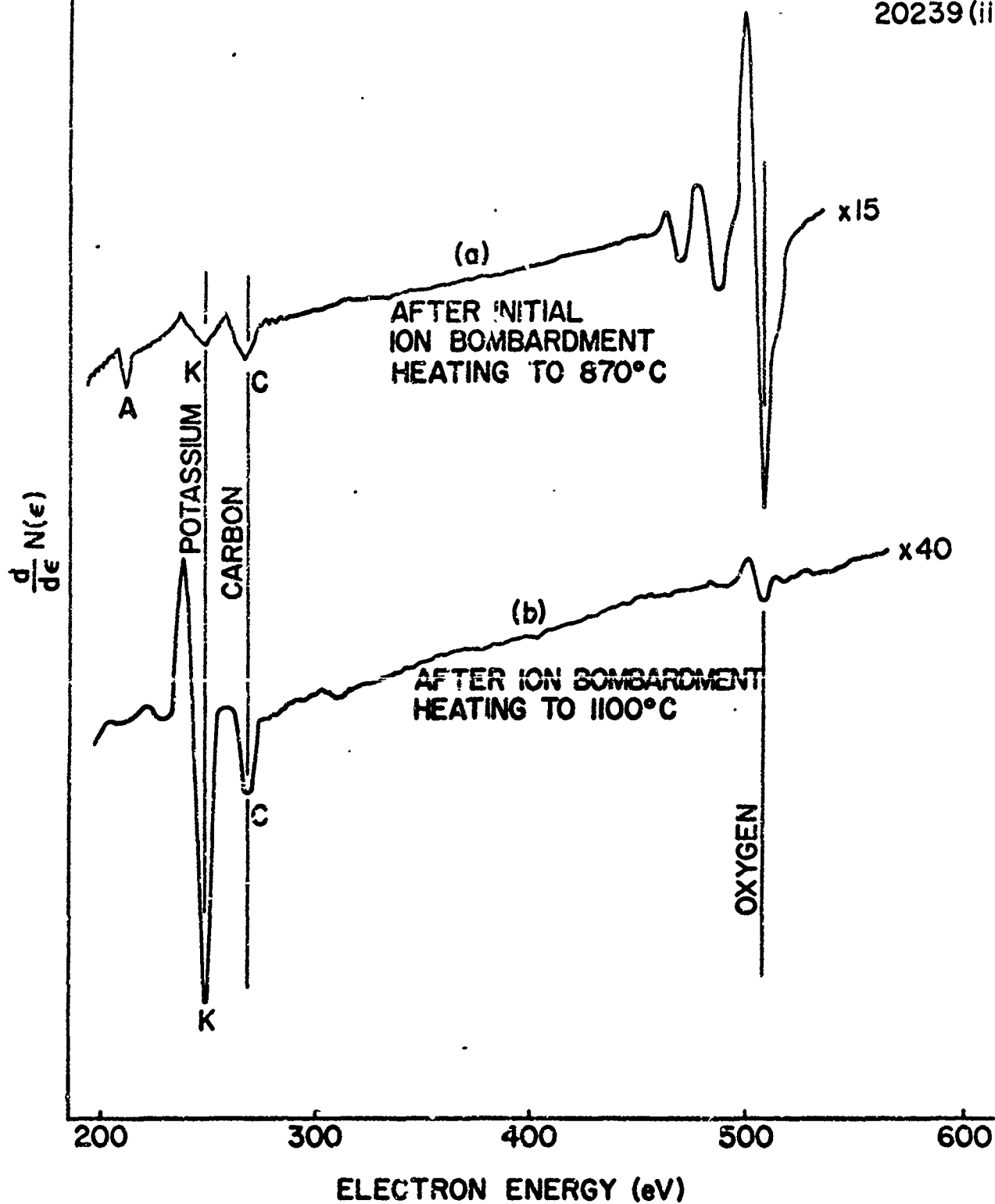
20226 (i)  
20239 (ii)

FIG 12 AUGER SPECTRA OF Si(100) DURING CLEANING PROCEDURE

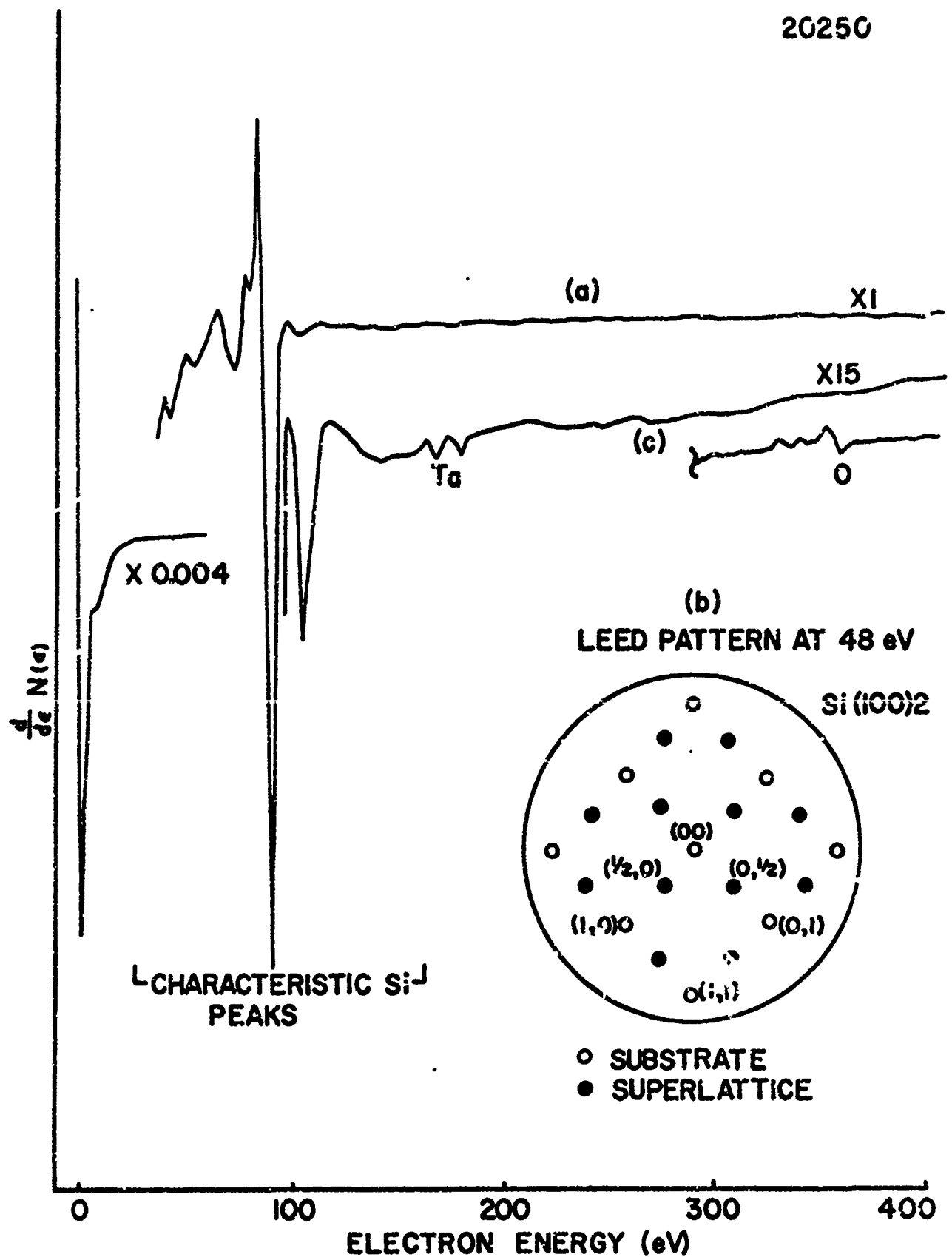


FIG 13 AUGER SPECTRUM FROM CLEAN Si (100)



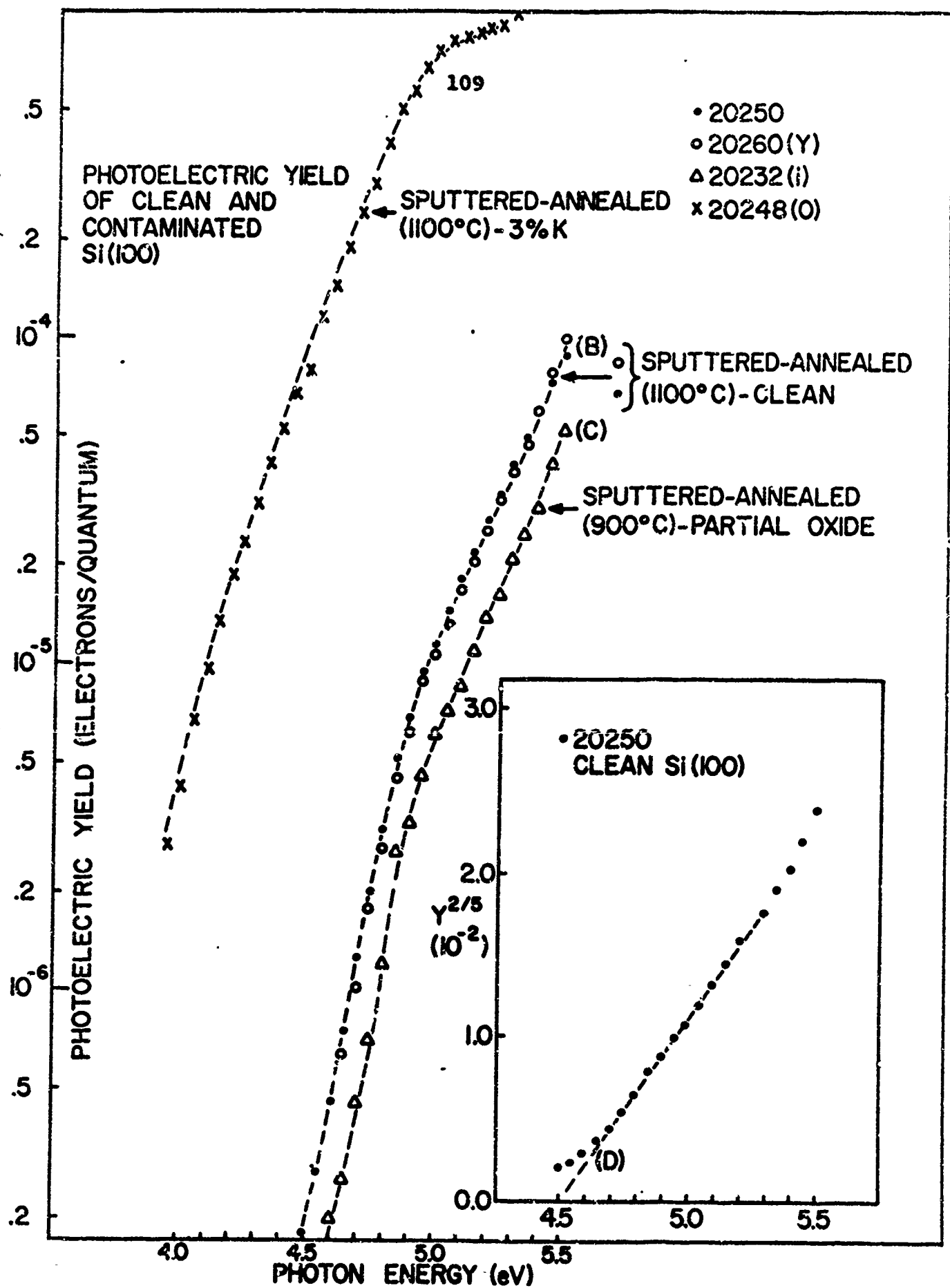


FIG 14 SPECTRAL YIELD FROM CLEAN AND CONTAMINATED Si(100)

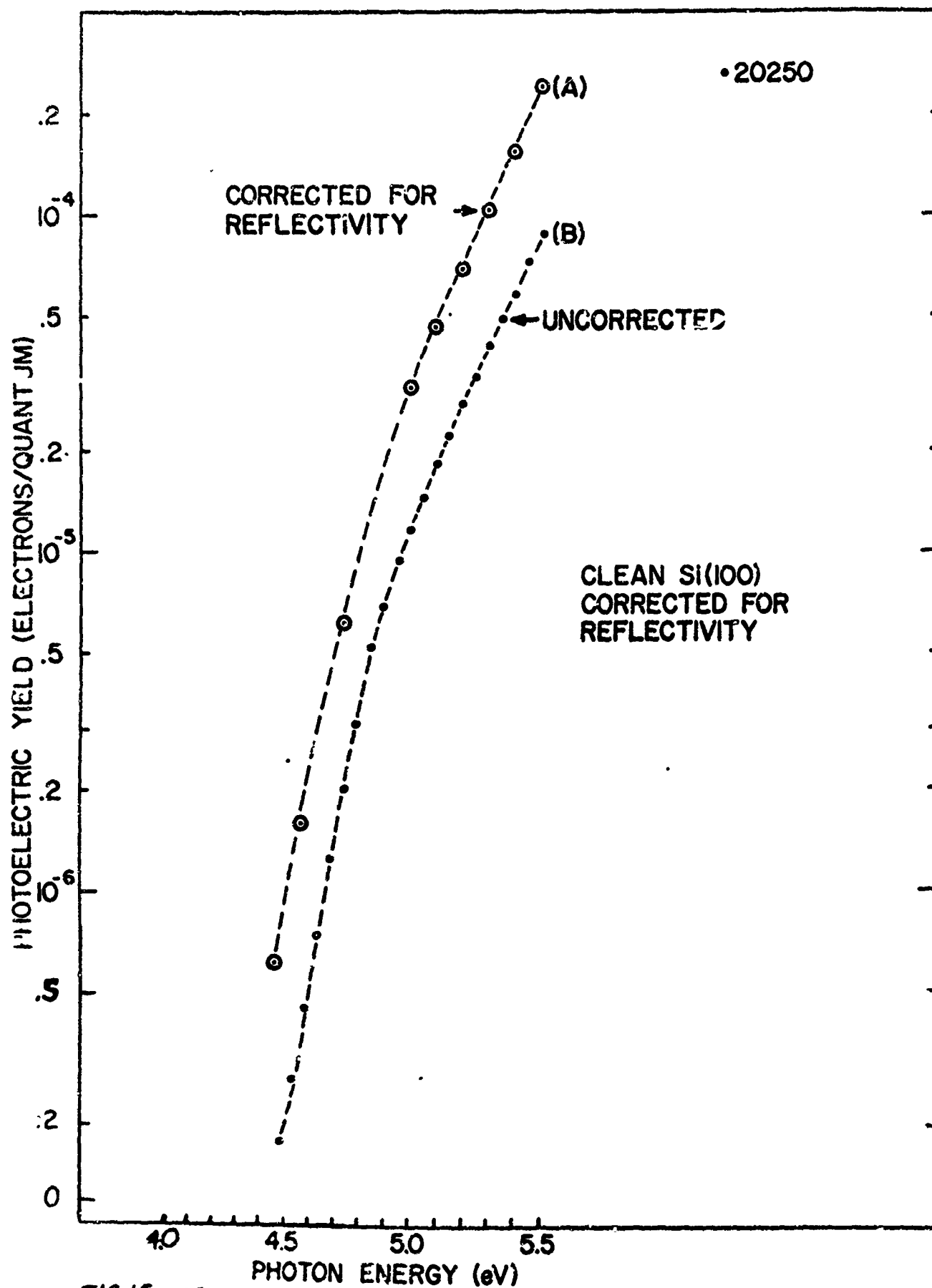


FIG 15 EFFECT OF REFLECTIVITY CORRECTIONS ON THE SPECTRAL YIELD OF CLEAN Si(100)

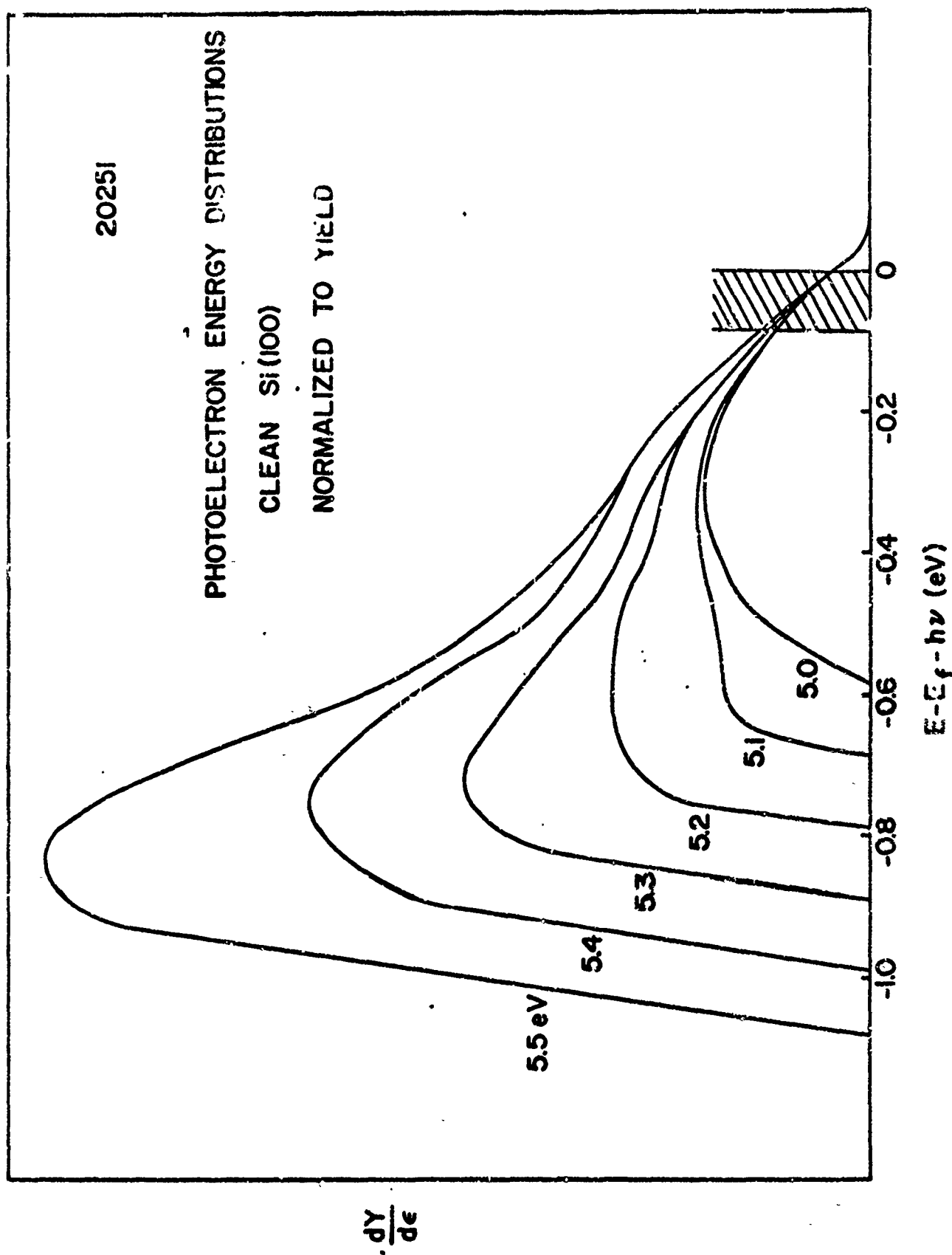


FIG 16 PHOTOELECTRIC ENERGY DISTRIBUTION CURVES FROM Si(100)

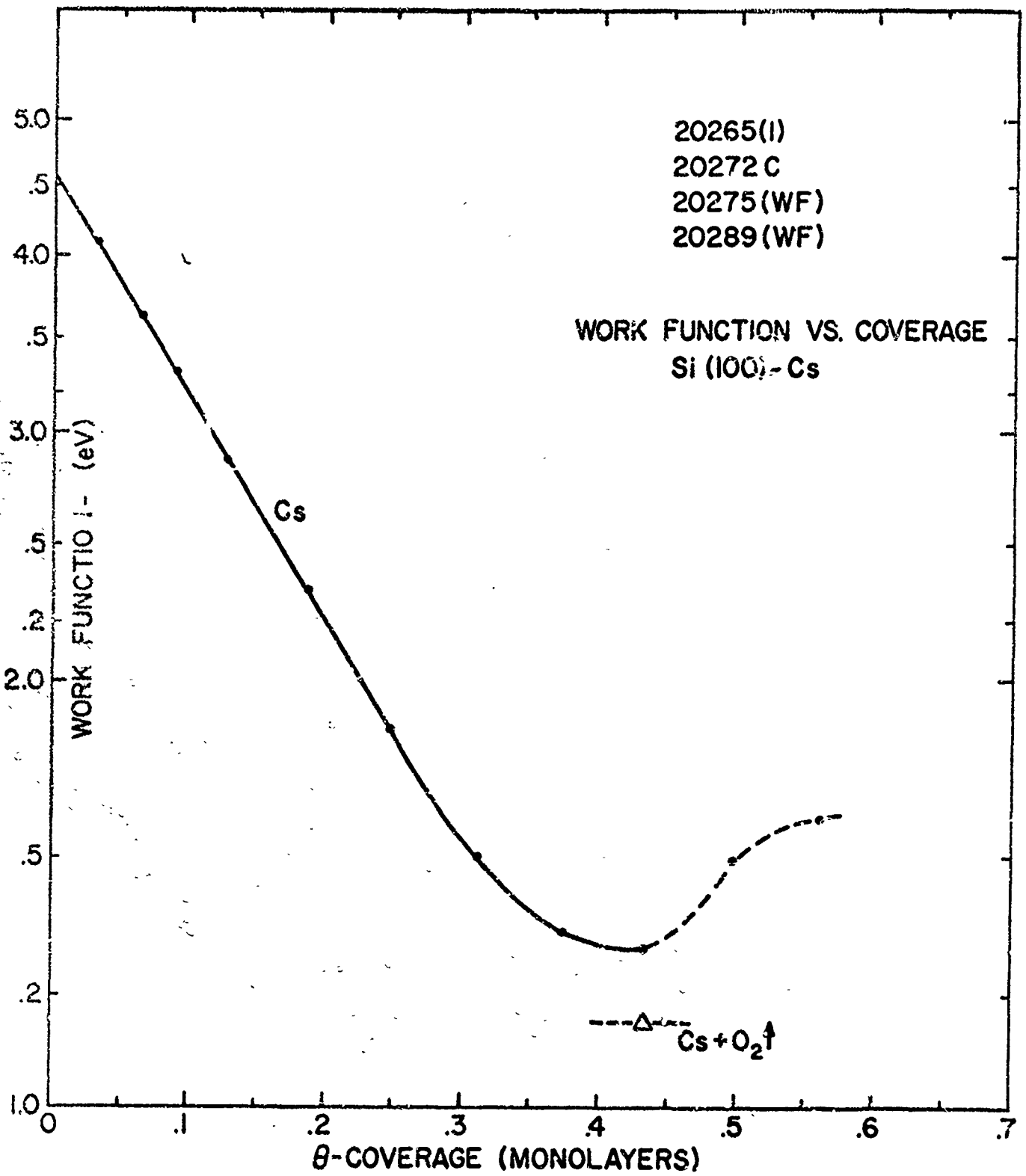


FIG 17 WORK FUNCTION OF Si(100) VS CESIUM COVERAGE

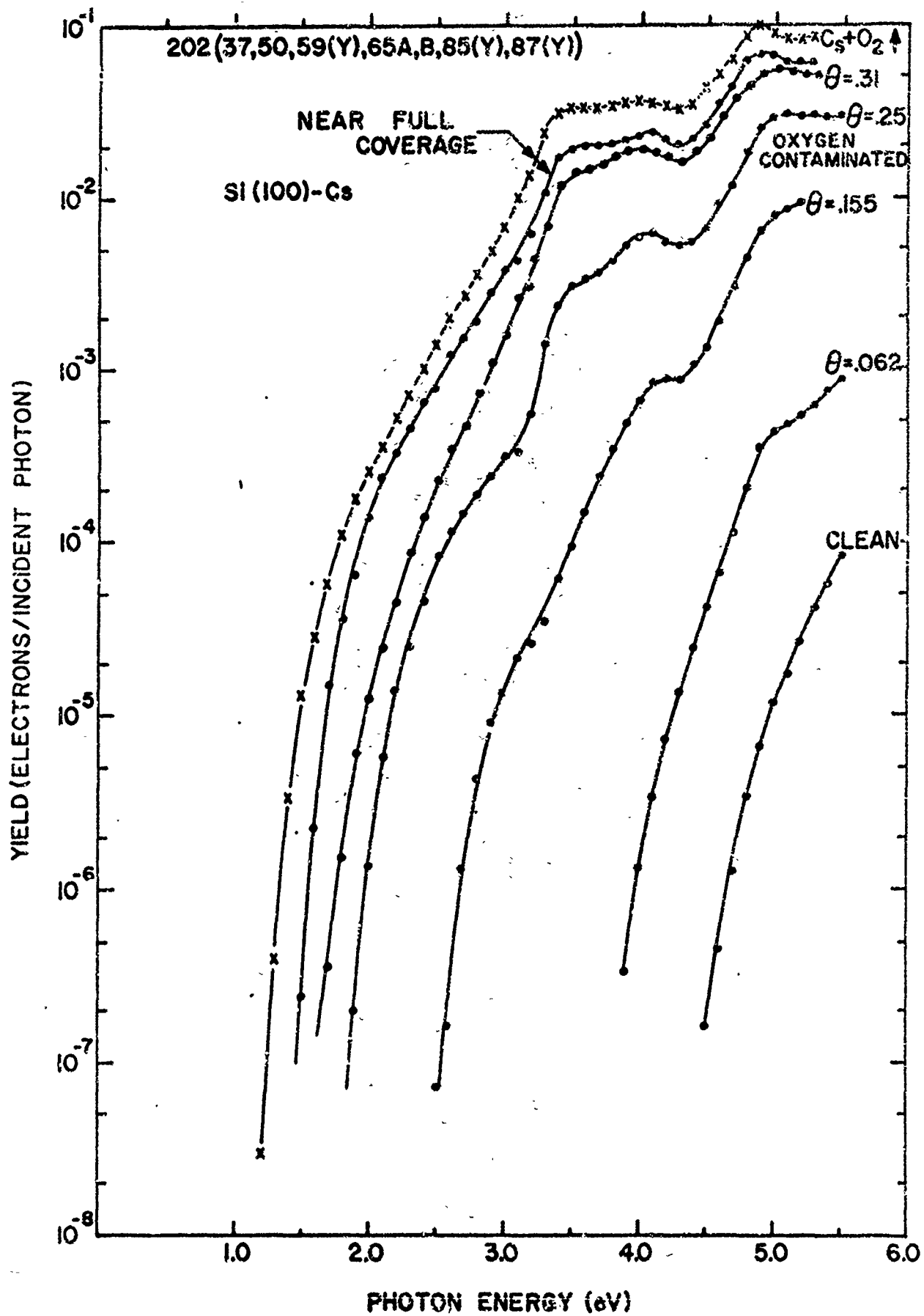


FIG 18 SPECTRAL YIELD OF SI(100)-CESIUM

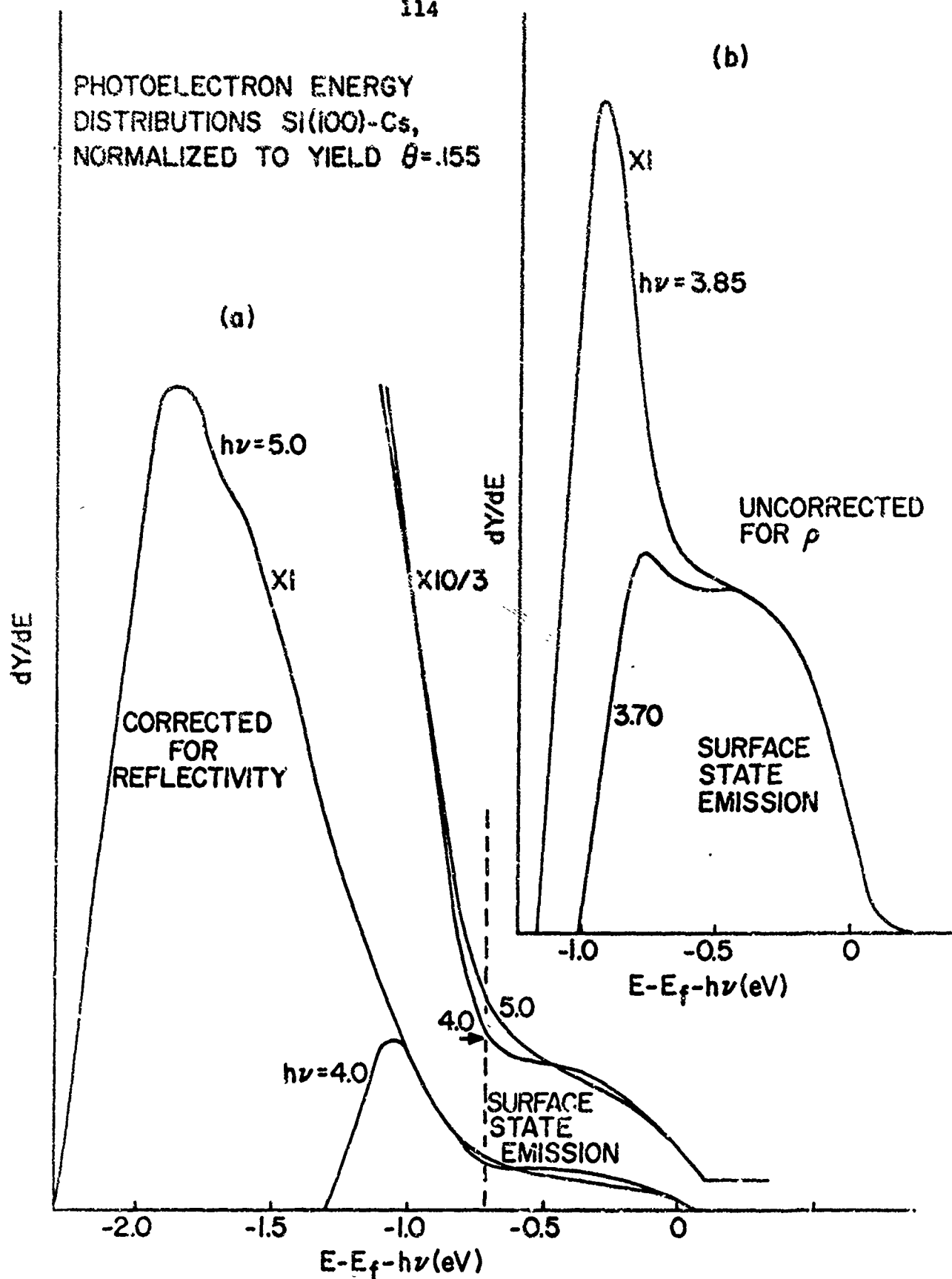


FIG 19 E.D.C.'s AT 0.155 MONOLAYERS CESIUM COVERAGE

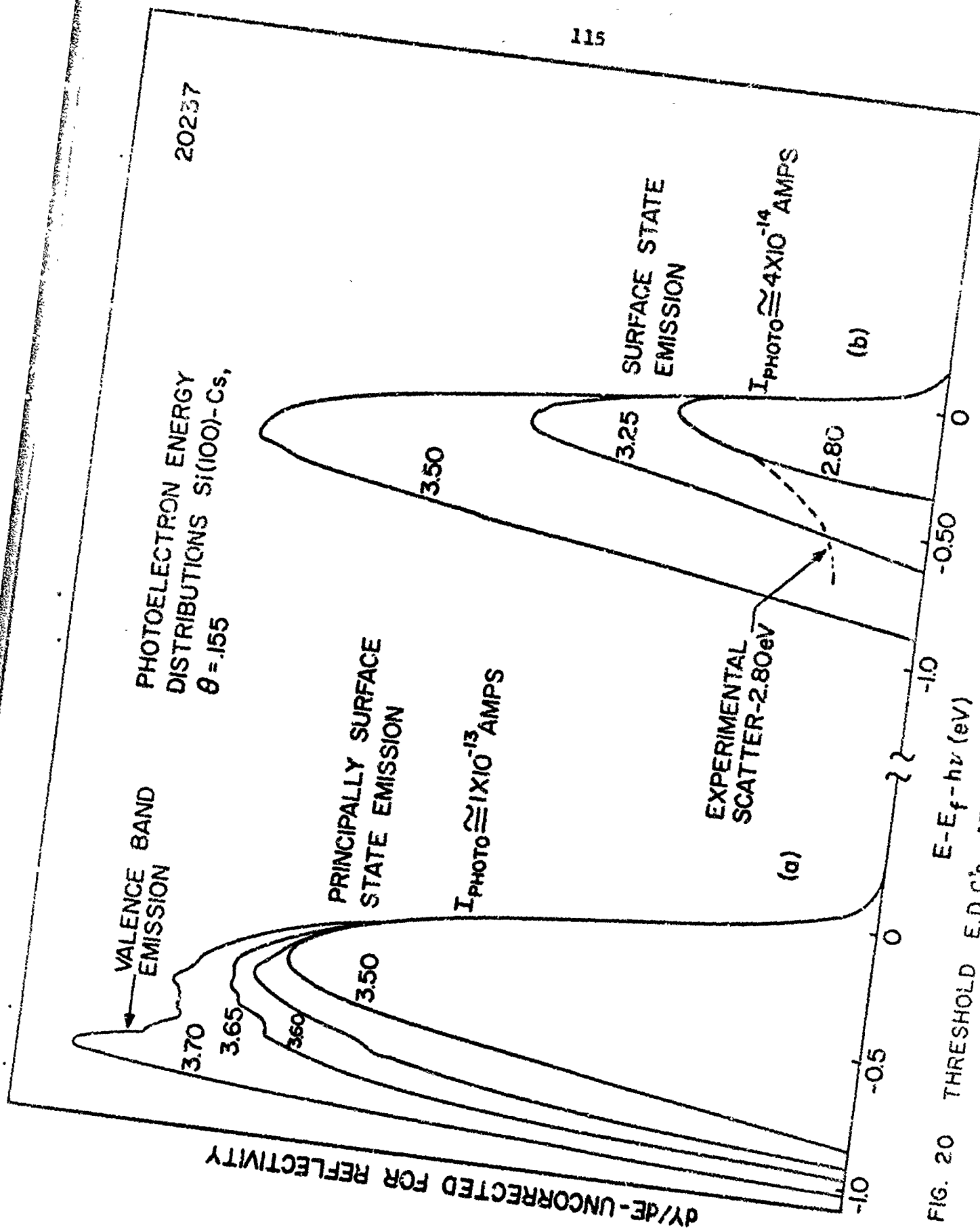


FIG. 20 THRESHOLD E.D.C's AT 0.155 MONOLAYERS CESIUM

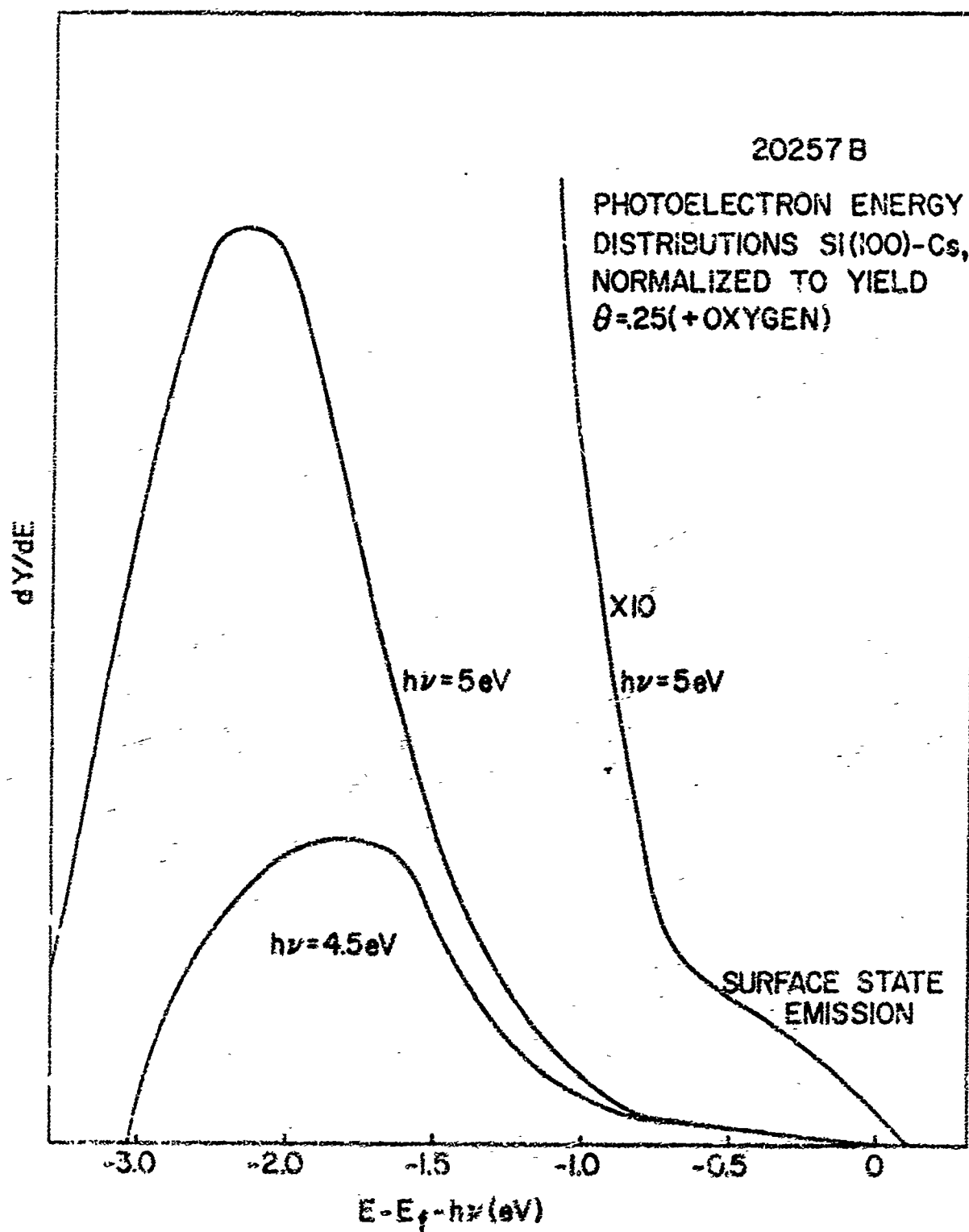


FIG 21 E.D.C.'s FOR  $h\nu \geq 4.5 \text{ eV}$ ,  $\theta = 0.25$  Cs (CONTAMINATED)



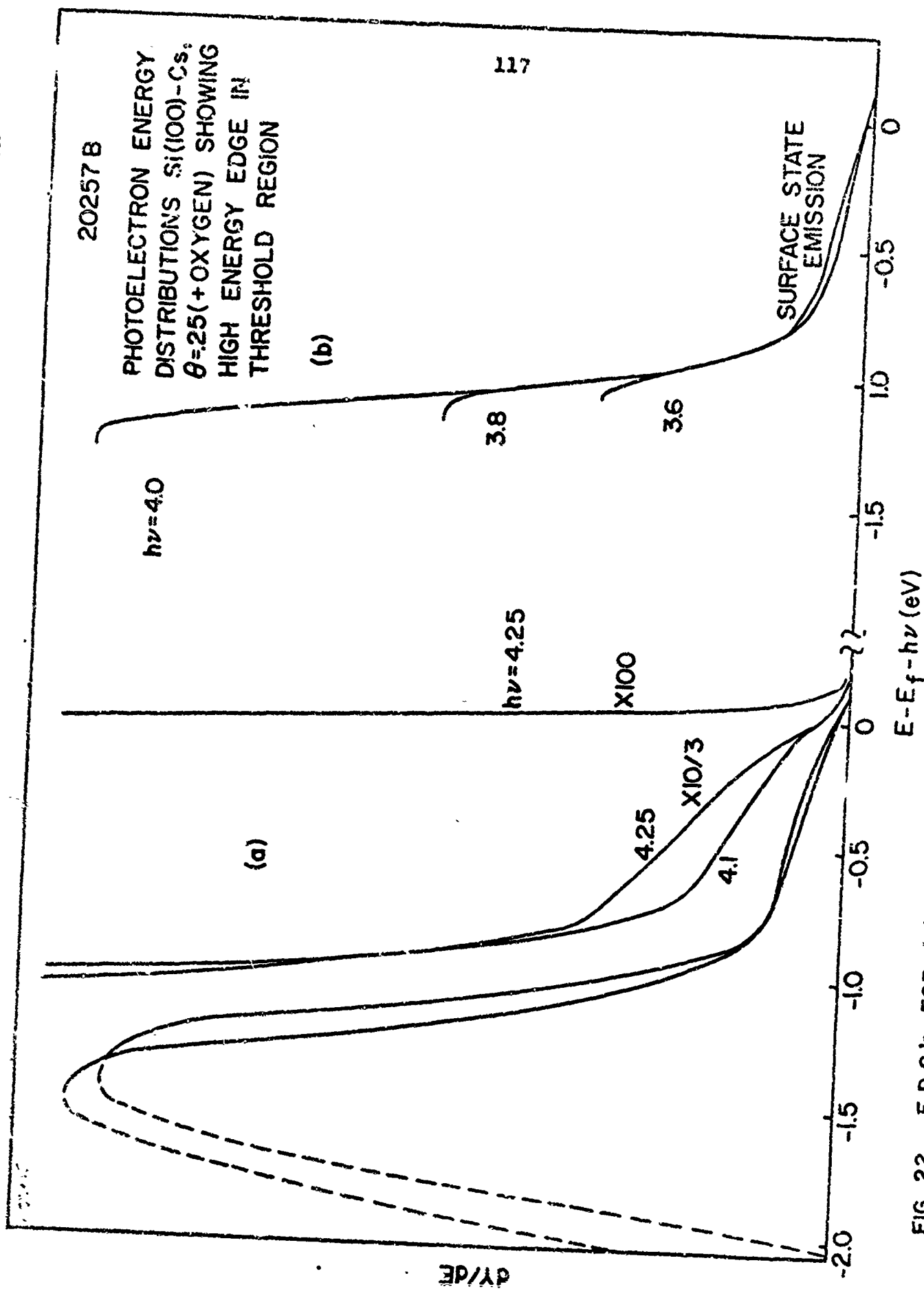


FIG 22 E.D.C.'s FOR (a)  $h\nu \geq 4.1$  eV AND (b)  $h\nu \geq 4.0$  eV SHOWING COINCIDENCE OF  
HIGH ENERGY EDGE

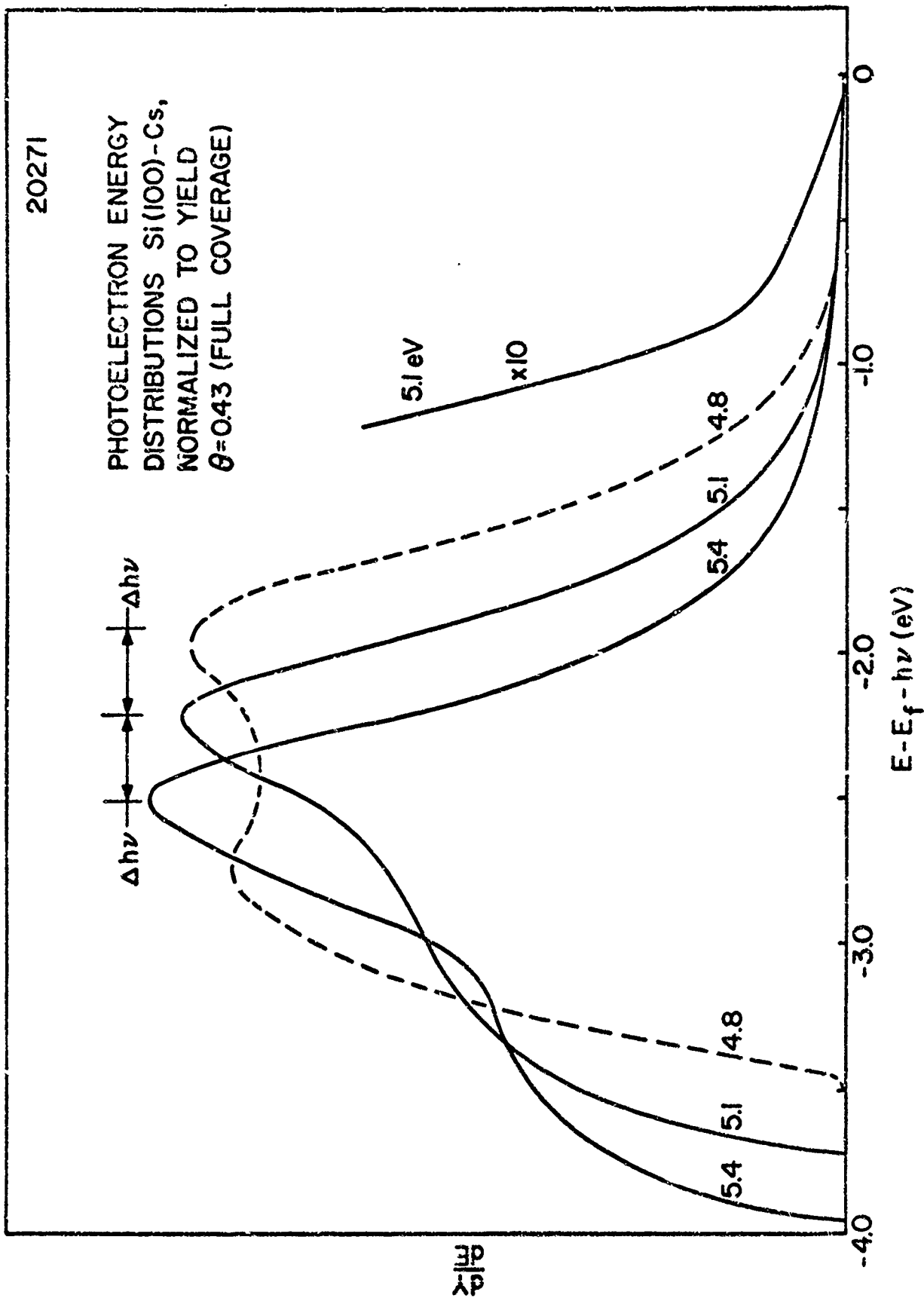


FIG. 23 E.D.C's AT HIGH PHOTON ENERGIES FROM FULLY CESIATED SILICON

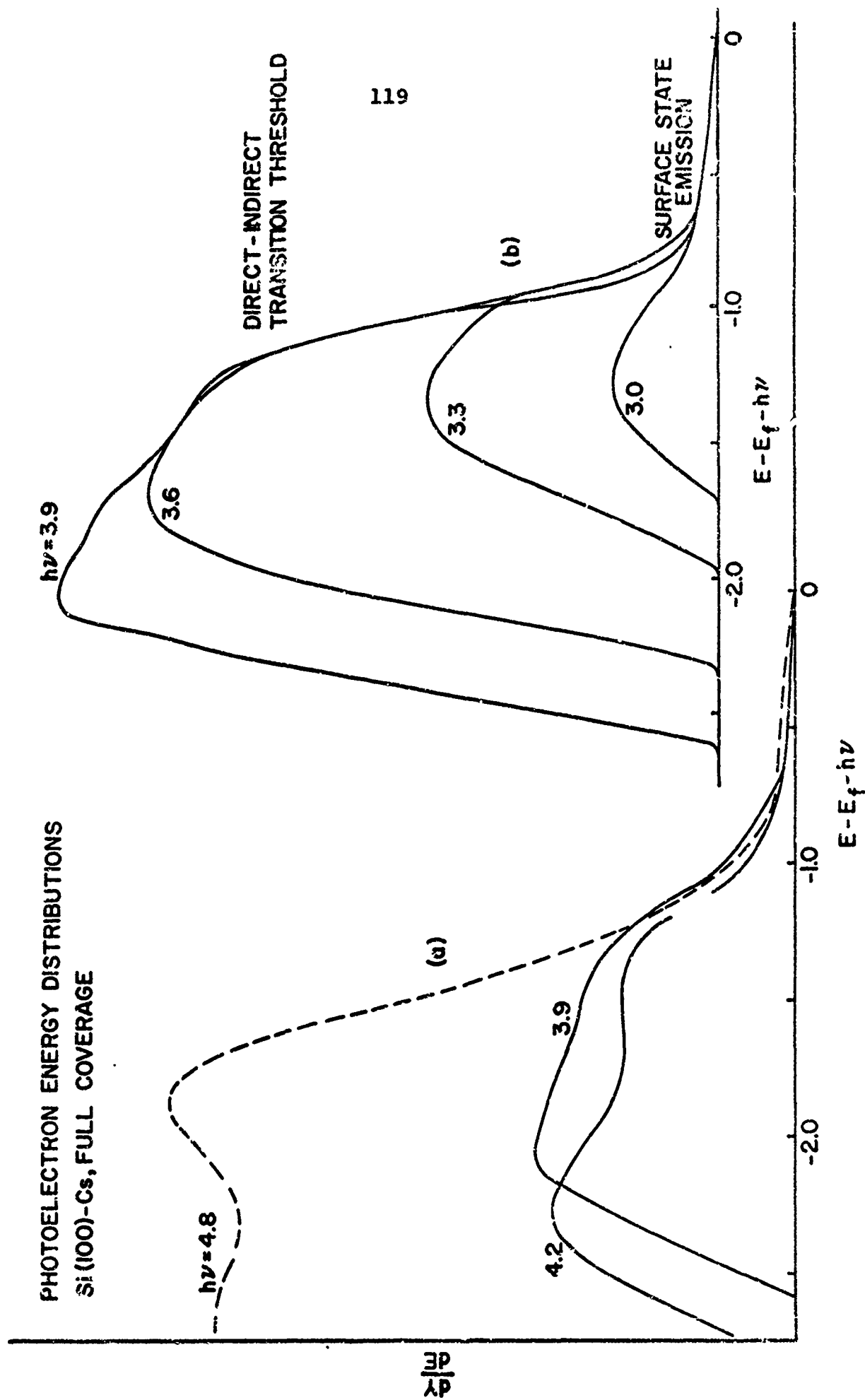


FIG. 24 E.D.C's FROM FULLY CESIATED SILICON BETWEEN  $h\nu = 5.0\text{eV}$  AND  $3.0\text{eV}$

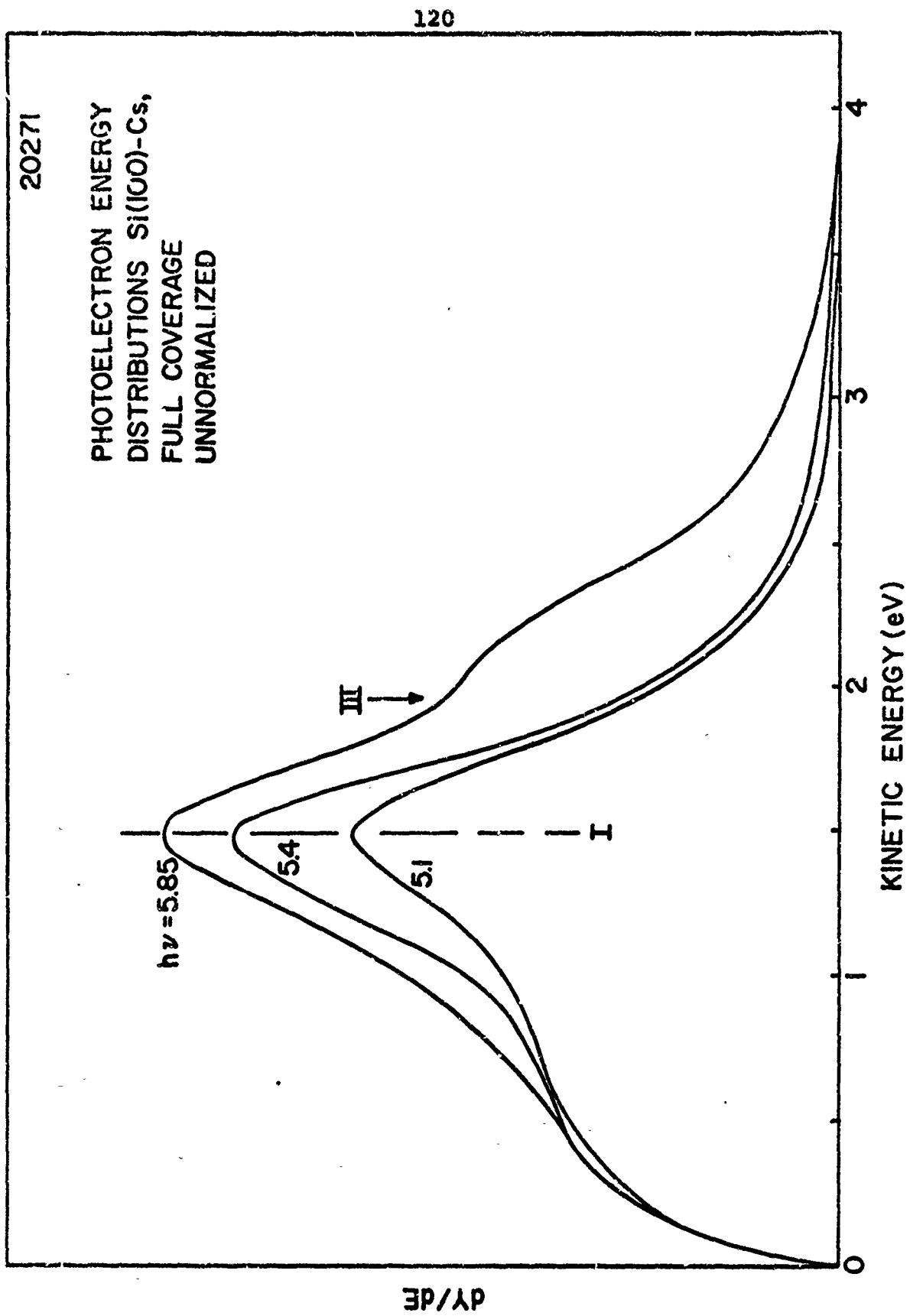
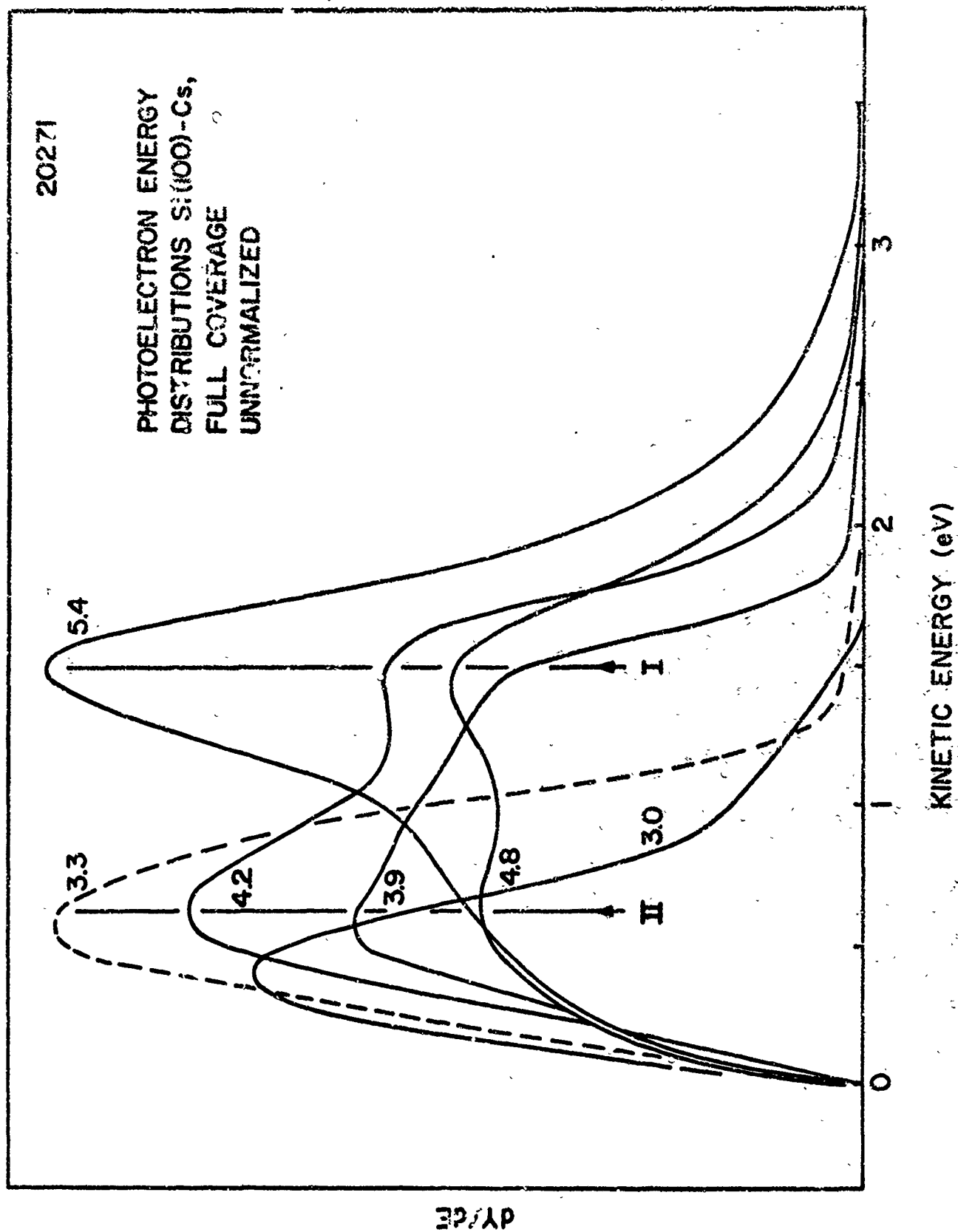


FIG. 25 E.D.C's FROM FULLY CESIATED SILICON ( $h\nu > 5.0$  eV)



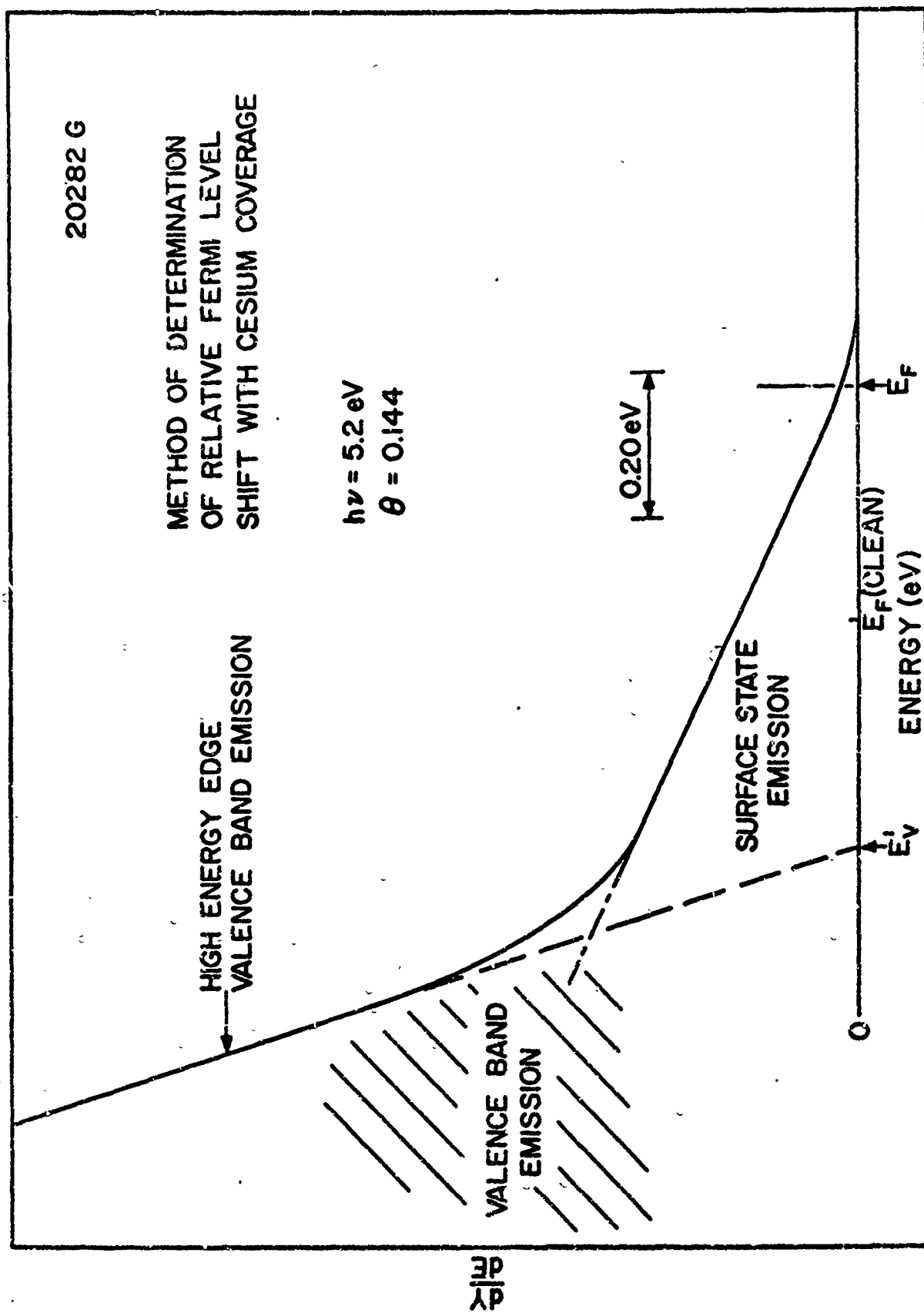
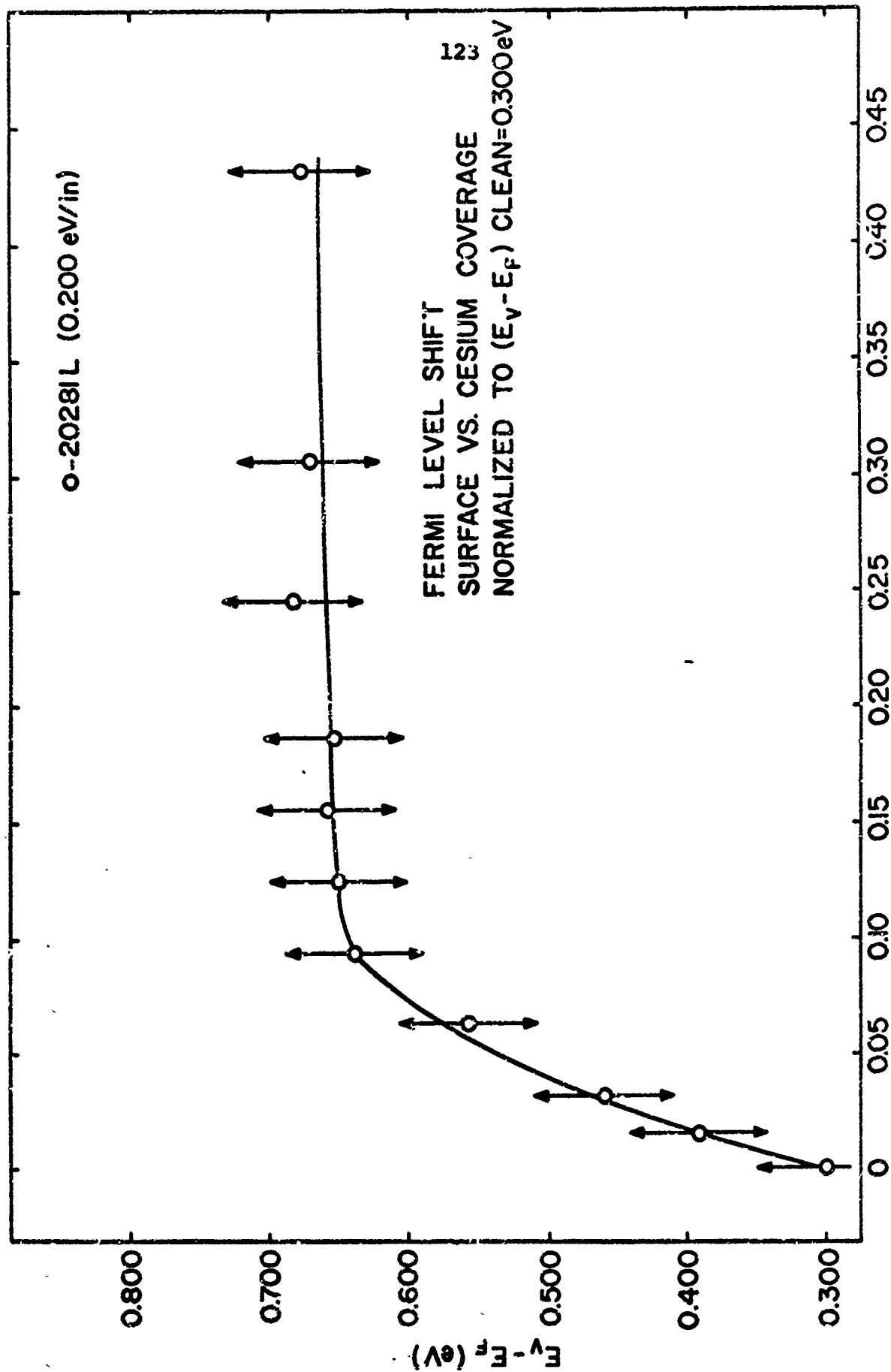


FIG. 27 METHOD OF DETERMINING BAND BENDING  $|E_V - E_F|$  VS. CESIUM COVERAGE



θ-CESIUM COVERAGE (MONOLAYERS)

FIG. 28 RESULTS OF BAND BENDING ANALYSIS USING E.D.C. DATA

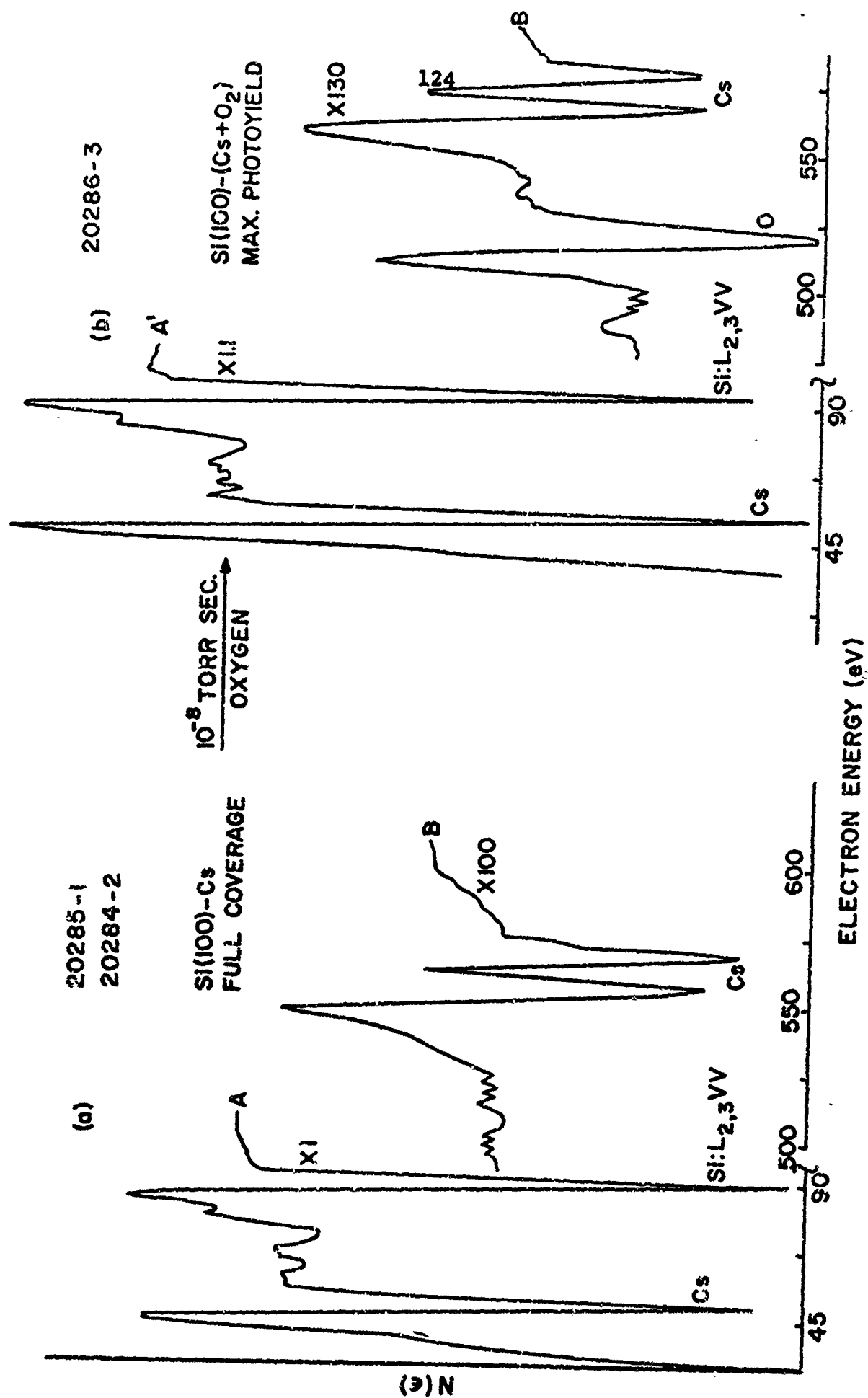


FIG. 29 AUGER SPECTRUM OF SI(100)-Cs (a) WITHOUT O<sub>2</sub> (b) WITH O<sub>2</sub> ADDED TO MAXIMIZE PHOTOYIELD



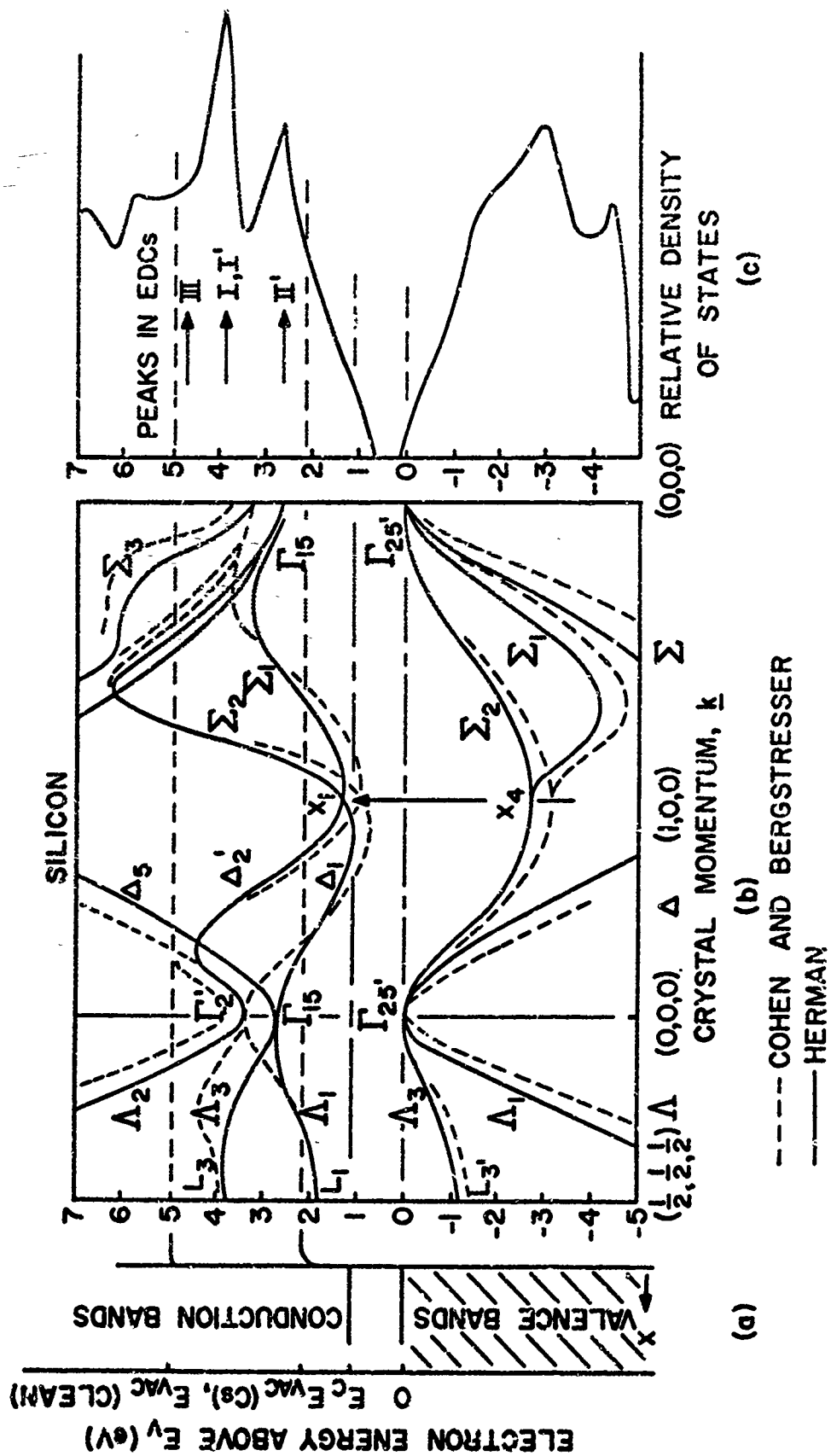


FIG 30 ENERGY BAND DIAGRAMS - SILICON (a)  $E$  vs  $k$  (b)  $E$  vs  $k$  (c)  $E$  vs DENSITY OF STATES

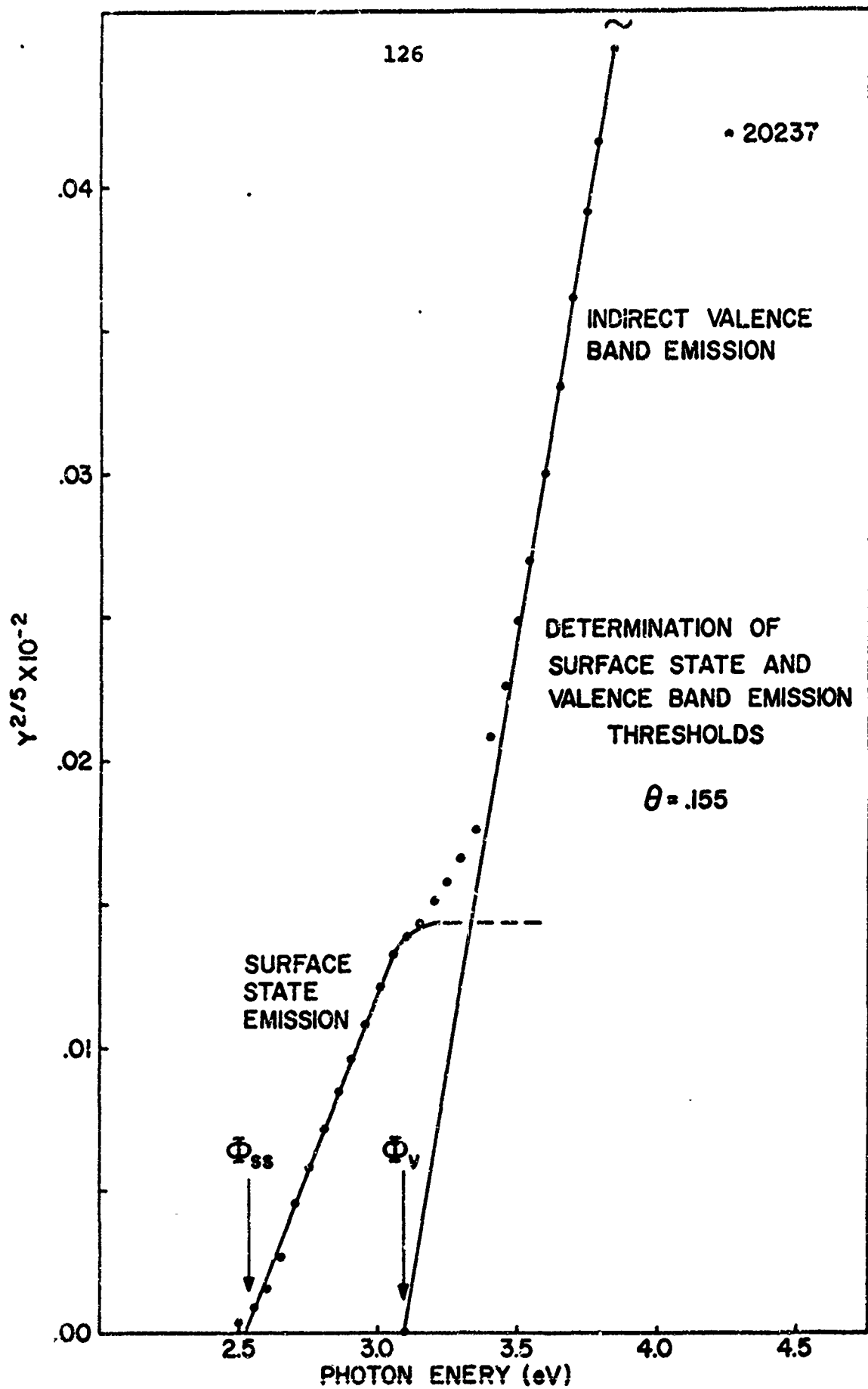
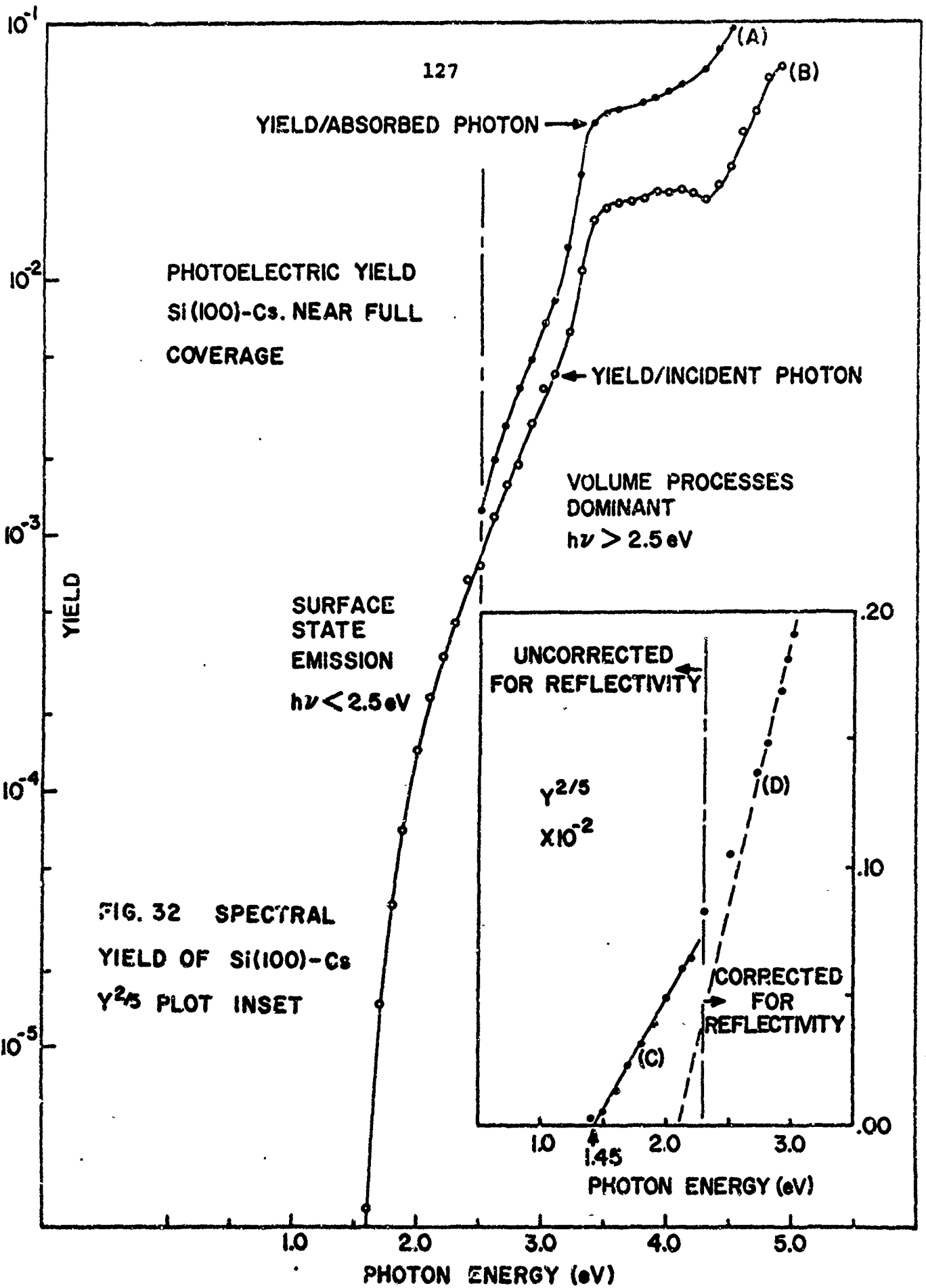


FIG.31 DETERMINATION OF PHOTOTHRESHOLDS  $\Phi_v$  AND  $\Phi_{ss}$  FROM  $Y^{2/5}$  PLOT



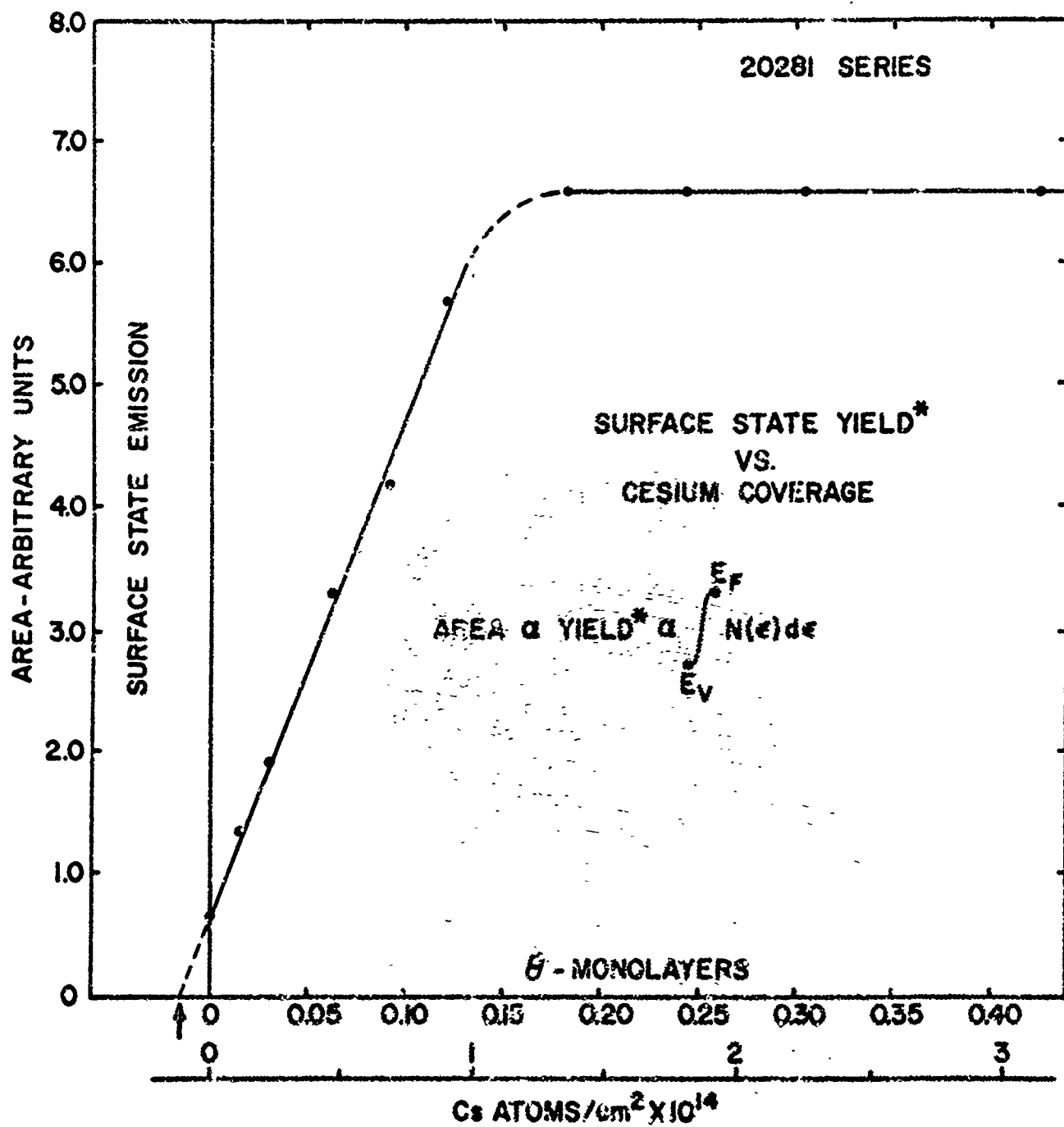


FIG. 33 SURFACE STATE EMISSION AS A FUNCTION OF CESIUM COVERAGE

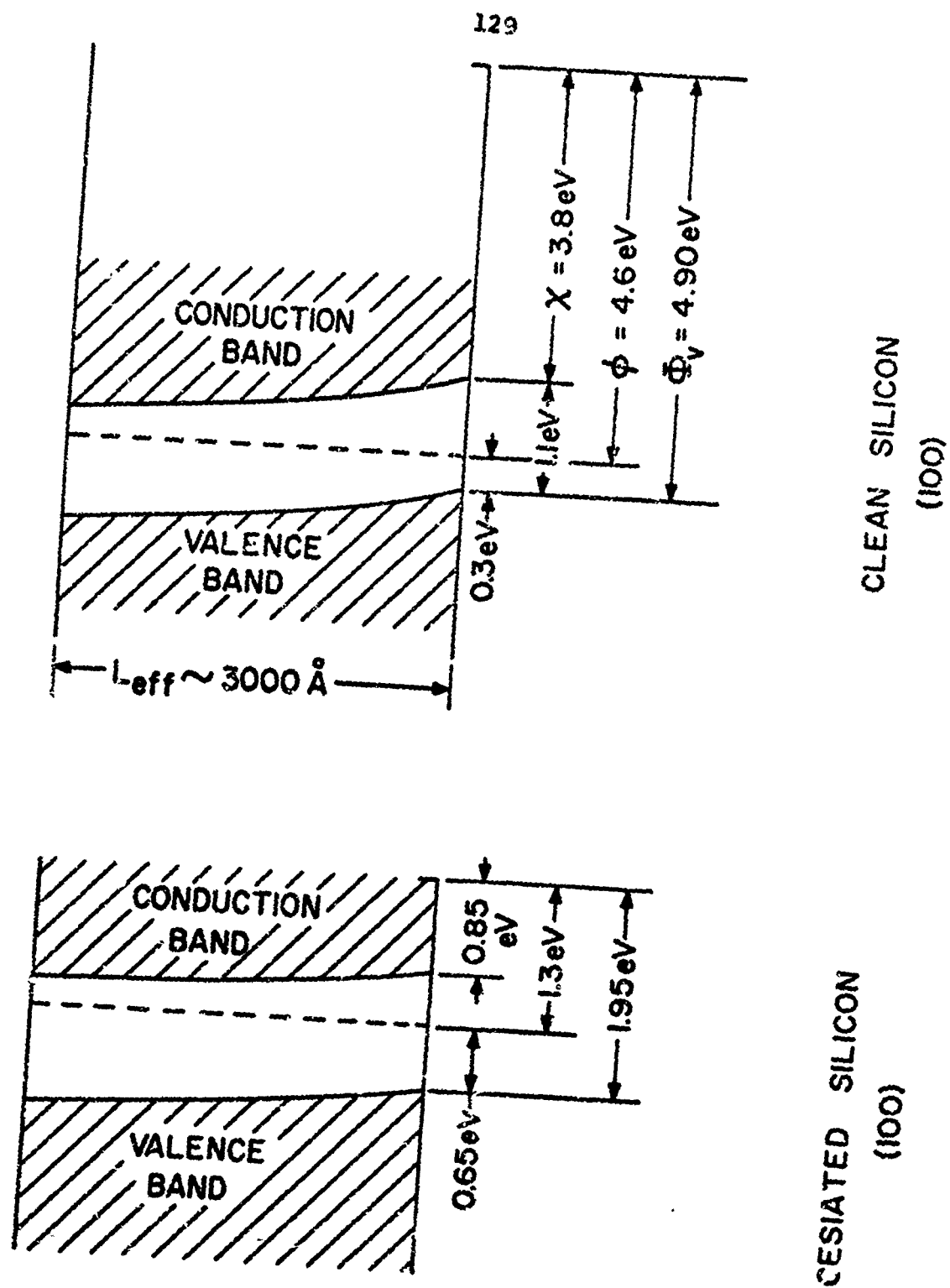


FIG.34 SCHEMATIC DIAGRAM SHOWING THE BAND BENDING PROFILES OF CLEAN AND CESIATED SI(100)

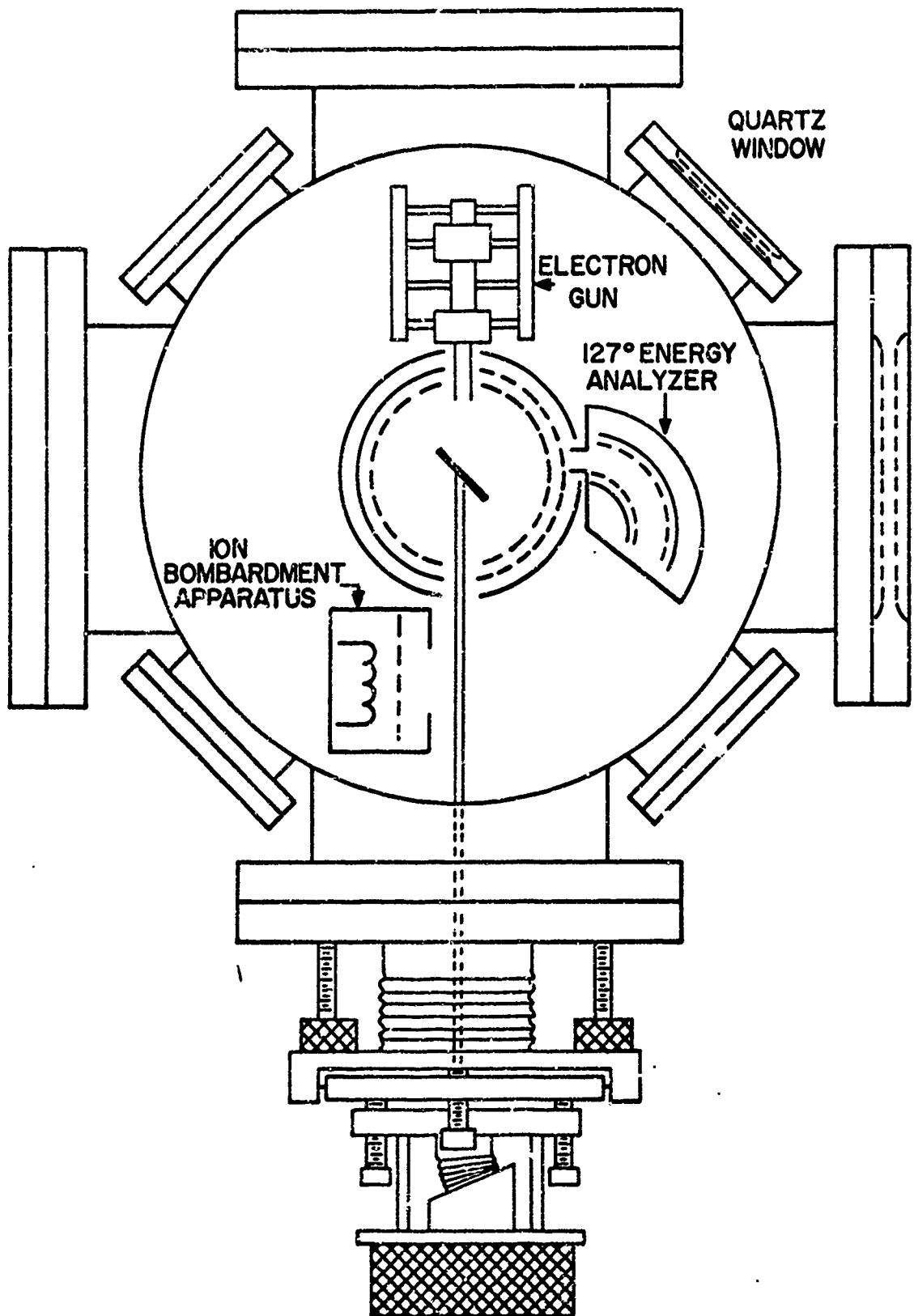


FIG. 35 SCHEMATIC DIAGRAM OF VACUUM CHAMBER

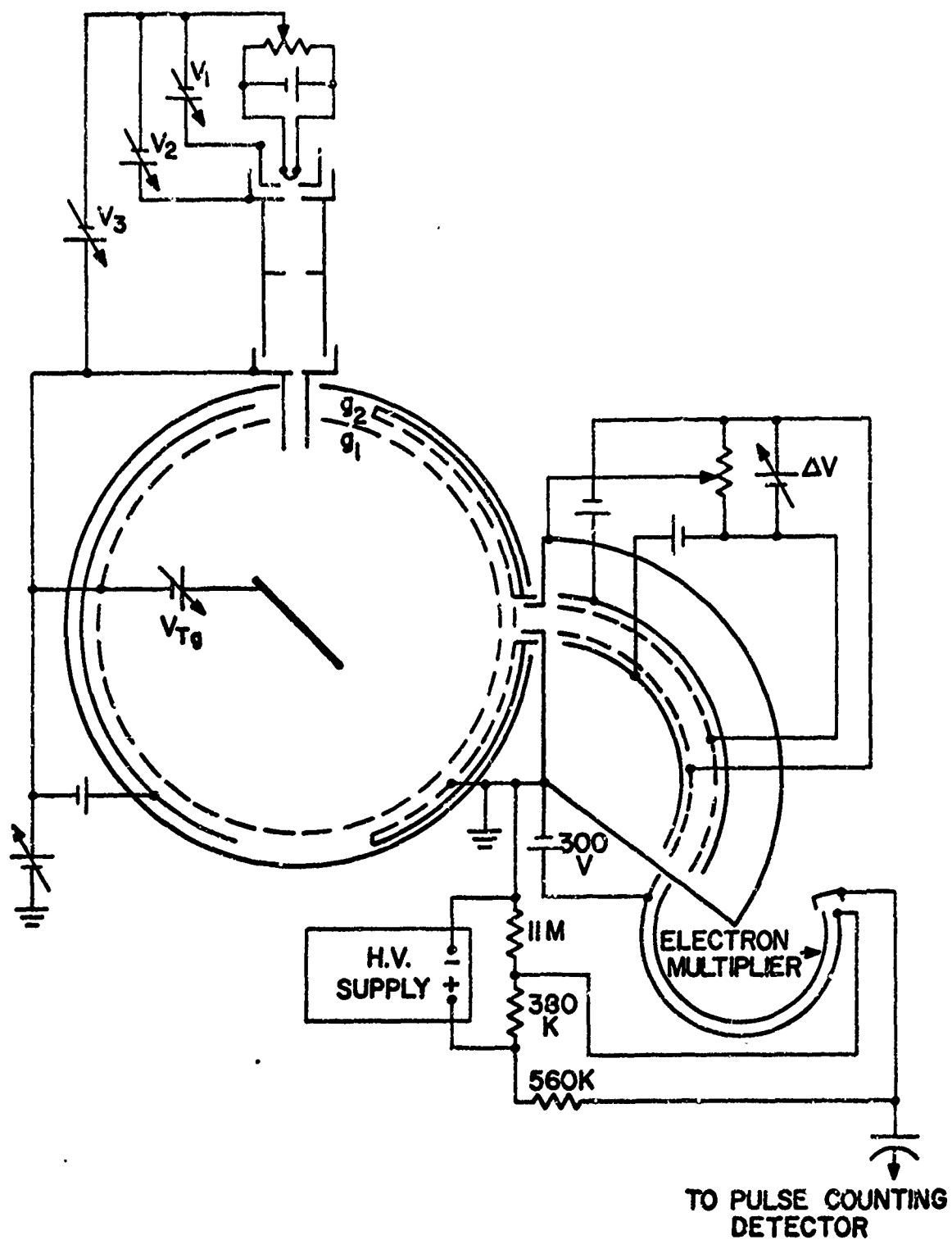


FIG. 36 SCHEMATIC DIAGRAM OF EXPERIMENTAL APPARATUS

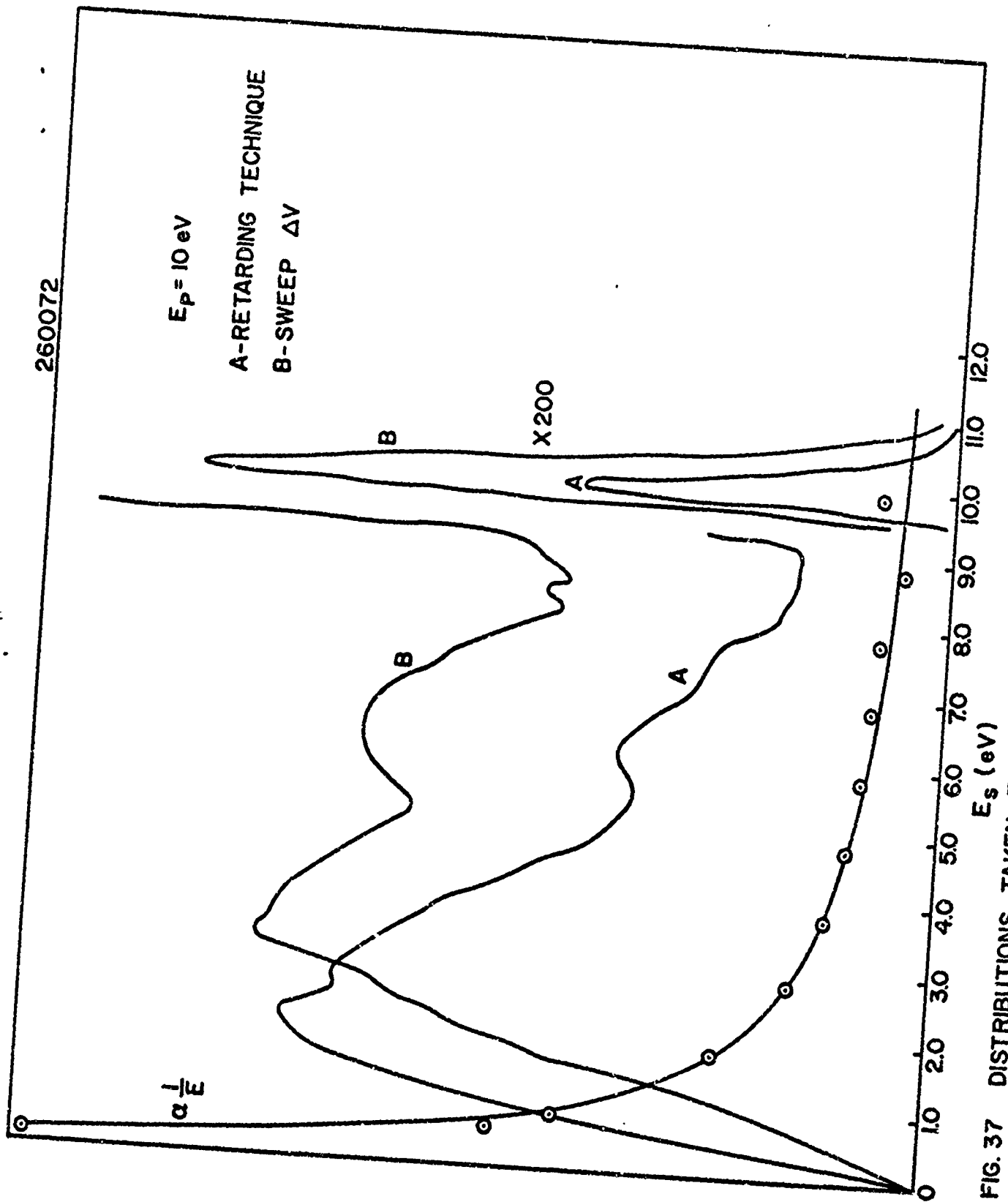


FIG. 37 DISTRIBUTIONS TAKEN FOR THE TWO MODES OF ANALYSER OPERATION



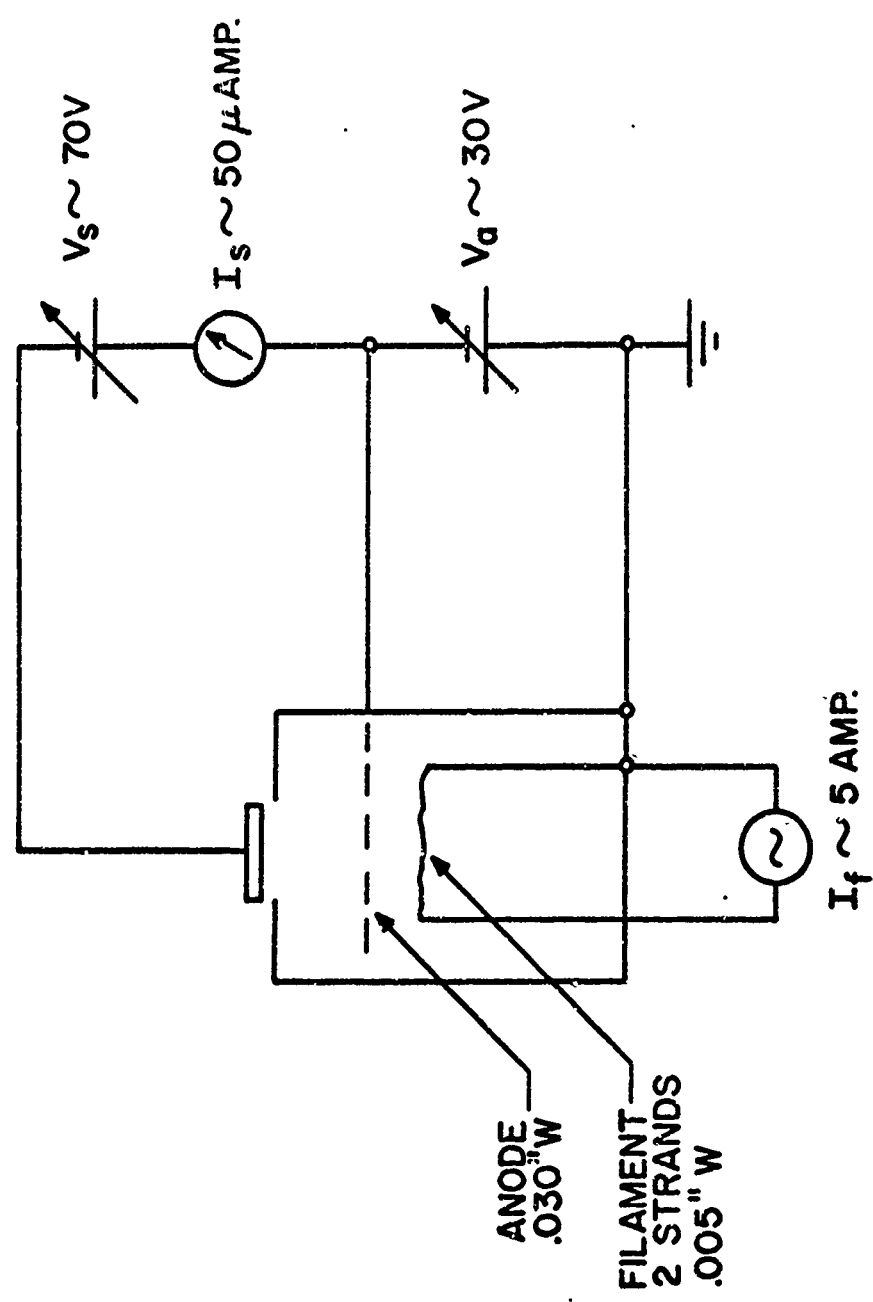


FIG.38 SCHEMATIC DIAGRAM OF ION BOMBARDMENT CLEANING APPARATUS

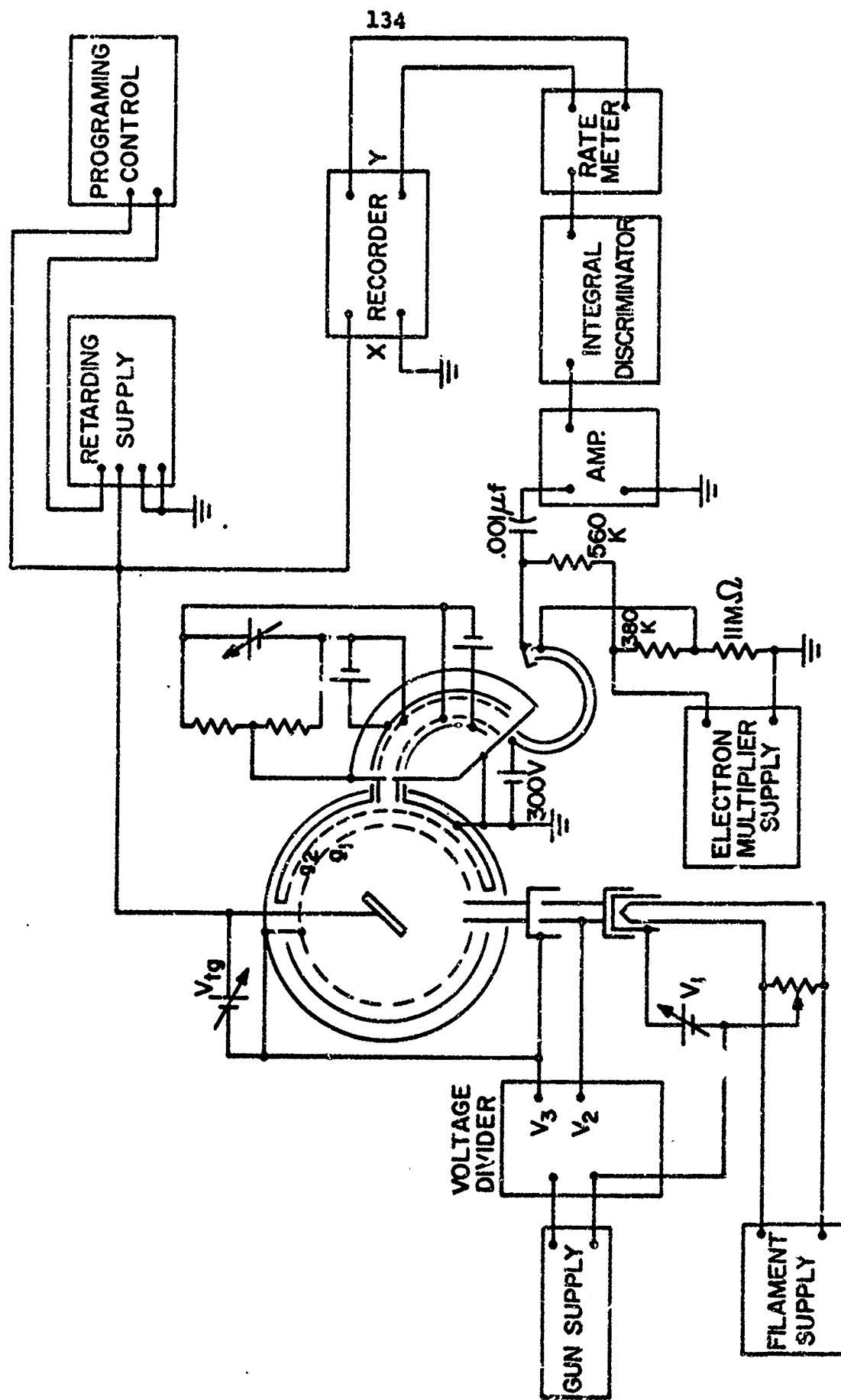
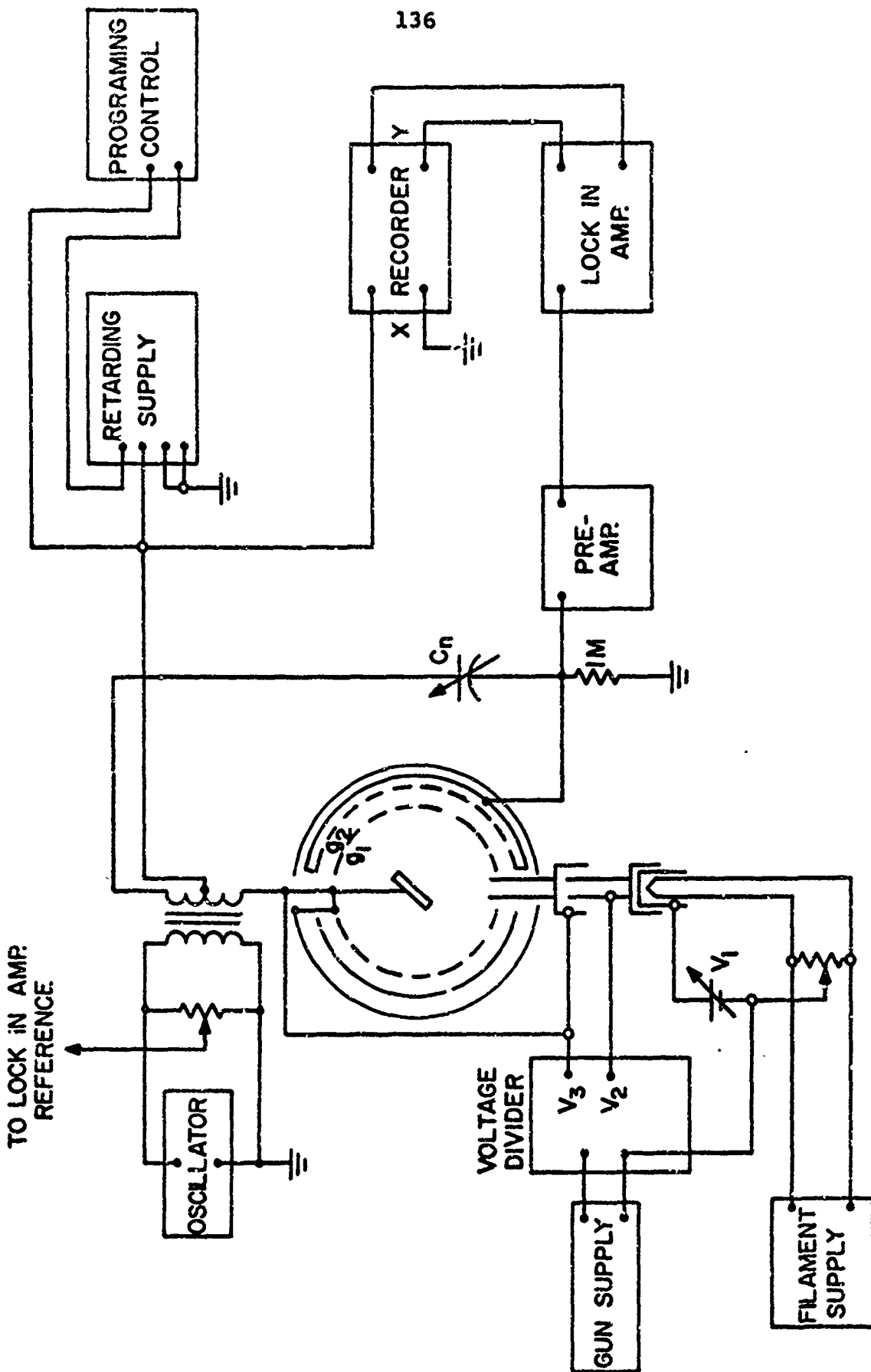


FIG. 39 SCHEMATIC DIAGRAM OF APPARATUS FOR SECONDARY ELECTRON MEASUREMENTS





**FIG. 4| SCHEMATIC DIAGRAM OF APPARATUS FOR AUGER MEASUREMENTS**

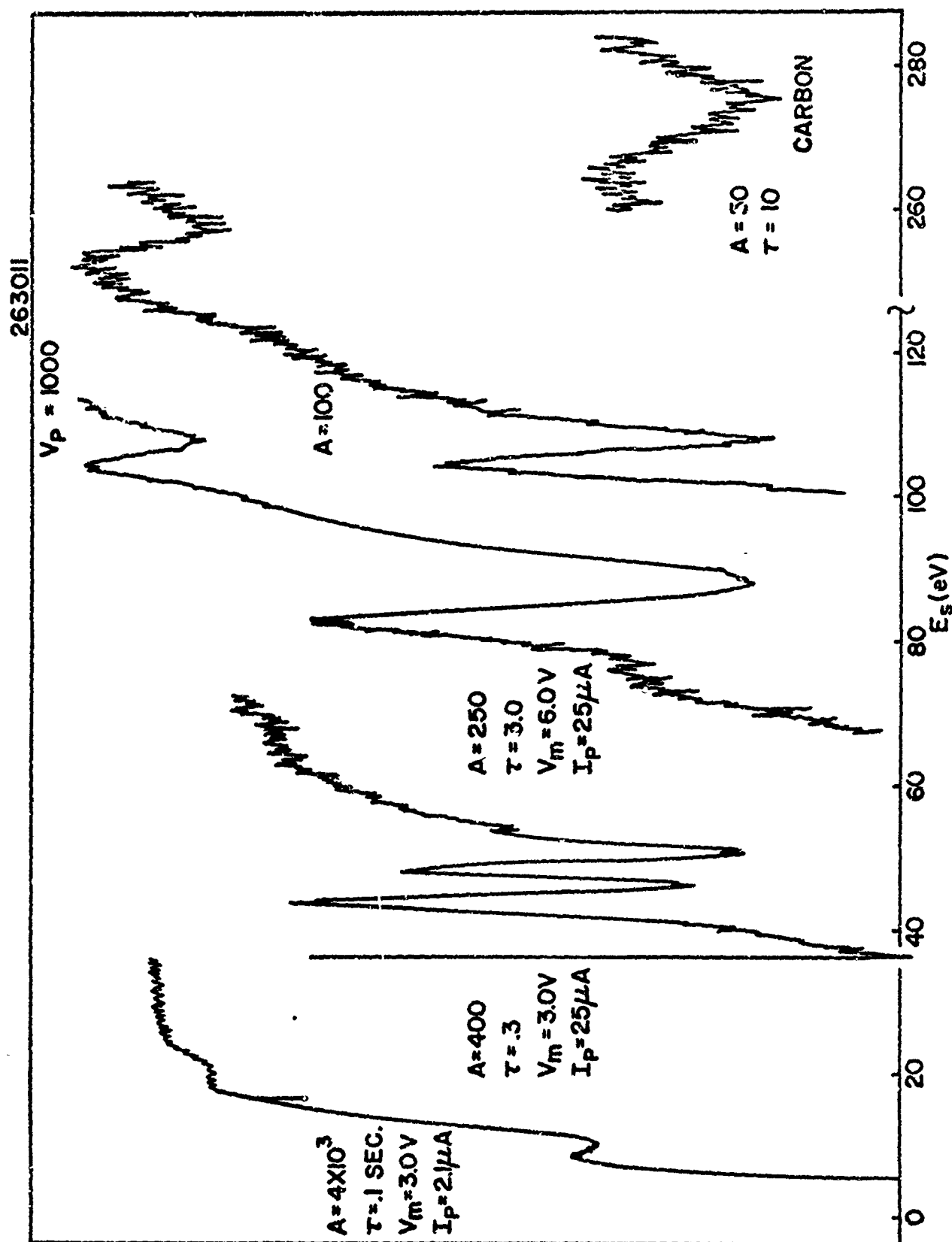


FIG. 42 AUGER SPECTRUM OF CARBON CONTAMINATED GERMANIUM

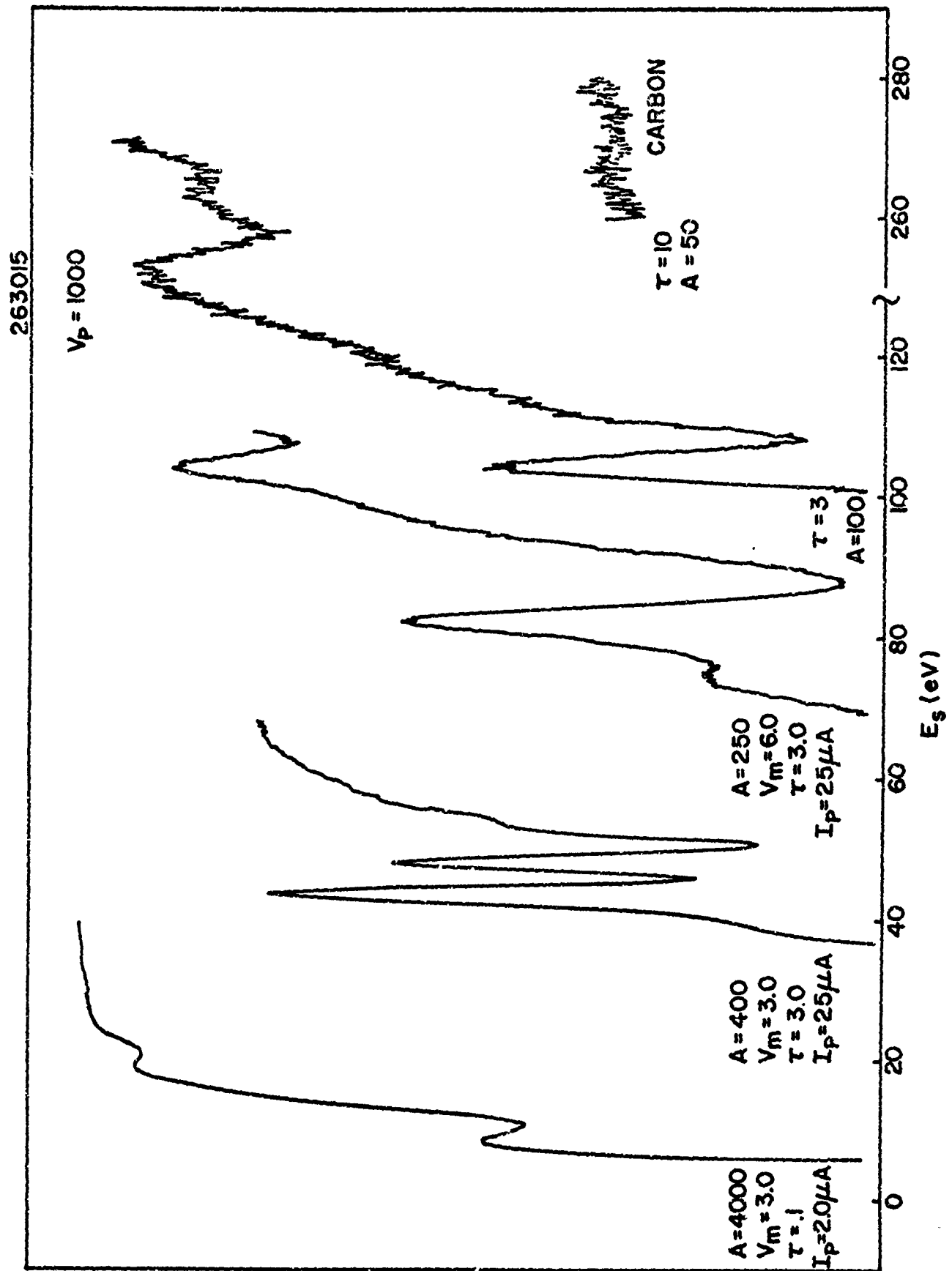
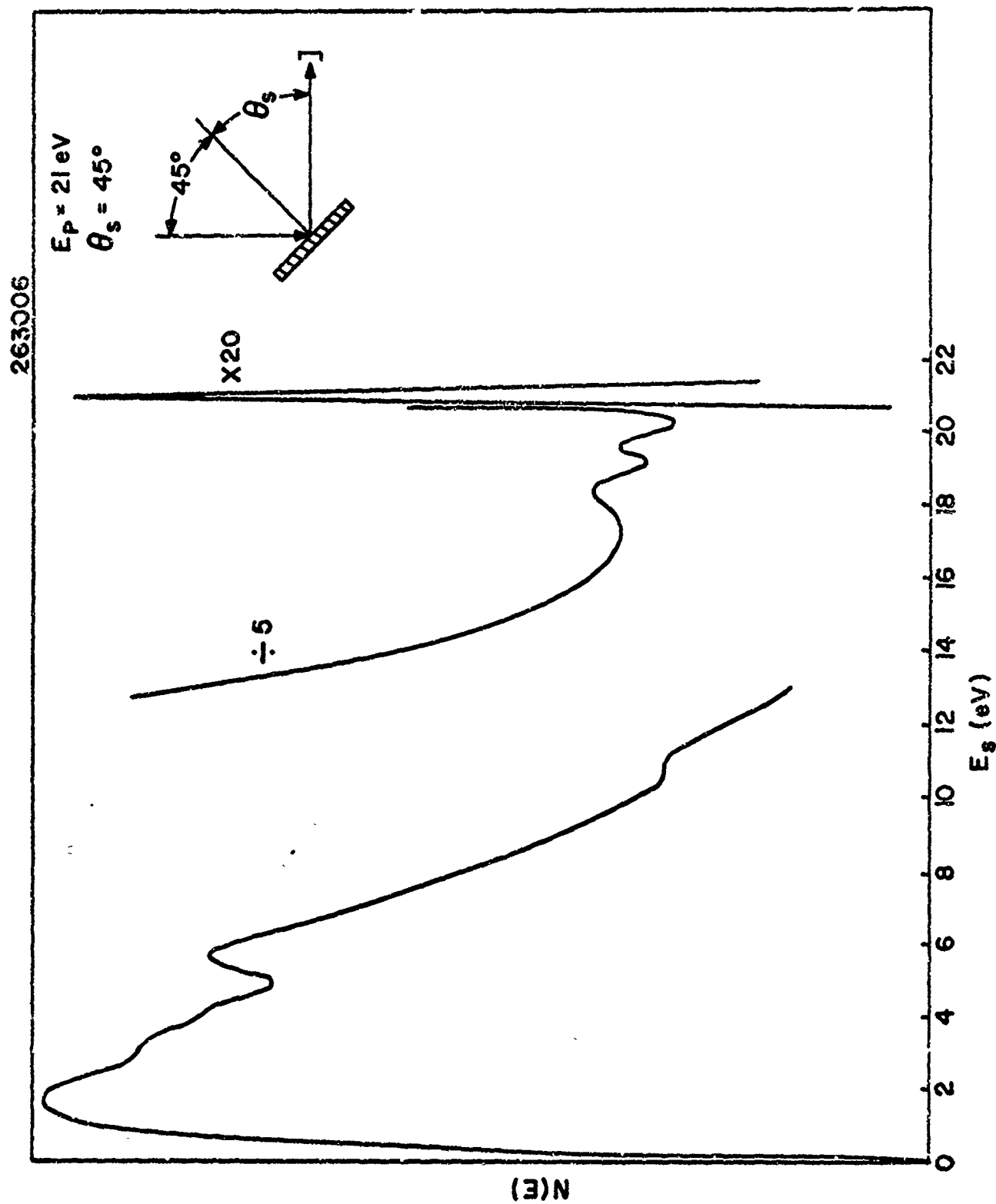
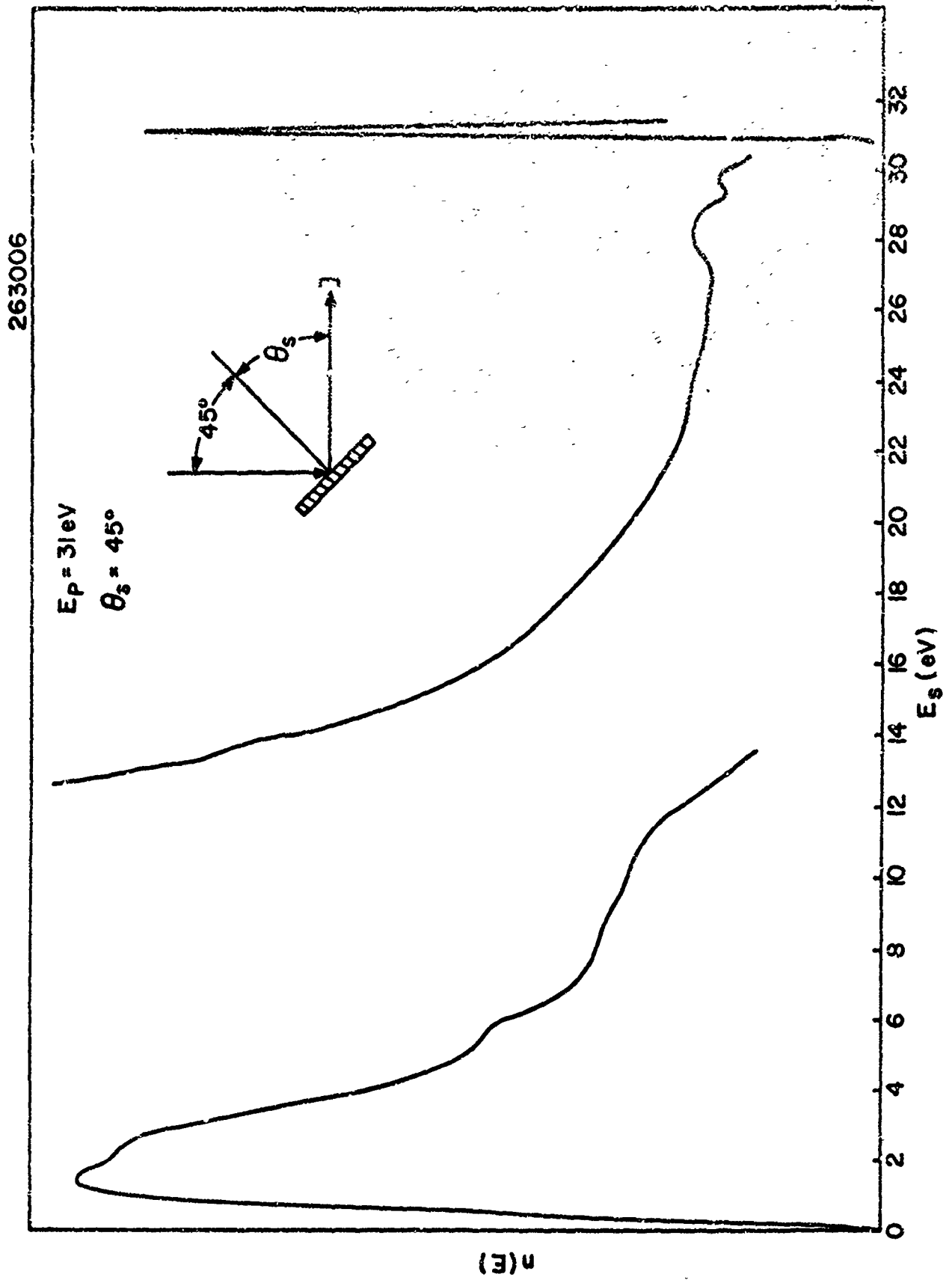


FIG. 43 AUGER SPECTRUM OF CLEAN GERMANIUM

FIG. 44 S.E.E.D. IN SPECULAR SCATTERING DIRECTION ( $E_P = 21 \text{ eV}$ )

FIG. 45 S.E.E.D. IN SPECULAR SCATTERING DIRECTION ( $E_p = 31 \text{ eV}$ )



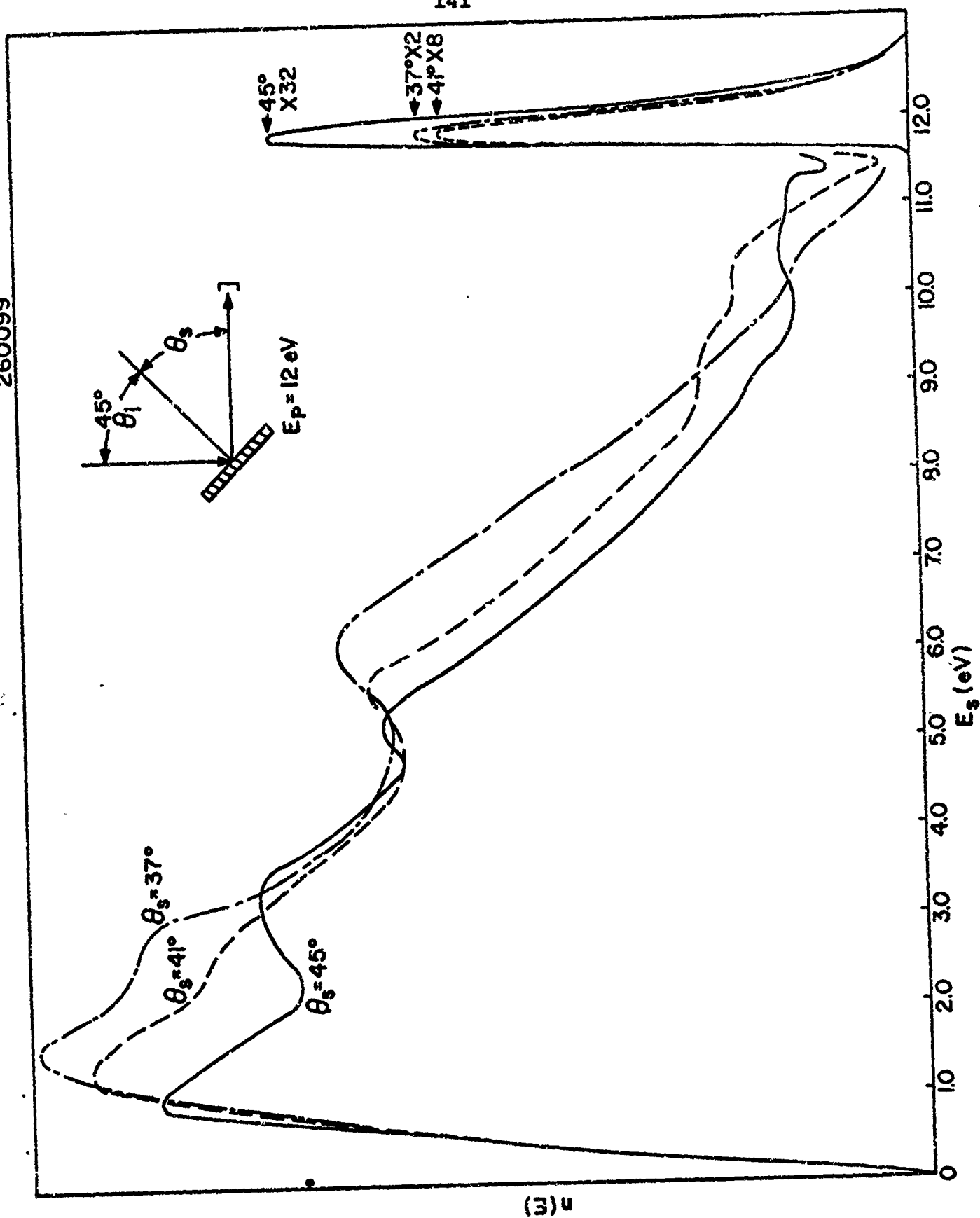


FIG. 46 S.E.E.D. AT SCATTERING ANGLES OF  $37^\circ$ ,  $41^\circ$ ,  $45^\circ$  FOR  $E_p = 12 \text{ eV}$

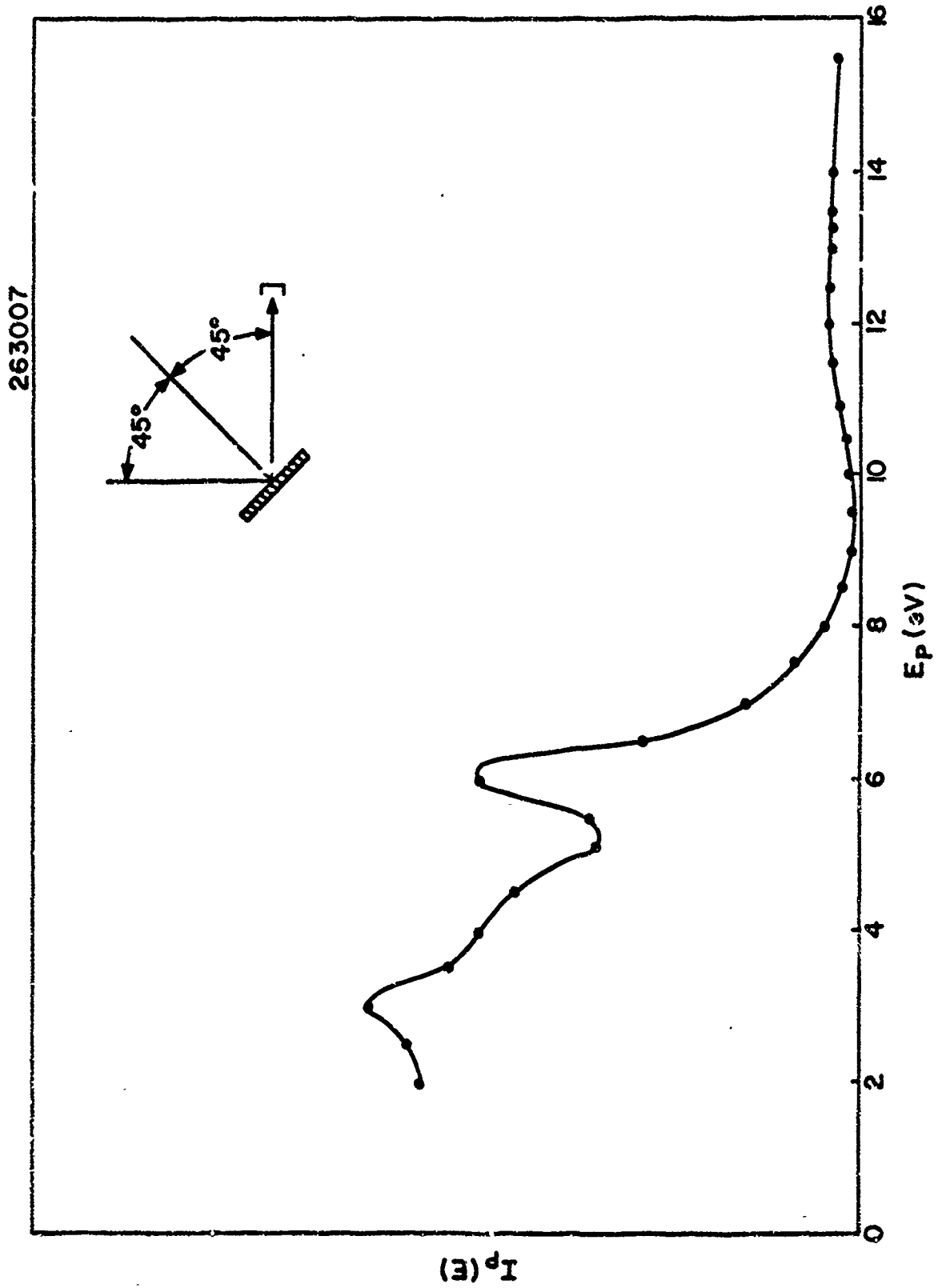


FIG. 47 ELASTIC SCATTERING INTENSITY PLOT FOR SPECULAR SCATTERING  
WITH 45° ANGLE OF INCIDENCE

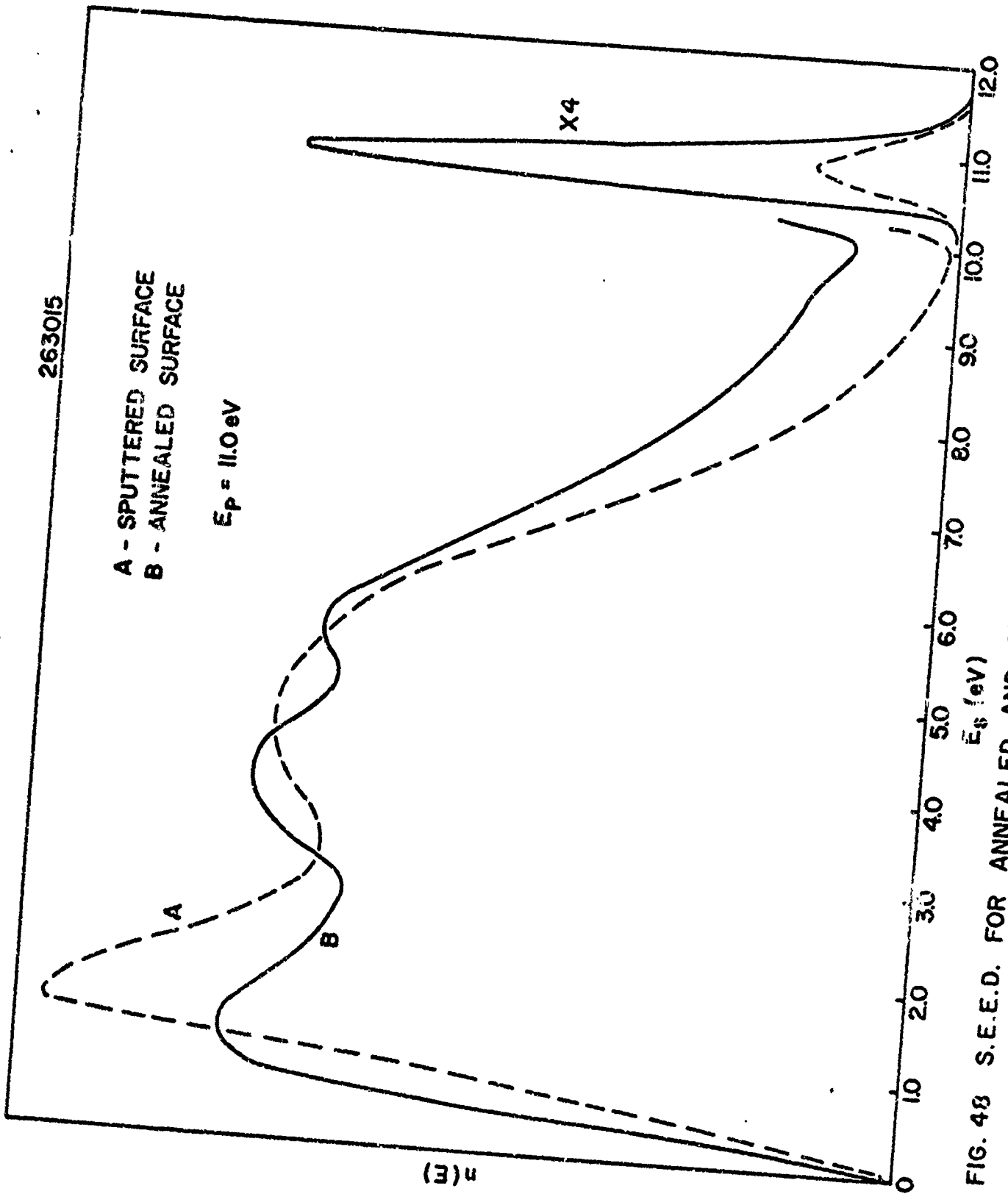


FIG. 48 S.E.E.D. FOR ANNEALED AND SPUTTERED SURFACES

263005

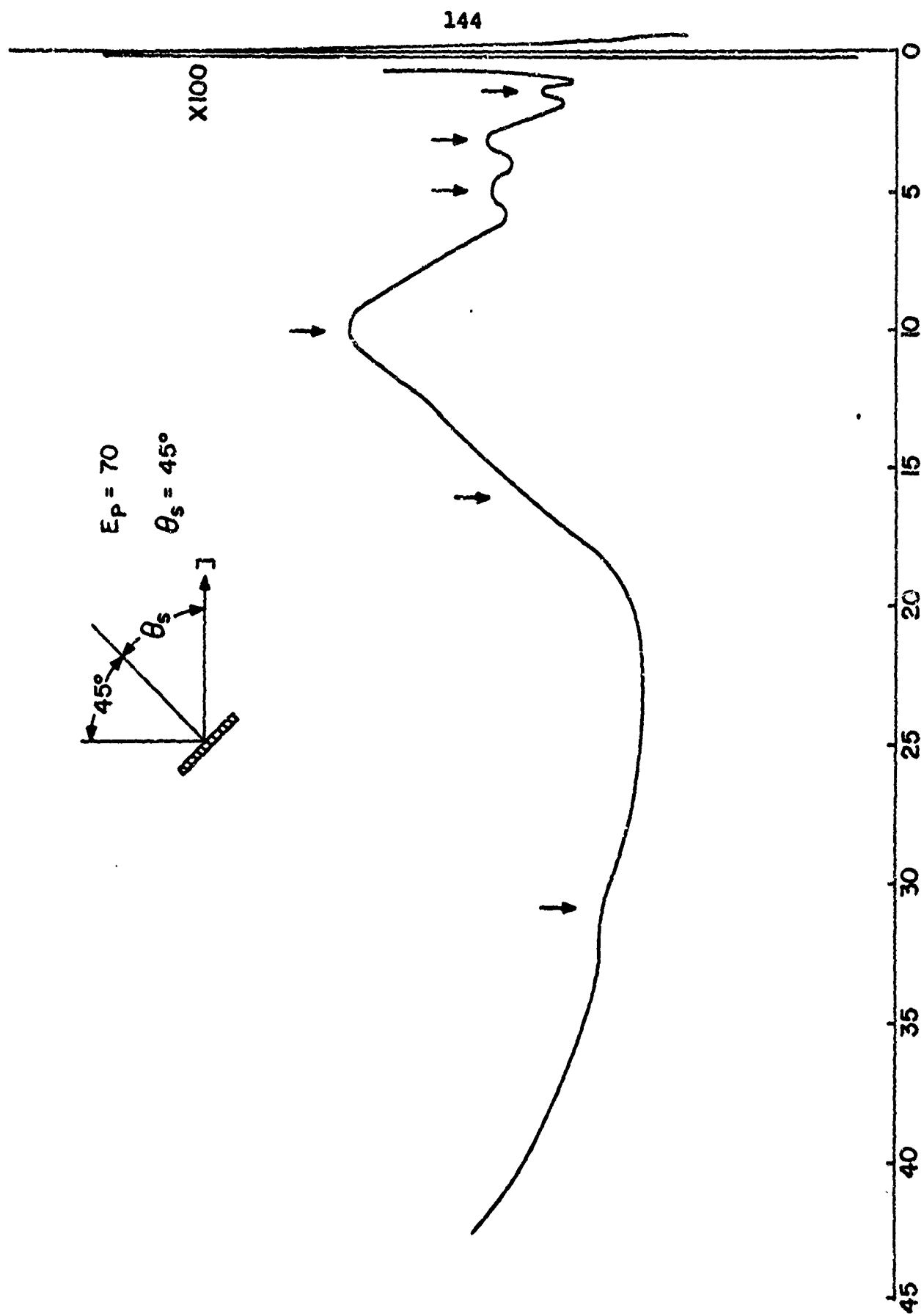


FIG. 49 TYPICAL CHARACTERISTIC LOSS SPECTRUM

145

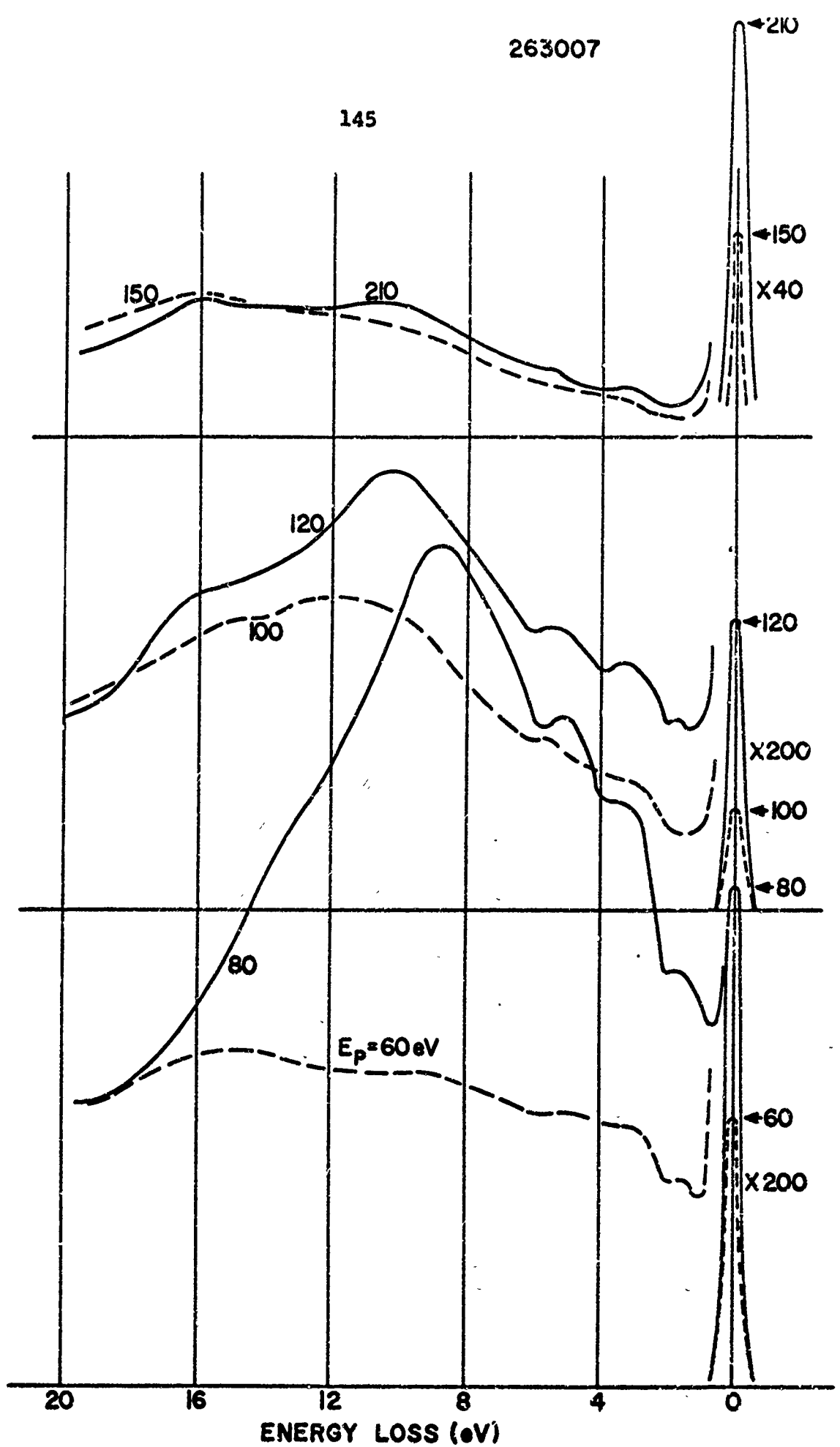


FIG. 50 CHARACTERISTIC LOSS SPECTRA

260065

$E_p = 70\text{ eV}$   
OI AZIMUTH

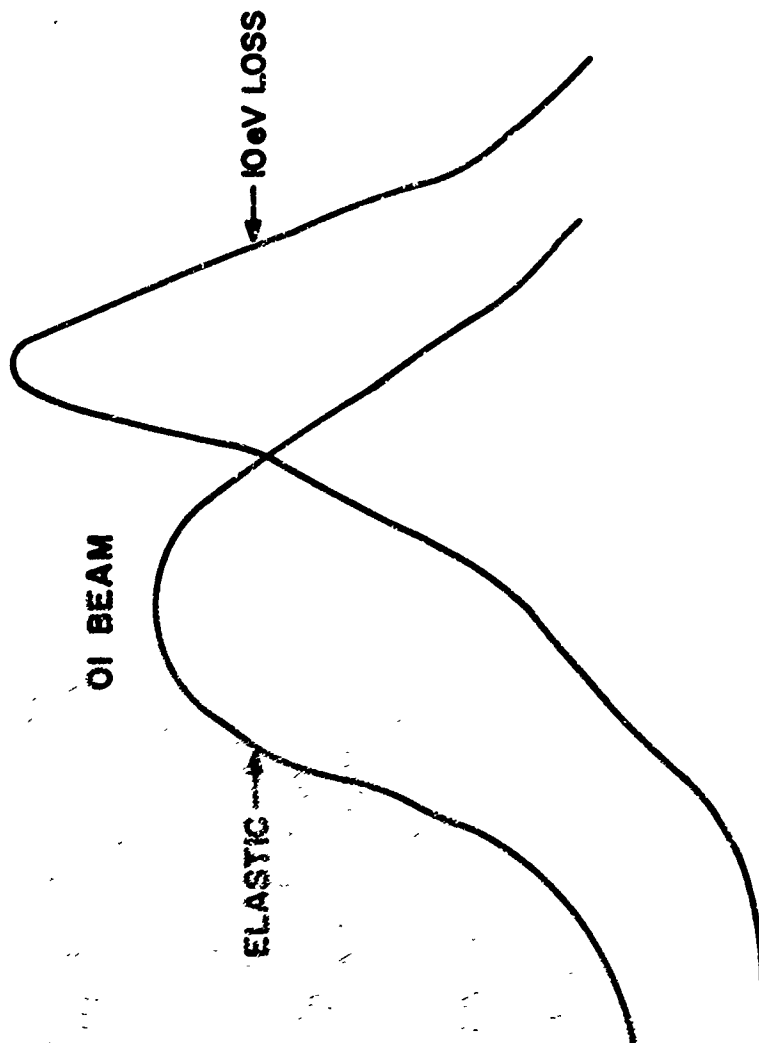
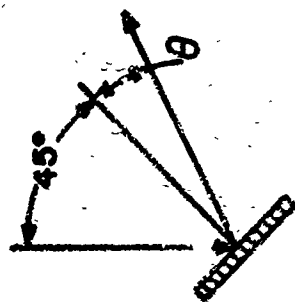


FIG. 5i INTENSITY VS. ANGLE FOR OI DIFFRACTION BEAM (OI AZIMUTH)

141132

GaAs(III) A-Cs

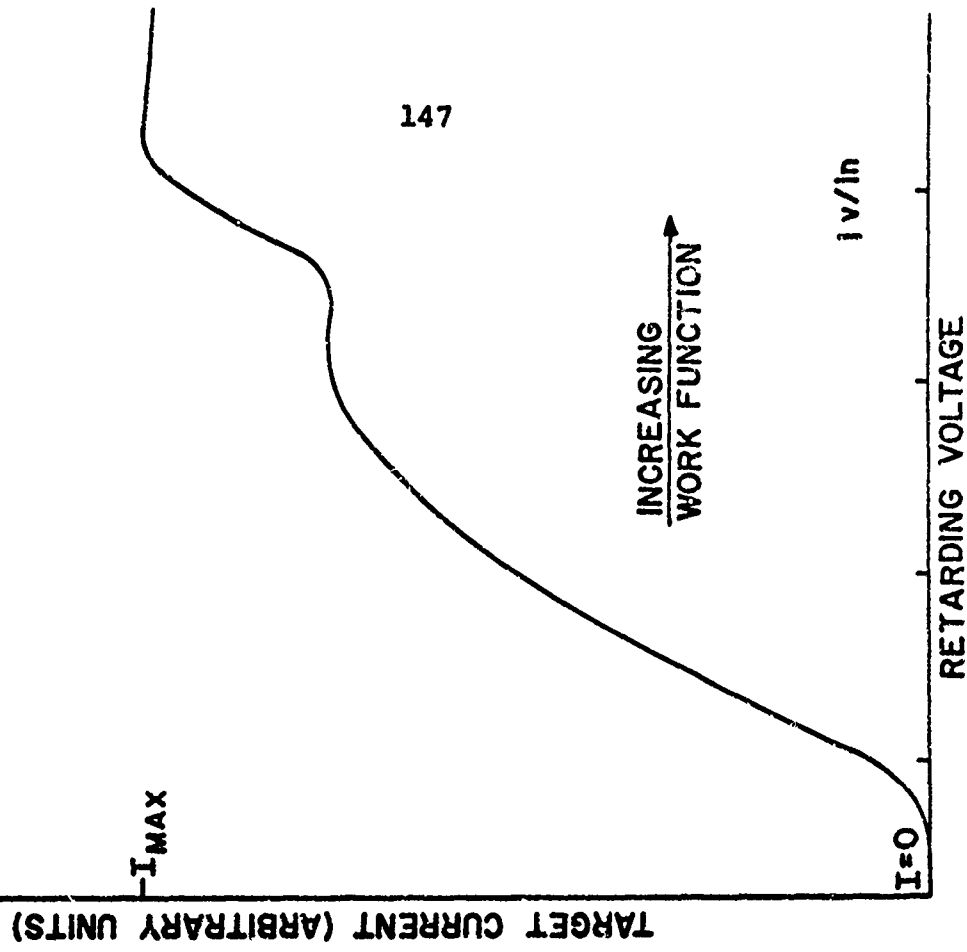


FIG 52(b) I-V CHARACTERISTIC SHOWING STRUCTURE DUE TO SURFACE PATCHES

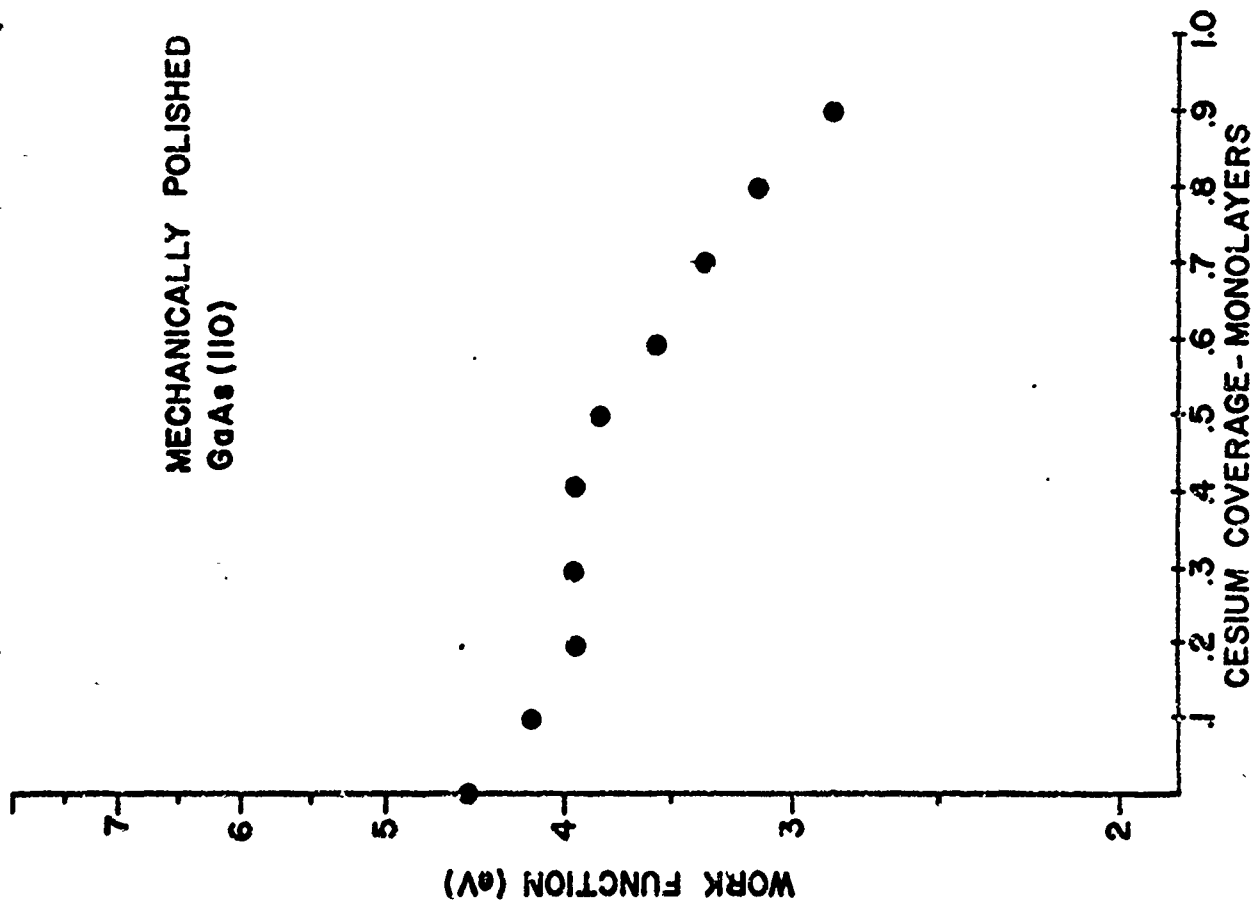


FIG 52(a) WORK FUNCTION VS. Cs COVERAGE FOR A HEATED GaAs (110) SURFACE

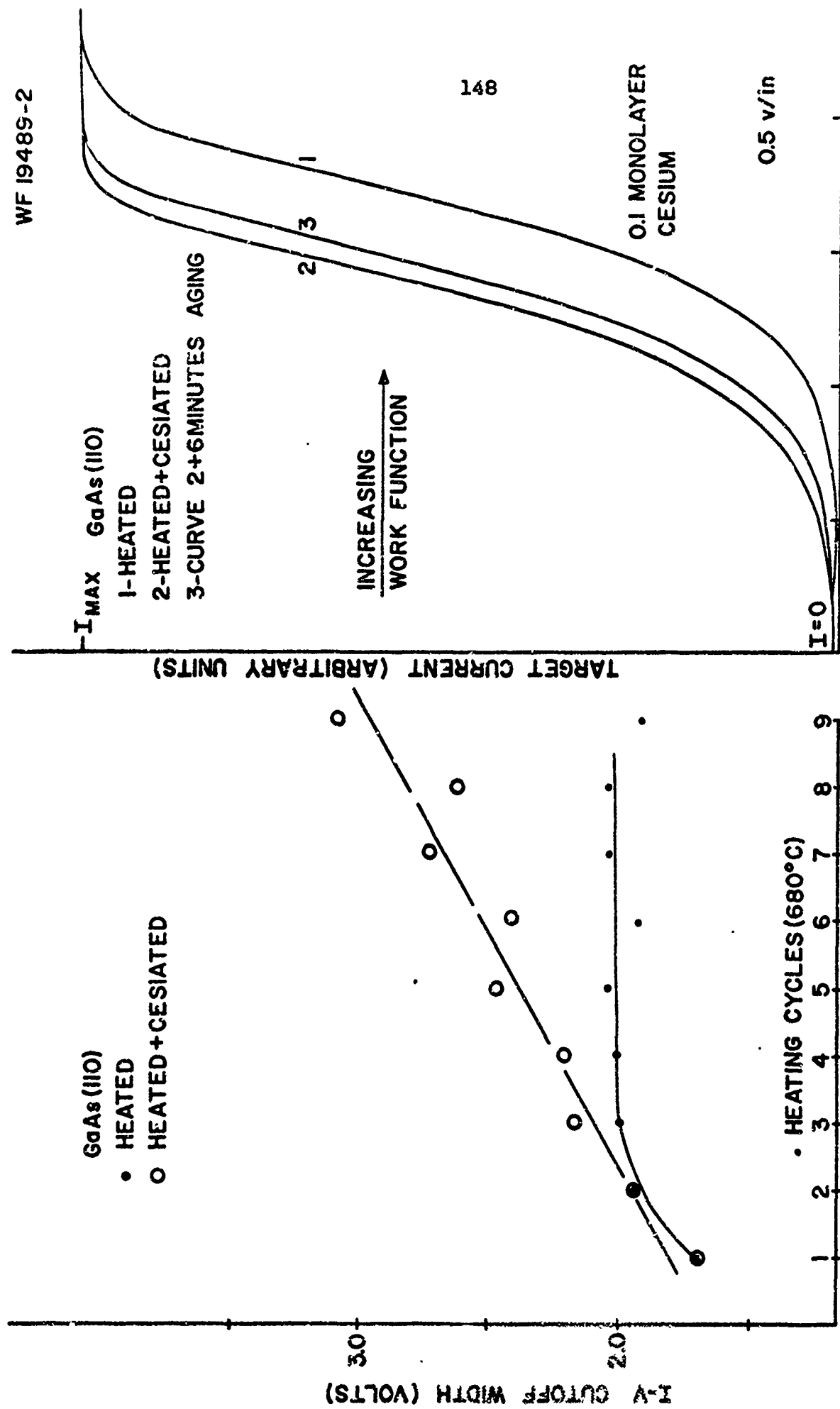
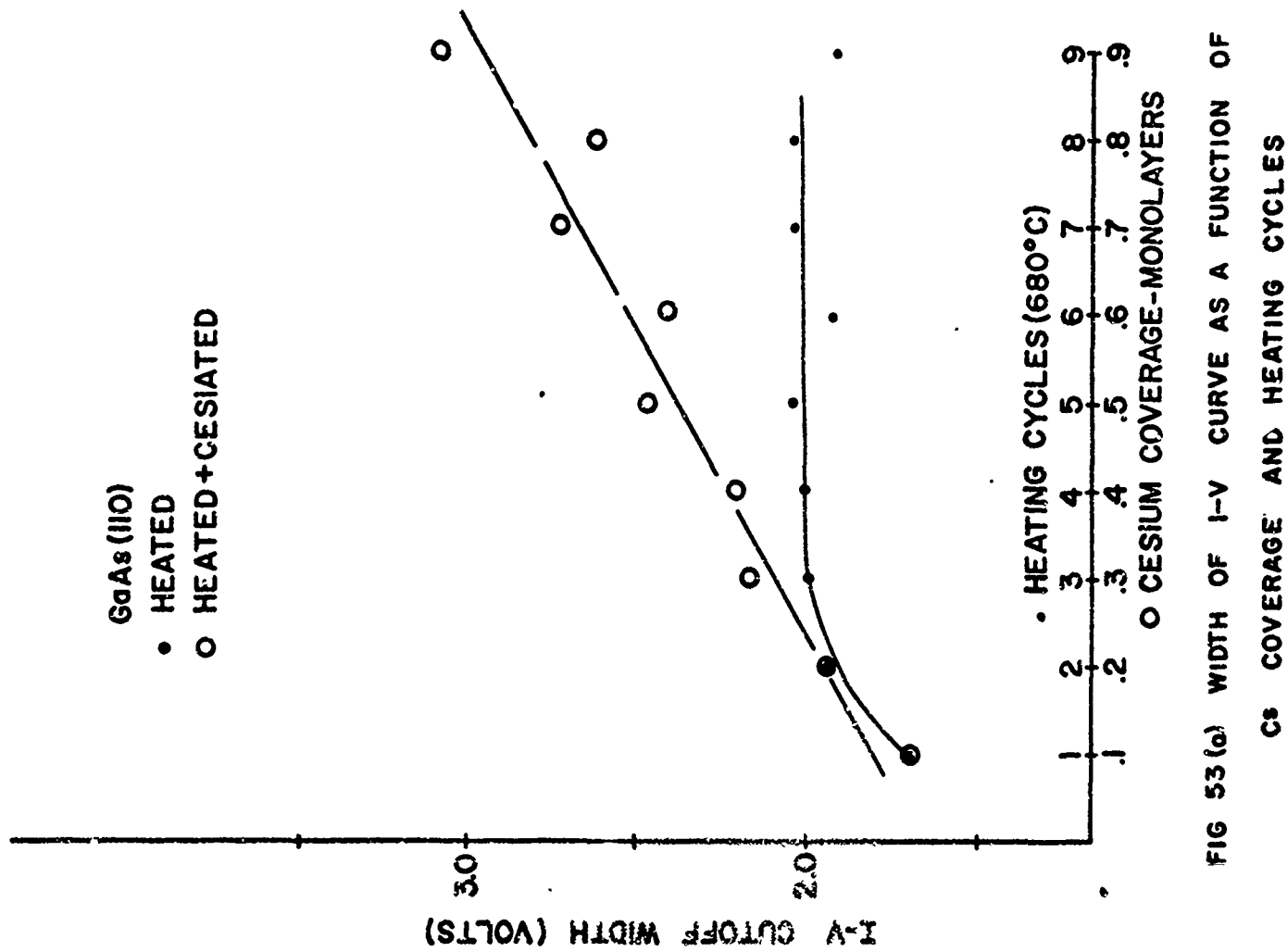


FIG 53 (b) I-V CHARACTERISTICS SHOWING THE SHIFT DUE TO CESIUM MIGRATION





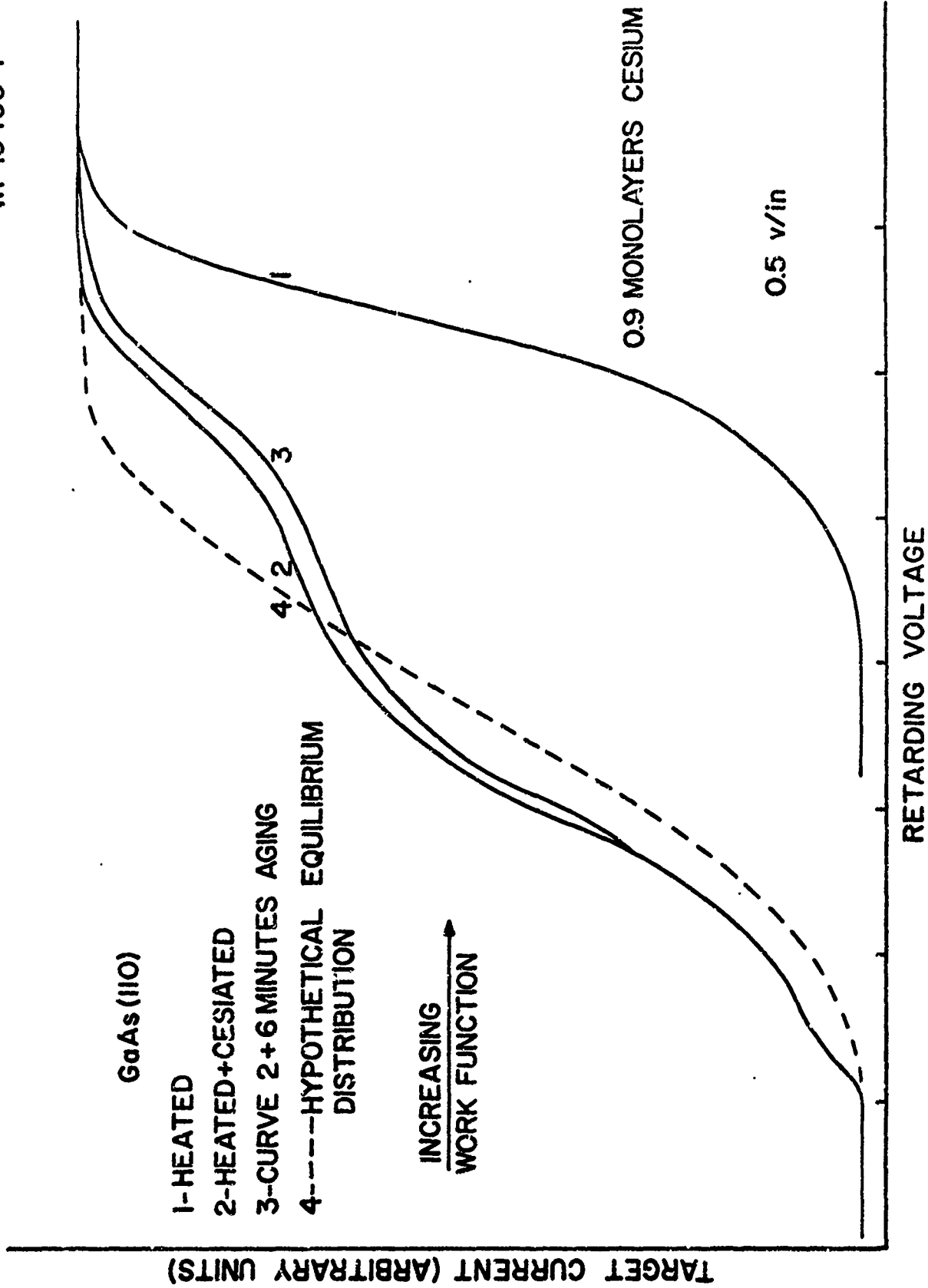


FIG 54 I-V CHARACTERISTICS SHOWING THE EFFECT OF SURFACE PATCHES UPON  $Cs^+$  MIGRATION

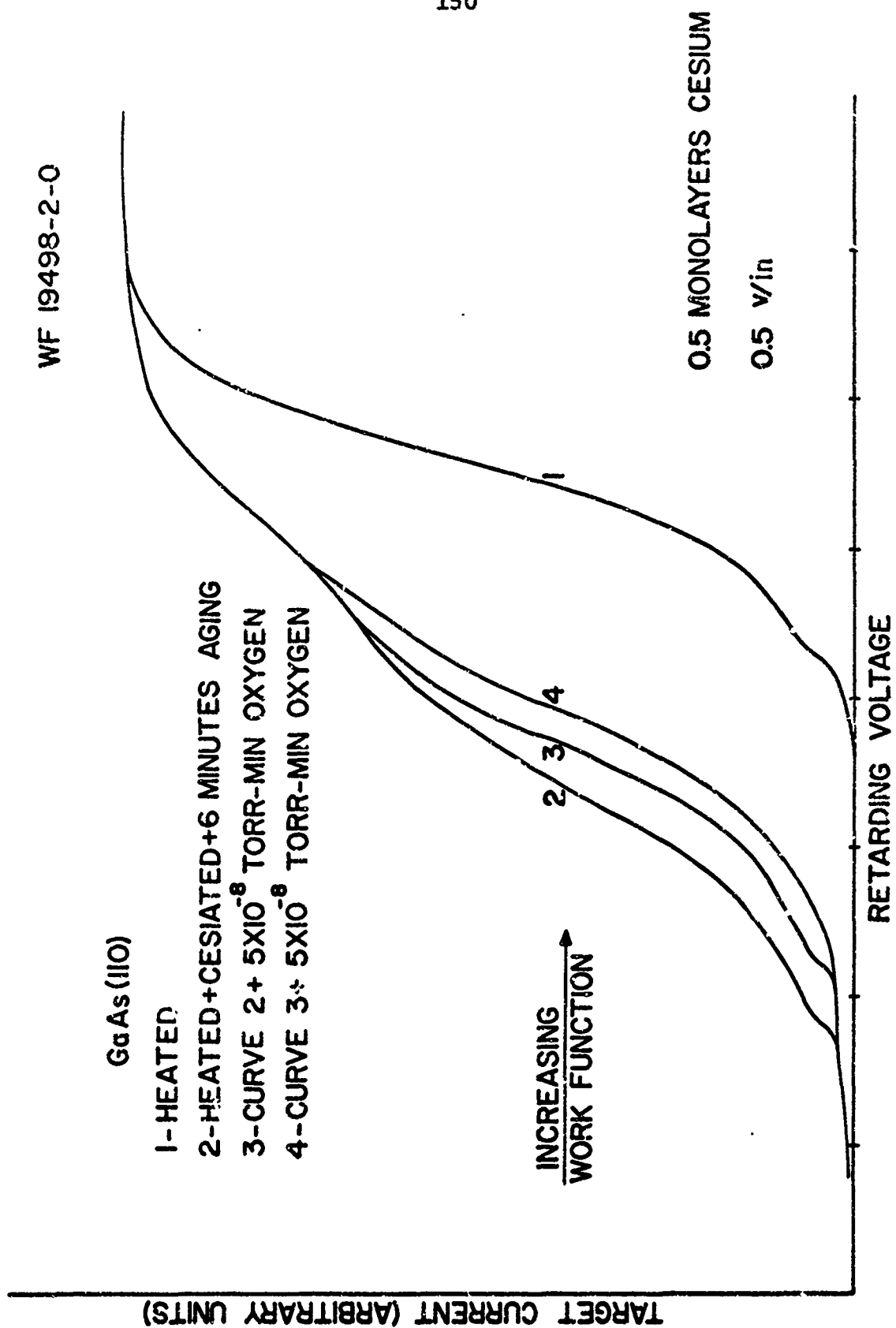


FIG 55 I-V CHARACTERISTIC SHOWING THE EFFECT OF OXYGEN SORPTION UPON THE COMPOSITE CESIATED SURFACE

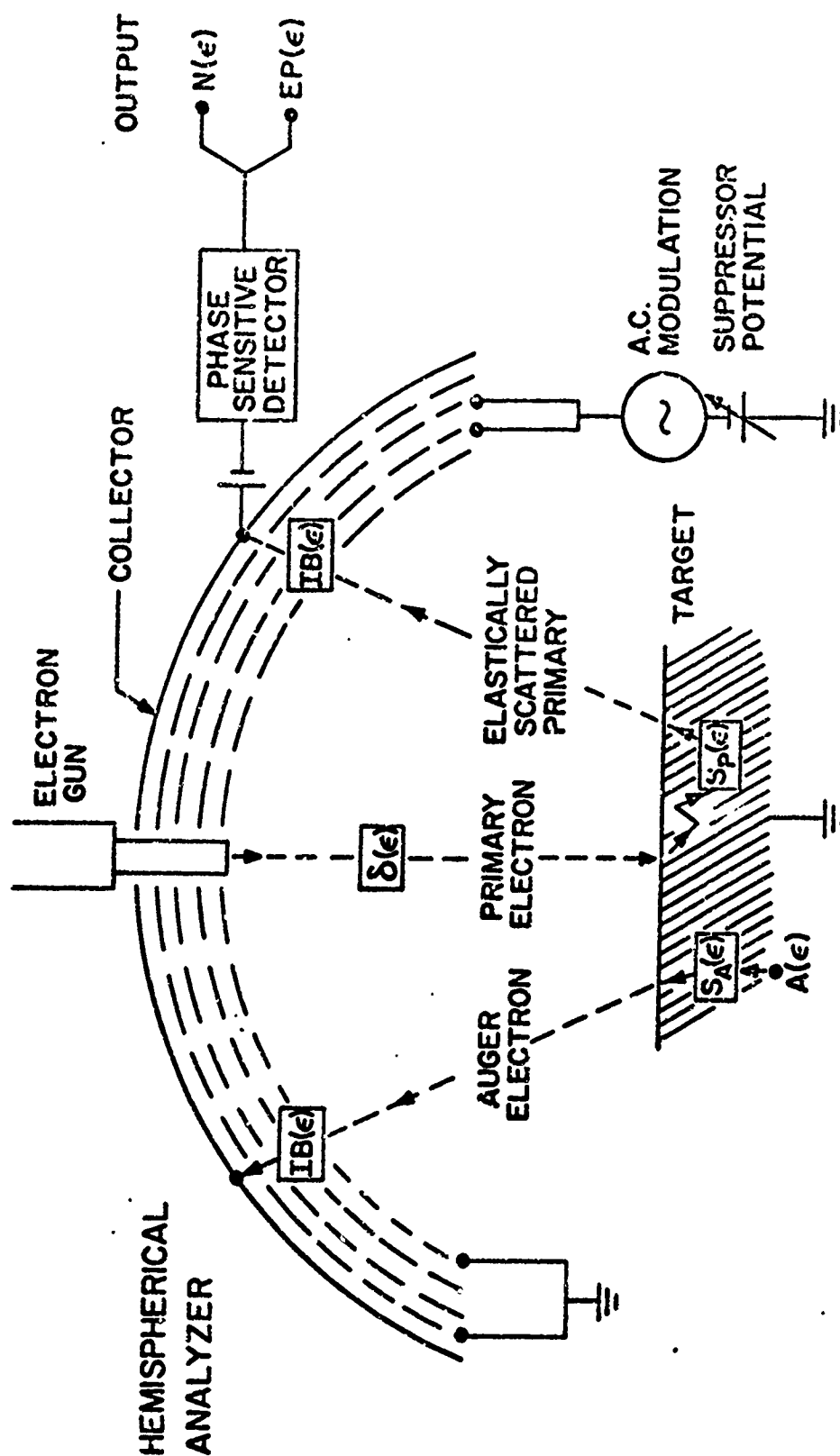
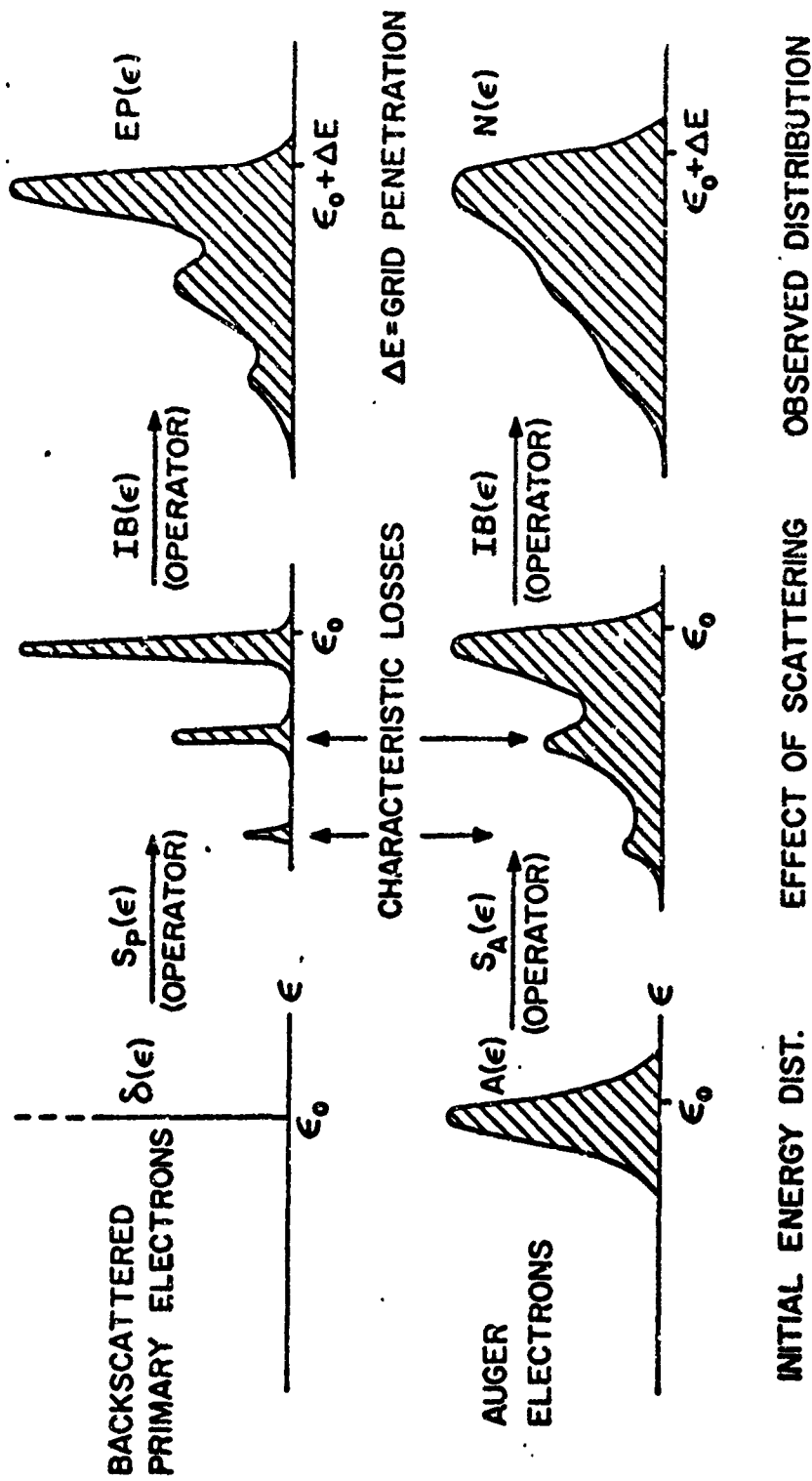


Fig. 56 Phenomenological model for Auger and primary electron energy broadening in a LEED-Auger spectrometer. The parameters  $S_A(\epsilon)$ ,  $S(\epsilon)$ , describe the scattering of each specie within the solid and  $IB(\epsilon)$  the subsequent instrumental broadening.



$$N(\epsilon) = \int_{-\infty}^{+\infty} A(\epsilon') EP(\epsilon - \epsilon') d\epsilon'$$

ELECTRON ENERGY -  $\epsilon$

Fig. 57 Illustration of hypothetical energy broadening encountered by Auger and primary electrons through scattering in the solid and instrument broadening.

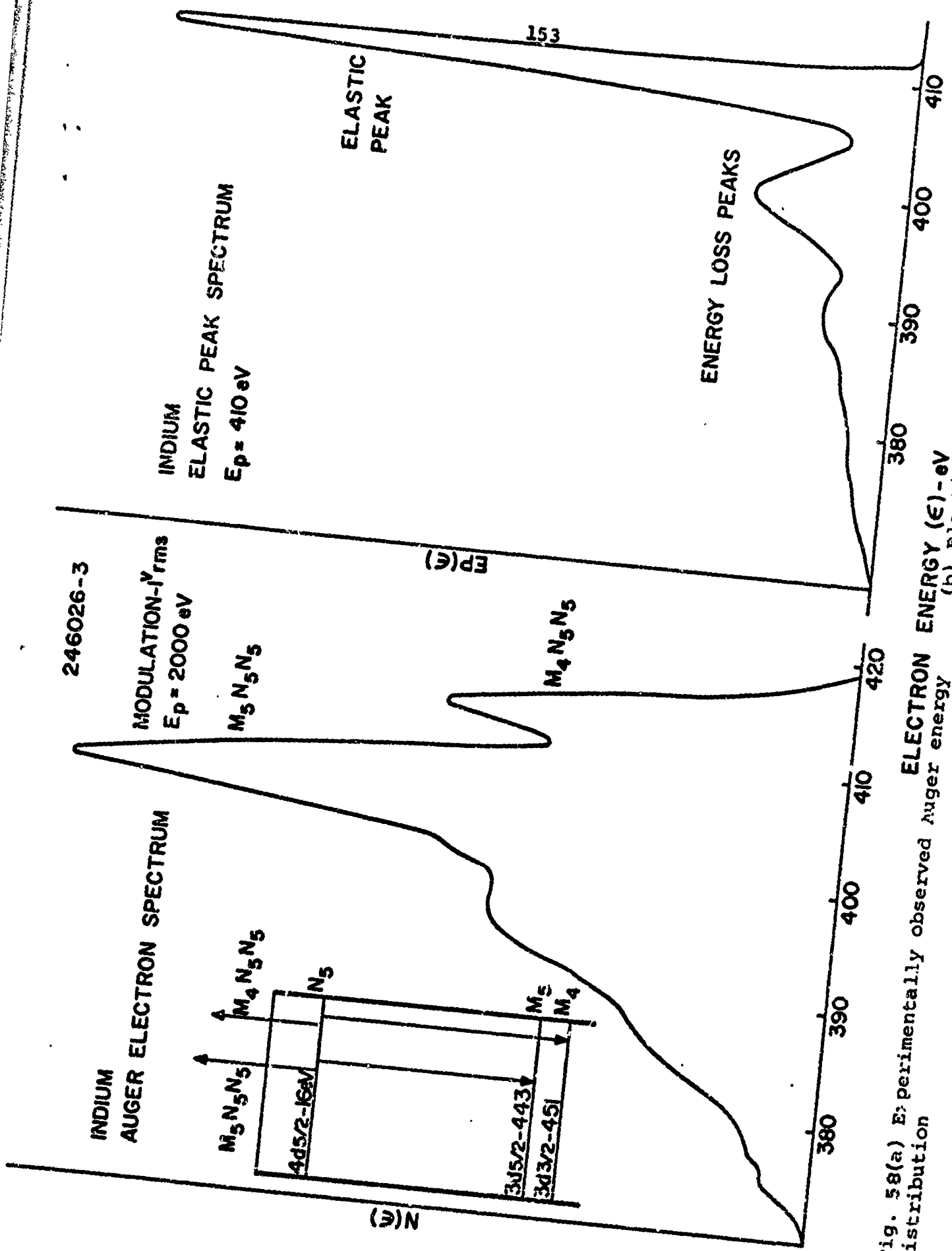
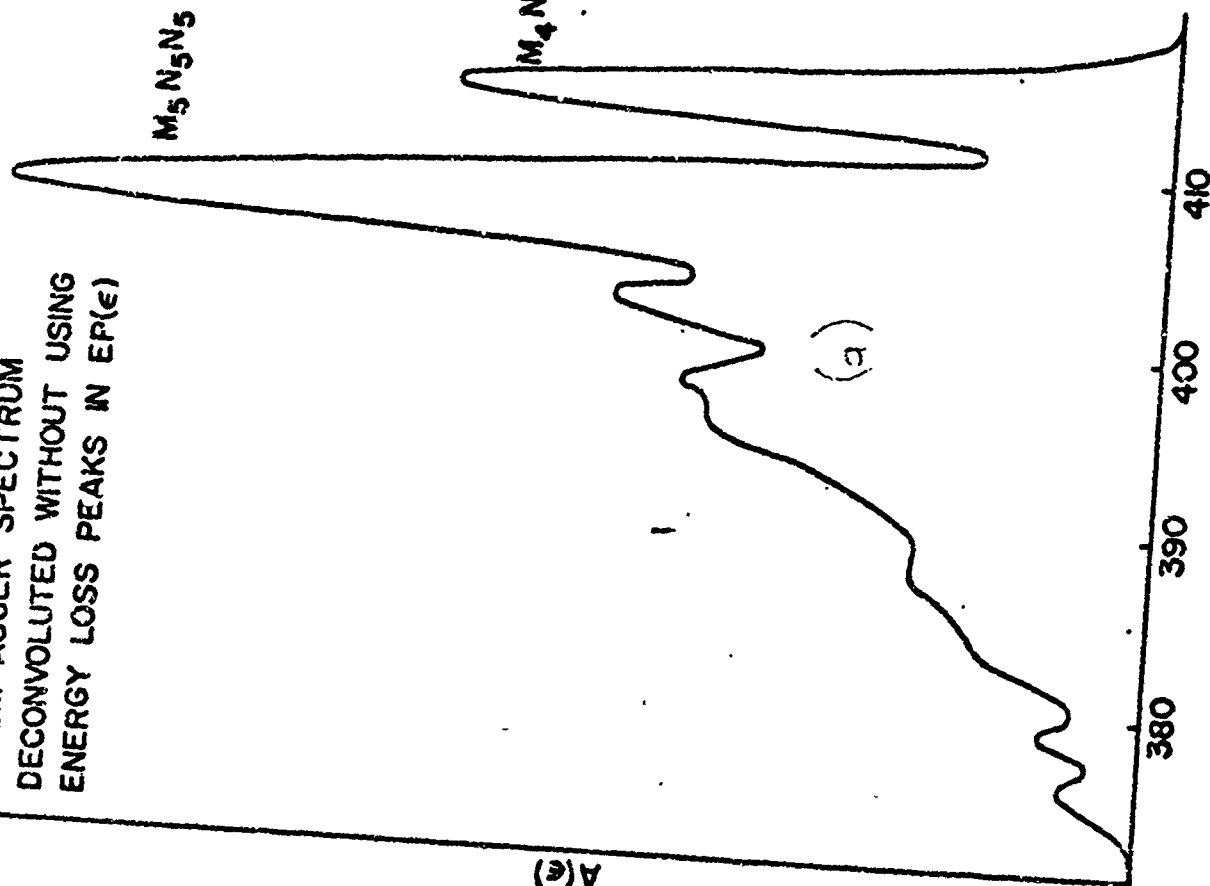


Fig. 58(a) Experimentally observed Auger energy distribution

INDIUM AUGER SPECTRUM  
DECONVOLUTED WITHOUT USING  
ENERGY LOSS PEAKS IN  $EP(\epsilon)$



INDIUM AUGER SPECTRUM  
DECONVOLUTED USING ENTIRE  
 $EP(\epsilon)$  SPECTRUM  
 $M_5N_5N_5$

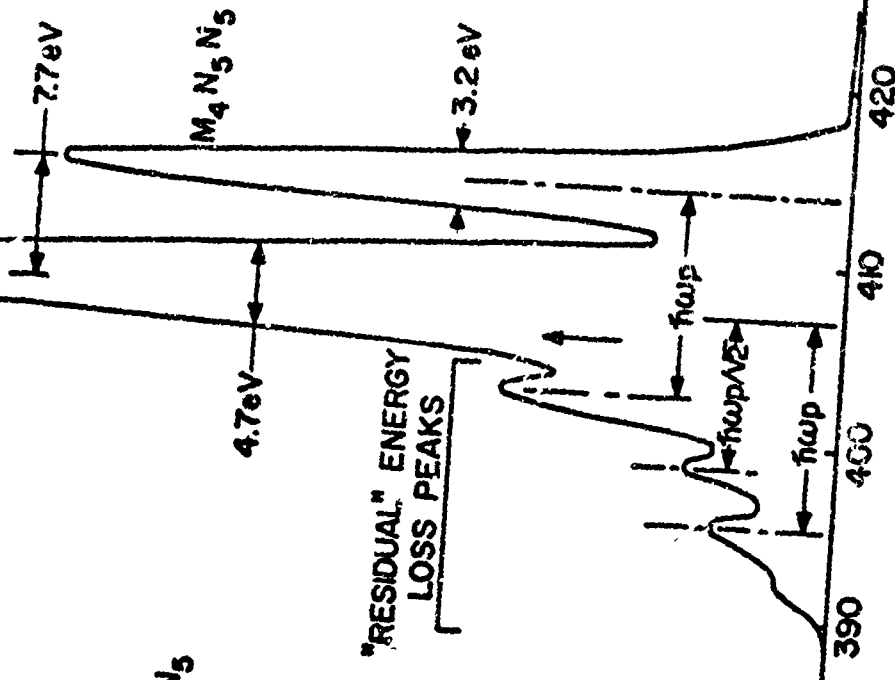


Fig. 59(a) In -  $M_{4,5}N_5N_5$  Auger spectrum deconvoluted using only the main elastic peak of  $EP(\epsilon)$   
 (b) In -  $M_{4,5}N_5N_5$  Auger spectrum, deconvoluted using entire  $EP(\epsilon)$  spectrum.

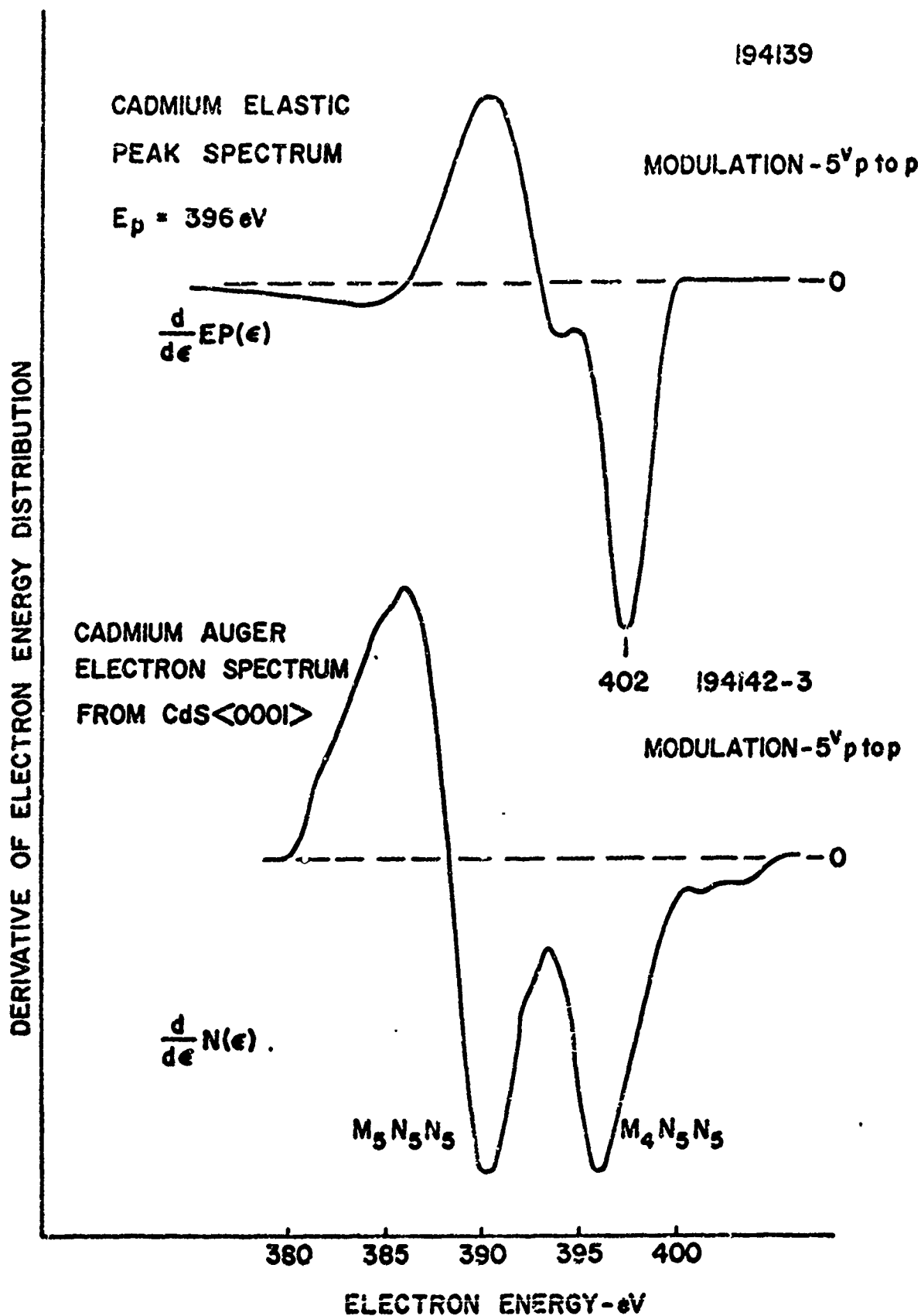


Fig. 60 Experimentally measured derivatives of the elastic peak and Cd -  $M_{4,5} N_5 N_5$  Auger energy distributions from CdS (0001).

194142-3, 194139-2

CADMIUM -  $\text{CdS} \langle 0001 \rangle$   
MODULATION -  $5^{\text{V}}$  p to p

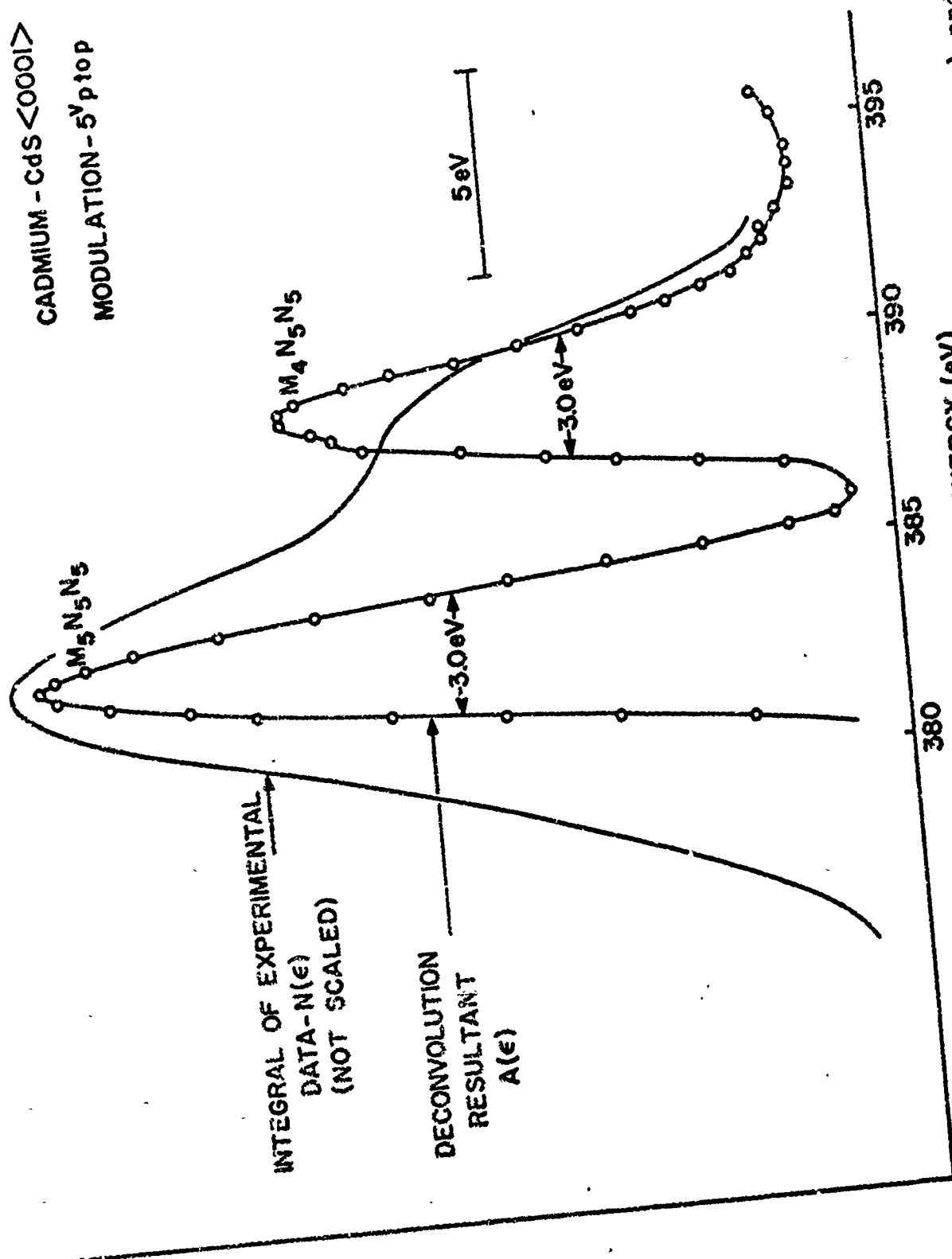


Fig. 61 Comparison of the integrated experimental data (Fig. A5 - bottom) and the deconvoluted Cd - M<sub>4,5</sub>N<sub>55</sub> spectrum.



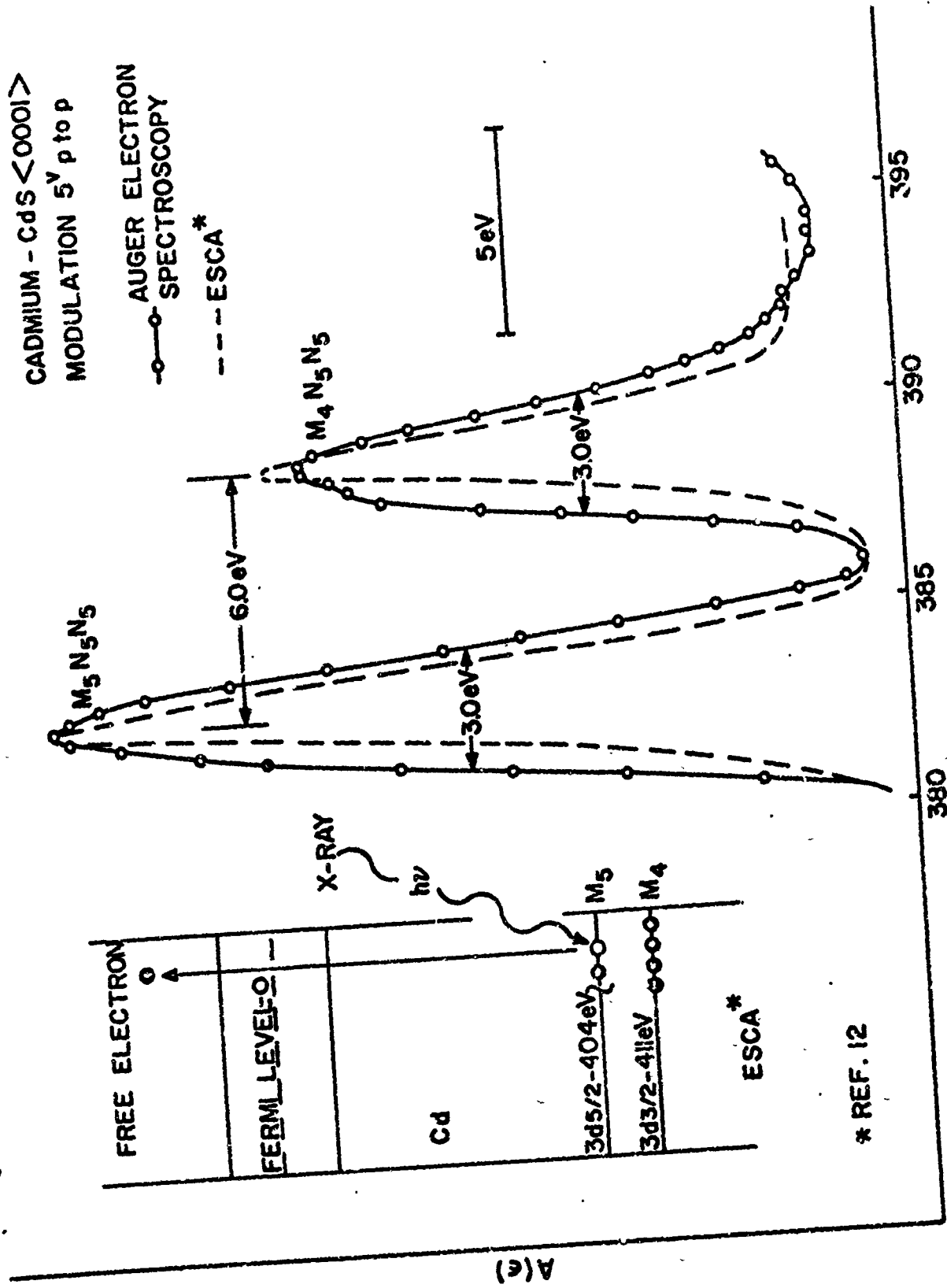


Fig. 62 Schematic energy level diagram showing the origin of the ESCA M<sub>4,5</sub> photoelectric doublet and a comparison of this photoelectric data with the deconvoluted M<sub>4,5</sub>N<sub>5</sub>N<sub>5</sub> spectrum.

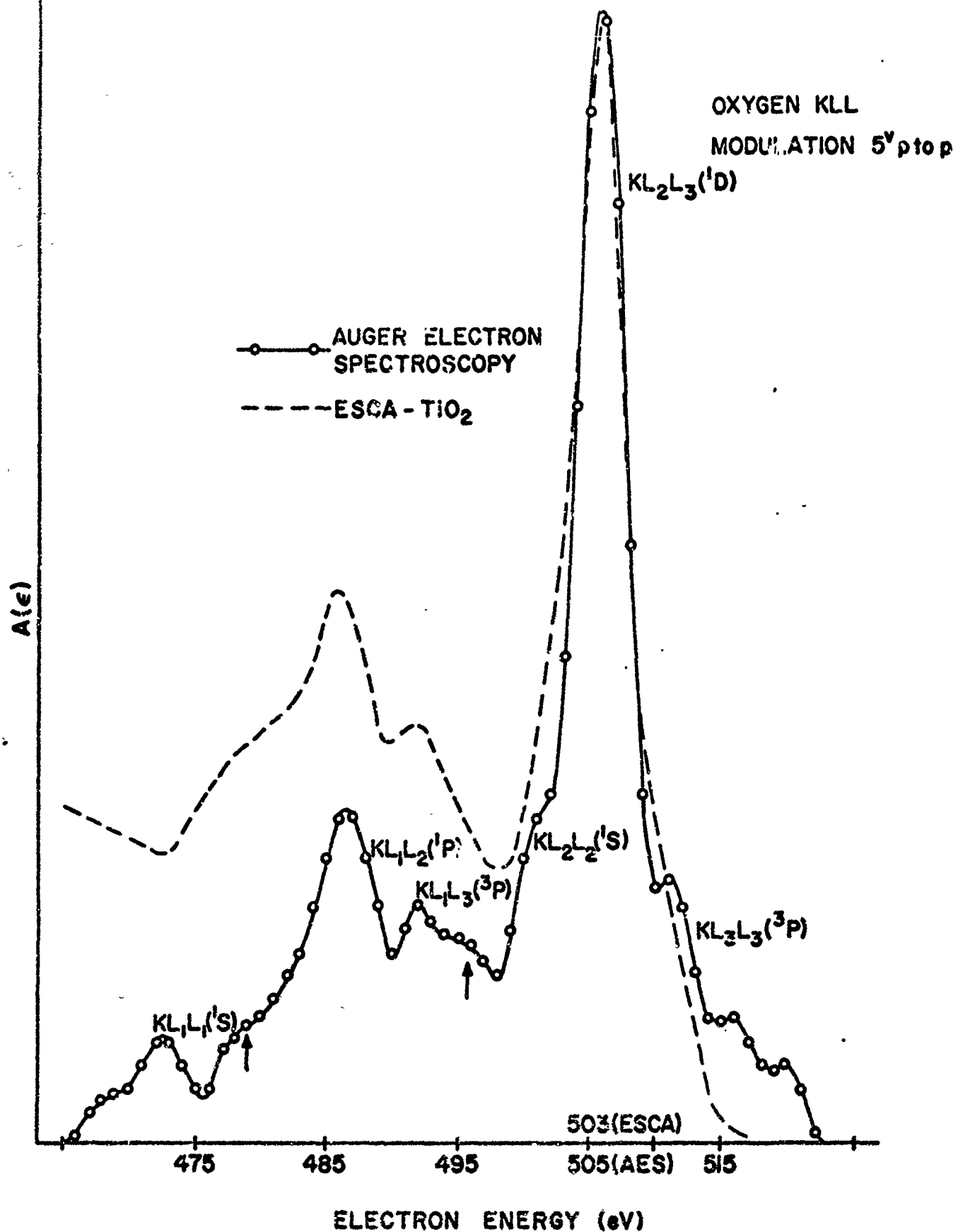


Fig. 63 Comparison of oxygen KLL Auger spectra from  $\text{TiO}_2$  using the ESCA technique and from oxidized Ti using deconvoluted AES data.

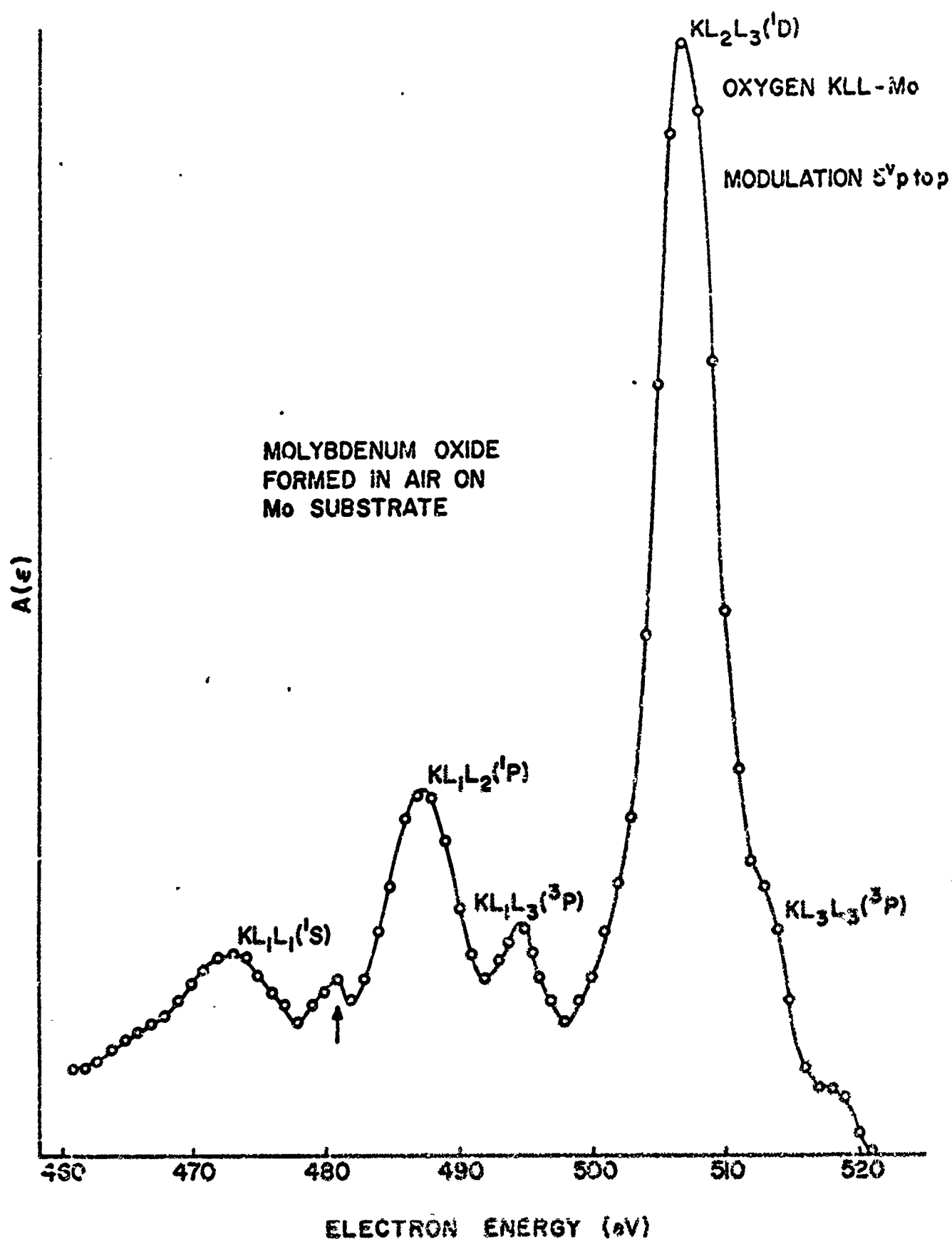


Fig. 64 Oxygen KLL spectrum of oxidized Mo, using deconvoluted AES data, showing the similarity in structure with O-Ti of Fig. A8.

